



HAL
open science

High-Tc Josephson mixers for terahertz detection

Maxime Malnou

► **To cite this version:**

Maxime Malnou. High-Tc Josephson mixers for terahertz detection. Condensed Matter [cond-mat]. Université Pierre et Marie Curie - Paris VI, 2015. English. NNT: . tel-01213100v1

HAL Id: tel-01213100

<https://theses.hal.science/tel-01213100v1>

Submitted on 7 Oct 2015 (v1), last revised 7 Dec 2015 (v2)

HAL is a multi-disciplinary open access archive for the deposit and dissemination of scientific research documents, whether they are published or not. The documents may come from teaching and research institutions in France or abroad, or from public or private research centers.

L'archive ouverte pluridisciplinaire **HAL**, est destinée au dépôt et à la diffusion de documents scientifiques de niveau recherche, publiés ou non, émanant des établissements d'enseignement et de recherche français ou étrangers, des laboratoires publics ou privés.

UNIVERSITÉ PIERRE ET MARIE CURIE - PARIS VI
École doctorale Physique en Île de France



THESIS

Specialization: Physics

by

Maxime MALNOU

High-Tc Josephson Mixers For Terahertz Detection

Presented to obtain the degree of

Doctor of the University Pierre and Marie Curie

Manuscript defended on July 7th, 2015
in front of the committee:

Laurence MÉCHIN	GREYC - ENSICAEN (Caen)	Referee
Olivier BOURGEOIS	TPS - Institut Néel (Grenoble)	Referee
Yuri DIVIN	IRE - RAS (Moscow)	Examiner
Carlo SIRTORI	MPQ - Paris 7 (Paris)	Examiner
Jérôme TIGNON	LPA - ENS (Paris)	Examiner
Roch ESPIAU DE LAMAESTRE	LETI - CEA (Grenoble)	Examiner
Jérôme LESUEUR	LPEM - ESPCI (Paris)	Supervisor
Nicolas BERGEAL	LPEM - ESPCI (Paris)	Supervisor

Laboratoire de Physique et d'étude des
Matériaux
École Supérieure de Physique et de
Chimie Industrielles
10 rue Vauquelin
75005 Paris

École doctorale Physique en Île de France
4 place Jussieu
75 005 Paris

Remerciements

Nombreuses sont les personnes qui m'ont accompagné, formé, soutenu tout au long de ces années d'études et de thèse. Elles ont permis que mon travail se déroule sous les meilleurs auspices. Sans prétendre à l'exhaustivité, je voudrais citer ici les noms de celles et ceux qui m'ont marqué et ont influencé mon parcours.

En premier lieu je souhaite adresser mes plus chaleureux remerciements à Nicolas Bergeal, Jérôme Lesueur et Cheryl Feuillet-Palma. Nicolas, Jérôme, jusqu'au bout nos discussions furent passionnantes et fécondes ; Cheryl, je suis grâce à toi initié aux arcanes de la lithographie électronique. Rigueur, perfectionnisme, technicité, goût pour l'effort, telles sont les valeurs que vous m'avez enseignées en étant mes mentors. Et, au-delà de vos connaissances scientifiques, pour lesquelles j'ai une admiration sans borne, je me suis épanoui dans votre équipe grâce à vos grandes qualités humaines.

Je tiens ensuite à remercier nos collaborateurs, sans qui ce travail n'aurait jamais vu le jour. Christian Ulysse au Laboratoire de Photonique et Nanostructures, dont la maîtrise des technologies de fabrication est sans égal, et avec lequel je me suis trouvé de nombreux points communs. Les équipes de salle blanche de l'Ecole Normale Supérieure et de Paris 7, avec en tête de file Michael Rosticher, dont je me souviendrai des innombrables services rendus. Yann Le Gall du Laboratoire ICube à Strasbourg, qui a effectué toutes les implantations ioniques, avec qui j'ai pu échanger tant sur le plan professionnel que personnel, discutant avec lui tout autant d'électronique de puissance que de l'Alleluia du messie de Haendel. Javier Villegas et Juan Trastoy-Quintela de Thales, qui m'ont fait participer à leurs projets, et grâce auxquels le vivant débat sur les simulations d'implantation a permis d'approfondir nos connaissances. Pascal Febvre de l'Université de Savoie, dont la très grande expertise en matière de circuits supraconducteurs et micro-ondes a été capitale. Olivier Seron et Sophie Djordjevic au Laboratoire National de Métrologie et d'Essais d'une part, et Alexandre Feret à l'Observatoire de Paris d'autre part, dont le prêt des sources térahertz m'a permis d'effectuer la majeure partie de mes expériences à haute fréquence. J'ajoute Thibaut Vacalet à l'Observatoire de Paris, dont la découpe des échantillons a été très utile. Enfin, je remercie Emmanuel Géron, Thierry Ditchi et Stéphane Holé de notre laboratoire, pour leur enseignement sur les thématiques d'adaptation d'impédances, et pour la disponibilité de leur matériel pour les micro-ondes, ainsi que Ludovic Olanier, qui a beaucoup aidé à la réalisation des pièces mécaniques du cryostat.

Je veux aussi témoigner mon profond respect à Thomas Wolf, dont j'ai repris les travaux, et dont les écrits ont été d'une aide précieuse, de même qu'à Rob Schoelkopf, dont le manuscrit de thèse est un modèle de clarté, et qui m'a beaucoup apporté lors de notre discussion.

Mais la liste de ceux ayant influencé mon parcours serait incomplète si je ne citais pas mes autres mentors. Je pense notamment à Roch Espiau de Lamaestre avec qui j'ai eu le plaisir de travailler par le passé, comme à Pascale Nouchi et son équipe d'optique à Thales. Il y a aussi Brigitte Leridon, qui a éveillé en moi la curiosité et le goût pour les matériaux supraconducteurs. Et puis bien sûr je remercie Michel Devoret, dont le génie en sciences physiques n'a d'égal que la modestie et l'humanité. Je n'aurais probablement jamais persévéré dans cette voie sans son

exemple et ses conseils avisés, prodigués depuis tant d'années.

Je remercie Laurence Méchin et Olivier Bourgeois pour avoir accepté d'être rapporteurs de cette thèse, ainsi que tous les membres du jury, Yuri Divin, Carlo Sirtori, Jérôme Tignon, Roch Espiau de Lamaestre, pour avoir accepté d'évaluer mes travaux.

Ces trois années ont été agrémentées de réflexions physiques et de moments de bonne humeur au sein du groupe grâce à l'apport indéfectible de Simon, Alexis et Saphia, un grand merci à eux trois. Par ailleurs, les joyeuses discussions autour de la table du déjeuner (et autour de celles de la rue Mouffetard) avec l'équipe des Quantum Dots furent un réel plaisir, grâce notamment à leurs thésards, Sophie, Gary et Silvia. J'ai aussi une pensée particulière pour Nicolas Lequeux et Emerson Giovanelli, qui m'ont formé et permis d'enseigner la microscopie électronique. Plus généralement, je remercie l'ensemble des membres du LPEM, permanents et administratifs, notamment Sophie et Marie-Claude, qui ont veillé à ce que ma thèse se déroule dans de bonnes conditions.

Enfin à titre personnel je remercie mes parents, Marie-France et Jean-François pour leur soutien inconditionnel tout au long de mes longues et mystérieuses années d'études. De même, je suis extrêmement reconnaissant envers mes amis de toujours, Arthur, Vladimir, Pierre-Yves, Baptiste, Thomas et Olivier. Dans leur inébranlable présence (ainsi que dans les innombrables sets et gyozas que nous avons partagés), j'ai puisé stabilité et sérénité. A l'heure où nos routes s'éloignent géographiquement, j'ose croire que nos liens sont inoxydables.

High-Tc Josephson Mixers For Terahertz Detection

Abstract

In this thesis, we used a high- T_c superconducting material, $\text{YBa}_2\text{Cu}_3\text{O}_7$, to make a heterodyne mixer. We aimed at evaluating its ability for terahertz detection. We also worked towards the fabrication of an on-chip local oscillator, designed with an array of Josephson junctions. The originality of this study stems from a unique way of engineering Josephson junctions, based on ion irradiation.

We described the complex physics of ion irradiated Josephson junctions through a modified version of quasi-classical Usadel equations, which have originally been derived for non-homogenous low- T_c superconductivity.

The d-c electronic transport measurements showed that our irradiated Josephson junctions are well described by the resistively shunted junction model. Furthermore, we explained the high-frequency mixing operations with the three-port model, and proved the heterodyne detection of signals up to 400 GHz. We identified the heterodyne conversion efficiency as a product of three terms: two depending on impedance mismatches and the third one characterizing the intrinsic down-conversion ability of the Josephson junction. The dynamic range of the mixer, its conversion efficiency and its dependence on local oscillator power were measured and found to be in agreement with simulations.

An array of synchronized junctions is necessary to create a powerful and spectrally pure local oscillator from Josephson oscillations. We identified the external locking as the only efficient mechanism to synchronize $\text{YBa}_2\text{Cu}_3\text{O}_7$ irradiated junctions, showing its effect in simulated systems. We also reported a first evidence of synchronization in a two dimensional array of irradiated Josephson junctions.

Keywords

Terahertz; superconductivity; detectors; heterodyne mixing; Josephson effect; $\text{YBa}_2\text{Cu}_3\text{O}_7$.

Mélangeurs Josephson à Haute Température Critique Pour la Détection TéraHertz

Résumé

Cette thèse porte sur la fabrication et caractérisation d'un mélangeur hétérodyne, fabriqué à partir d' $\text{YBa}_2\text{Cu}_3\text{O}_7$, un matériau supraconducteur à haute température critique. Nous avons évalué son potentiel pour la détection d'ondes térahertz.

La physique complexe des jonctions irradiées a été correctement décrite en modifiant légèrement les équations quasi-classiques d'Usadel, originellement développées pour les supraconducteurs inhomogènes à basse température critique.

Les mesures de transport électronique ont montré que nos dispositifs respectent le modèle de la jonction résistivement shuntée. Nous avons expliqué leur fonctionnement à haute fréquence au moyen du modèle à trois ports, et démontré la détection d'ondes jusqu'à 400 GHz. Nous

avons identifié l'efficacité de conversion du mélange hétérodyne comme le produit de trois termes: deux rendent compte des adaptations d'impédances en entrée et sortie du mélangeur, le troisième caractérise la conversion à basse fréquence des signaux térahertz. La puissance de l'oscillateur local nécessaire, l'étendue dynamique du mélangeur ainsi que son efficacité de conversion ont été mesurées, s'accordant bien avec les simulations numériques.

Le recours à un réseau de jonctions Josephson synchronisées est incontournable pour parvenir à créer un oscillateur local puissant et spectralement fin à partir de l'oscillation propre des jonctions. Nous avons identifié le verrouillage par une boucle externe comme l'unique mécanisme efficace de synchronisation et simulé son effet. Enfin nous avons mesuré la première signature d'une synchronisation dans un réseau à deux dimensions de jonctions irradiées.

Mots-clefs

Térahertz ; supraconductivité ; détecteurs ; mélange hétérodyne ; effet Josephson ; $\text{YBa}_2\text{Cu}_3\text{O}_7$.

Contents

Introduction	13
1 Terahertz technologies	15
1.1 Range and specifics	16
1.1.1 Range	16
1.1.2 Benefits	16
1.1.3 Limitations	18
1.2 Applications	20
1.2.1 Pharmaceutical and medical sciences	20
1.2.2 Security	20
1.2.3 Communications	21
1.2.4 Astronomy and Astrophysics	22
1.3 Sources	23
1.3.1 Frequency up/down conversion	23
1.3.2 Radiation from accelerated charges	24
1.3.3 THz lasers	27
1.4 Detectors	29
1.4.1 Figures of merit for a detector	29
1.4.1.1 SNR, NEP, T_N	29
1.4.1.2 Square-law detection	30
1.4.1.3 Electrical noise, total NEP of a heterodyne detector	32
1.4.2 Direct detectors	33
1.4.2.1 Thermal sensors	34
1.4.2.2 Pair breaking photon detectors	35
1.4.3 Coherent detectors	36
1.5 Conclusion - terahertz technologies and high- T_c superconductors	38
2 Fabrication of irradiated Josephson junctions	41
2.1 Fabrication of high- T_c Josephson junctions	42
2.1.1 Josephson junctions with intrinsic interfaces	42
2.1.2 Josephson junctions with extrinsic interfaces	43
2.1.3 An alternative: irradiated Josephson junctions	43
2.2 Ion Implantation	44
2.2.1 Transport of ions into matter	44
2.2.2 Plain sheet dpa	46
2.2.3 Implantation through a mask	47
2.3 Ion irradiation on $\text{YBa}_2\text{Cu}_3\text{O}_7$	48
2.3.1 Reduction of T_c	48
2.3.2 Transport measurements	50

2.4	Fabrication steps	51
2.4.1	Structuring the gold layer	51
2.4.2	Patterning the $\text{YBa}_2\text{Cu}_3\text{O}_7$ layer	51
2.4.3	Creating the weak-link.	53
2.5	Other groups fabricating ion irradiated junctions	55
3	Electronic transport in $\text{YBa}_2\text{Cu}_3\text{O}_7$ irradiated Josephson junctions	57
3.1	Theory of the Josephson effect	57
3.1.1	Quasiparticle tunneling in SIS junctions	58
3.1.2	Josephson equations	60
3.1.3	Interpretation of the Josephson equations	61
3.2	Transport measurements in ion irradiated junctions	62
3.2.1	RT curves	63
3.2.2	IV curves	63
3.2.3	Critical current	64
3.3	RCSJ - RSJ model	64
3.3.1	Ideal weak-link Josephson junction	65
3.3.2	Dynamics of the junction	67
3.3.2.1	Under-damped regime	67
3.3.2.2	Over-damped regime	68
3.3.3	Model of a real Josephson junction	70
3.3.3.1	Fluctuations	70
3.3.3.2	Numerical resolution	71
3.4	Conclusion on the electronic transport	72
4	Proximity effects in irradiated Josephson junctions	73
4.1	Proximity effects in metals and damaged superconductors	74
4.1.1	SNS and SS'S	74
4.1.2	Critical current	75
4.2	Theory of proximity effects	75
4.2.1	Gorkov - Nambu theory	76
4.2.2	Perturbative expansion: Eilenberger equation	78
4.2.3	Usadel equations	78
4.2.4	θ and χ parametrization	79
4.3	Adaptation for irradiated Josephson junctions	80
4.3.1	Usadel equations in irradiated $\text{YBa}_2\text{Cu}_3\text{O}_7$	80
4.3.2	Simulations results	81
4.4	Conclusion on the quasi-classical approach of proximity effects	84
5	D-c and a-c characterization of the Josephson mixer	85
5.1	Experimental setups	86
5.1.1	RT curves: low frequency a-c setup	86
5.1.2	IV curves: d-c setup	86
5.2	D-c and a-c measurements	88
5.2.1	Josephson regime	88
5.2.2	Flux-flow regime	89
5.2.3	Shapiro steps	90
5.2.3.1	Voltage source model	90
5.2.3.2	Shapiros steps on IV curves	91
5.2.3.3	Differential resistance	93

5.3	Comparison of the RSJ model with experimental data	95
5.3.1	Normal resistance at low current bias	95
5.3.1.1	Saturated r-f	95
5.3.1.2	Linear extrapolation of the normal state resistance	95
5.3.1.3	Derivative of IV curves	95
5.3.2	Higher current biases	96
5.3.3	Fit of IV curves and Shapiro steps	97
5.4	Characteristics of other fabricated junctions	99
5.4.1	RT curves, critical currents, normal resistances	99
5.4.2	500 nm wide junctions and annealing	100
5.5	Conclusion on the d-c characterization	100
6	Three-port model	103
6.1	Impedance matrix	103
6.1.1	Frequencies of interest in heterodyne detection	104
6.1.2	Definition of the mixer's impedance matrix	104
6.1.3	Terms of the impedance matrix as a function of currents and voltages	106
6.1.4	Discussion on the impedance matrix terms	107
6.2	Conversion efficiency	108
6.2.1	Definition	108
6.2.2	Mixer connected to a circuit	108
6.2.3	Conversion efficiency in terms of impedances	109
6.2.4	Numerical simulations, principle	110
6.3	Physical approach of the Josephson mixer	111
6.4	Conclusion on the three-port model	112
7	High frequency mixing properties of the Josephson mixer	113
7.1	Experimental setup	113
7.1.1	Test bench	113
7.1.2	Microwave design and r-f reading line	115
7.1.2.1	Antenna	115
7.1.2.2	CPW lines	116
7.1.2.3	Dielectric microwave line	117
7.1.3	Conversion efficiency in the experimental setup	117
7.2	Heterodyne detection of high frequencies	118
7.2.1	Modulation of the intermediate frequency power	119
7.2.2	Dynamic range	120
7.2.2.1	Evaluation of losses and gain in the setup	120
7.2.2.2	Dynamic range measurements	121
7.2.3	Influence of the LO power	122
7.2.4	Conversion efficiency simulations	123
7.2.5	Mixing beyond 140 GHz	124
7.3	Conclusion on the high-frequency mixing measurements	124
8	Improvements and perspectives for the Josephson mixer	127
8.1	An Array of Josephson junctions as a detector	127
8.2	Optimization of the design - electromagnetic simulations	128
8.2.1	Antenna	128
8.2.2	Chebyshev impedance transformers	129
8.2.3	Chebyshev filters integrated to the antenna	130

8.3	Noise measurements	132
8.3.1	Origin of noise	132
8.3.2	Measurement of noise	134
8.4	Self-pumped Josephson mixer	135
8.5	Conclusion on the improvements and perspectives	138
9	Josephson oscillators: synchronization of Josephson junctions	139
9.1	Effects of junctions synchronization	140
9.1.1	Need for arrays of Josephson junctions	140
9.1.1.1	Linewidth of synchronized junction arrays	140
9.1.1.2	Power of synchronized junction arrays	141
9.1.2	Rules of thumb to achieve phase-locking	142
9.1.3	Coupling mechanisms	142
9.1.3.1	Short range interactions	142
9.1.3.2	Long range interactions	143
9.2	Designs and circuitry for synchronization	144
9.2.1	Possible designs for junction arrays	145
9.2.1.1	1D arrays	145
9.2.1.2	2D arrays	146
9.2.2	Effect of an external feedback loop	147
9.2.2.1	Open-loop circuit	148
9.2.2.2	Closed-loop: LR shunt	148
9.2.3	Simulation results	150
9.2.3.1	Overlapping <i>IV</i> curves	150
9.2.3.2	Parameter spread	151
9.3	Characterization of externally coupled Josephson junctions	152
9.3.1	Fabricated 2D array	152
9.3.2	Evidences of synchronization in the <i>IV</i> curves	153
9.4	Conclusion on the synchronization of Josephson junctions	155
	Conclusion	157
A	Fluctuations of a thermal and coherent radiation on a direct detector	159
A.1	Absorbed power	159
	Thermal radiation	159
	Coherent radiation	160
A.2	Fluctuations	160
	Thermal radiation	160
	Coherent radiation	161
A.3	Number of collected modes	161
A.4	NEP in direct detection	162
B	Fabrication details of $\text{YBa}_2\text{Cu}_3\text{O}_7$ irradiated Josephson junctions	165
B.1	Step 1: structuring the gold layer	165
B.2	Step 2: patterning the $\text{YBa}_2\text{Cu}_3\text{O}_7$ layer	166
B.3	Step 3: creating the weak-link.	167
C	Numerical resolution of the RSJ equations	169

D	Numerical resolution of the Usadel equations	171
D.1	Equations to solve	171
D.2	Boundary conditions	171
D.3	Algorithm	172
E	Quasi-static impedance of a CPW line	173
F	Expression of the matrix impedance terms	175
F.1	Complex differentiation	175
F.2	Replacement of the differential terms	176
G	Expression of conversion efficiency with impedances	179
	Bibliography	181

Introduction

Lying between classical electronics and optics, research in the terahertz range has been driven over the past fifty years by its huge importance in astronomy and astrophysics. Since the early 2000s, many of its key aspects appeared also beneficial for many other fields, such as communications, medical sciences or security controls.

The ultimate sensitivity and spectral resolution that requires space observations leads inevitably to use superconducting heterodyne detectors. In this frame, sensors fabricated from low- T_c superconductors, typically Aluminum and Niobium, were improved over the years up to the quantum limit. Nowadays, superconducting-insulating-superconducting (SIS) junctions or superconducting hot electron bolometers (HEB) reach breathtaking performances, and work up to several terahertz. However, they lack autonomy, limited by the requirement of very low bath temperatures, and they still need fairly high local oscillator powers.

In this thesis, we took an alternative route. We used $\text{YBa}_2\text{Cu}_3\text{O}_7$, a high- T_c superconducting material, to fabricate a heterodyne mixer. Up to date, no clean tunnel barrier exists in high- T_c materials, therefore one cannot fabricate high- T_c SIS junctions. Thus, the nonlinearity inherent to mixers either pertains to the hot electron bolometer mechanism, or to the Josephson effect. The latter is particularly interesting, because not only a Josephson junction can be used as a mixer, but it also oscillates naturally in the terahertz range. Therefore we endeavored to create, with the same technology, a detector and a local oscillator source. Our hope to make this possible stems from a unique way of fabricating Josephson junctions, based on ion irradiation. It allows a competitive advantage in design flexibility, where we can position as many junctions as we want anywhere in the $\text{YBa}_2\text{Cu}_3\text{O}_7$ superconducting film.

The high- T_c based technology offers obvious advantages compared to its low- T_c alter ego: one can work at much higher temperatures, and possibly also at higher frequencies. Indeed $\text{YBa}_2\text{Cu}_3\text{O}_7$ has a superconducting gap at about 30 meV, corresponding to a cut-off frequency of 7.3 THz, much higher than with conventional low- T_c materials. Along the way, we will also show that the local oscillator power that needs the Josephson mixer is much lower than the one required in SIS or HEB mixers. However, much work remains to be done, so as to compete with these existing technologies, in terms of sensitivity and spectral resolution. Our work in this thesis has been to evaluate the potential of high- T_c Josephson junctions as THz mixers and sources.

We review in the first chapter of this manuscript the existing terahertz technologies, the main fields of applications, and we define the figures of merit that are used to characterize any heterodyne detector. Then chapter two focuses on the fabrication process. It details in particular the ion implantation technique, supported by numerical simulations. Chapter three is a general discussion on the electronic transport in $\text{YBa}_2\text{Cu}_3\text{O}_7$ irradiated Josephson junctions and introduces the resistively shunted junction (RSJ) model, an equivalent circuit for weak-link Josephson junctions. Chapter four explains the origin of the Josephson coupling, arising from proximity effects. Numerical simulations lead to experimental sets of parameters that explain how to choose the implantation dose.

The second part of this thesis focuses on the experiments that we performed. Chapter five

shows the characterization of our irradiated Josephson junctions through electronic transport measurements. Chapter six introduces the three-port model, a prerequisite knowledge to understand high-frequency mixing experiments. Allied with the RSJ model, we explain the behavior of the Josephson mixer and fit the experimental data at various operating frequencies in chapter seven. Next, in chapter eight we propose several roads to improve the efficiency of the Josephson mixer. They should be investigated in further studies. Finally, chapter nine deals with the synchronization of Josephson junctions, mandatory for the fabrication of a strong local oscillator source. We present the methods to achieve phase-locking, argued by promising numerical simulations, and we show the first results of synchronization in a two-dimensional Josephson junction array.

Chapter 1

Terahertz technologies

Contents

1.1	Range and specifics	16
1.1.1	Range	16
1.1.2	Benefits	16
1.1.3	Limitations	18
1.2	Applications	20
1.2.1	Pharmaceutical and medical sciences	20
1.2.2	Security	20
1.2.3	Communications	21
1.2.4	Astronomy and Astrophysics	22
1.3	Sources	23
1.3.1	Frequency up/down conversion	23
1.3.2	Radiation from accelerated charges	24
1.3.3	THz lasers	27
1.4	Detectors	29
1.4.1	Figures of merit for a detector	29
1.4.2	Direct detectors	33
1.4.3	Coherent detectors	36
1.5	Conclusion - terahertz technologies and high-T_c superconductors	38

Over the past decade, there has been a tremendous effort of the scientific community towards the emergence of terahertz (THz) technologies. Around 15000 scientific articles with the word "terahertz" in their title were published since 2010, and more than 23000 since 2005. The main reasons for such a success are the very wide range of applications and potential improvements that THz technologies can and will bring.

However, manipulating THz waves still remains a challenge due to the lack of performant, affordable, and integrable sources and detectors [156], and scientific breakthroughs are yet to be made in order to master and use daily the whole THz range. There is no doubt that many technologies will be involved and along with them, the next decade will see the emergence of standards in this frontier science between optics and electronics. Many applications have already emerged today, others are within reach.

1.1 Range and specifics

1.1.1 Range

The THz region has been qualified as a "technological gap" due to the lack of suitable sources and detectors (not to be confused with the energy gap between the valence and the conduction band of semi-conductors). There is no standard definition, but it is commonly referred as the region spanning from 0.1 to 10 THz [185, 76, 124, 173, 146]. It merges with other existing spectral bands such as the millimeter-wave band, the submillimeter-wave band and the far infrared (FIR) band. Thus, on the lower part of the electromagnetic spectrum lies the microwave frequencies (300 MHz - 300 GHz) and on the upper part the FIR radiations (1 to 12 THz). Depending on the community, electronics or optics, different units are used to refer at the same photons. Usually, the microwave community speaks in terms of frequency or energy, whereas opticians speak in terms of wavelength or wave number. Figure 1.1 makes the correspondence between these different units and in this thesis we will mostly use the frequency scale.

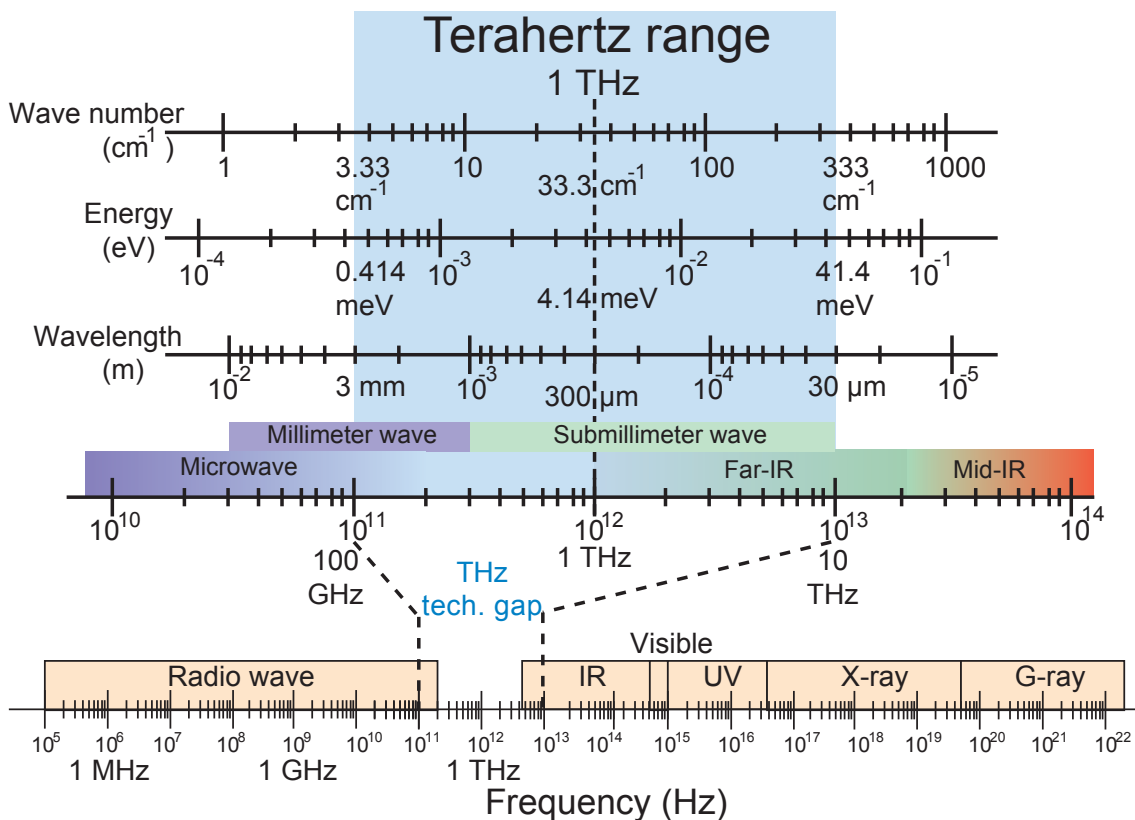


Figure 1.1: Terahertz band in the electromagnetic spectrum. Adapted from [124].

1.1.2 Benefits

There are four main reasons that explain the numerous fields of applications for THz radiations.

Resolution. First, the photons wavelength λ is short enough to obtain a good resolution in imaging. In most cases their propagation is quasioptic, i.e. the beam radiation diameter collected by a detecting system with a typical size L is only moderately large when measured in wavelength [83]. For shorter wavelengths (when $\lambda \rightarrow 0$), ray optics describes the propagation very well and

when $\lambda \simeq L$, diffraction prevails. In quasioptics the propagation is well described by Gaussian beams: the lateral distribution of the field has a Gaussian shape. It includes the effect of diffraction within reasonable limits. Hence the resolution R_{es} of an object observed at a wavelength λ , at a distance R , with a system of typical size L is given by [86]:

$$R_{es} = \lambda \frac{R}{L} = \frac{c}{\nu} \frac{R}{L} \quad (1.1)$$

where ν is the frequency and c the speed of light. Thus, for $L = 1$ m (a maximum practical limit), at 100 GHz we have a resolution of 3 mm at a distance $R = 1$ m, 6 cm at $R = 20$ m and 15 cm at $R = 50$ m. At 1 THz, resolutions are ten times smaller. Thus, for a practical imaging applications, a compromise between distance and resolution has to be found.

Penetration power. At the same time THz radiations have wavelengths long enough to penetrate many materials. As an example, table 1.1 gathers some measured attenuation values for clothing, fabric, and building materials [81]. Attenuation in A_{dB} upon incident signal excitation is defined as $A_{dB} = 10\log_{10}(I_0/I)$ where I is the collected signal with the sample in the measuring setup and I_0 when it is removed. As we can see, the A_{dB} is quite small in the terahertz range especially below 200 GHz. Similarly, longer wavelength than IR light make THz frequencies more immune against scattering and attenuation under certain atmospheric conditions like fog or dust [76, 137]. This ability to see-through makes THz radiations of particular interest for security applications.

		Attenuation A_{dB} in dB $A_{dB} = 10\log_{10}(I_0/I)$							
		94 GHz		326 GHz		584 GHz		1042 GHz	
material	thickness (mm)	parallel	perp.	parallel	perp.	parallel	perp.	parallel	perp.
cotton shirt	0.30	0.2	0.1	0.3	0.5	1.0	1.1	3.1	3.2
denim	0.635	0.7	0.7	1.3	1.4	3.4	2.9	10.0	7.9
leather	1.29	0.7	0.6	2.3	2.1	6.0	5.2	17.9	15.3
sweater	2.13	0.4	0.4	3.8	4.0	14.5	13.7	19.1	21.4
cardboard	3.9	1.2	1.3	2.8	3.2	4.4	5.0	9.0	9.4
plywood	6.35	5.3	4.5	18.2	16.7	31.3	30.2	n/t	61.9
concrete	11.12	9.8	10.5	47.7	49.2	n/t	n/t	n/t	n/t
glass	2.21	4.5	4.3	10.8	11	25.3	25.4	n/t	n/t
n/t - no transmission									

Table 1.1: Attenuation values for clothing, fabric, and building materials. The attenuation in dB is defined as $A_{dB} = 10\log_{10}(I_0/I)$ where I is the intensity of the signal with the sample in the measuring setup and I_0 when it is removed. The measurements were made with a normal incident beam, and the samples were measured with two lateral orientations, parallel and perpendicular, at 90° with respect to each other. Adapted from [81].

Spectroscopy. Thirdly, many molecules have their rotational transitions or their vibrational modes in the THz region, which are tabulated (see for example the Hitran database [7]). Some intermolecular vibrations also lie in the THz [145]. Thus many spectroscopic applications are possible.

Non ionizing. Finally let us mention that THz radiations are non ionizing, therefore they are not thought to be hazardous, contrary to microwaves, and their coherent emission is safe for the eye, contrary to infrared (IR) lasers.

1.1.3 Limitations

Three principal difficulties make THz frequencies delicate to use. The first one comes from the intrinsic nature of the wave and the two others occur in many targeted applications.

Short propagation. The propagation of THz waves is difficult to address over long distances: metal or dielectric waveguides are too lossy, due to a finite conductivity and a the high absorption coefficient respectively [193]. Furthermore one needs a non dispersive media in many broadband applications. From a free space propagation point of view, a THz signal transmitted between an emitting and a receiving antenna can be evaluated using the Friis formula, whose a simplified version is [137]:

$$P_r = P_t \frac{A_{et} A_{er}}{r^2 \lambda^2} \quad (1.2)$$

where A_{et} and A_{er} are respectively the effective aperture of the transmitting and the receiving antenna, P_r and P_t are respectively the power received and transmitted, r is the distance between the antennae, and λ the wavelength. Mann [137] then evaluates the maximum distance for data transmission at 400 GHz to 2 km (at which the received power is 1 pW). Thus, only short range distances are accessible.

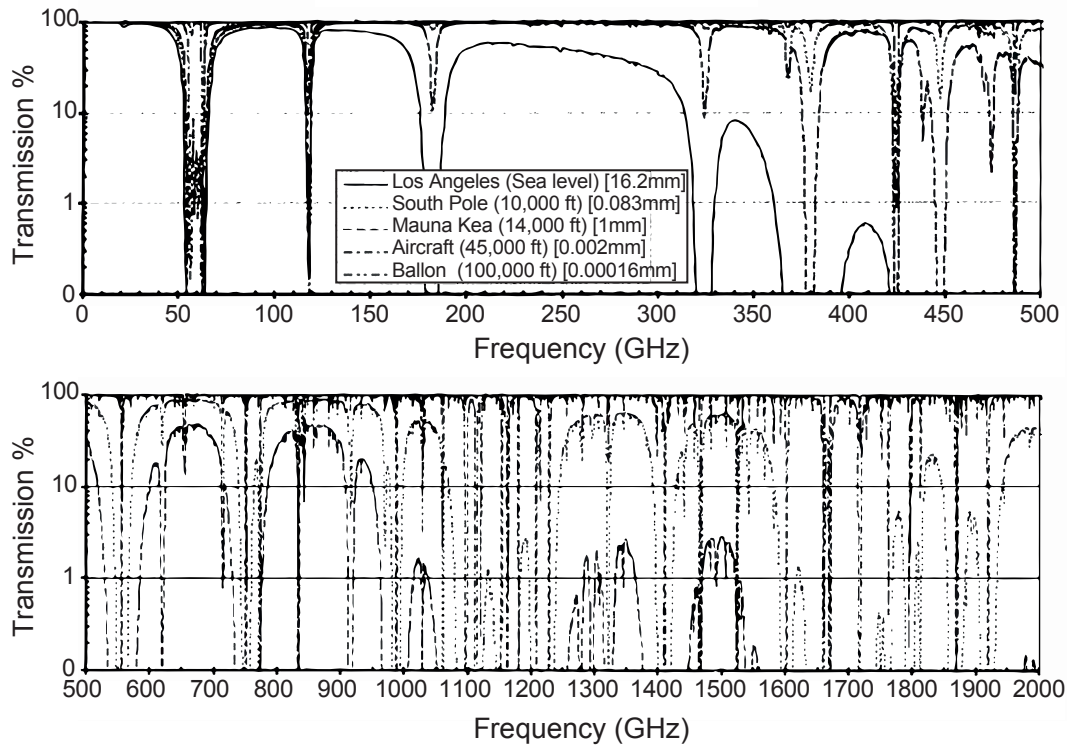


Figure 1.2: Atmospheric transmission in the THz region at various locations and altitudes, for given precipitable water vapor pressure (in millimeter). Taken from [169].

Water vapor absorption. Second, THz atmospheric transmissions face a main challenge: water vapor absorption. In fact, being a polar molecule, water has a strong absorption over all the THz band, even at low frequencies due to the O-H group. Vibrational and rotating modes

of H₂O are tabulated in the Hitran database, from which one can compute atmospheric transmission/absorption with radiative transport codes like "Fascode". Figure 1.2 represents calculated transmissions for various atmospheric conditions, up to 2 THz.

Thus, only some windows are available for THz atmospheric transmission, as we will see in section 1.2.3.

Weak thermal background. Thirdly, many *passive* detectors will face the fact that the contrast between a target and its background is tenuous. In fact the thermal radiations of the background are given by:

$$L = \frac{2h\nu^3}{c^2} \frac{1}{e^{\frac{h\nu}{k_B T}} - 1} \quad (1.3)$$

where L (in $W/m^{-2}/sr/Hz$) is the spectral radiance, i.e. the spectral density of radiated flux per unit solid angle and projected area, and ν the frequency. L is represented for a few blackbodies in figure 1.3. In particular we see that the 2.7 K source has a maximum at 159 GHz. It corresponds to the cosmic background temperature, and explains why the THz region has been driven by astronomy applications over the past 30 years [46]. When applying formula 1.3 on a 1x1 mm detector, working at 100 GHz, with an integration bandwidth of 100 GHz, we can compute that it receives about 600 pW from a background at 290 K. The image contrast will typically be 200 pW for outdoor situations, and 10 pW for indoor situations [86], thus one will have to use very sensitive detectors, and in this context, cryogenic heterodyne systems are required.

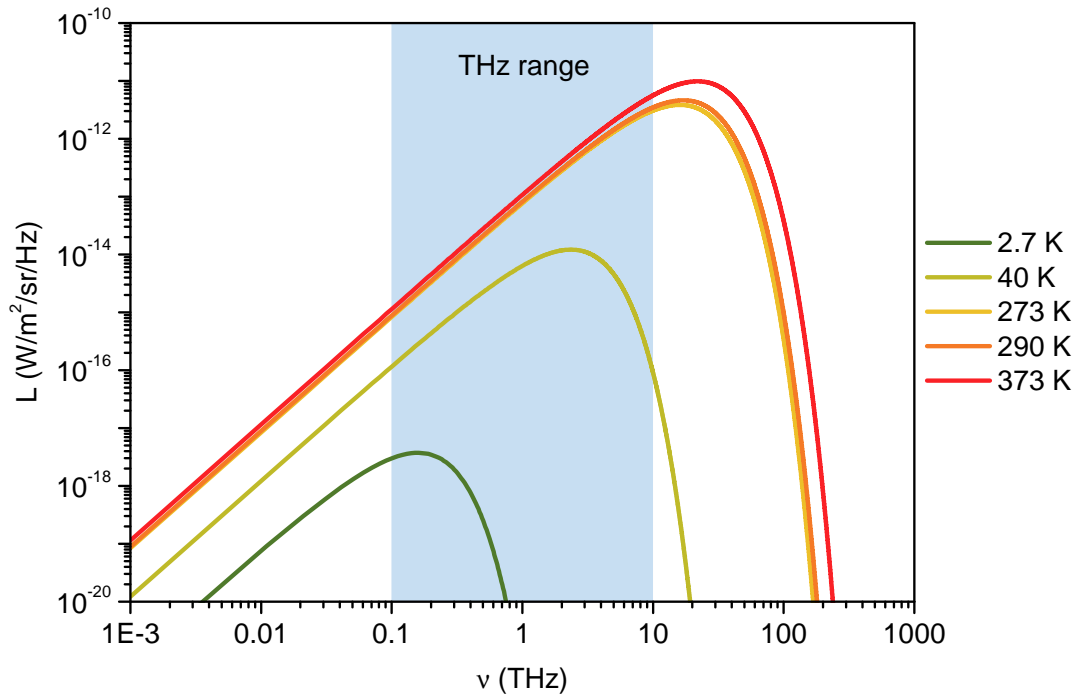


Figure 1.3: Simulated blackbody radiations at different temperatures.

1.2 Applications

We will review here the principal application fields along with their technologies [185] that benefit from one or several of the above key aspects. It concerns applications in imaging, spectroscopy or communications. In terms of technology readiness assessment (TRL) [4], some are still at a very early developing stage (low TRL) whereas others are already commercialized (high TRL). We will refer to this criterion to emphasize their maturity [156]. Several companies already provide THz systems for spectroscopy or imaging: Teraview (U.K.), Picometrix (U.S.), Toptica (Germany), Menlo Systems (Germany), Advantest (Japan), and Zomega (U.S.).

1.2.1 Pharmaceutical and medical sciences

Terahertz time domain spectroscopy (THz-TDS, see 1.3.2) and terahertz pulse imaging (TPI) has proven useful in detection and diagnosis of various early stages cancers [22, 200, 47, 176]. In fact many diagnosis are done by visual assessments first, and when there is a doubt, a biopsy is performed. Existing technologies in the field are still limited: high frequency ultrasound can image tumors, but is unable to differentiate benign and malignant lesions. Visible and near IR light microscopy are limited by penetration depth to a few micrometers. High resolution imaging such as optical coherence tomography or confocal microscopy have a small field of view, typically 250x250 μm and a small penetration depth. Thus, THz technologies are very interesting: they can achieve a good lateral and depth resolution, typically 500 μm and 50 μm respectively [176, 200], a good penetration depth (1 mm), with a large field of view (typically 25x25 mm). The discrimination between sane and cancerous tissues stems from the fact that the latter tend to accumulate more water. Furthermore, it is possible to determine different refraction indexes encountered by the beam, thus providing valuable informations on different types of sane or tumorous tissues [47, 22].

THz-TDS and TPI has also proven very promising in pharmacology with non destructive evaluation (NDE) of pharmaceutical tablets [167], for which the measurement of coating thickness of pills is an important parameter in the drug delivery process. Compared to Fourier transform infrared spectroscopy (FTIR) or Raman spectroscopy, THz spectroscopy is able to penetrate much deeper in structures [156], has the unique ability to identify chemicals inside pills, and can even discriminate different polymorph structures. Thus a 3D chemical mapping is possible. Finally, many intermolecular vibrations lie in the THz range, which makes it suitable for research in molecular interactions [145].

In terms of maturity, THz technologies applied to pharmaceutical and medical sciences are particularly advanced: for instance, the TeraView Terapulse 4000 spectrometer and imaging system is a commercial instrument that can image and make spectral analysis from 60 GHz to 4 THz [12]. Hence they rank high on the TRL scale, at 8-9, with "actual system completed and qualified through test and demonstration in an operational environment" [4], and it is possible for non THz specialists to operate the systems.

1.2.2 Security

Many explosives and related compounds (ERC) have spectral fingerprints in the THz region, due to intramolecular and intermolecular vibrational modes or phonon modes [52, 115]. Similarly, illicit drugs have a THz signature [106]. Besides, the unique property to see through soft materials (see table 1.1) such as clothing or paper makes THz spectroscopy of prime interest in security applications like mail scanning [96] or airport body scanners. However, due to atmosphere absorption and possible complex covering layers, long range (> 1 m) analysis still present fundamental challenges.

Nevertheless continuous wave (CW) sources below 200 GHz are far less affected by water vapor absorption. Furthermore at those frequencies many clothings are transparent, and the resolution has still a centimeter accuracy within a few meters distance (equation 1.1). Besides, THz radiations have a lower attenuation than IR under certain atmospheric conditions such as smoke or fog [76]. Therefore, if only a binary information skin/no skin is required so as to detect concealed weapons in a close distance situation, THz radiations can be used [156].

Such *active* remote scanners, in which a source is required to shine THz radiations on a target, rank high in TRL, about 7 to 8: mail scanning prototypes are being proposed [96] and body scanners are being already deployed in U.S. airports [156]. However *passive* detection, which only operates with the blackbody radiation of the target is far less advanced [85], because as already mentioned the sensitivity to obtain a good contrast requires a cryogenic detector, and a coherent detection (see section 1.4.3).

1.2.3 Communications

Perhaps the most unavoidable innovations in a very near future will concern the use of terahertz frequencies in communication systems. The spectrum has already been allocated for specific applications up to 300 GHz in the USA by the National Telecommunication and Information Administration [14] and up to 275 GHz in Europe by the Electronic Communications Committee within the European Conference of Postal and Telecommunications Administrations [5]. Furthermore the World Radiocommunication Conference (WRC) held in 2012 investigated possible allocations beyond 275, up to 1 THz, and the next WRC due in November 2015 will undoubtedly discuss further regulations for this range.

Indeed there is a crucial need to develop technological solutions for wireless communication up to 1 THz: for example, the mobile traffic rate at the end of 2014 was reaching 2.5 exabytes (10^{18} bytes) per months, i.e. more than 40 times the rate of 2010 [110]. Over 2014, the mobile data traffic was nearly 30 times the size of the entire global Internet in 2000 [3]. In order to keep up with fiber-optic networks, wireless data rates beyond 10 Gbit/s are mandatory and will only be possible with new frequency bands [110]. However due to atmospheric absorption (see figure 1.2) and to free space loss proportional to $(c/4\pi fd)^2$ (Friis formula), THz transmissions are conceivable only inside certain transmission windows (75-100 GHz, 110-150 GHz, 220-270 GHz and near 300, 350, 410 and 670 GHz) and over short distances, typically less than 2 km [76]. Thus they are well adapted for the "first" and "last mile" problem [137]. Indoor applications might be better adapted than outdoor scenarios [76, 175], however one still needs to address inherent issues such as multiple reflections, people moving in the beam's path, diffraction and wall absorption. To that end, ray-tracing algorithms are being used [110]. Furthermore, THz waves are more directional than microwaves, therefore some progress remains to be done in the design of high gain and integrable antennas. Some solution already exist: for reading out a hard drive on a desk, horn antennas are adapted, and for cellular communications, phased array antennas or planar antennas on dielectric lenses are being explored [76, 110].

THz free space communication experiments were performed. Depending on the carrier frequency, the maximum distance spans between 800 m (at 120 GHz) and less than 1 m at 300 GHz. [76]. A variety of systems were used, either optoelectronic-based or photonic-based. One of the most striking trial is a successfully live broadcast of the 2008 Olympic games in Beijing by Nippon Telegraph and Telephone (NTT) [110]. Using a photonic-based 120 GHz system similar to the one shown on figure 1.4, they transmitted uncompressed (compression causes delay) high-definition TV signals over 800 m [93, 94, 110]. A laser generates an optical subcarrier whose intensity is modulated at 125 GHz ("photonic THz-wave generator") and fed to an array waveguide grating (AWG) that acts as an optical filter, outputting two modes separated by 125 GHz. Then an amplitude shift-keying (ASK) scheme modulates the optical signal with data ("data modulator") using

a Mach-Zehnder modulator (MZM). The output is amplified with an erbium-doped fiber amplifier (EDFA) and fed into an uni-travelling carrier photodiode (UTC-PD) which converts the modulated optical signal into a THz signal, finally amplified with a high electron mobility transistor (HEMT) and fed to a horn antenna. Received signals are amplified and demodulated with a monolithic microwave integrated circuit (MMIC). Demodulated signals then amplified by a low-noise amplifier (LNA) and enter the clock and data recovery (CDR), finally converted to an optical signal (E/O converter). Table 1.2 gathers the main specifications of the system.

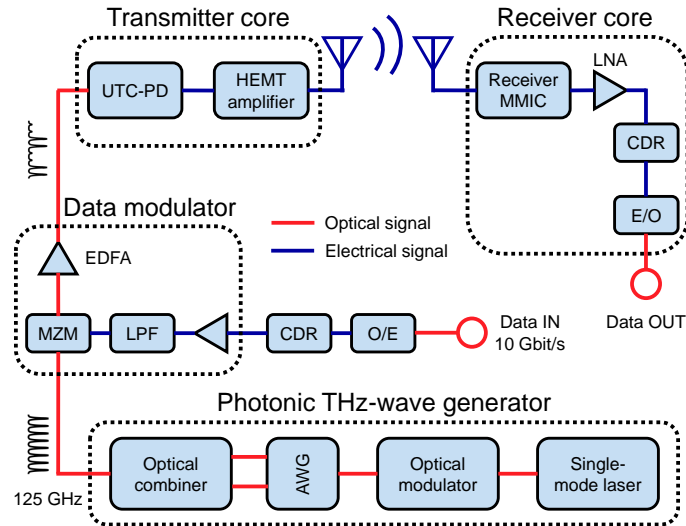


Figure 1.4: Block diagram of the 120-GHz-band wireless link system. Adapted from [93, 146].

Center Frequency	125 GHz
Modulation	ASK
Occupied Bandwidth	116.5-133.5 GHz
Transmission rate	10 GBits/s
Antenna diameter	450 mm (Cassegrain)
Antenna	Horn Antenna
Antenna Gain	23.3 dBi
Power consumption	600 W
Output power	10 mW

Table 1.2: Main specifications of the 120-GHz-Band wireless link system. Adapted from [93, 110].

The maturity of THz communications depends on the carrier frequency. At 120 GHz and below, we estimate it to be at level 6 in terms of TRL, whereas at higher frequencies, long distance data transmission have yet to be demonstrated, hence it is only at TRL 4-5 [76, 93, 94, 110, 156]. Besides, according to the International Technology Roadmap for Semiconductors (ITRS), the cut-off frequency of Si-CMOS will exceed 500 GHz within a few years [110], along with promising new devices like ballistic transistors and lithographic resolutions of a few nanometers [8, 9]. That is why, even if some electrical engineering work remains to be done, we believe that in a foreseeable future THz communications will integrate many communication systems.

1.2.4 Astronomy and Astrophysics

As already mentioned above, development of THz technologies has been driven by its use for Astronomy and Astrophysics observations over the last 30 years, because millimeter and submil-

limeter waves play a key role: the cosmic microwave background (CMB) radiates at 2.7 K, hence has its maximum emission power at 159 GHz (see figure 1.3), and the total amount of energy in the submillimeter light in the universe equals the sum of energies in the UV, visible and near-IR band [205].

Three important telescopes have used THz detectors: the Herschel space observatory, the Planck spacecraft and the Atacama large millimeter/submillimeter array (ALMA) telescope. Herschel contains a heterodyne instrument for the far-infrared (HIFI), which makes very precise spectrometry of two bands, at 480-1250 GHz, and 1410-1910 GHz [6]. The ultimate spectral resolution required ($\lambda/\Delta\lambda \sim 10^7$) imposes the use of cryogenic heterodyne detectors. The 480-1250 GHz observations employs superconducting-insulating-superconducting (SIS) mixers (see 1.4.3) whereas the 1410-1910 GHz band uses hot electron bolometers (HEB). HIFI enables to quantitatively observe the abundance of molecules in interstellar clouds, such as OH^+ (972 GHz), H_2O^+ (1115 GHz) or H_3O^+ (984 GHz), so as to understand the early chemistry of water [82, 148]. Similarly, Planck has 52 polarization-sensitive bolometers operated at 100 mK to map the sky in six frequency bands from 100 to 857 GHz [95]. Until the ^3He depletion in early 2012, it gave very precise pictures of the CMB which, for example, enabled to test inflation theory. Finally the ALMA telescope has (or will have, some detectors are still in the qualification process) SIS cryogenic detectors that covers the 84-950 GHz range [1].

Once again, the maturity of THz technologies for astronomy and astrophysics applications is not uniform, because such huge scientific projects always demand new devices for specific applications. Thus, even if the (low- T_c) SIS and HEB spectrometer technology is at the highest TRL level (9), with actual succeeded missions, many aspects on the detectors could (and will) be improved. In particular, people are eager to find lower power consuming local oscillators and higher temperature operating devices, so as to increase their lifetime. For example, the next generation THz space observatory, called Millimetron, will be placed at the L2 Lagrange point. Its launch date is planed for 2019/2020, and it will be able operate its cryogenic detectors for 3 years. The THz observation range will be from 275 GHz up to 5.36 THz (all SIS or HEB). The bath temperature will be 10 K, but the cooling power at 4.5 K will be less than 100 mW, and less than 15 mW at the 1.7 K stage.

1.3 Sources

Historically the THz range has been difficult to address because of the lack of sources. On one hand, the semiconductor technology has been intrinsically limited in speed by the traveling time of the charge carriers or by the intrinsic RC constants in circuits. It leads to a power decreasing typically with frequency as $1/\omega^4$. On the other hand, the optics techniques are limited by the lack of appropriate materials with sufficiently small bandgaps. For example, salt lasers do not extend below 15 THz [197].

However solutions exist, and there are three general ways to generate THz radiations: frequency up/down conversion, radiation from accelerated charges, and laser emission, which can all produce narrow-band (continuous wave) or broadband (impulsions) radiations. We will briefly review these methods.

1.3.1 Frequency up/down conversion

A convenient way to create THz radiations is to start from electrical or optical frequencies and use nonlinear effects in diodes or crystals to respectively up and down convert them into the THz range.

Electronics. Three types of electronic devices can up-convert microwaves at room temperature [74]:

- frequency multipliers based on planar GaAs Schottky diodes. Record: 100 μW @ 1.2 THz, 15-20 μW @ 1.5-1.6 THz and 3 μW @ 1.9 THz;
- oscillators with transistors like InP Gunn devices, heterojunction bipolar transistor oscillators (HBT) or impact ionization avalanche transit-time (IMPATT) diodes. Record: 50 mW @ 220 GHz, 10 mW @ 338 GHz (IMPATT);
- active two-terminal devices like resonant tunneling diodes (RTD) or tunnel-injection transit-time (TUNNETT) devices. Predicted: 160 mW @ 200 GHz and 20 mW @ 300 GHz.

In addition, performances increase at cryogenic temperatures. However, as for every semiconductor devices operated at these extremely high frequencies, many thermal issues remain and they often burnout during operation.

We used a commercially available Gunn oscillator as one of our sources during our experiments.

Optics. Down-conversion of optical frequencies can be achieved by optical rectification in electro-optical crystals (EOC), a second order non linear effect. Commonly used materials can be traditional semiconductors crystals (GaAs, ZnTe) or organic crystals such as the ionic salt 4-dimethylamino-N-methylstilbazolium tosylate (DAST) [77].

1.3.2 Radiation from accelerated charges

Accelerated electrons, either in free space propagation or in a solid state system can create THz radiations.

synchrotron radiations. A beam of electrons periodically modulated or simply deviated by a magnetic field creates THz synchrotron radiations. Free electron lasers use bunches of electrons propagating in vacuum through a strong, spatially varying field [77]. Mirrors confine photons to the beam line, which forms the gain medium for the laser. Such THz sources are the most powerful and bright known to date (the p-germanium laser can emit peak power of 10 W in the frequency range from 1 to 4 THz [185]), but require devoted facilities and prohibitive costs. Similarly, smaller systems exist like backward-wave oscillators (BWO): an electron beam is modulated periodically in a vacuum tube, thus creating THz waves. We used a (BWO) during our experiments. One of the advantages is that such sources are easily tunable, they can create continuous wave (CW) radiations over a wide bandwidth.

THz impulses from PCA - THz-TDS. Most broadband solid state sources are based on the excitation of a semiconductor with a femtosecond (fs) laser pulse (usually generated by a Ti:sapphire laser), as is the case of the photoconductive antennae (PCA). A PCA is a planar metallic antenna patterned onto a semiconductor substrate, and biased at a constant voltage of several kV/cm (see figure 1.5 (a)) [173]. One sends a pump laser pulse onto the center of the antenna, chosen in order to have photons energy greater than the bandgap of the material. It generates electron-hole pairs which are accelerated by the static bias field, thus creating a fast time-varying photocurrent. The latter radiates a short pulse whose spectrum is a broadband THz signal. It is coupled to free space by the antenna and collimated through an hemispherical lens. For an efficient THz radiation it is desirable to have a rapid photocurrent rise and decay time hence use semiconductors with small effective electron mass, like III-V materials (low-temperature-grown

(LTG) GaAs, InGaAs) or InP, InAs [77]. Let us also mention that even though PCA are mostly used for pulsed THz generation, it can also generate continuous waves, by photomixing of two optical frequencies, whose beating is in the THz range.

The same PCA structure can act as a (coherent) detector of THz pulses (see figure 1.5 (b)). The probe laser beam creates free carriers, and the THz electric field modulates their acceleration, then a measurable current arise. A delay stage between the pump line and the probe line enables to reconstruct coherently the THz spectrum.

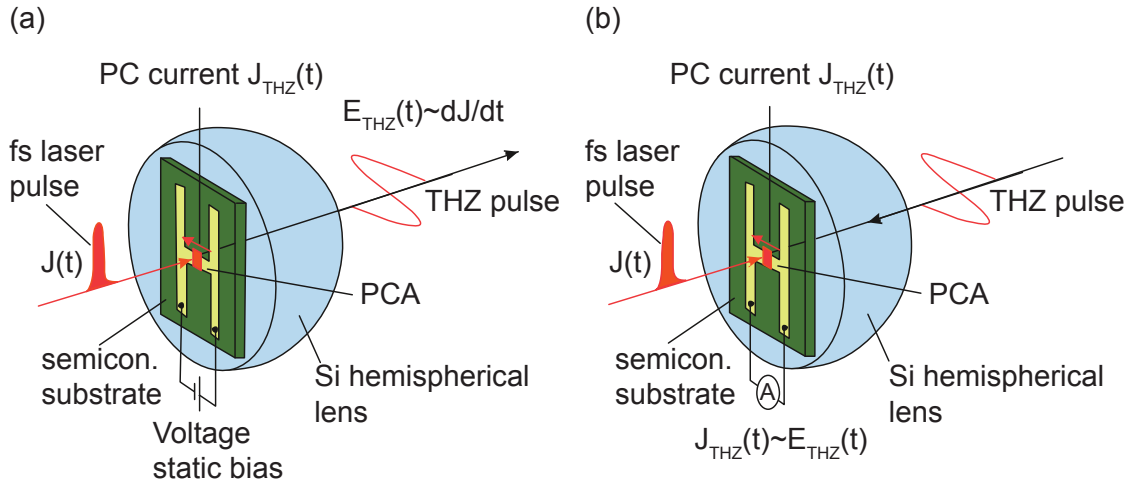


Figure 1.5: THz pulse emission (a) and detection (b) with a photoconductive antenna. Adapted from [173].

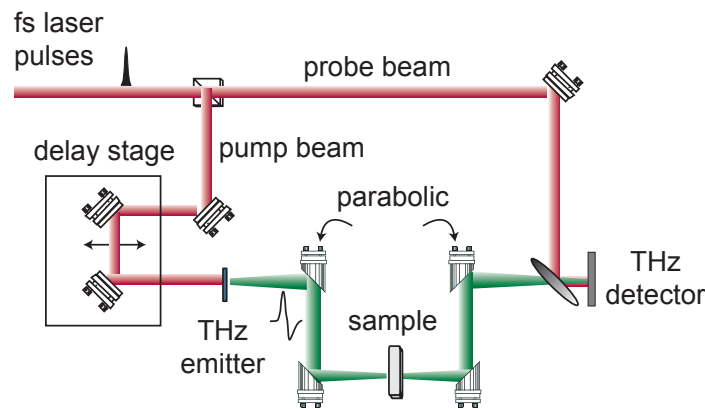


Figure 1.6: Illustration of a THz-TDS system. Adapted from [77].

Such a generation and detection technique of THz broadband radiations has been extensively used in THz time-domain spectroscopy (TDS), in which one analyzes the THz transmission spectrum of a sample placed in the path of the THz pulse. Figure 1.6 illustrates the principle of THz-TDS. Instead of a PCA, an EOC can also be used for generation and detection of THz pulses: second order non linear effect creates a THz radiation from optical rectification of the laser pump, and on the detecting side the THz electric field modulates the birefringence of the crystal, hence the polarization of the optical probe, which can be measured.

UTC-PD. The recent advances in semiconductor technologies allowed fabrication of new photodiodes whose response is extremely fast, in the THz range. They are called uni-traveling carrier photodiodes (UTC-PD) [146] and their underlying principle stems on a selective movement of the carriers. Then UTC-PD can act as a photomixer and produces powerful THz radiations from the mixing of two laser diodes.

In conventional PIN-PD (see figure 1.7 (b)), both electrons and holes movements ensure the response of the PD. They are created when a photon hits the intrinsic (depleted) region (typically InGaAs), and separated by the permanent electric field. The speed at which they reach respectively the N and P-contacts limits the speed of response. One can increase it by reducing the thickness of the depletion layer but it is inevitably accompanied with an increase of capacitance, hence a lower cut-off frequency [149]. However, the drift velocity of electrons v_e is usually much higher than the one of the holes v_h ($v_e \sim 10^7$ cm/s and $v_h \sim 10^6$ cm/s), therefore the latter limit the speed of the device. In UTC-PD, a careful engineering increases the speed at which electrons and holes reach the N and P-contacts without shrinking the depletion zone. In fact it consists of two layers: a light absorption layer (p-InGaAs, typically 200 nm), next to an undoped collection layer (InP, typically 300 nm) in which electrons exhibit a velocity overshoot. Thus, the holes reach very quickly the P-contact because the absorption layer is close and thin, and the electrons reach quickly the N-contact because of velocity overshoot in the collection layer (see figure 1.7 (a)). The overall zone remains thick enough to avoid capacitive effects. The photomixing of UTC-PD output power is higher than conventional LTG-GaAs diodes, with about 100 μ W at 500 GHz [146]. However UTC-PD often overheat and burnout during operations [110].

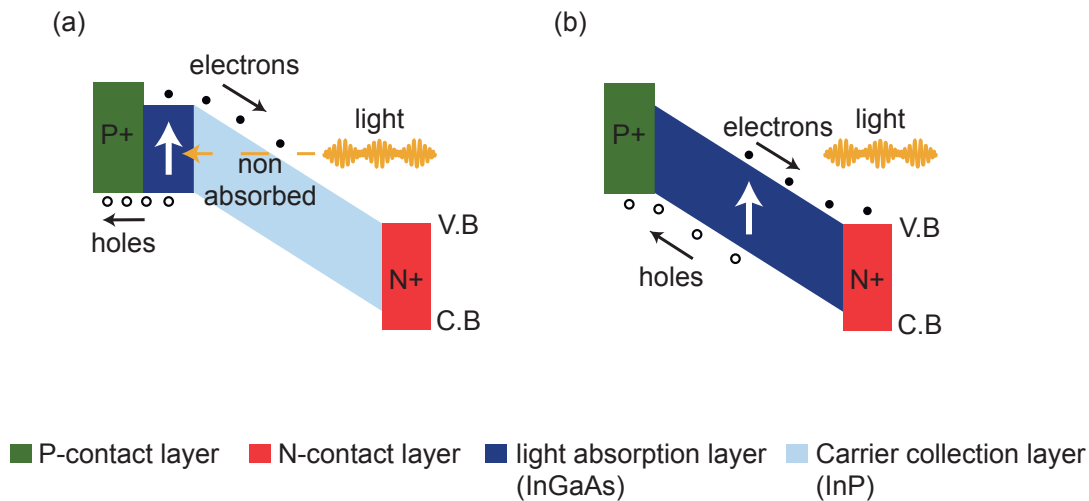


Figure 1.7: Band diagram of a UTC-PD (a) and a PIN PD (b). Adapted from [146].

Bi₂Sr₂CaCu₂O₈ mesa devices. In 2007 a new THz radiation phenomenon was found in Bi₂Sr₂CaCu₂O₈ (Bi2212) high- T_c superconductor [151], which originates from coherent oscillation of intrinsic Josephson junctions (IJJs). In fact the Bi2212 structure consists in alternating two layers of superconducting CuO₂ and one insulating Bi₂O₂ within a unit cell. A Josephson coupling exists between the CuO₂ planes, hence a 1 μ m thick Bi2212 stacks 652 identical layers of IJJs [103]. When d-c biased, a Josephson junction (JJ) emits a THz radiation: due to the a-c Josephson effect (see section 3.1.2) quasiparticles (QP) oscillate at THz frequencies. Under certain conditions, an array of JJs can synchronize (phase-lock) and then emit a stronger and narrower THz oscillation than a single JJ. In fact, if N is the number of synchronized junctions, the emitted

power scales with N^2 and the linewidth scales with $1/N$ [100]. This is what happens in IJJs of Bi2212, where atomic closeness favors synchronization.

Figure 1.8 (a) shows a typical IV curve of a Bi2212 rectangular mesa ($64 \times 400 \times 1.35 \mu\text{m}^3$). It is strongly hysteretic and shows small jumps, due to the variation on the number of junctions that switched into the resistive state. The negative resistance observed (negative slope) is due to Joule heating [103]. In fact, in the voltage state the system faces an enormous heat, around 10^6 W/cm^3 . To date, heat evacuation is still a problem in these systems. Nevertheless they can create a strong and narrowband THz emission, as shown by the spectra in the inset of figure 1.8 (a) obtained by Fourier transform infrared (FTIR) spectroscopy. The center frequency is 18.079 cm^{-1} i.e. 542 GHz. Further work showed that the emission frequency can be tuned up to 12% [31], that a single rectangular mesa emits up to $30 \mu\text{W}$ at 0.44 THz (the system being cooled at 55 K) [165], and that the coupling of several mesas with each other provides up to $610 \mu\text{W}$ at 0.51 THz (with a bath temperature of 40-55 K)[30]. Finally, depending on the mesa geometry, different cavity modes can be excited, leading to different radiation patterns[103].

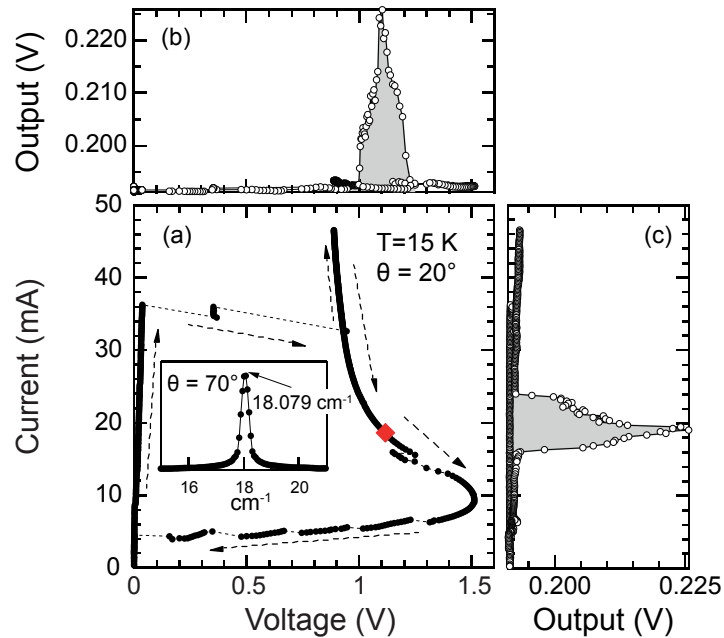


Figure 1.8: IV curve (a) and detected emission with a Si-composite bolometer (b),(c). The inset of figure (a) is the spectrum obtained by Fourier-transform infrared spectroscopy, at the bias point indicated by a red square. θ is the angle between the c -axis of the Bi2212 crystal and the Si bolometer. Adapted from [103].

The physics of coherent THz emission from Bi2212 IJJs is extremely rich and inspiring for our work on $\text{YBa}_2\text{Cu}_3\text{O}_7$: in fact, as we shall see in chapter 9, we attempted to engineer an *extrinsic* array of JJs, in order to obtain the same synchronization effects that lead to a strong and narrowband THz emission. It is of utmost interest in the design of a heterodyne detector, with an on-chip local oscillator.

1.3.3 THz lasers

Gas lasers and more recently solid state lasers can provide THz continuous wave radiations.

Gas lasers. Gas laser are another common THz source. They use intermolecular transitions between molecules, such as carbon dioxide. These sources are monochromatic and not continu-

ously tunable. Furthermore they usually require large facilities. However they can provide high output powers, up to 30 mW [77].

QCL. Quantum cascade lasers (QCL) are semiconductor lasers that have raised a great deal of interest in the scientific community over the last 15 years, because of their ability to generate a strong pulsed or continuous wave (CW) THz emission. The first QCL was fabricated in 1992 by Capasso, Sirtori, Faist et al. [51], and shortly after they demonstrated a first THz emission at Bell Labs in 1994 [75]. It had a lasing frequency at 75 THz. In 2002 a QCL was demonstrated to lase at 4.4 THz [114]. Nowadays QCL can cover the range 0.84-5 THz, with powers of 250 mW for pulsed lasers (operated at 169 K) and 130 mW for CW lasers (operated at 117 K) [197]. However below 2 THz their performance degrade and they need a fairly strong magnetic field to operate (see 1.9).

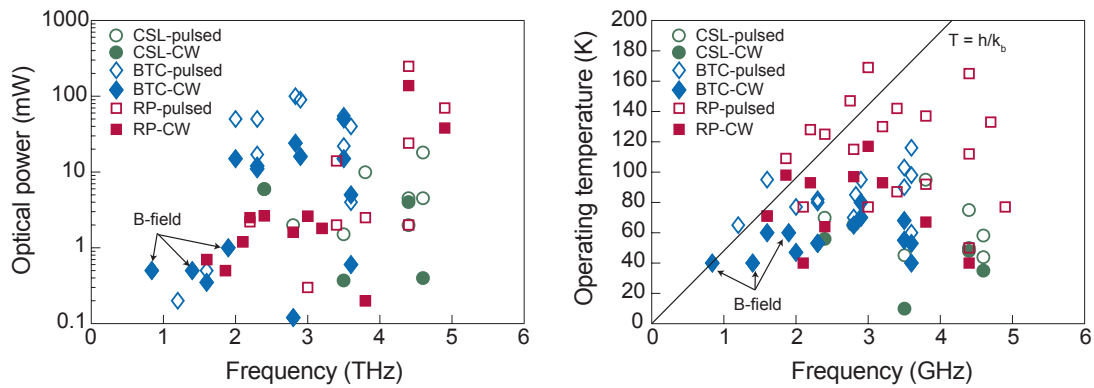


Figure 1.9: Reported peak performances of QCL (a) and maximum operating temperatures (b). Various structures are compared: chirped superlattices (CSL), bound to continuum (BTC), and resonant phonon (RP). Adapted from [197].

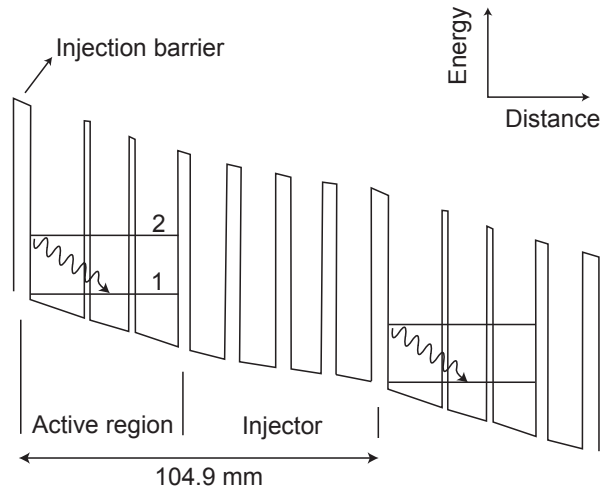


Figure 1.10: Simplified conduction band of a QCL. Electrons are injected through the AlGaAs injection barrier into the upper lasing level of the active region (GaAs). Transition to the lower lasing level results in the emission of a THz photon. Due to the applied electric field, the band diagram is tilted and electrons escape to the subsequent injector band. Adapted from [75, 77].

QCL are based on quantum wells (QW) put in series. Each one is typically made with a GaAs

layer (10-20 nm) sandwiched between potential barriers in AlGaAs (0.5-4.3 nm). The quantum confinement of each well creates sub-bands whose spacing is in the THz range. Now, a series of QW defines a superlattice structure in which there is an injector from which electrons arrive, a collector from which they tunnel into the next identical structure, and a gain medium. By putting an external electric field, the injector is connected to the upper lasing level, the collector to the lower one, and also connected to the injector of the next superlattice. After population inversion is reached, electrons transit from the upper lasing level into the lower lasing level and tunnel into the next structure in which they undergo the same lasing mechanism. Figure 1.10 represents the simplified conduction band structure of a QCL.

1.4 Detectors

There are two kinds of receiver architecture: *incoherent* (sometimes referred as direct), and *coherent*. Within the incoherent architecture there are two subcategories: *power* and *photon detection*. There are also two subcategories for coherent detection: *homodyne* and *heterodyne*. Independently, a detector is said to be *active* if it shines the target with a signal and detects back a fraction of it (like radars). Conversely a *passive* detector only uses the (generally incoherent) radiation of the target surroundings as the illumination source.

An incoherent detector rectifies a radiation from r-f (or THz) frequency to a baseband signal. Almost always, it is a power-to-voltage or a power-to-current conversion. A coherent detector combines the incoming radiation with another one from a local oscillator (LO) in a non linear element called mixer. In *heterodyne* conversion, signal and LO frequency are different and the mixer generates a beat-note at an intermediate frequency (IF). In *homodyne* conversion, signal and LO frequency are equal and the beat-tone degenerates into d-c. The down-conversion from the signal into IF or d-c can greatly enhance the sensitivity of detection compared to an incoherent system, because the mixer uses power from the LO to generate a strong beat-note, even with a small signal. In addition, high-quality low-cost passband filters at the IF enable to have a high spectral resolution for the signal, and the amplitude generated at the IF is generally proportional to the one at signal frequency. Therefore coherent detection is particularly suited for spectroscopy. However spectral bandwidth is more limited than in incoherent detection, that is why the latter is preferred for imaging applications.

1.4.1 Figures of merit for a detector

In this section we define and discuss important parameters used to characterize any detector in terms of noise and sensitivity. In the zoology of sensors, there are many scenarios from which derive different expressions for the minimum noise added by a detecting system. We summarize here the main results, taken from the monograph of Brown [46], with an emphasis on heterodyne detectors.

1.4.1.1 SNR, NEP, T_N

When characterizing the sensitivity of a detector, the first figure of merit that one can think of is the ratio between the average absorbed signal power and the rms noise power. It is called the power signal to noise ratio (SNR):

$$SNR = \frac{S}{N} = \frac{\langle P \rangle}{\sqrt{\langle (\Delta P)^2 \rangle}} = \frac{\langle P \rangle}{S_P(\nu)B_{EN}} \quad (1.4)$$

where B_{EN} is the equivalent noise bandwidth. A drawback is that the SNR depends on the signal received, hence one cannot use it to compare different sensors. A more useful way to define a

metric is to fix the SNR to some arbitrary value and then give the corresponding signal power. In statistics one can show that only post-detection SNR values greater than unity are useful. Hence one defines the noise equivalent power (NEP) as the input signal power to the sensor required to achieve a SNR of unity:

$$SNR = 1 \iff S = NEP \quad (1.5)$$

For square-law detectors (like heterodyne or homodyne detectors) one has to distinguish NEP_{BD} before detection and NEP_{AD} after detection, since we translate information from a bandwidth $\Delta\nu$ to a (lower) bandwidth Δf . They are related by:

$$NEP_{AD} = NEP_{BD} \sqrt{\frac{2\Delta f}{\Delta\nu}} \quad (1.6)$$

Strictly speaking the NEP is in W, but it is conventional to divide it by the square root of the post-detection bandwidth, so as to compare different technologies. It yields to the normalized - or specific - NEP':

$$NEP' = \frac{NEP}{\sqrt{2\Delta f}} \quad (1.7)$$

in W/\sqrt{Hz} . Thus with equation 1.6:

$$NEP'_{AD} = \frac{NEP_{BD}}{\sqrt{\Delta\nu}} \quad (1.8)$$

For passive detection of thermal targets, the noise equivalent temperature difference, NE ΔT (in K) is more useful:

$$NE\Delta T = \frac{NEP_{AD}}{dP_{inc}/dT} \quad (1.9)$$

It is the smallest temperature difference that the detector can measure. NEP' and NE ΔT are usually employed for incoherent detectors. For coherent heterodyne sensors the noise-equivalent temperature T_N is typically used:

$$T_N = \frac{NEP_{AD}}{k_B 2\Delta f} \quad (1.10)$$

It represents the temperature of a load which produces a SNR of unity after detection. These figures of merit are detailed in appendix A for a direct detector, in the case of a coherent and thermal radiation.

1.4.1.2 Square-law detection

A square-law detector is a device for which the output signal is proportional to the square of the input signal: $X_{out} = GX_{in}^2$. Any mixer used in a coherent detector has, at least at first order, a square-law behavior. In the case of a heterodyne mixer $X_{in} = X_{LO} + X_{sig}$ where $X_{LO} = A_{LO}\cos(\omega_{LO}t)$ and $X_{sig} = A_{sig}\cos(\omega_{sig}t)$ and we get:

$$X_{out} = G\left(A_{LO}^2 \frac{1 + \cos(2\omega_{LO}t)}{2} + A_{sig}^2 \frac{1 + \cos(2\omega_{sig}t)}{2} + A_{sig}A_{LO} [\cos(\omega_{sig} + \omega_{LO})t + \cos(\omega_{sig} - \omega_{LO})t]\right) \quad (1.11)$$

Hence we see that an IF at $\omega_{IF} = \omega_{sig} - \omega_{LO}$ is created by the mixer, which can be at much lower frequency than LO and signal frequencies. In general the sensor has a limited bandwidth B_{IF} around the IF so that only the low frequency terms are detected:

$$X_{out} = G\left(\frac{A_{LO}^2}{2} + \frac{A_{sig}^2}{2} + A_{sig}A_{LO}\cos(\omega_{sig} - \omega_{LO})t\right) = \eta \mathcal{R}(P_{LO} + P_{sig} + 2\sqrt{P_{LO}P_{sig}}\cos(\omega_{sig} - \omega_{LO})t) \quad (1.12)$$

where η is the fraction of absorbed LO and signal power, \mathcal{R} is the responsivity of the detector, in A/W or V/W, and P_{sig} (P_{LO}) the signal (LO) power. A_{LO} can greatly amplify X_{out} : once again the LO acts as a pump from which we take energy. The output power at the IF is given by:

$$P_{IF} = DX_{out}^2 = D(\eta\mathcal{R})^2 2P_{LO}P_{sig} \quad (1.13)$$

where D accounts for any impedance mismatch between the mixer and IF reading line. Usually one puts all the parameters other than P_{sig} and η into G_{mix} , the gain of the mixer:

$$P_{IF} = \eta^2 G_{mix} P_{sig} \quad (1.14)$$

Here we see the linear relation between the signal power and the IF power. In the case of a homodyne detection, $P_{IF} = 2\eta^2 G_{mix} P_{sig}$.

The signal to noise ratio of a coherent detector is subtle to compute since both fluctuations of signal and LO must be taken into account. However, when $P_{LO} \gg P_{sig}$ one can show that:

$$(\Delta X_{out})^2 = 2\mathcal{R}^2 (\Delta P_{sig})^2 \frac{B_{IF}}{\Delta\nu} \quad (1.15)$$

for a unimodal LO, from equations A.8, A.10 and A.20 of appendix A one has:

$$(\Delta P_{sig})^2 = \eta h\nu_{LO} \Delta\nu P_{LO} \quad (1.16)$$

Thus, with equation 1.13:

$$\sqrt{\langle (\Delta P_{IF})^2 \rangle} = D \langle (\Delta X_{out})^2 \rangle = 2D\mathcal{R}^2 \eta h\nu_{LO} P_{LO} B_{IF} = G_{mix} \eta h\nu_{LO} B_{IF} \quad (1.17)$$

Hence, heterodyne radiation-noise-limited SNR is given by the ratio between 1.14 and 1.17:

$$SNR_{IF} = \frac{\eta \langle P_{sig} \rangle}{h\nu_{LO} B_{IF}} \quad (1.18)$$

and for the homodyne case, $SNR_{IF} = 2\frac{\eta \langle P_{sig} \rangle}{h\nu_{LO} B_{IF}}$. Taking the SNR at unity one finds the radiation-noise-limited NEP (before detection), where the LO power does not appear:

$$NEP_{HET} = \frac{h\nu_{LO} B_{IF}}{\eta} \quad (1.19)$$

and for the homodyne case:

$$NEP_{HOM} = 2\frac{h\nu_{LO} B_{IF}}{\eta} \quad (1.20)$$

One defines the specific NEP (before detection) for heterodyne detectors as:

$$NEP'_{HET} \equiv \frac{NEP_{HET}}{B_{IF}} \quad (1.21)$$

which is in W/Hz and not in W/\sqrt{Hz} as for direct detectors. It is because the output of the mixer P_{IF} is linear with the input P_{sig} . An equivalent way of seeing it is to say that two powers arrive on the mixer, LO and signal, each one accounting for one square root of Hz in the NEP.

The two famous expressions 1.19 and 1.20 are important because they show the fundamental limit of a coherent detector, which stems directly from a quantum mechanics postulate: any detector measure a radiating field by extracting photons from it, which has a built-in granularity. It leads to a minimum precision for the measure of $h\nu/\eta$, where the coupling constant η accounts for the strength of interaction between the field and the detector. The occurrence at which we make the measurement is given by the bandwidth B_{IF} , equivalent to a sampling rate. Hence the NEP results from a probabilistic measurement: it is equal to the sampling rate B_{IF} times the expectation value $h\nu/\eta$.

1.4.1.3 Electrical noise, total NEP of a heterodyne detector

The process of measuring a radiating field induces noise, but up to now we considered that the electronic circuit was noise free. However it is never the case. We will deal with two categories of noise: first thermal noise, caused by voltage or current fluctuations at the terminals of a dissipating device. It is given by the Nyquist theorem:

$$\Delta V_{rms} = \sqrt{4k_B T_D \Re(Z_D) \Delta f} \quad (1.22)$$

where T_D , Z_D and Δf are the temperature, differential impedance and bandwidth of the device. Second, shot noise originating from the granular nature of electric charges, transported between an emitter and a collector. With a similar reasoning than the one employed in appendix A to derive *photon* shot noise, one can show that the mean square current fluctuations of this *electron* shot noise are given by the Schottky expression:

$$\langle (\Delta I)^2 \rangle = 2eI_{dc}\Delta f \quad (1.23)$$

To effectively include them in figures of merit characterizing the whole detecting line, we assume that it is AWGN (additive white gaussian noise), so that we can add the variances of each source of noise, and we include all the electric noises into a specific NEP'_{elec} (in W/Hz, and not as conventional specific NEP' in W/\sqrt{Hz}). Then the total noise and specific noise equivalent power after detection, NEP_{AD} and NEP'_{AD} , for a heterodyne (double side band) detector are given by:

$$NEP_{AD} = \left[\frac{h\nu_{LO}}{\eta_R} + NEP'_{elec} \right] 2B_{IF} \quad (1.24)$$

$$NEP'_{AD} = \left[\frac{h\nu_{LO}}{\eta_R} + NEP'_{elec} \right] \sqrt{2B_{IF}} \quad (1.25)$$

where η_R accounts for the photon absorption efficiency of the antenna and for any mismatch between antenna and mixer. If we define the total conversion efficiency η_{HET} such as:

$$\frac{1}{\eta_{HET}} = \frac{1}{\eta_R} + \frac{NEP'_{elec}}{h\nu_{LO}} \quad (1.26)$$

we can write NEP_{AD} and NEP'_{AD} with a form similar to equation 1.19:

$$NEP_{AD} = \frac{h\nu_{LO}}{\eta_{HET}} 2B_{IF} \quad (1.27)$$

$$NEP'_{AD} = \frac{h\nu_{LO}}{\eta_{HET}} \sqrt{2B_{IF}} \quad (1.28)$$

When the incident signal is a thermal noise contained in the same monomode as LO, we get (equation A.5 of appendix A) $\langle P_{sig} \rangle = k_B T B_{IF}$. Hence, in the Rayleigh-Jeans limit ($k_B T \gg h\nu_0$), the efficiency of a passive detection of a heterodyne sensor is characterized by:

$$NE\Delta T'_{AD} = \frac{NEP'_{AD}}{dP_{inc}/dT} = \frac{NEP'_{AD}}{k_B B_{IF}} = \frac{h\nu_{LO}}{k_B \eta_{HET}} \sqrt{\frac{2}{B_{IF}}} \quad (1.29)$$

Finally, the receiver noise temperature T_{Nrec} is found by replacing the NEP_{AD} by its value (equation 1.27) in equation 1.10:

$$T_{Nrec} = \frac{1}{k_B} \left[\frac{h\nu_{LO}}{\eta_R} + NEP'_{elec} \right] = \frac{h\nu_{LO}}{k_B \eta_{HET}} \quad (1.30)$$

which is related to NEP'_{AD} by:

$$NEP'_{AD} = k_B T_{Nrec} \sqrt{2B_{IF}} \quad (1.31)$$

Figure 1.11 represents the calculated noise temperature T_{Nrec} and specific noise equivalent power after detection NEP'_{AD} as a function of LO frequency, for a double side band (DSB) heterodyne mixer, having an IF bandwidth of 4 GHz. The two metrics are computed for different values of the conversion efficiency η_{HET} . As we will see in chapter 7, we have a conversion efficiency of a few percent for our *unmatched* Josephson mixer, hence we expect a noise temperature of a few thousands of Kelvins and a NEP'_{AD} of about 10^{-15} at 100 GHz. By improving η_{HET} with matching microwave designs, one expect to greatly improve those figures.

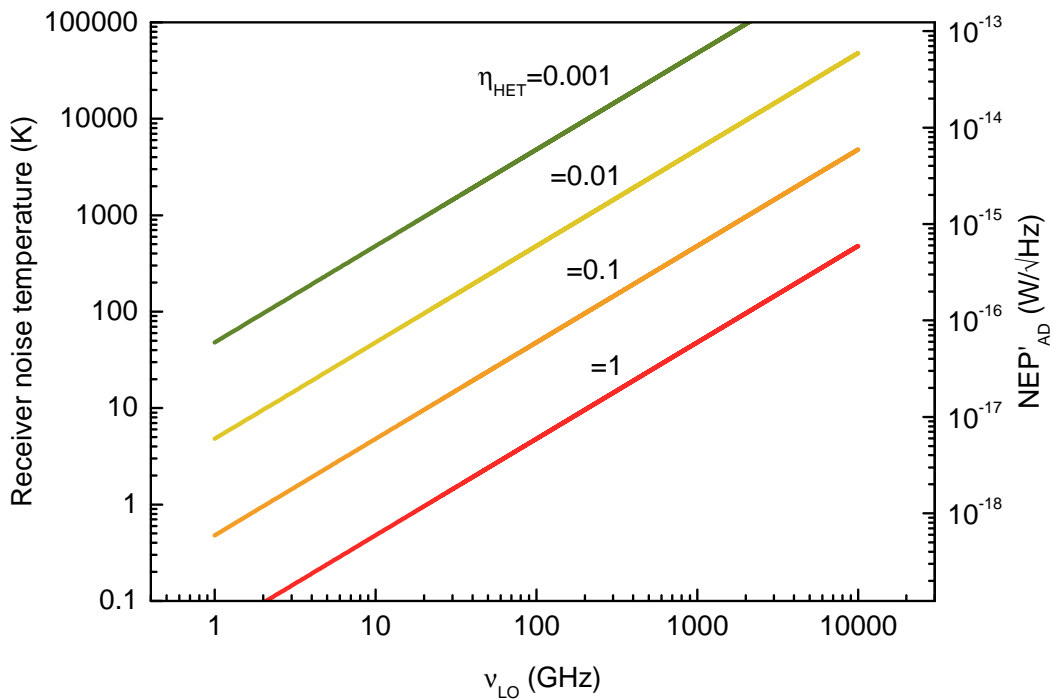


Figure 1.11: Noise temperature T_{Nrec} (a) and noise equivalent power temperature difference $NEAT$ of a DSB mixer, having $B_{IF} = 4$ GHz. Calculations from equations 1.29 and 1.30.

1.4.2 Direct detectors

Direct detectors are particularly suited for imaging applications, given their moderate sensitivity and their ability to be implemented into arrays (multiplexing is straightforward, unlike in heterodyne detectors). Some operate at room temperature, but of course, cooled sensors achieve better sensitivities (less thermal noise). Most of them rely on a thermal effect, with an absorbing element coupled to a heat sink, and speed of use limited by heat evacuation time. Hence they typically operate at a slower pace than heterodyne detectors but reach nowadays a few hundreds of MHz [157]. They are sensitive to a very broad radiation band, usually from a few tens of GHz to IR, hence not adapted to spectroscopic applications and they require filters. Let us briefly review the main direct detectors; typical figures of merit are summarized in table 1.3.

Detector type	Operating temperature (K)	NEP' (W/\sqrt{Hz})	Speed (Hz)	spectral width (THz)
pyroelectric sensor [13]	ambient	10^{-9}	10^3 to 10^6	0.02 - 3
Golay cell [13]	ambient	10^{-8} to 10^{-10}	~ 100	0.01 - 20
Si Bolometer [2]	1.6 - 4.2 K	10^{-13} to 10^{-15}	200 to 400	0.15 - 20
InSb Bolometer [2]	4.2 K	$\leq 8.10^{-13}$	6.10^3	0.06 - 1.5
VOx Bolometer [173, 122]	ambient	$\geq 3.10^{-10}$ (increases with ν)	$\leq 10^6$	≤ 30
Superconducting HEB [157, 173]	300 mK - 4.2 K	2.10^{-14} @ 4.2 K 10^{-19} @ 300 mK	10^5 to 10^{10}	≥ 10
TES [205, 173]	300 mK	10^{-19} - 10^{-20}	40.10^3	≥ 10
STJ [173, 20, 21, 140]	300 mK	10^{-16} to 10^{-18}	$\geq 10^6$	≤ 1
MKID [202, 28]	100 mK	10^{-18} to 10^{-19}	~ 100	≤ 1

Table 1.3: Comparison of different direct detectors.

1.4.2.1 Thermal sensors

Pyroelectric sensor. The incoming radiation produces a current variation on a pyroelectric material, like a LiTaO_3 crystal.

Golay cell. An incoming radiation on a polyethylene or diamond input window induces a gaz dilatation in a sealed chamber, hence a pressure variation.

Bolometer. A schematic diagram of a bolometer is shown on figure 1.12. A radiation of power P is converted into heat by an absorber whose heat capacity is C_{th} , at a rate $dT_B/dt = P/C_{th}$, and measured by a thermometer. Absorber and thermometer are in general the same material, that exhibits a strong temperature-resistance (dR/dT) dependence. Then heat is evacuated via a thermal conductance G_{th} to a heat sink, generally the supporting substrate. When the radiation is turned off, the absorber goes back to T_S with a time constant τ_{th} . There is a trade-off to be found between sensitivity and response time: in fact in these devices $NE\Delta T$ is proportional to $\sqrt{G_{th}}$ whereas τ_{th} is inversely proportional to G_{th} . For typical uncooled bolometers, $C_{th} \sim 2.10^{-9}$ J/K, $G_{th} \sim 10^{-7}$ W/K and $\tau_{th} \sim 20$ ms [173]. Classical bolometers are made with heavily doped semiconductors in Ge, hence called "semiconductor bolometer", or with vanadium oxide, "VOx bolometers".

The term hot electron bolometer (HEB) usually refers to cryogenic bolometers. Historically "hot electrons" refers to nonequilibrium electrons in semiconductors, and is commonly used to qual-

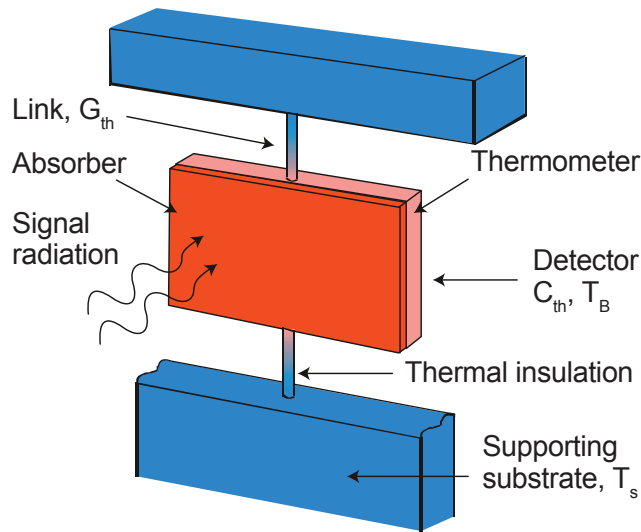


Figure 1.12: Schematic diagram of a thermal detector. Adapted from [173].

ify thermal effects in cryogenic bolometers, hence called hot electron bolometers (HEB). Typical HEB are made with InSb, operated at 4K and below.

TES and superconducting HEB. A transition edge sensor (TES) is a superconducting film of critical temperature T_c , held within its transition region, and weakly coupled to a heat sink at $T \sim T_c/2$. Due to the abrupt change of resistance close to T_c , TES is very sensitive to any heat brought by an incoming radiation. Many materials and designs can be used for TES fabrication, typically the absorber is a low-stress silicon nitride membrane, and the superconductor is aluminum based. TES are usually voltage biased [98] to give a negative electrothermal feedback: a low impedance resistance of a few $m\Omega$ (R_{sh} in figure 1.13) is placed in parallel to the TES whose impedance is much higher, about 1Ω . Thus, a constant power $P_B = RI^2$ flows in the TES, ensuring a linear response, a large bandwidth and an immunity against temperature variations of the heat sink. The reading of resistance variation is done through a superconducting quantum interference device (SQUID) coupled to a coil.

A superconducting HEB (or just "HEB") is very similar to a TES: a superconducting film is biased in its transition, hence a small change of temperature caused by absorption of an incident radiation creates a huge change in its resistance. The main difference is that in HEB, the radiation absorber *is* the superconductor [173], and good electron-phonon coupling ensures a fast heat evacuation. Thus, HEB can operate at higher frequencies than TES.

1.4.2.2 Pair breaking photon detectors

Quantum limited sensors can be fabricated with superconductors because at temperatures $T \ll T_c$ most of the electrons are paired: random generation and recombination of quasiparticles decreases as $e^{-\Delta/(k_B T)}$, and hence thermal noise [205]. Subsequently, if an incoming photon has an energy greater than twice the superconducting gap, it will break a Cooper pair and produce quasiparticles, that one can detect through different schemes.

STJ detector. A superconducting tunnel junction (STJ) - or SIS junction - is a sandwich of an insulating layer between two superconducting bulks (see section 3.1.1 for an explanation of

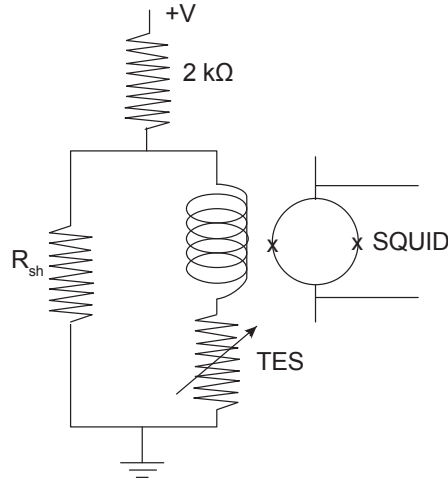


Figure 1.13: TES voltage bias circuit. The shunt impedance $R_{sh} \sim 10 \text{ m}\Omega$ is much smaller than the TES impedance of about $1 \text{ }\Omega$. Adapted from [205].

its physics), through which we can have only quasiparticles (QP) crossing. Typically the barrier is $\sim 20 \text{ \AA}$ thick and the junction is about $1 \text{ }\mu\text{m}^2$. When biased at $V_b < 2\Delta$, incoming photons of energy $h\nu$ may assist the tunneling of QP, which occurs if $h\nu > 2\Delta - qV_b$. However SIS tunnel junctions are mostly used for coherent detection.

MKID. The surface impedance of a superconducting line is highly inductive due to the kinetic energy of moving Cooper pairs, thus called kinetic inductance. The latter is very sensitive to the amount of QP. Therefore, a high-Q microwave resonator (for example a superconducting CPW line) will see its resonant frequency shifted as a photon hits it, which can be monitored through a microwave readout system. It is the functioning principle of microwave kinetic inductance detectors (MKIDs). MKIDs have shown to be very sensitive [28, 202], are fairly easy to multiplex, hence are very promising for imaging applications.

1.4.3 Coherent detectors

As already mentioned, coherent detectors are particularly suited for spectroscopic applications, owing to the high spectral resolution $\lambda/\Delta\lambda = 10^5 - 10^6$ that they can provide [205].

Fundamentally, any electronic device with a non linear current-voltage relation can be used as a mixer, because then the Taylor expansion has a quadratic term, and thus it is at first order a square law component. In the devices described above some have a non linear IV characteristics and that is why they are also (and in fact mostly) used for coherent detection. Those are: SBDs, HEB and SIS junctions. We will very briefly review here their main properties and give in table 1.4 their typical figures of merit. Figure 1.15 compares the noise temperature of different technologies as a function of the operating frequency. We deliberately put aside the photoconductive antenna, because even if it is also a THz mixer, we believe that it is mostly inherent to the THz-TDS technique, rather than a detector in itself.

There are two distinct modes of operation for a mixer: *double-side band* (DSB) and *single-side band* operation. In DSB operation the upper-side band, where $\omega_{sig} > \omega_{LO}$ and the lower-side band, where $\omega_{sig} < \omega_{LO}$ are both converted into the IF band. In SSB operation, only the upper-side band or the lower-side band is converted into the IF band. For sensitivity, it is important to notice that DSB operation down-converts two times more noise than SSB operation.

Let us also point out that compared to direct detectors, an additional and extrinsic problematic comes into play: the generation of a strong enough LO, which limits sometimes the implementation of the technology.

Detector type	Operating temperature (K)	DSB Noise temperature (K)	Maximum operating frequency	LO power
SBD [173, 138]	4.2 - 300 K	55 K @ 100 GHz, 20 K 200 K @ 100 GHz, 300 K 1000 K @ 600 GHz, 300 K 70000 K @ 5 THz, 300 K	≤ 25 THz	1 - 10 mW
SIS [173, 205]	≤ 300 mK	530 K @ 1.2 THz	1.4 THz (Nb) 1.6 THz (NbN - NbTiN)	40 - 100 μ W
HEB (Nb, NbN) [173, 205]	~ 4 K	1500 K @ 1.5 THz (NbN)	~ 5 THz	100 - 500 nW
HEB (YBCO) [168, 173]	≥ 50 K	~ 3000 K @ 600 GHz	-	-

Table 1.4: Comparison of different heterodyne detectors. The maximum operating frequency and the minimum LO power required for high- T_c HEB are not reported in the literature and still need to be investigated.

SBD mixer. A Schottky barrier diode is an electronic element made by a point contact between a metal and a semiconductor (GaAs). An incoming radiation on a SBD can produce four transport mechanism: thermionic emission, photon assisted tunneling and generation-recombination inside or outside the depletion region, hence a detectable current.

SBDs are historically the first devices that have been used for THz heterodyne detection, with a gas laser as LO. The IV characteristics of a SBD is exponential, and given by [56]:

$$I = I_{sat} e^{\left(\frac{V}{V_0}\right)} \quad (1.32)$$

where $V_0 = \eta k_B T / q$, with q the electronic charge, and η the efficiency of the thermoionic emission. The first whisker contacts in GaAs based diodes in the 1960s were replaced by planar technology in the 1980s, which enabled to work at higher frequencies. But beyond 1 THz the shunt capacitance degrades mixing performances. One can reduce it by reducing the size of the contact, but at the same time it increases the series resistance. Also, SBDs require a powerful LO, from 1 to 10 mW. Cooling SBDs improve their performances but not as much as competing with SIS or HEB mixers. Overall they are of interest for room temperature mixing operations.

SIS mixer. The superconducting-insulating-superconducting (SIS) mixer exploits the non linearity of the quasiparticle tunneling process: at a voltage bias $V_b \simeq 2\Delta$ (where Δ is the superconducting gap), the IV characteristic is strongly non linear (see section 3.1.1). As for direct STJ detectors, the photon assisted tunneling (PAT) occurs when $h\nu > 2\Delta - qV_b$, where ν is the photon frequency. However when $h\nu > 2\Delta + V_b \simeq 4\Delta$, the same PAT process allows a reverse tunneling, hence degrades the non linearity. Therefore all-Nb SIS mixers are limited to $\nu < 4 * 1.76k_B T_c / h = 1.4$ THz, and 1.6 THz for NbN or NbTiN junctions. Nevertheless, below these cut-off frequencies, SIS junctions are among the most sensitive detectors, and can operate

close to the quantum limit given by equation 1.30: $k_B T_N \geq h\nu_{LO}/\eta$ (SSB). They have to be operated well below T_c , in order to have most of electrons into Cooper pairs. However up to now they remain difficult to implement into large arrays. They require much less LO power than SBDs, typically 40-100 μW . Figure 1.14 represents simulated IV curves of a niobium SIS mixer, with and without LO illumination, as well as the IF frequency response as a function of bias voltage. P_{IF} is optimum close to 2Δ .

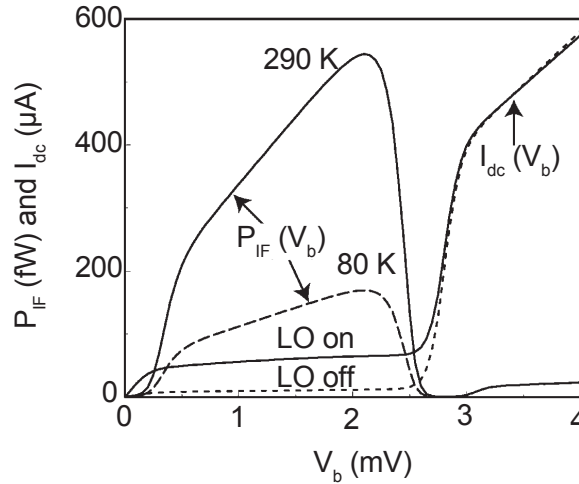


Figure 1.14: Simulations of IV curves and IF response of a niobium SIS mixer. Adapted from [205].

HEB mixer. Unlike SIS mixers, the physics of HEB mixers stems on a thermal effect: close to T_c , the resistance is very sensitive to the electron temperature: it is non linear, hence the non-linear IV characteristic. In addition, the electron-phonon relaxation time τ_{eph} can be made short by having a superconducting film of a few nm, which effectively couples it to the substrate and thus achieve GHz output bandwidth at the IF. Furthermore, the electron specific heat C_e should be smaller than the phonon specific heat C_{ph} so that energy flows from the former to the latter. A 3 nm NbN films has typically $\tau_{eph} \sim 10$ ps and $C_e/C_{ph} = 6.5$ [173]. There is no fundamental restriction to operate HEB mixers at high frequencies (no noticeable capacities), and that is why they are used above 1 THz, up to several THz (see section 1.2.4). Also, the required LO power is about one order of magnitude lower than for SIS mixer, between 100 and 500 nW, which is of prime interest for space applications.

Finally, let us underline that $\text{YBa}_2\text{Cu}_3\text{O}_7$ superconducting HEB mixers are of great interest, because not only they operate at higher temperature, but also $\tau_{eph} \sim 1$ ps, i.e. about one order of magnitude less than for NbN, and $C_e/C_{ph} = 38$. Thus one could have a broader bandwidth.

1.5 Conclusion - terahertz technologies and high- T_c superconductors

As we have seen all along this chapter, little work has been done to address THz frequencies with high- T_c superconductors (HTS), and this for two main reasons: First, their fragile crystalline structure make them delicate to process, as we shall see in chapter 2. With the current technologies, the device fabrication remains challenging and for instance, to date there is no high- T_c equivalent of the low- T_c SIS junctions. Second, their physics is still hardly understood, and theories describing most of the low- T_c cannot be immediately transposed to HTS. We modified some of the theoretical

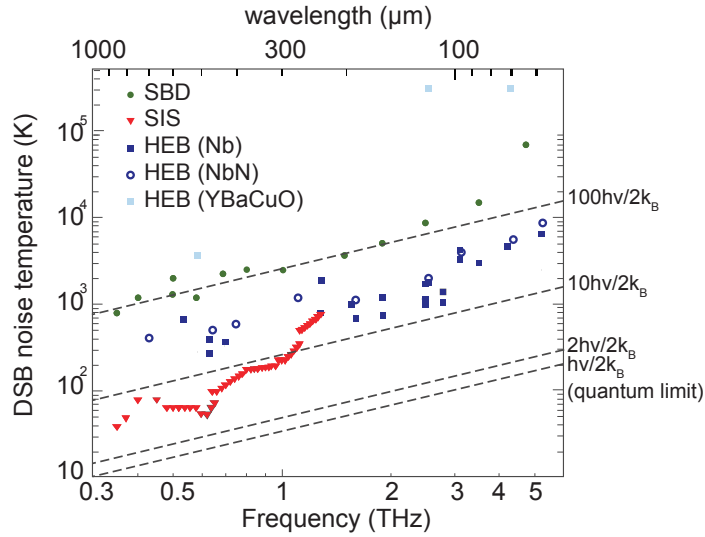


Figure 1.15: Comparison of DSB noise temperatures of the different mixer technology. Adapted from [173].

low- T_c models to explain the physics of the electronic transport in our high- T_c Josephson junctions in chapter 3.

Nevertheless, they operate at much higher temperatures than many recent technologies, where cryogenic cooling as low as 300 mK is commonly required. In a context where helium scarcity on earth could be a forthcoming issue, nitrogen cooled high- T_c technologies would prove valuable. Even working between 30 and 80 K is interesting, because it is much easier to implement in operating systems than colder temperatures.

High- T_c Josephson mixers (HTS-JM) could have an interest in long term space missions, because the exhaustion of helium reserves limits the current lifetime of low- T_c detectors. Furthermore, as we shall see in chapter 7, the local oscillator power required in our system is extremely low, in fact lower than for the low- T_c . HTS-JM could also be useful to implement affordable and reliable short range communication systems, where the semiconductor technology seems limited by output powers and heating related issues.

High- T_c THz sources in $\text{Bi}_2\text{Sr}_2\text{CaCu}_2\text{O}_8$ are very promising, and pave the way to available on-chip local oscillators. High- T_c $\text{YBa}_2\text{Cu}_3\text{O}_7$ superconducting hot electron bolometers are promising due to intrinsic properties of the material that could give detectors with broader IF bandwidth than their low- T_c equivalent.

In this thesis we aimed at evaluate the performances of a high- T_c Josephson mixer for THz detection. We also worked towards the fabrication of an on-chip extrinsic local oscillator, designed with an array of Josephson junctions.

Chapter 2

Fabrication of irradiated Josephson junctions

Contents

2.1 Fabrication of high-T_c Josephson junctions	42
2.1.1 Josephson junctions with intrinsic interfaces	42
2.1.2 Josephson junctions with extrinsic interfaces	43
2.1.3 An alternative: irradiated Josephson junctions	43
2.2 Ion Implantation	44
2.2.1 Transport of ions into matter	44
2.2.2 Plain sheet dpa	46
2.2.3 Implantation through a mask	47
2.3 Ion irradiation on $\text{YBa}_2\text{Cu}_3\text{O}_7$	48
2.3.1 Reduction of T_c	48
2.3.2 Transport measurements	50
2.4 Fabrication steps	51
2.4.1 Structuring the gold layer	51
2.4.2 Patterning the $\text{YBa}_2\text{Cu}_3\text{O}_7$ layer	51
2.4.3 Creating the weak-link.	53
2.5 Other groups fabricating ion irradiated junctions	55

The fabrication of high- T_c Josephson junctions (JJs) has drawn tremendous interest and work since the early nineties, yet it remains a technological challenge. Even if some very recent work on $\text{YBa}_2\text{Cu}_3\text{O}_7$ junctions fabricated with an helium focused ion beam (FIB) is very promising [62], to that day there is still no clean high- T_c tunnel junctions. Conversely, the fabrication of low- T_c junctions has been mastered for decades [89], and it generally consists in a trilayer technology $Al - Al_2O_3 - Al$ or $Nb - Al - Al_2O_3 - Nb$. The oxide growth being a self-terminating process, it provides an easy way to make reproducible thin barriers of a few tens of Å.

With high- T_c superconducting (HTS) materials, it is much more challenging. It is in fact extremely delicate to epitaxially grow an insulating layer between two superconducting layers, since the crystalline fit imposes lots of constraints [113]. Furthermore, the superconducting coherence length is extremely short: typically 2 nm in the ab plane and 0.2 nm in the c -axis direction (to be compared with micrometer coherence length in aluminum). Therefore, the barrier must reach a perfection at the monolayer level, in order to have a tunneling effect.

There has been some attempts to obtain tunnel junctions with HTS, using trilayers $\text{YBa}_2\text{Cu}_3\text{O}_7 / \text{PrBa}_2\text{Cu}_3\text{O}_7 / \text{YBa}_2\text{Cu}_3\text{O}_7$, but the unclear barrier contained localized states, inducing a complicated transport. Nonetheless, Josephson effect was observed [34, 36]. Others used trilayers $\text{YBa}_2\text{Cu}_3\text{O}_7 / \text{PrBa}_2\text{Cu}_3\text{O}_7 / \text{HoBa}_2\text{Cu}_3\text{O}_7$ [57], and demonstrated a clean tunnel conductance-voltage curve, but the results were never reproduced afterwards.

However non-tunnel JJs can be obtained by various methods, which we will describe in section 2.1. Then we will present in section 2.2 and 2.4 the alternative technique that we used, which consists in using ion implantation.

2.1 Fabrication of high- T_c Josephson junctions

For any Josephson junction, two parameters are of prime importance: the critical current I_c and the normal resistance R_n . As we shall see in the next chapters, the higher the $I_c R_n$ product, the better heterodyne terahertz detection is.

Depending on the fabrication, two classical categories of high- T_c junctions stand out: those with intrinsic and those with extrinsic interfaces. Our junctions belong to another category, those with no interfaces.

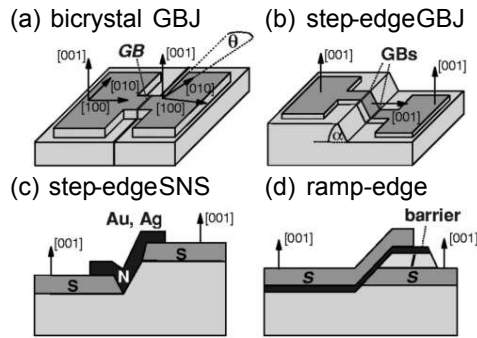


Figure 2.1: Categories of high- T_c Josephson junctions, taken from [113].

2.1.1 Josephson junctions with intrinsic interfaces

The first class gathers the so-called grain boundary junctions (GBJs), in which there is a weak coupling between two crystallographic orientations of the superconducting film.

In *bicrystal GBJs*, the $\text{YBa}_2\text{Cu}_3\text{O}_7$ layer is epitaxially grown on a bicrystal substrate (LaAlO_3 , SrTiO_3 , MgO , sapphire, ...) with two crystalline orientations (figure 2.1 (a)). The high- T_c film is oriented in-plane according to the substrate, and a Josephson junction is created at the joining frontier between the grains [92, 113]. Transport properties depend strongly on the misorientation angle θ which typically spans between 20° and 30° but overall, they have a reasonably high critical current density (depending on θ) and a fairly high $I_c R_n$ product. The table 2.1 gathers typical values found in the literature. However it is not possible to arbitrary place many junctions in the superconducting film with this technique, and it is difficult to control the junction's parameters (critical current I_c and normal resistance R_n). This type of high- T_c junctions is widely used for detectors.

In *step-edge GBJs*, a 200-300 nm step is created in the substrate through standard lithography and Ar-milling (figure 2.1 (b)), then the $\text{YBa}_2\text{Cu}_3\text{O}_7$ layer is grown and the c -axis orientation of the film changes at the step, creating two GBJs. The position of the step on the substrate can be freely chosen and its angle α typically spans between 50° and 60° . Once again, transport

properties strongly depend on this angle [123] and the spread in parameters is greater than for bicrystals GBJs (more than 20%).

2.1.2 Josephson junctions with extrinsic interfaces

The second class gathers the junctions whose interlayer, a normal metal or an oxide, is placed between two superconducting electrodes. Overall, the fabrication process are much more complicated than for intrinsic interfaces.

In *step-edge SNS* junctions (figure 2.1 (c)), a 50-60 nm step is cut in the substrate and then a high- T_c film is directionally grown, so that it does not grow on the step. One fills the gap in situ afterwards, by off-axis sputter deposition of Au or Ag. High normal resistances and very high $I_c R_N$ product have been observed [40] (see 2.1). As controlling the interfaces during fabrication remains very tricky, the reproducibility is poor and the transport properties are difficult to understand. They involve complicated models such as SINIS sandwiches [158].

Ramp-edge junctions' fabrication (figure 2.1 (d)) is the closest to the low- T_c spirit: a $\text{YBa}_2\text{Cu}_3\text{O}_7$ film covered by an insulating layer is deposited, then a ramp is patterned with ion milling. An oxide barrier ($\text{PrBa}_2\text{Cu}_3\text{O}_7$ or ruthenates) covered by the $\text{YBa}_2\text{Cu}_3\text{O}_7$ top electrode is epitaxially grown in situ afterwards. One advantage is that the superconducting/normal interfaces are buried under the top electrode, thus protecting the junction from thermal cycling or aging. Furthermore, the top electrode shields the junction against the normal magnetic field component [113]. However, once again transport properties are difficult to understand, involving localized states in the barrier or in the interface. The normal resistance and the $I_c R_n$ product are moderately high.

		Typical characteristics	remarks [113]
JJs with extrinsic interfaces	bicrystals GBJs [154, 92]	$R_N = 1-2 \Omega$ $I_c R_N = 6-8 \text{ mV @ } 4.2 \text{ K}$ $I_c R_N = 1.2 \text{ mV @ } 77 \text{ K}$ K	RSJ like Large spread of parameters Geometrical constraints
	step-edge GBJs [79, 142, 144, 143, 23]	$R_N = 3-10 \Omega$ $I_c R_N = 3-5 \text{ mV @ } 4.2 \text{ K}$ $I_c R_N = 2 \text{ mV @ } 40 \text{ K}$ $I_c R_N = 150-200 \mu\text{V @ } 77 \text{ K K}$	RSJ like Excess supercurrent Large spread of parameters
JJs with intrinsic interfaces	step-edge SNS [158, 40, 113]	$R_N = 2-10 \Omega$ $I_c R_N = 1 \text{ mV @ } 77 \text{ K}$ $I_c R_N = 8.8 \text{ mV @ } 4.2 \text{ K}$	Poor reproducibility Not RSJ like Large excess supercurrent
	ramp-edge [108, 113]	$R_N = 0.2 \Omega$ $I_c R_N = 0.7-1.2 \text{ mV @ } 30 \text{ K}$ $I_c R_N = 0.3-0.7 \text{ mV @ } 50 \text{ K}$ $I_c R_N = 0.1 \text{ mV @ } 77 \text{ K}$	Not RSJ like Large spread of parameters

Table 2.1: Typical data of high- T_c Josephson junctions taken from the literature, depending on the fabrication technology. RSJ refers to the resistively shunted junction model, that will be developed in the next chapter. The large excess supercurrent means that the Josephson effect is not the only transport mechanism for the supercurrent (see chapter 5).

2.1.3 An alternative: irradiated Josephson junctions

Our fabrication technique of Josephson junctions is different from what we have seen above. It consists in using ion implantation - also called ion irradiation - to create a barrier in a $\text{YBa}_2\text{Cu}_3\text{O}_7$ thin film. It relies on the extreme sensitivity of HTS to defects, owing to the d-wave symmetry

of their order parameter. As we are going to explain, disorder induced in the material by irradiation reduces the superconducting transition temperature and increases the resistivity because of enhanced scattering.

When covered by a mask (a patterned protecting resist), only selective regions in the film undergo irradiation. That way, one can design a slit in which superconductivity is reduced, thus creating a weak-link Josephson junction.

Few groups performed terahertz mixing measurements with high- T_c junctions, and in this context, we will show that the irradiated technology has many advantages regarding others: good reproducibility, and planar junctions; hence easy integration for complicated designs, mandatory for Josephson junction arrays. It has been developed and improved over the past ten years, starting with the PhD work of Xavier Grison and Nicolas Bergeal [33, 35, 36, 170].

2.2 Ion Implantation

The ion implantation - or irradiation - technique consists in modifying the properties of a given material by exposing it to a directed high energy ion beam. The latter usually spans between a few tens of keV to a few MeV, and the number of implanted ions, called dose, varies typically between 10^{12} to 10^{17} ions.cm⁻². Below it, hardly anything is implanted and above it, sputtering effects become predominant so that the sample surface is etched during the process.

Ion implantation has been used for material science and in the semi-conductor industry since the 1980s, to dope silicon and make p-n junctions [49, 48]. At the same time, powerful enough computers emerged and enabled to perform numerical simulations [159, 198], which played a major role in its success. Indeed they are essential to understand and optimize the process because analytical approaches [41, 133] based on a statistical behavior are not accurate enough.

Let us also mention here that YBa₂Cu₃O₇ SQUIDs fabricated with ion irradiation were the first high- T_c superconducting (HTS) devices tested in space on board on the space shuttle Discovery in 1993 [182].

In the frame of irradiated Josephson junctions, one sends oxygen ions (O⁺) on YBa₂Cu₃O₇. It is used twice in the fabrication process: first with a high dose, that completely amorphizes the superconducting film on selective areas; second with a low dose, to locally reduce the critical temperature of the film, and make the junction's barrier. Here, we are going to quantify and simulate the amount of disorder induced by irradiation. To that end we introduce a parameter called the displacement per atom (dpa). It is the percentage of displaced atoms in the crystalline structure.

2.2.1 Transport of ions into matter

We used a Monte Carlo simulation program called TRIM (transport of ions into matter), developed by J. F. Ziegler and J. P. Biersack at IBM. It is based on the stopping and range of ions into matter (SRIM) theories [204]. TRIM calculates the interaction of energetic ions onto a target. From the density of a material, its chemical composition and the displacement energies of each element, it calculates trajectories of implanted ions and the position of the created defects. It uses an analytical formula to determine the atom-atom collision, derived from the screened Coulomb scattering (Rutherford scattering corrected with fitting parameters) and a quantum approach for the interatomic potentials. The collisions of a given ion are spatially separated by an energy dependent free flight path. Thus, a particle's free flight path is longer at high energies and is steadily reduced in the course of slowing down. It considerably improves the calculation time by omitting negligible interactions (where the amount of energy transferred causes a negligible deflection angle). It operates with the following model approximations:

- target is considered amorphous, with atoms at random locations, and thus the directional properties of the crystal lattice are ignored. This approximation remains valid from a few tenths of keV/u (energy/mass) to a few MeV/u, where the binary collisions (lower limit) and the relativistic effect (higher limit) are negligible;
- every ion is calculated with the assumption of zero dose, i.e the target is perfect and previous ions have no effect on subsequent ions;
- target's temperature is 0 K, so that there are no thermal effects changing the distribution of ions (thermal diffusion) or affecting the target damage (thermal annealing).

The TRIM program can record the effects of incoming ions in the target material [204]. Each can generate:

- a vacancy i.e. a hole left behind when a recoil atom moves from its original site;
- a replacement collision i.e. an element replacing the same element that has been displaced;
- an interstitial atom;
- an atoms leaving the target.

Furthermore, TRIM also records all the events of collision cascades. It stops when the transferred energy is lower than the lowest displacement energy. Figure 2.2 represents simulated trajectories and cascades of 100 O^+ ions sent *from a point source* onto a 70 nm $YBa_2Cu_3O_7$ film. The trajectories of implanted ions are white, the recoil oxygen atoms are blue and the recoil copper atoms are violet.

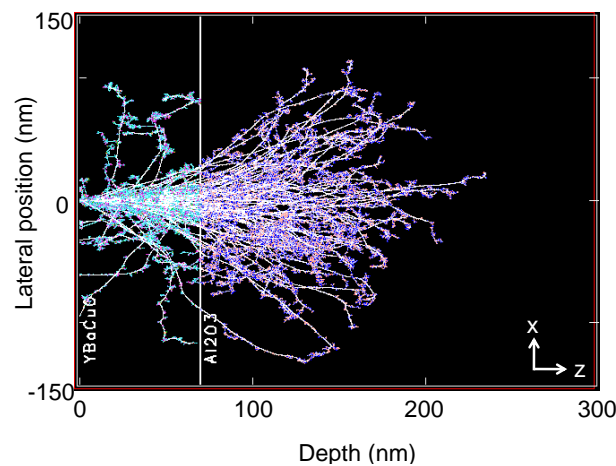


Figure 2.2: Simulation of 100 O^+ ions implanted at 110 keV in a 70 nm $YBa_2Cu_3O_7$ film, projected in the (x, z) plane. The trajectories of implanted ions are white, the recoil oxygen atoms are blue and the recoil copper atoms are violet. In Al_2O_3 the recoil oxygen atoms and aluminum are respectively violet and orange.

Since we send O^+ ions and since oxygen already exists in the structure, they either finish in a replacement collision, interstitial site or leave the target. Thus, the implantation process disturbs as little as possible the fragile structure of $YBa_2Cu_3O_7$. In particular, it does not modify oxygen doping, since the amount of ions is negligible compared to the amount of ions already present in the structure.

2.2.2 Plain sheet dpa

From TRIM simulations, homemade C programs compute the dpa for a given dose and energy. An important parameter is the collision events C (that can be obtained directly in TRIM software). For a plain sheet implantation, $C = C_{ps}(z)$ is the number of defects (vacancies or interstitial atoms) per ions implanted per unit of depth z , hence in defects/ions/Å. To correctly calculate the dpa into $\text{YBa}_2\text{Cu}_3\text{O}_7$ layer (thickness z_0), one has to extract $C_{ps}(z < z_0)$ from the TRIM output file. It is the *total* number of defects per ion implanted inferior to a depth z_0 (thickness of the film). Then the plain sheet $\text{dpa}_{ps}(z < z_0)$ is given by:

$$\text{dpa}_{ps}(z < z_0) = \frac{C_{ps}(z < z_0)\phi}{d} \quad (2.1)$$

where ϕ (in ions/Å²) is the dose and d (in at/Å³) is the material's density. For $\text{YBa}_2\text{Cu}_3\text{O}_7$ $d = 7.53 \cdot 10^{-2}$ at/Å³. The $\text{dpa}_{ps}(z < z_0)$ is in defects/atoms, that is to say a percentage of defects. It is worth noticing that it varies linearly with the dose, but its evolution with the ions' energy is less intuitive. In fact the inset in figure 2.3 represents the total plain sheet dpa for a 70 nm $\text{YBa}_2\text{Cu}_3\text{O}_7$

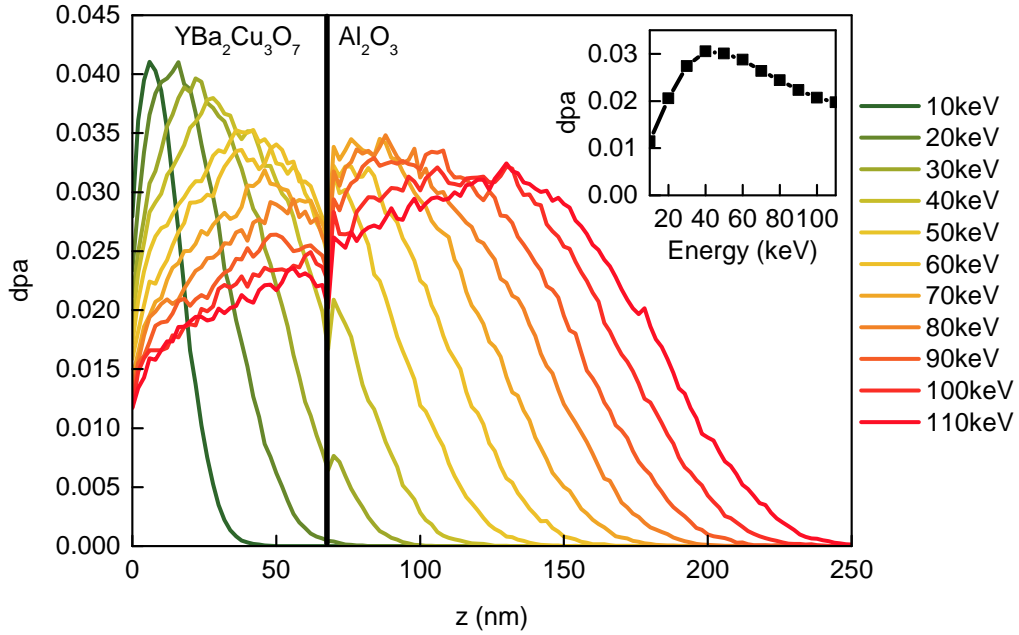


Figure 2.3: Simulations of the plain sheet dpa_{ps} as a function of the depth z . Inset: simulation of the total plain sheet dpa_{ps} for $z < 70$. The dose is $5 \cdot 10^{13}$ ions. cm^{-2} . The simulated sample is a $\text{YBa}_2\text{Cu}_3\text{O}_7$ layer on top of the Al_2O_3 substrate, as in figure 2.2.

layer with the Al_2O_3 substrate at a dose of $5 \cdot 10^{13}$ ions. cm^{-2} , as a function of the implanted ions energy. It increases from low energies, reaches a maximum at 40 keV and then decreases. As the energy increases, damages are buried deeper in the target (due to the energy dependence of the free flight path), so that for a given thickness of a layer the maximum dpa_{ps} is a trade off between the ions' energy and the localization of defects. Figure 2.3 underlines this by showing dpa_{ps} as a function of depth z for various implantation energies. Consequently, if one wants to achieve a high dpa (as in the amorphization step, see 2.4), one should better work with low energies (40 to 70 keV) so that, all things being equal, one uses lower doses, henceforth avoiding to burn any

protecting resist. Conversely for a given thickness, the lateral straggling diminishes as energies increases. Thus a geometry designed in the (x, y) plane by ion implantation is better defined at high energies. That is why we used 110 keV during the second step of implantation. It is the highest energy that can be stopped by 500 nm of PMMA resist (see section 2.4).

2.2.3 Implantation through a mask

We performed simulations of two particular shapes of masks: slits and holes. The former addressed the junction's fabrication, while the latter were used in a partner's project on vortex pinning in $\text{YBa}_2\text{Cu}_3\text{O}_7$ [187].

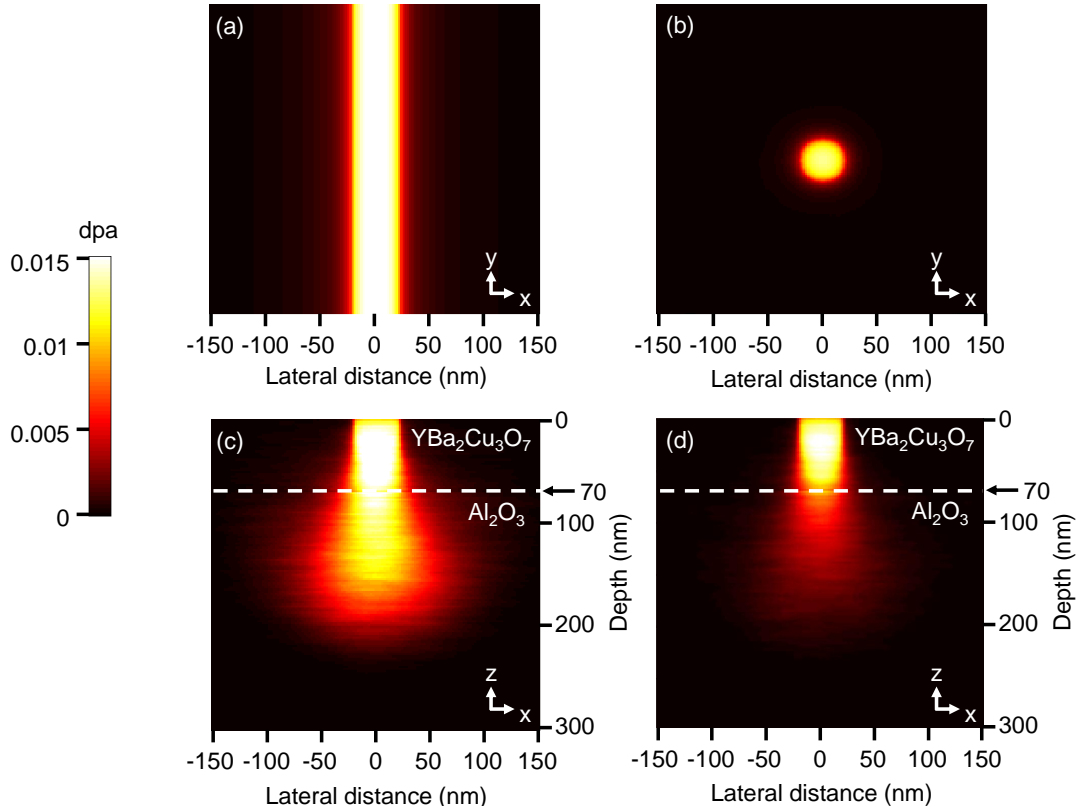


Figure 2.4: Simulated dpa for implanted ions at 110 keV and 5.10^{13} ions. cm^{-2} . (a) $\text{dpa}(x, y, z < 70 \text{ nm})$ in the (x, y) plane for a 40 nm slit and (b) for a 40 nm hole in diameter. (c) simulated $\text{dpa}(x, |y| < 2 \text{ nm}, z)$ in the (x, z) plane of the slit, and (d) for the hole.

When ions are implanted through mask defined in a resist by electron beam lithography, see section 2.4, the collision events C and the dpa must be calculated locally in the material. Thus, one has to extract $C(x, y, z < z_0)$, which is in defects/ions/ \AA^3 . Then the local $\text{dpa}(x, y, z < z_0)$ at the position (x, y) on the film is given by:

$$\text{dpa}(x, y, z < z_0) = \delta_x \delta_y \frac{C(x, y, z < z_0) \phi}{d} \quad (2.2)$$

where $\delta_x = \delta_y = 2 \text{ nm}$ are the discretization lengths of the film, respectively in x and y direction, used in simulations.

Figures 2.4 (a) and (b) represent the simulated $\text{dpa}(x, y, z < z_0)$ for $z_0 = 70 \text{ nm}$ in the (x, y) plane, respectively for a 40 nm wide slit and hole. Figures 2.4 (c) and (d) show the same slit and hole when the dpa is computed in the (x, z) plane, for $|y| < 2 \text{ nm}$. In other words they are a slice

of the dpa in the (x, z) plane. The ions' energy is 110 keV and the dose $5 \cdot 10^{13}$ ions.cm⁻². Due to the constriction in the x and y directions for the hole, the dpa at its center is smaller than the dpa at the center of the slit, where the constriction is only along the x direction.

This effect comes from the tails in the dpa distribution, which appears clearly on simulations of figures 2.5 (a) and (b). They represent a slice of dpa around $y = 0$, that is to say $\text{dpa}(x, |y| < 2 \text{ nm}, z < 70 \text{ nm})$, when the size of the slit (a) and hole (c) vary. For a slit the dpa distribution extends on more than 100 nm whereas for a hole the distribution is sharper. Consequently, the precision at which one can draw a structure by the implantation technique is limited by this effect. Overall, the minimum closeness at which one can place two holes or slits is about 50 nm.

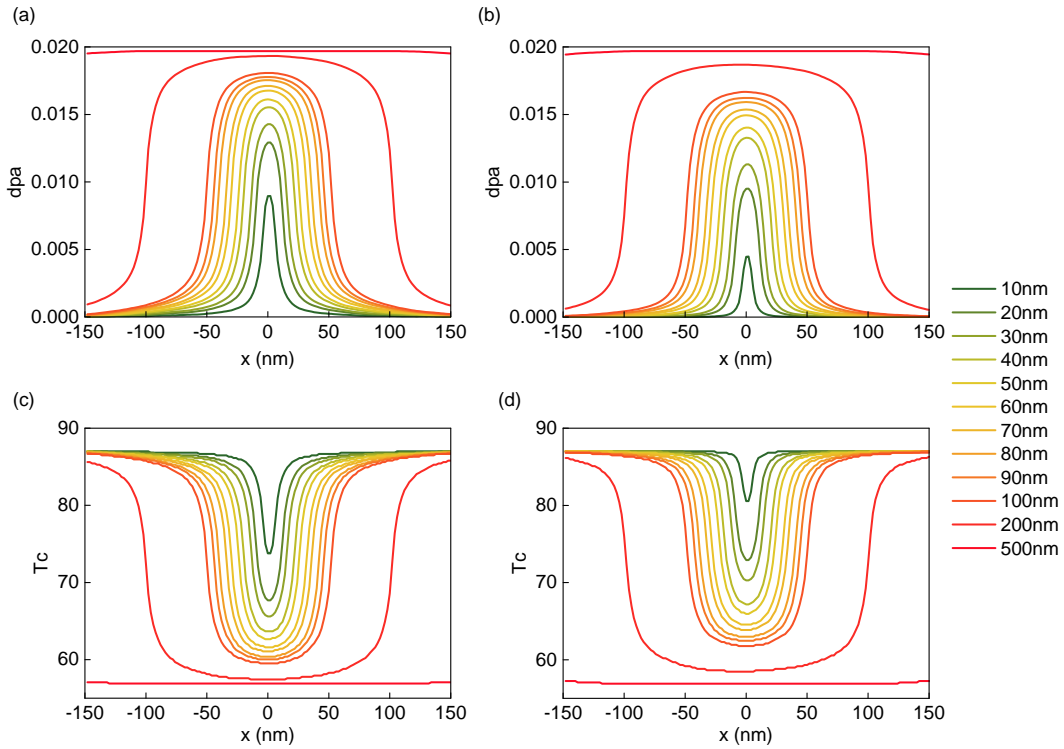


Figure 2.5: Simulated $\text{dpa}(x, |y| < 2 \text{ nm}, z < 70 \text{ nm})$ for different sizes of slit (a) and holes (c). (b) and (d): their respective critical temperature. The ions are implanted at 110 keV and at $5 \cdot 10^{13}$ ions.cm⁻². $\text{dpa}_c = 0.042$ and $T_c = 87\text{K}$.

2.3 Ion irradiation on $\text{YBa}_2\text{Cu}_3\text{O}_7$

As opposed to low- T_c superconductors, (Nb, Al, Pb,...) which are only weakly sensitive to the presence of non-magnetic impurities (Anderson's theorem), HTS are strongly affected by disorder. Ion irradiation has therefore been extensively used to study the puzzling superconducting mechanisms.

2.3.1 Reduction of T_c

The driving mechanism for the reduction of T_c has been disputed. Legris et al. [125] and after them Tolpygo et al. [184] evaluated the displacement energies of the oxygen and copper atoms. They found 10 eV for the oxygen (8.4 eV for the oxygen in the CuO_2 planes) and 15 eV for the copper. In TRIM, default displacement energies for $\text{YBa}_2\text{Cu}_3\text{O}_7$ are 28 eV and 25 eV respectively, and we kept those energies. In any case, due to such low values it was first argued that the decrease of T_c

with ion irradiation comes from induced disorder in the CuO chains. Gupta et al. [88] calculated that completely disordered CuO chains block the charge transfer between CuO₂ planes, therefore inducing the insulating state.

However, Hall coefficient measurements on irradiated YBa₂Cu₃O₇ are still an open debate to know whether changes in R_H account for a change in the carrier density or result from scattering processes. Overall it seems that the later would be the best explanation, with defects localized on CuO₂ planes [189, 183, 184]. Direct observations of damage-induced ion irradiation were done with transmission electron microscopy [160, 109, 53] and x-ray diffraction [71, 201] but they do not give a precise description of the damaged structure, since even a small dpa drastically changes the transport properties of YBa₂Cu₃O₇. Indeed, Lesueur et al. [127] showed that the critical displacement per atom (dpa_c) needed to completely suppress superconductivity is about 0.04, which cannot account for the fully disordered CuO chains.

Consequently a second mechanism was proposed [127, 126] based on an Abrikosov-Gorkov depairing like mechanism [16]. In the same way as magnetic impurities break Cooper pairs in s-wave superconductors, the d-wave symmetry of the superconducting parameter in YBa₂Cu₃O₇ (represented in figure 2.6) makes them very sensitive to any scattering center, i.e. crystalline impurities.

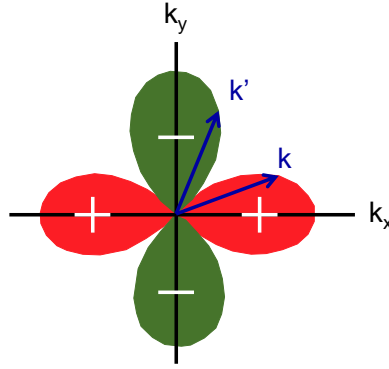


Figure 2.6: The d-wave symmetry of the superconducting wave function in YBa₂Cu₃O₇. A scattering event can induce a phase jump from \mathbf{k} to \mathbf{k}' , which breaks the Cooper pair.

In the Abrikosov-Gorkov depairing mechanism the reduction of T_c is given by [15, 16]:

$$\ln\left(\frac{T_c}{T_{cb}}\right) = \Psi\left(\frac{1}{2}\right) - \Psi\left(\frac{1}{2} + \frac{\hbar}{4\pi k_B T_c \tau_S}\right) \quad (2.3)$$

where Ψ is the digamma function, T_{cb} is the initial critical temperature and τ_S is the pair-breaking scattering time. In the case of a critical temperature reduction induced by defects in HTS, one can infer the pair-breaking rate:

$$\Gamma = \frac{1}{\tau_S} = \frac{dpa}{dpa_c} \Gamma_c \quad (2.4)$$

where Γ_c is the critical pair-breaking rate i.e. the one for which $T_c = 0$, and is taken equal to:

$$\Gamma_c = \frac{\Delta(0)}{\hbar} = 1.76 \frac{k_B T_{cb}}{\hbar} \quad (2.5)$$

The reduction of the critical temperature is then given by [15, 16, 126]:

$$\ln\left(\frac{T_c}{T_{cb}}\right) = \Psi\left(\frac{1}{2}\right) - \Psi\left(\frac{1}{2} + 0.14 \frac{dpa}{dpa_c} \frac{T_{cb}}{T_c}\right) \quad (2.6)$$

2.3.2 Transport measurements

In order to validate the depairing model, we performed ion irradiation on $\text{YBa}_2\text{Cu}_3\text{O}_7$ thin films (70 nm). The resistivity of the films as a function of temperature, for different doses, are shown in figure 2.7 (a). The change in resistivity is in agreement with what has been reported in the literature [195]. For each dose, we calculated the corresponding dpa with Monte Carlo simulations (equation 2.1). We then extracted the critical temperatures, and plotted (dots) T_c/T_{cb} as a function of the dpa in figure 2.7 (b). On the same figure, we plotted (blue curve) the Abrikosov-Gorkov depairing law 2.6, when taking a critical $\text{dpa}_c = 0.042$. The law describes well the experimental reduction of T_c , and our dpa_c is close to the one that Lesueur et al. [127] found in the nineties (they had $\text{dpa}_c = 0.037$).

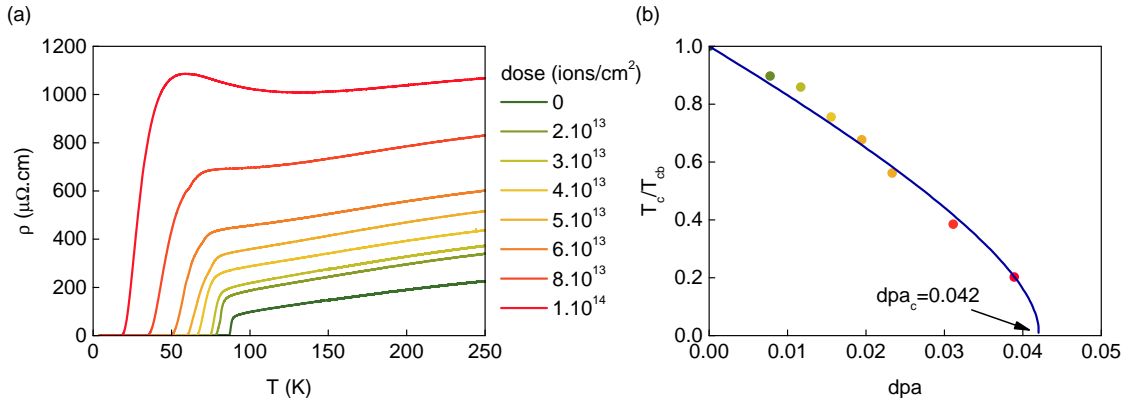


Figure 2.7: (a) Resistivity as a function of temperature of 70 nm thick $\text{YBa}_2\text{Cu}_3\text{O}_7$ films. The samples underwent an irradiation of O^+ ions at 110 keV and doses of (0, 2, 4, 5, 6, 8 and 10) $\times 10^{13}$ ions.cm $^{-2}$. (b) Evolution of T_c (normalized with T_{cb}) as a function of the dpa. The plain line represents the fit with the Abrikosov-Gorkov depairing like law with $\text{dpa}_c = 0.042$.

At low doses ($< 8 \times 10^{13}$ ions.cm $^{-2}$), the dependence of the resistivity ρ with the dpa is weak. In this regime we experimentally find:

$$\begin{aligned} \rho(\text{dpa})_{@250\text{K}} &= \rho_0(1 + 40\text{dpa} + 1260\text{dpa}^2) \\ \rho_0 &= 226 \mu\Omega.\text{cm} \end{aligned} \quad (2.7)$$

where ρ_0 is the resistivity of the undamaged film at 250 K. Also, the resistivity decreases linearly with temperature [37]. We experimentally find:

$$\begin{aligned} \frac{d\rho}{dT} &= \alpha_0(1 + 9.7\text{dpa}) \\ \alpha_0 &= 0.8 \mu\Omega.\text{cm}/\text{K} \end{aligned} \quad (2.8)$$

At high doses there is a transition to an insulating state and some studies [189, 183, 184] suggest that electrons follow a Mott variable-range hopping mechanism, with a resistivity given by:

$$\rho \sim \rho_0 \exp\left(\frac{E_A}{k_B T}\right)^{\frac{1}{d+1}} \quad (2.9)$$

with d the dimension of the material, and E_A an activation energy. This regime is slightly visible on the $\rho(T)$ curve corresponding to the highest dose.

Taking the dpa_c at 0.042 and the T_{cb} at 87 K, figures 2.5 (c) and (d) represent the *local* critical temperatures corresponding to a slit and a hole, respectively. Along the x axis, there is a continuous transition between T_{cb} and T_c in the central irradiated part. Therefore the operating temperature

sets the length of the normal part. In the range of temperatures where the slope of the local T_c is high, we can expect at first order a linear variation of the normal part's length as a function of temperature.

Let us finally indicate that the absolute values for the dpa and the local T_c are to be taken with some precaution: the displacements per atom calculated here neither take into account any channeling effect in epitaxial heterostructures, nor any particular imperfection in the design of the slit or hole.

2.4 Fabrication steps

The junction's fabrication consists in several steps of clean room processes and two steps of ion implantation. The following method is reproducible and allows design flexibility. To that end, we chose to use only electron beam lithography, a major asset in the quest of the best detector's architecture and local oscillator source. Furthermore, the spread of modified scanning electron microscopes for e-beam in local clean rooms granted a fast execution. Finally, it enabled to fabricate structures down to a few tenth of nm.

The fabrication process is summarized in figure 2.8. It can be divided into three parts: structuring the gold layer, patterning the $\text{YBa}_2\text{Cu}_3\text{O}_7$ layer and creating the weak-link. Appendix B regroups all the fabrication parameters and the detailed recipe.

2.4.1 Structuring the gold layer

We start from commercial samples of 70 nm $\text{YBa}_2\text{Cu}_3\text{O}_7$ films, that we buy from the Ceraco firm. On $\text{YBa}_2\text{Cu}_3\text{O}_7$, is grown in situ 250 nm of a gold layer. The substrate is Al_2O_3 . Figure 2.8 (a) represents the virgin sample.

The first step consists in structuring the gold layer with e-beam: the aim is to pattern d-c connecting pads, microwave circuitry and antennas for the detectors. To that end we first deposit an electro-sensitive resist, namely the *MAN-2405*. Then one makes the first lithography. Figure 2.8 (b) represents the sample after this procedure.

The next step, figure 2.8 (c), is a dry etching (ion beam etching - IBE): the gold uncovered by the resist is to be removed. It is done with Ar ions, sent onto the sample at 500 eV. After cleaning, the sample is a $\text{YBa}_2\text{Cu}_3\text{O}_7$ layer on top of which the gold layer has been patterned. Figure 2.8 (d) represents a spiral antenna embedded in a microwave transmission line at the end of such a step

Figure 2.9 (a) is a SEM picture (taken with a tilted angle of 30°) of the *MAN-2405* resist on the gold layer after the chemical development. The line is 200 nm wide and 500 nm thick. The developing time as well as the e-beam dose are correctly adjusted because the edges of the line are sharp. Figure 2.9 (b) is an optical photography of the center of a spiral antenna (dark yellow areas) drawn with the *MAN-2405* on the gold layer, and a photograph after dry etching is at figure 2.9 (c).

2.4.2 Patterning the $\text{YBa}_2\text{Cu}_3\text{O}_7$ layer

We now need to form insulating parts in the sample. The $\text{YBa}_2\text{Cu}_3\text{O}_7$ under the gold will always remain superconducting, however one needs to process the uncovered parts. For detectors, a superconducting micro-bridge ought to be placed at the center of the antennas, and for arrays of Josephson junction a superconducting geometry has to be designed between d-c lines. Consequently we perform a second e-beam lithography to pattern another deposition of the *MAN-2405* resist.

After development, a micron size structure is rightfully placed between Au lines. Figure 2.10 represents a 750 nm wide bridge that links the two parts of a spiral antenna.

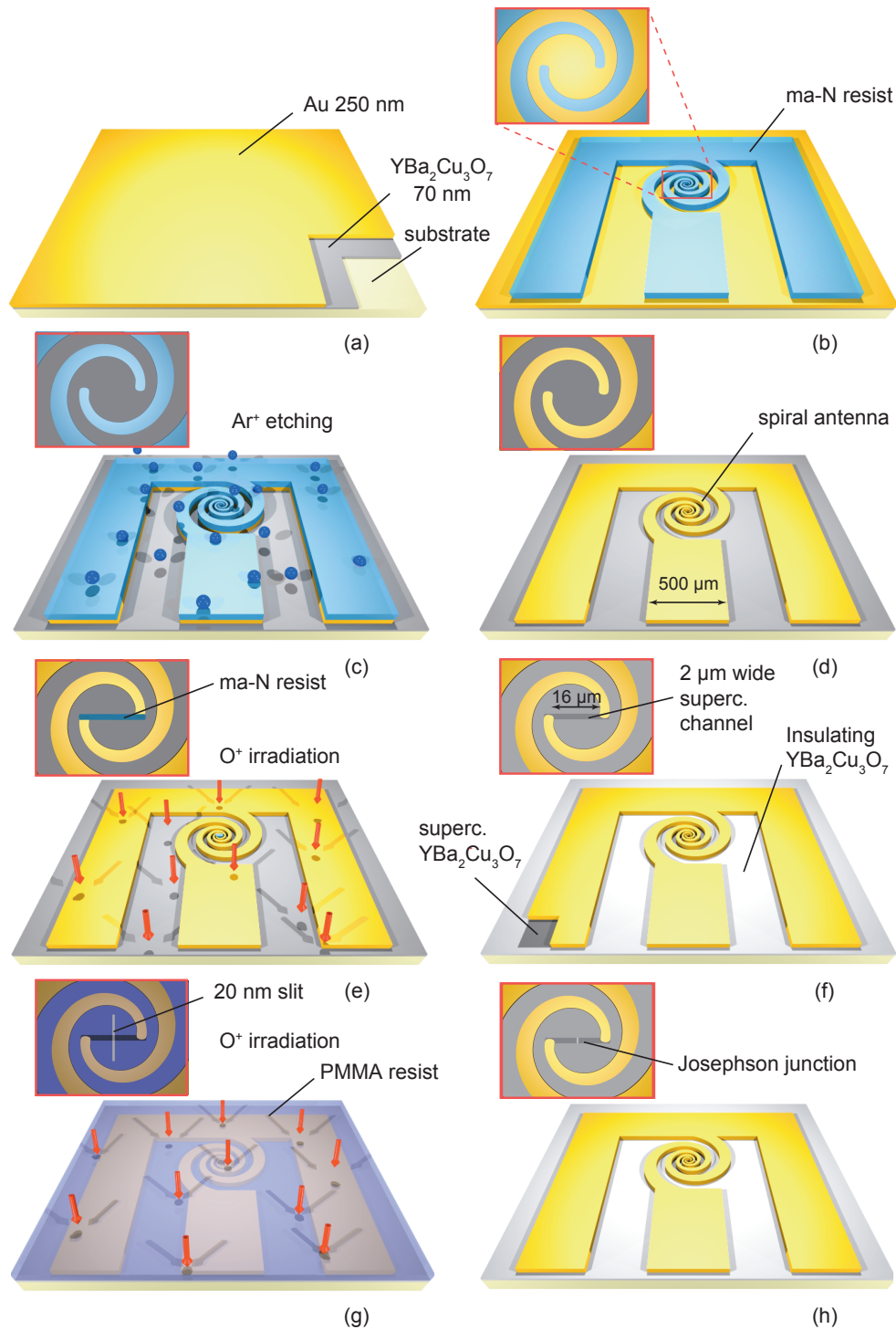


Figure 2.8: Illustration of the fabrication process steps: (a) 70 nm thick $\text{YBa}_2\text{Cu}_3\text{O}_7$ film grown on sapphire covered by an in situ 250 nm gold layer; (b) spiral antenna in the CPW transmission line defined in a 500 nm thick MAN-2405 negative e-beam resist; (c) 500 eV Ar ion-beam-etching of the gold layer; (d) gold antenna in the CPW transmission line on $\text{YBa}_2\text{Cu}_3\text{O}_7$; (e) high-dose 70 keV oxygen ion irradiation to create insulating regions in exposed $\text{YBa}_2\text{Cu}_3\text{O}_7$. A 2 μm wide channel in the center of the antenna is protected by a 500 nm thick MAN-2405 resist mask; (f) patterned superconducting and insulating $\text{YBa}_2\text{Cu}_3\text{O}_7$ regions; (g) low-dose 110 keV oxygen ion irradiation of the Josephson junction patterned as a 20 nm-wide slit in a 500 nm thick PMMA resist; and (h) device after resist cleaning. From [135].

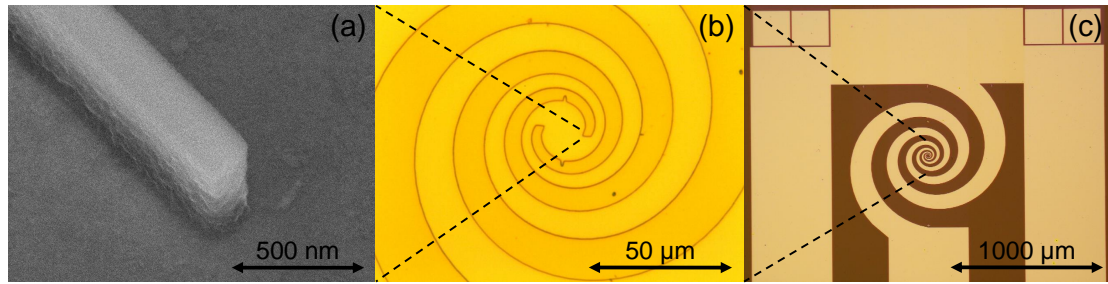


Figure 2.9: (a) SEM picture (taken with a tilted angle of 30°) of a MAN-2505 resist line patterned with e-beam lithography, on a gold layer. (b) Optical photo of a MAN-2405 spiral design (dark yellow areas) on a gold layer. (c) Optical photo of such a spiral embedded in a microwave transmission line after the ion beam etching.

Then we do the first implantation to amorphize all the $\text{YBa}_2\text{Cu}_3\text{O}_7$, everywhere but underneath the gold and the resist, see figure 2.8 (e). It is done at INESS Laboratory in Strasbourg. We have seen that the depth at which one finds the highest dpa increases with ion's energy (inset of figure 2.3). That is why we use low energies (70 keV) for this amorphization step, in order to place as much defects as possible for a minimum irradiation dose ($2 \cdot 10^{15}$ ions. cm^{-2}).

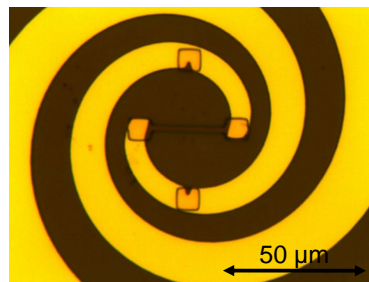


Figure 2.10: Optical photo of a MAN-2405 micro bridge (750 nm wide, 15 μm long) at the center of a spiral antenna.

2.4.3 Creating the weak-link.

In the last part, we open a 20-40 nm slit (or several slits for Josephson junction arrays) in a 500-550 nm thick layer of poly-methyl methacrylate (PMMA) resist (see photo figure 2.11), and make a second ion irradiation. One needs such thickness to protect the parts that shouldn't see the irradiation.

During the second ion irradiation, once again we send O^+ ions, at 110 keV and 3 to $5 \cdot 10^{13}$ ions. cm^{-2} . Compared to the first one, this higher energy diminishes the straggling, and the dose is chosen so that the device operates at temperatures between 40 and 60 K (see chapter 5).

The temporal stability and the normal resistance can be improved by thermal annealing [170, 182].

Figure 2.12 (a) is a SEM picture of two 30 nm slits taken in the (x, z) plane (same axes as in 2.4). The slits were fabricated on a silicon wafer, easier to cleave. We can see that they are well defined in the 500 nm thick PMMA. The figure 2.12 (b) is a histogram of the gray shades in the

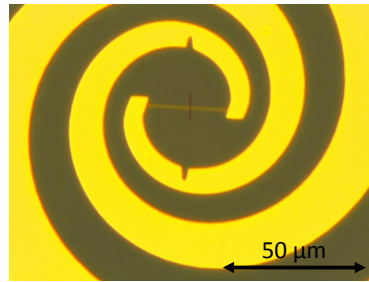


Figure 2.11: Optical photo of a 40 nm slit patterned in the PMMA, prior to the second ion implantation.

square rectangle around the right slit of (a). It gives a quantitative measurement for the size of the slit, approximately 30 nm.

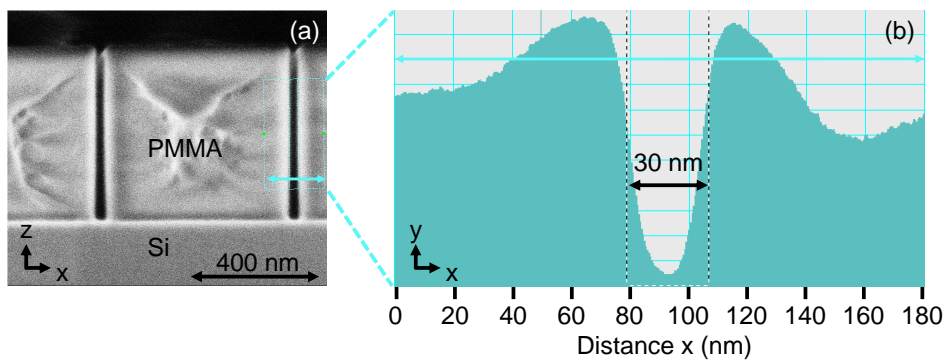


Figure 2.12: (a) SEM picture of two 30 nm slits taken in the (x, z) plane (same axes as in 2.4). The slit were e-beam lithographed and the sample was cleaved afterwards. (b) Histogram of the gray shades in the square rectangle around the right slit of (a). Courtesy of C. Ulysse and Thales Research and Technology.

2.5 Other groups fabricating ion irradiated junctions

Since the pioneering work of White et al. on irradiated $\text{YBa}_2\text{Cu}_3\text{O}_7$ [195], many groups have developed fabrication processes of ion irradiated Josephson junctions. Let us mention here the most relevant studies: the Tincev's group, first to observe a Josephson behavior in weak-links irradiated junctions, at the Institute of Electronics in the Bulgarian Academy of Sciences [181, 182, 26]. The Dynes' group at the University of California, who has been working over the past 30 years on the matter [195, 104, 105, 63, 59]. The Blamire's group at the University of Cambridge [44, 152, 153] and a team at Jülich in Germany [102, 178].

Table 2.2 gathers typical characteristics of Josephson junctions fabricated by these groups. Our junctions have fairly higher normal resistances than what is reported, about 2-5 Ω . However, our $I_c R_n$ products are about the same than the ones of the Jülich group, about 200 μV , as we shall see in chapter 5.

Different types of ions have been used: some used light particles such as helium, protons or electrons, others used heavier ions such as Neon or oxygen. Overall it seems that O^+ irradiation is advantageous since created defects are stable: oxygens atoms do not diffuse too much in the film, and unlike light ions they don't anneal too fast.

Group	ions & energy	JJ characteristics	R_n	$I_c R_n$
Dynes [104, 105]	Ne^+ 200 keV	$w = 2 - 4 \mu\text{m}$ $l = 20 - 100 \text{ nm}$ $t = 100 \text{ nm}$	0.2 - 0.3 Ω	50 - 200 μV @ 45 - 65 K
Tincev [182]	O^+ 100 keV	$w = 5 \mu\text{m}$ $l = 300 \text{ nm}$ $t = 200 \text{ nm}$	1 Ω	10 μV @ 77 K
Blamire [44, 152]	e^- 350 keV	$w = 2 - 3 \mu\text{m}$ $l = 15 \text{ nm}$ $t = 200 \text{ nm}$	0.5 Ω	300 μV @ 77 K 650 μV @ 40 K
Jülich [102, 178]	O^+ 200 keV	$w \sim \mu\text{m}$ $l = 50 \text{ nm}$ $t = 80 \text{ nm}$	0.5 - 1 Ω	100 - 300 μV @ 40 K

Table 2.2: Characteristics of irradiated Josephson junctions, fabricated by other groups. w is the bridge's width, l the weak-link's length and t the $\text{YBa}_2\text{Cu}_3\text{O}_7$ thickness.

Chapter 3

Electronic transport in $\text{YBa}_2\text{Cu}_3\text{O}_7$ irradiated Josephson junctions

Contents

3.1	Theory of the Josephson effect	57
3.1.1	Quasiparticle tunneling in SIS junctions	58
3.1.2	Josephson equations	60
3.1.3	Interpretation of the Josephson equations	61
3.2	Transport measurements in ion irradiated junctions	62
3.2.1	RT curves	63
3.2.2	IV curves	63
3.2.3	Critical current	64
3.3	RCSJ - RSJ model	64
3.3.1	Ideal weak-link Josephson junction	65
3.3.2	Dynamics of the junction	67
3.3.3	Model of a real Josephson junction	70
3.4	Conclusion on the electronic transport	72

Josephson effect is the occurrence of a superconducting current through a non-superconducting barrier. This current is controlled by the phase difference between the two reservoirs on both side of the *Josephson junction*.

We will present more precisely this effect in section 3.1 and will converge towards its manifestation in weak-link junctions, such as our irradiated Josephson junctions. Then in section 3.2 we will show its signature in experimental measurements, and finally we will expose in section 3.3 the equivalent circuit model classically used to account for its physics. We will extensively use this model in chapters 5 and 7 to fit out experimental data.

The next chapter will describe more fundamentally the mechanisms behind the existence of the Josephson effect in weak-links junctions.

3.1 Theory of the Josephson effect

Two kinds of electronic transport can take place in superconducting devices. One is related to unpaired electrons (quasiparticles) and one concerns Cooper pairs. The Josephson effect [101] is the dissipationless transport mechanism of Cooper pairs, which takes place between two superconductors separated by a barrier. Thus, the current-voltage (*IV*) characteristic of such "Josephson"

junctions involves always two branches: the Josephson branch at $V = 0$ for the superfluid, and the quasiparticle branch at $V \neq 0$ for the metallic fluid.

In this section, we will first present the transport mechanism in superconductor-insulating-superconductor (SIS) tunnel junctions. Indeed, a semi-conductor approach that takes into account the tunneling effect and the superconducting density of states qualitatively explains the quasiparticle transport. Then we will derive the Josephson equations from the model proposed by Feynman, Leighton and Sands [78], of which we will give some physical interpretations. Lastly we will qualitatively discuss the transport mechanism and the shape of the IV curves in weak-link junctions.

3.1.1 Quasiparticle tunneling in SIS junctions

In a 3D normal metal the electronic density of states (DOS) is given by:

$$\nu(E) = \frac{V}{2\pi^3} \left(\frac{2m}{\hbar^2}\right)^{3/2} \sqrt{E} \quad (3.1)$$

where E is the energy (referenced to the Fermi energy E_F), V is the total volume of the bulk and m is the effective electron mass. The square root dependence gives a nearly flat DOS at the Fermi level since in usual materials $T_F \sim 1000$ K and we deal with temperatures of a few Kelvins around the Fermi temperature. In a conventional superconductor the BCS theory [25] gives the following expression for the DOS:

$$\begin{cases} \nu(E) = \nu(0) \frac{E}{\sqrt{E^2 - \Delta^2}} & |E| \geq \Delta \\ \nu(E) = 0 & |E| < \Delta \end{cases} \quad (3.2)$$

where $\nu(0)$ is the DOS at the Fermi level. Thus it diverges at Δ (superconducting gap), and there is no any accessible energy in the gap between $E_F - \Delta$ and $E_F + \Delta$.

When one forms a normal-insulating-normal (NIN) or an SIS junction, classical mechanics forbids any transport for any particle with energy lower than the barrier height. However in quantum mechanics, electrons are represented by a wave-function whose square modulus represents their probability density of presence. This wave function decays exponentially in the barrier, hence if the latter is thin enough, there is a non negligible probability for electrons to "tunnel" across the insulator.

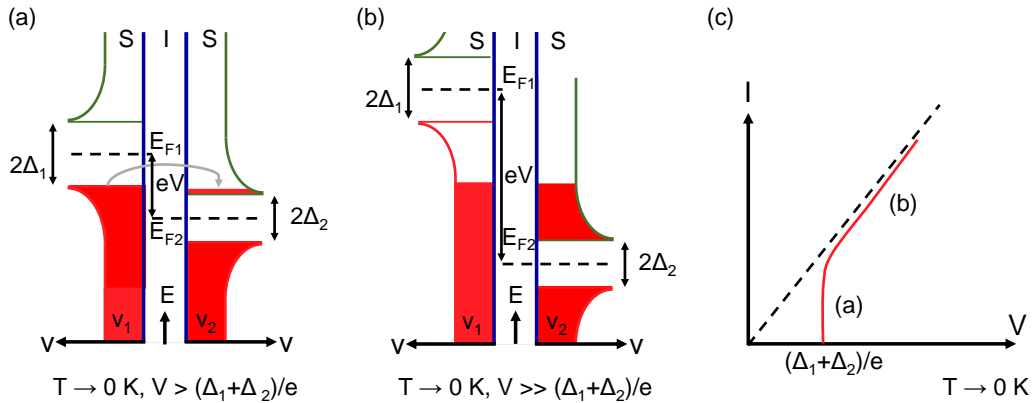


Figure 3.1: (a) and (b): semi-conductor model of the quasiparticle tunneling effect in a SIS junction. The DOS ν_1 and ν_2 of each superconducting reservoir is given by the BCS theory (equations 3.2). (c): corresponding quasiparticle branch in the IV characteristics. The vertical part of the branch corresponds to situation (a), and the linear part corresponds to situation (b).

Now, following a semi-conductor approach (as for pn junctions), if one applies a voltage difference at the SIS or NIN terminals one can align the filled electronic bands of one side with the

empty bands of the other (see figure 3.1 (a), (b)). Then, electrons can tunnel through the insulator and a current appears.

Let us find the expression of this tunneling current I_t . Since electrons can go from side 1 (left) to side 2 (right) and vice versa, I_t is given by:

$$I_t = (J_{1 \rightarrow 2} - J_{1 \leftarrow 2})A \quad (3.3)$$

where $J_{1 \rightarrow 2}$ ($J_{1 \leftarrow 2}$) is the current density flowing from side 1 to side 2 (2 to 1), and A is the section of the barrier. If we consider the tunneling coupling as a perturbation represented by the Hamiltonian H_T , then the probability $W_{1 \rightarrow 2}$ for one electron with an energy between E and $E + dE$ to transit from $|1\rangle$ to $|2\rangle$ is given by Fermi's golden rule:

$$W_{1 \rightarrow 2} = \frac{2\pi}{\hbar} |\langle 2 | H_T | 1 \rangle|^2 v_2(E) (1 - f(E)) \quad (3.4)$$

where $v_2(E)$ is the DOS in side 2 and f is the Fermi-Dirac distribution $f(E) = \frac{1}{e^{\frac{E-E_F}{k_B T}} + 1}$. The density of available states of energy E in side 2 is given by $v_2(E)(1 - f(E))$. To obtain the tunneling current density $J_{1 \rightarrow 2}$ one has to sum $W_{1 \rightarrow 2}$ over the occupied states $v_1(E)f(E)$ in side 1. Hence, when a voltage difference V is applied at the junction terminals:

$$J_{1 \rightarrow 2} = e \int W_{1 \rightarrow 2} v_1(E - eV) f(E - eV) dE \quad (3.5)$$

$$J_{1 \rightarrow 2} = e \frac{2\pi}{\hbar} |T|^2 \int v_2(E) (1 - f(E)) v_1(E - eV) f(E - eV) dE \quad (3.6)$$

where the amplitude of transition probability through the barrier $T = H_{12} = H_{21}^* = \langle 2 | H_T | 1 \rangle$ is taken independent of E . Similarly the current density flowing from side 2 to 1 is given by:

$$J_{1 \leftarrow 2} = e \frac{2\pi}{\hbar} |T|^2 \int v_1(E - eV) (1 - f(E - eV)) v_2(E) f(E) dE \quad (3.7)$$

Thus, the total current is:

$$I_t = Ae \frac{2\pi}{\hbar} |T|^2 \int_{-\infty}^{+\infty} v_1(E - eV) v_2(E) [f(E - eV) - f(E)] dE \quad (3.8)$$

We can see that it strongly depends on the DOS of both sides. In addition, the difference $[f(E - eV) - f(E)]$ only depends on V . Its value is close to 1 for energies below eV and it decreases strongly beyond. The tunneling spectroscopy is a way to measure the DOS of materials and it stems from such a dependence for the current.

In the case of an SIS junction, v_1 and v_2 are given by 3.2. Thus at $T \rightarrow 0$ K there is no quasiparticle tunneling until $eV = \Delta_1 + \Delta_2$, situation at which there is a brutal increase of the current because the highest density of occupied states on side 1 (left side in figure 3.1 (a)) is at the same energy level than the highest density of empty states on side 2 (right side). It corresponds to the vertical part in the IV curve of tunnel junctions, on the quasiparticles branch (figure 3.1 (c)). For $eV \gg \Delta_1 + \Delta_2$ the density of occupied (empty) states on side 1 (respectively 2) is practically constant (equation 3.2) and the tunneling current is linear with V : the junction has an ohmic behavior (figure 3.1 (b)).

When $T \neq 0$ K (strictly speaking when $k_B T > \min(2\Delta_1, 2\Delta_2)$), there is in addition a subtle effect below $\Delta_1 + \Delta_2$. In fact when $eV = |\Delta_1 - \Delta_2|$ the two highest occupied bands are aligned. They are not completely filled because thermal agitation depletes them, and then electrons can go through the barrier. Thus, a tunnel current exists and a bump appears in the IV curve at $|\Delta_1 - \Delta_2|/e$.

3.1.2 Josephson equations

We now deal with the superfluid. As we shall see here, even at $V = 0$ a tunnel current exists, called the Josephson current [101]. It cannot be explained within the frame of the semi-conductor approach (figure 3.1), since we deal with Cooper pairs. We derive here the Josephson equations from the Feynman model [78, 27], which is simpler than the microscopic models based on the tunneling Hamiltonian. Let us call ψ_1 (ψ_2) the pair wave function for the left (right) superconductor. We indicate by $|1\rangle$ ($|2\rangle$) the base state for the left (right) superconductor. Then:

$$\langle 1 | \psi_1^* \psi_1 | 1 \rangle = |\psi_1|^2 = n_1 \quad \langle 2 | \psi_2^* \psi_2 | 2 \rangle = |\psi_2|^2 = n_2 \quad (3.9)$$

where n_1 (n_2) is the superfluid density in the left (right) reservoir. If we take into account the weak coupling existing between the two superconductors, transitions between the two states $|1\rangle$ and $|2\rangle$ can occur. This coupling is due to the overlap between the two pair wave functions ψ_1 and ψ_2 . Then the system is described by the state vector:

$$|\psi\rangle = \psi_1 |1\rangle + \psi_2 |2\rangle \quad (3.10)$$

that is to say it is in the superposition of $|1\rangle$ and $|2\rangle$ with probability amplitudes ψ_1 and ψ_2 respectively. Now the temporal evolution $|\psi\rangle$ is deterministically determined by the Schrödinger equation:

$$i\hbar \frac{\partial |\psi\rangle}{\partial t} = H |\psi\rangle \quad (3.11)$$

where H is the total Hamiltonian of the system:

$$H = H_1 + H_2 + H_t \quad (3.12)$$

where $H_1 = E_1 |1\rangle\langle 1|$ and $H_2 = E_2 |2\rangle\langle 2|$ are the Hamiltonian of the unperturbed states $|1\rangle$ and $|2\rangle$, with E_1 and E_2 the ground states energies of the two superconductors.

$$H_t = K[|1\rangle\langle 2| + |2\rangle\langle 1|] \quad (3.13)$$

is the tunneling Hamiltonian between the two states. K is the coupling amplitude between the two states of the system and it depends on the characteristics of the barrier. For a typical tunnel junction and in the absence of a vector potential \mathbf{A} , K can be assumed to be real. Then the Schrödinger equation 3.11 can be written in base $\{|1\rangle, |2\rangle\}$:

$$\begin{cases} i\hbar \frac{\partial \psi_1}{\partial t} = E_1 \psi_1 + K \psi_2 \\ i\hbar \frac{\partial \psi_2}{\partial t} = E_2 \psi_2 + K \psi_1 \end{cases} \quad (3.14)$$

In the two isolated superconductors, the ground state energies of the condensates are given by $E_1 = 2E_{F1}$ and $E_2 = 2E_{F2}$. Then if one applies a voltage across the junction, the Fermi energies are shifted by eV , and consequently $E_1 - E_2 = 2eV$. We choose the origin of the energies at $(E_{F1} + E_{F2})/2$, hence:

$$\begin{cases} i\hbar \frac{\partial \psi_1}{\partial t} = eV \psi_1 + K \psi_2 \\ i\hbar \frac{\partial \psi_2}{\partial t} = -eV \psi_2 + K \psi_1 \end{cases} \quad (3.15)$$

we can substitute ψ_1 and ψ_2 with their expressions:

$$\psi_1 = \sqrt{n_1} e^{i\phi_1} \quad \psi_2 = \sqrt{n_2} e^{i\phi_2} \quad (3.16)$$

And separating real and imaginary parts in the system 3.15:

$$\begin{cases} \frac{\partial n_1}{\partial t} = \frac{2}{\hbar} K \sqrt{n_1 n_2} \sin \phi \\ \frac{\partial n_2}{\partial t} = -\frac{2}{\hbar} K \sqrt{n_1 n_2} \sin \phi \end{cases} \quad (3.17)$$

$$\begin{cases} \frac{\partial \phi_1}{\partial t} = \frac{K}{\hbar} \sqrt{\frac{n_1}{n_2}} \cos \phi + \frac{eV}{\hbar} \\ \frac{\partial \phi_2}{\partial t} = \frac{K}{\hbar} \sqrt{\frac{n_1}{n_2}} \cos \phi - \frac{eV}{\hbar} \end{cases} \quad (3.18)$$

where $\phi = \phi_1 - \phi_2$. Since the pair current density is given by:

$$J = \frac{\partial n_1}{\partial t} = -\frac{\partial n_2}{\partial t} \quad (3.19)$$

Equations 3.17 give the d.c. Josephson equation:

$$J = J_c \sin \phi \quad (3.20)$$

where $J_c = \frac{2}{\hbar} K \sqrt{n_1 n_2}$. Even though n_1 and n_2 are considered constant, their time derivative J is not. There is no contradiction if we take into account the presence of a current source at the junction's terminals, that constantly replaces the pair tunneling across the junction. This current source is however absent in this model.

The current-phase relation could be more complicated than a pure sinus, and we could account for it by taking a complex constant K (in equation 3.15). In a first order approximation, the simple relation 3.21 is sufficient.

The equations 3.18 give the a.c. Josephson equation:

$$\frac{\partial \phi}{\partial t} = \frac{2e}{\hbar} V \quad (3.21)$$

3.1.3 Interpretation of the Josephson equations

The constitutive equations 3.20 and 3.21 of the Josephson effect gave rise to a very rich Physics, and it is the foundation of all superconducting electronics.

First, equation 3.20 is the expression of a current flowing through the junction without dissipation, the "Josephson supercurrent" $I_J = I_c \sin \phi$, up to a maximal value called the critical current I_c equal to $J_c A$ where A is the section of the junction. The particles transporting this supercurrent are the Cooper pairs (or, as we shall see in section 4.2, Andreev pairs in our case). Its signature on the IV curves is a vertical line at $V_{dc} = 0$ up to I_c , what we call the Josephson branch.

The phase ϕ is a degree of freedom, that we constraint externally with the d-c bias current I_b or the bias voltage V_b . For $I_b < I_c$ and at $T = 0$, the transport is only supported by a supercurrent and $\langle V \rangle = V_{dc} = 0$. Hence $\langle d\phi/dt \rangle = 0$ (equation 3.21), which implies that $\langle \phi \rangle = cte$ (but not necessarily $\phi(t) = cte$).

In the frame of the BCS theory, Ambegaokar and Baratoff [18] calculated the maximal critical current for a SIS tunnel junction as being:

$$I_c(T) = \frac{\pi \hbar k_B T \Delta_1(T) \Delta_2(T)}{e R_N} \sum_{-\infty}^{+\infty} \frac{1}{\sqrt{(\omega_n^2 + \Delta_1^2(T))(\omega_n^2 + \Delta_2^2(T))}} \quad (3.22)$$

where $\omega_n = (2n + 1)\pi k_B T$ are the Matsubara frequencies and $\Delta_1(T)$ ($\Delta_2(T)$) is the left (right) superconducting gap. For a symmetrical SIS junction $\Delta_1 = \Delta_2 = \Delta$ and the expression becomes:

$$I_c(T) = \frac{\pi \Delta(T)}{2 e R_N} \tanh\left(\frac{\Delta(T)}{2 k_B T}\right) \quad (3.23)$$

When $I_b > I_c$, the flux of the superfluid is such that all the Cooper pairs cannot cross the barrier. Some are broken at the superconducting-insulating frontier and electrons cross as quasiparticles: the electronic transport involves two fluids. Consequently, a d-c voltage rises at the junction

terminals: $V_{dc} \neq 0$ and the superconducting phase difference ϕ between the two reservoirs evolves according to 3.21. Then, the superconducting current oscillates in time such as:

$$J(t) = J_c \sin\left(\phi_{ini} + \frac{2e}{\hbar} V_{dc} t\right) \quad (3.24)$$

Thus, the junction behaves as a voltage-controlled oscillator (VCO): its oscillation frequency is controlled by the d-c voltage bias. It can easily be at very high electronic frequencies, since the ratio $\frac{2e}{\hbar}$ equals to 483.6 GHz/mV. This oscillation is at the core of this thesis. As pointed out by Jain and Likharev [100], a fixed current bias (at $V \neq 0$) implies also that the quasiparticle current counter-oscillates in the junction with the same frequency. Figure 3.2 (a) depicts the typical IV curve of a Josephson tunnel junction. When the current increases, from 0 to I_c we are on the Josephson branch. Then the system brutally shifts to the corresponding voltage on the quasiparticle branch as the right empty band immediately fills (figure 3.1 (a)). When lowering the current from $I > I_c$, the system follows the quasiparticle branch down to $I = 0$, as the filled valence band on the right unloads on the left conduction band. Thus, the IV curve of a SIS tunnel junction is hysteretic.

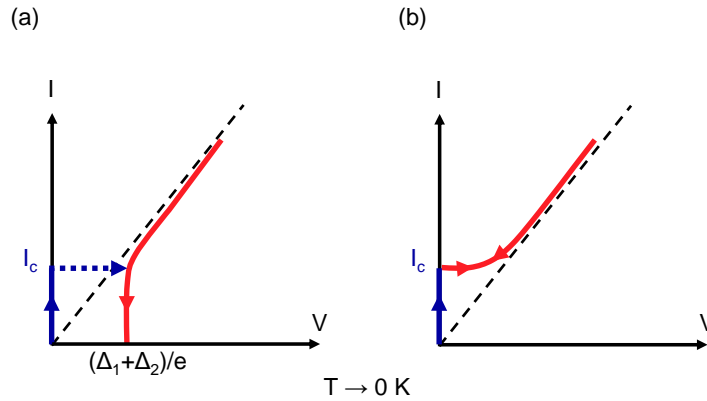


Figure 3.2: Schematic current-voltage curves of a tunnel (a) and a weak-link (b) Josephson junction. The quasiparticle branch is in red and the Josephson branch is in blue, signature of a supercurrent that flows at $V = 0$ up to the critical current I_c . In a tunnel junction there is no quasiparticle tunneling below the gap while in a weak-link junction a current exists even at low voltages.

In weak-link junctions, the Josephson effect is also present, i.e. a coupling interaction exists between the two superconductors. However the quasiparticle transport mechanism differs and the semi-conductor approach is not enough anymore. First because often, there are accessible electronic states in the barrier, and second because in our case we deal with a material with a d-wave superconducting gap, hence with nodes ($\Delta = 0$ in certain crystallographic directions, see 2.3.1). Thus, there is always a quasiparticle current, even at low voltages. Consequently, the typical IV curve of a weak-link Josephson junction resembles figure 3.2 (b). A complete description will be presented in chapter 4.

In the next section we will present the typical behavior of irradiated Josephson junctions observed in transport measurements, after what we will present the equivalent circuit model that explains it. In particular it allows to understand the shape of IV curves such as the one in figure 3.2 (b).

3.2 Transport measurements in ion irradiated junctions

The first people who fabricated irradiated $\text{YBa}_2\text{Cu}_3\text{O}_7$ Josephson junctions were Katz et al., in 1998 [104]. Since then, several groups successfully fabricated and characterized these devices, and

we present here typical results of transport measurements. Focusing on what should be observed experimentally, we do not intend to explain in details all the underlying physics, which shall be done in the next chapters.

3.2.1 RT curves

Figure 3.3 (a) shows typical RT curves of irradiated $\text{YBa}_2\text{Cu}_3\text{O}_7$ junctions, for different lengths weak-links. The transition at $T_c = 90$ K corresponds to the critical temperature of the electrodes, after what follows a plateau, which is the RT curve of the weak-link.

A second transition occurs when the resistance drops to zero, depending on the length of the weak-link. We call it T_j . At first, it may seem surprising, because in this experiment, all weak-links underwent the same irradiation dose and therefore the same damage. Thus, T_j should be independent of the weak-link's length, whereas it is not experimentally the case. Katz et al. attributes the observed discrepancy to proximity effects, which will be indeed explained in chapter 4. This dependence shows that T_j is not the critical temperature of the weak-link. As we will see, the latter transits in fact at a lower temperature, called T'_c , which we do not see here on the figures.

The irradiation dose also influences the position of T_j , as shown by Bergeal et al., figure 3.3 (b): RT curves of $5 \mu\text{m}$ wide channels and length 20 nm , irradiated from right to left with oxygen doses spanning from 1.5×10^{13} to $6 \times 10^{13} \text{ ions.cm}^{-2}$. Thus, the higher the dose, the lower the T_j .

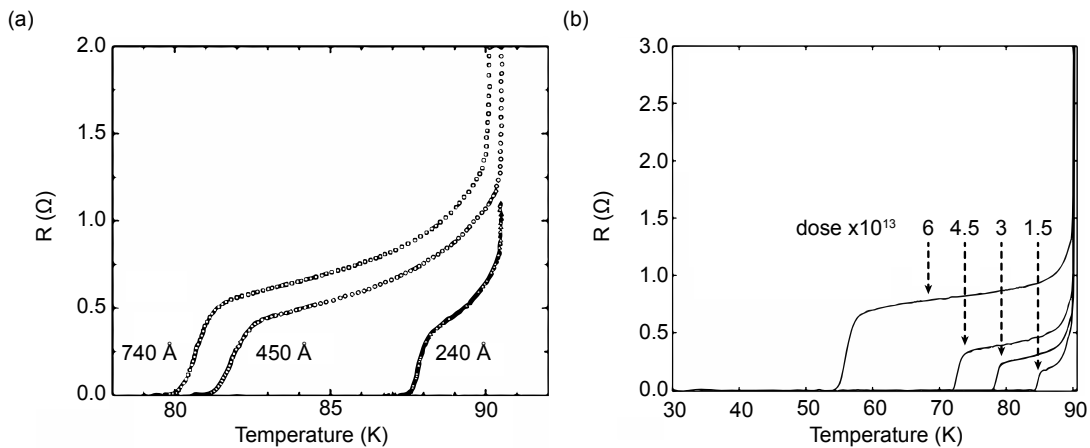


Figure 3.3: RT curves of ion irradiated $\text{YBa}_2\text{Cu}_3\text{O}_7$ Josephson junctions. (a) Junctions with various lengths, irradiated at the same dose (and with Ne^+ at 200 keV) [105]. (b) Junctions of the same length (20 nm), irradiated from right to left at doses 1.5×10^{13} , 3×10^{13} , 4.5×10^{13} , and $6 \times 10^{13} \text{ ions.cm}^{-2}$ (oxygen ions, at 100 keV) [36].

3.2.2 IV curves

When below T_j , typical IV curves of the junction are represented in figure 3.4, at different temperatures. They clearly exhibit the characteristic shape of a weak-link IV , figure 3.2 (b). In figure 3.4 (b), notice the downward curvature close to I_c , typical of weak-links, and well explained by the circuit model (see section 3.3).

As the temperature decreases, one gets closer to T'_c (at which the weak-link itself becomes superconducting), and therefore the system progressively behaves like a homogeneous superconductor. In chapter 5, we will call it the *flux-flow* regime. It is evidenced by an upward curvature at I_c [33], visible in figure 3.2 (a), along with a large excess supercurrent as we shall see in the next chapters.

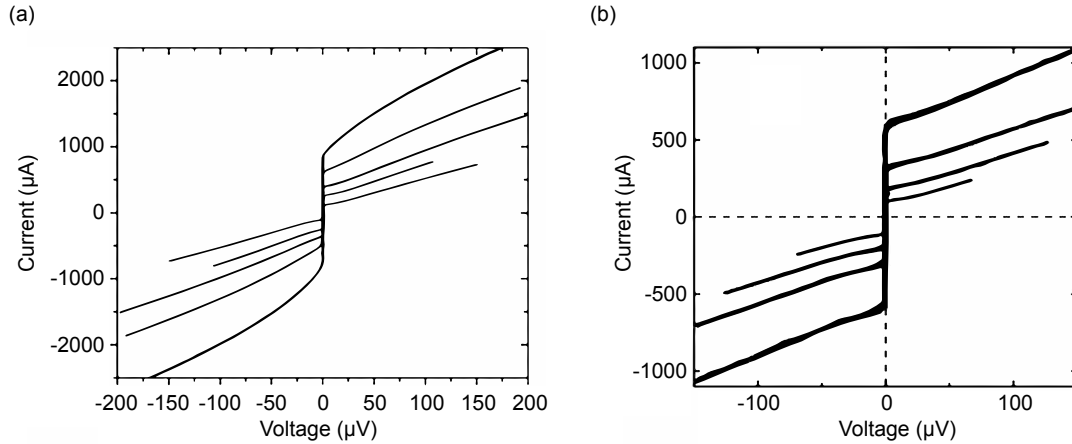


Figure 3.4: Typical IV curves of $\text{YBa}_2\text{Cu}_3\text{O}_7$ irradiated Josephson junctions, for various temperatures. (a) From top to bottom: $T = 75.6, 76.9, 77.8,$ and 79.5 K [61]. (b) From top to bottom $T = 40, 43.9, 46.3,$ and 48.5 K [36]. The IV curves in (b) correspond to the same junction whose RT curve is in figure 3.3 (b), with the 6×10^{13} ions. cm^{-2} dose.

3.2.3 Critical current

Figure 3.5 (a) shows the dependence of the critical current I_c with temperature. It is consistent with $I_c \sim (1 - T/T_c)^2$ [105], and can be explained with a proximity effects model, in the diffusive regime, developed by De Gennes and Werthamer [66, 65, 194] and detailed in section 4.1.1.

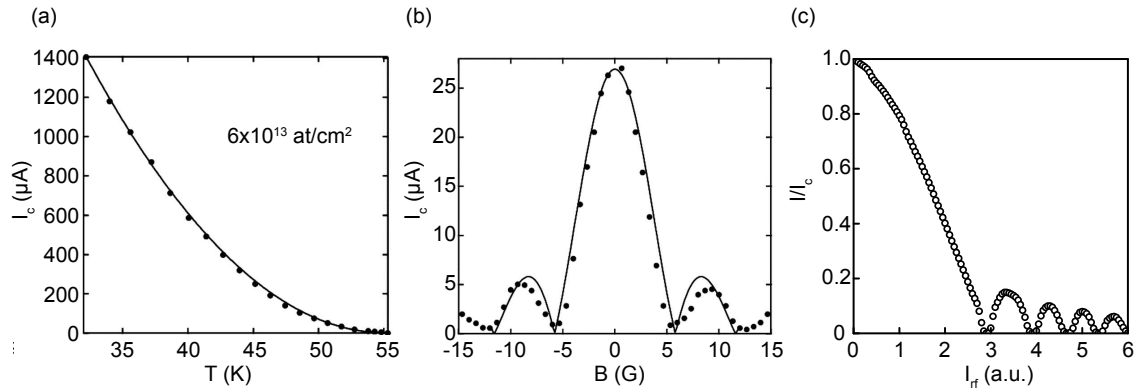


Figure 3.5: (a) Variation of the critical current with temperature, following a quadratic law, and (b) Modulation of the critical current with an external magnetic field, following a sinc function. Adapted from [36]. (c) Modulation of the critical current with an external r-f field, following a Bessel function. Adapted from [136].

Figure 3.5 (b) shows the critical current modulation with a magnetic field, following a *sinc* function, and with an r-f field, figure 3.5 (c), following a Bessel function. These modulations are the true evidence of Josephson effect in a weak-link, because both Josephson equations must be valid, in order to explain them. We will focus on the modulation with an r-f field in section 5.2.3.

3.3 RCSJ - RSJ model

In 1968 McCumber [141] and Stewart [177] independently proposed an equivalent circuit model to explain the shape of the weak-link IV curves, like the ones that we have. It is called the RCSJ model and fundamentally, it stems from the fact that we can separately account for the supercurrent

and the QP current. The circuit model is a powerful tool since it provides analytical solutions for simplified situations, and for general situations numerical simulations can be performed and give quantitative results.

3.3.1 Ideal weak-link Josephson junction

Given a driving current source with a high impedance (which is the case in many practical situations and particularly in ours) the circuit modeling an *ideal* junction contains a non dissipative element that accounts for the Josephson effect, resistively and capacitively shunted, as shown on figure 3.6. Hence it is called the resistively and capacitively shunted junction (RCSJ) model. The parallel resistive branch represents the conductance of the QP. The capacitive branch models the charge imbalance between the two superconducting bulks, originating either from QP or Cooper pairs. In our ion irradiated junctions we will see that we can neglect the capacitance, and then the model reduces to a resistively shunted junction (RSJ). A rigorous approach of the RSJ model is given in the seminal work by Vystavkin, Likharev and Semenov [191].

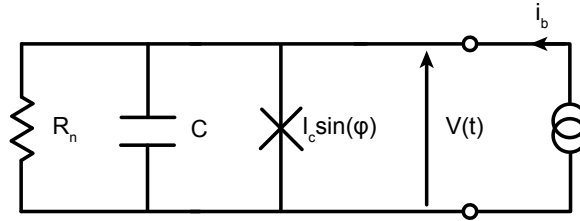


Figure 3.6: Equivalent circuit of an ideal weak-link Josephson junction: resistively and capacitively shunted junction (RCSJ) model.

The current circuit equation is then given by:

$$I = I_c \sin \phi + \frac{V}{R_n} + C \frac{dV}{dt} \quad (3.25)$$

where V is the voltage developed across the junction, related to the phase difference ϕ by the a-c Josephson equation 3.21. Thus it rewrites as:

$$I = I_c \sin \phi + \frac{\hbar}{2e} \frac{1}{R_n} \frac{d\phi}{dt} + C \frac{\hbar}{2e} \frac{d^2 \phi}{dt^2} \quad (3.26)$$

In order to write it with a general form, it is common to introduce dimensionless variables for the current, voltage and time. Here, two normalizations for the time exist in the literature: the "Johnson" normalization, usually used in the RCSJ model and the "McCumber" normalization, commonly used in the RSJ model. For clarity and generality, we explicit in table 3.1 the correspondence between the normalized and the unnormalized variables for the two methods. Besides, both introduce useful parameters when discussing the limit cases of equation 3.26. We gathered them in table table 3.2.

Let us also introduce three other parameters frequently seen when talking about Josephson junctions.

- $E_J = I_c \phi_0 = \frac{I_c \hbar}{2e}$ the Josephson energy, which is the maximum energy stored by the Josephson supercurrent: $E = \int V(t) I_J(t) dt = -E_J \cos \phi$
- $E_C = \frac{e^2}{2C}$ the charging energy, which is the stored energy in the capacitance: $E_C = \int U I_C dt = C \int U \frac{dU}{dt} dt = \frac{C}{2} U^2 = \frac{e^2}{2C}$

- $L_J = \frac{\hbar}{2eI_c \cos\phi}$ the Josephson inductance, is such that $V(t) = L_J(t) \frac{dI_J(t)}{dt}$

Physics quantity	variable	normalization constant	normalized variable
Current	I	I_c	$i = \frac{I}{I_c}$
Voltage	V	$I_c R_n$	$v = \frac{V}{I_c R_n}$
Time	t	$\omega_p = \sqrt{\frac{2eI_c}{\hbar C}}$ (Johnson)	$\tau = \omega_p t$ (Johnson)
		$\omega_c = \frac{2eI_c R_n}{\hbar}$ (McCumber)	$\tau = \omega_c t$ (McCumber)

Table 3.1: Normalization constants in the RCSJ - RSJ model.

Johnson normalization	McCumber normalization
plasma frequency $f_p = \sqrt{\frac{2eI_c}{\hbar C}}$	characteristic frequency $f_c = \frac{2eI_c R_n}{\hbar}$
Quality factor $Q = R_n C \omega_p = \frac{1}{\beta_J}$	McCumber parameter $\beta_c = \frac{2eI_c R_n^2 C}{\hbar}$

Table 3.2: Parameters of the Johnson and McCumber normalization.

Note that $\beta_c = \frac{1}{\beta_J^2} = Q^2$. Starting at the characteristic frequency f_c , the current flows more in the resistive branch, at the expense of the non linear mixing branch.

Time normalization gives, $d\tau = \omega_{p/c} dt$ and $d\tau^2 = \omega_{p/c}^2 dt^2$. Therefore equations 3.26 and 3.21 rewrite in the forms presented in table 3.3.

Johnson normalization	McCumber normalization
$\begin{cases} \ddot{\phi} + \beta_J \dot{\phi} + \sin\phi = i \\ \dot{\phi} = Qv \end{cases} \quad (3.27)$	$\begin{cases} \beta_c \ddot{\phi} + \dot{\phi} + \sin\phi = i \\ \dot{\phi} = v \end{cases} \quad (3.28)$

Table 3.3: RCSJ equations in the Johnson and McCumber normalization. Here the point symbol denotes normalized derivatives.

System 3.27 has a different time normalization than 3.28, hence one cannot change from one system to the other only by using $\beta_c = 1/\beta_J^2$. In this thesis we will use system 3.28. It cannot be solved in closed form for the general case where $C \neq 0$. Furthermore, an external periodic drive can lead to very complex behaviors, such as bifurcation or deterministic chaos. However in the heavily-damped regime where $\beta_c \ll 1$ there exists analytical solutions.

3.3.2 Dynamics of the junction

An analog system driven by 3.28, is the one a particle moving on a washboard potential $U(\phi)$. In fact, considering a particle with a mass β_c , a velocity v and a position ϕ , 3.28 can be interpreted as a Newton's second law of motion. The potential $U(\phi)$ is found by integration as¹:

$$U(\phi) = E_J(1 - \phi i - \cos\phi) \quad (3.29)$$

Thus, the overall slope of the washboard increases with bias current. Figure 3.7 shows the shape of the potential $U(\phi)$ for different values of bias current i . A mechanical analog is a rigid pendulum of mass β_c , whose position is determined by the angle ϕ with the vertical. The capacitance C is then analog to its moment of inertia, the conductance $1/R$ to a viscous damping coefficient, I to an externally applied torque and I_c to the maximum torque due to gravity.

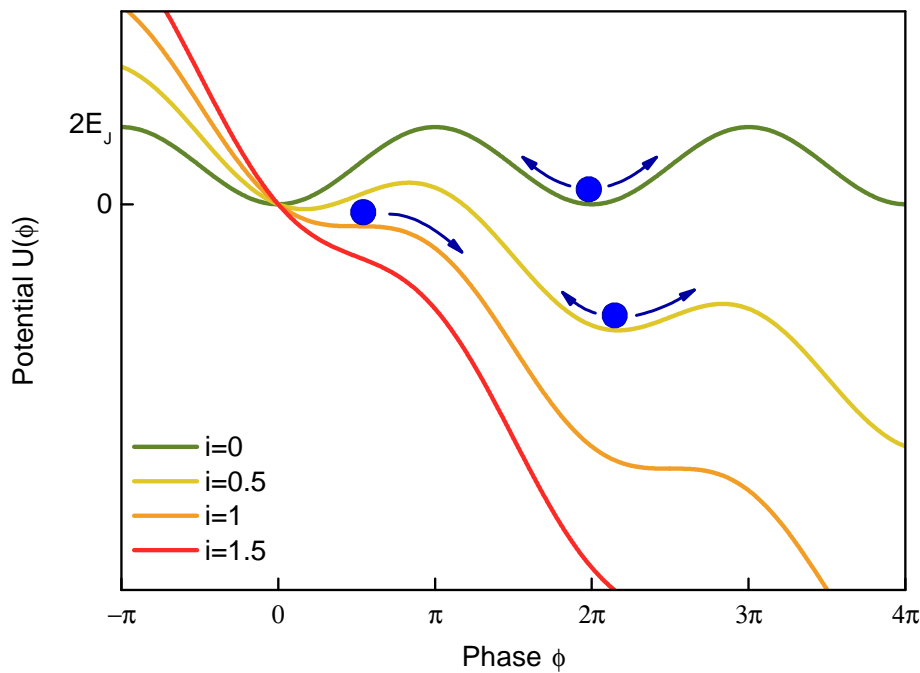


Figure 3.7: Analog system to the RCSJ model: a particle of mass β_c moves along a washboard potential. The current i tilts the overall slope, and motions the particle at a velocity $\dot{\phi} = v$, where v is the voltage across the junction. When $i > 1$, the particle moves freely on the washboard and $\langle v \rangle \equiv v_{dc} \neq 0$. Adapted from [163].

3.3.2.1 Under-damped regime

When $|i| < 1$, $U(\phi)$ has local minimums at $\phi_m = 0[2\pi]$, hence a particle initially at rest and close to one of these positions does not have enough energy to cross the barrier and move along the washboard. It oscillates (at the plasma frequency ω_p in the Johnson normalization) around ϕ_m , and its mean position is constant $\langle \phi \rangle = cte$. In the mechanical analogy, the pendulum oscillates around the stable position $\phi = 0$.

¹The integration is actually not trivial, because one needs to extract the Gibbs energy of the system, to be distinguished from its free energy. A rigorous calculation is found in [129]

When $\beta_c > 1$, or similarly in the Johnson normalization when $Q > 1$, the junction is under-damped. If the particle's initial kinetic energy is high enough, it will roll along the washboard potential, hence $\langle v \rangle \equiv v_{dc} \neq 0$. If not, as when initially at rest, it will stay trapped in a potential well, hence $v_{dc} = 0$. Thus, the IV characteristics of under-damped JJ depend on the particle's initial energy: they are hysteretic. Figure 3.8 shows simulations of IV curves, for different values of β_c . It increases with capacitance, and the hysteresis is more pronounced. This situation where $i < 1$ and $\beta_c > 1$ contains a very rich physics, in particular the particle can hop from one local minimum to another by thermal activation or macroscopic quantum tunneling [97].

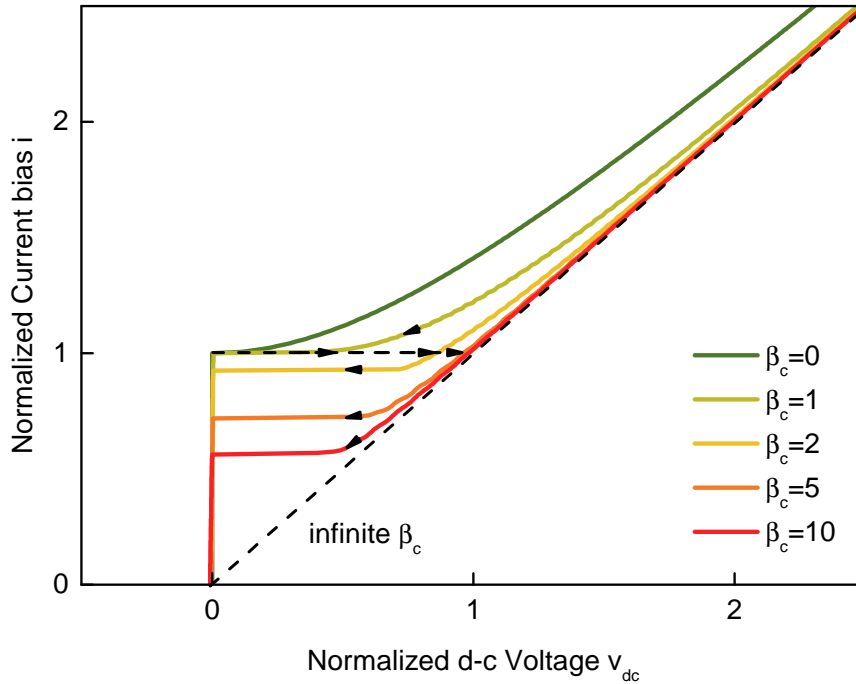


Figure 3.8: Simulations of IV curves in the RCSJ model, for various values of the McCumber parameter. For $\beta_c = 0$ the curve is not hysteretic: the path is the same when i increases or decreases. For $\beta_c > 1$, the curves are hysteretic and when i increases, a switching occurs from $i = 1$ (at the critical current) to a position indicated by dashed arrows. When i decreases the path is indicated by arrows on the curves. Adapted from [163].

3.3.2.2 Over-damped regime

When $\beta_c < 1$ ($Q < 1$) the junction is over-damped. Our junctions are heavily damped $\beta_c \ll 1$. It is expected from irradiated high- T_c Josephson junctions, as the capacitance C is low due to the presence of delocalized (metallic) states in the barrier. It will be observed experimentally by having non hysteretic IV curves. Neglecting the capacitive branch, the JJ is described by the RSJ model. In the mechanical analogy, the pendulum undergoes such important viscous friction, that its oscillation tends to a mean position given by the solution of the system:

$$\begin{cases} \dot{\phi} + \sin\phi = i \\ v = \dot{\phi} \end{cases} \quad (3.30)$$

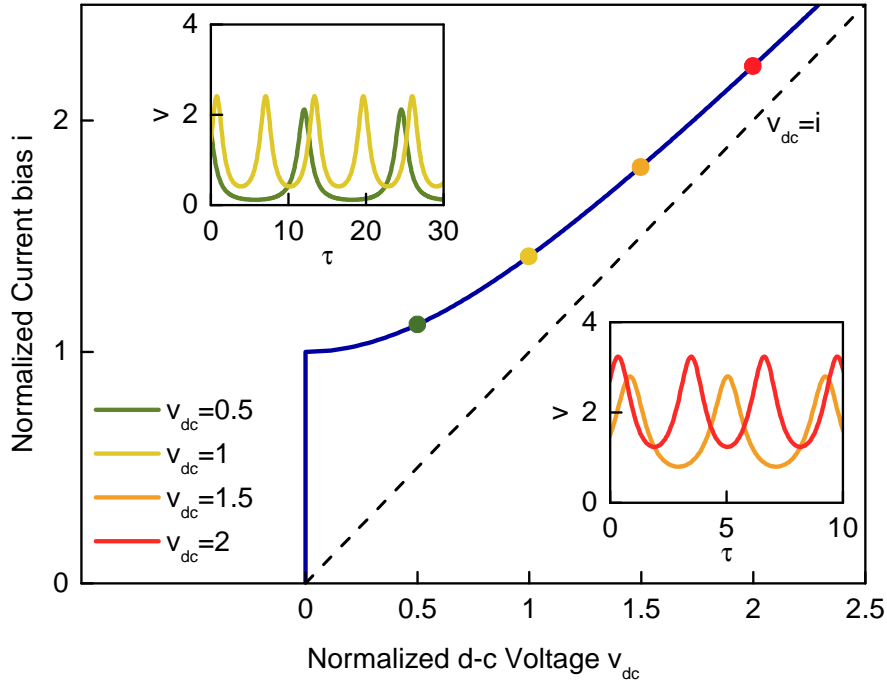


Figure 3.9: Simulation of a IV curve with no capacitance (pure RSJ model), and corresponding voltage temporal oscillations in normalized units, at different values of d-c voltage $\langle v \rangle = v_{dc}$. The oscillation period is given by 3.35. As the current bias increases, the oscillations have a sinus shape, and the average of the a-c Josephson effect is null, only leaving the d-c component: $v_{dc} = i$.

When $|i| < 1$, the solution is:

$$\phi(\tau) \rightarrow \arcsin(i) = cte, \text{ as } v \rightarrow 0 \quad (3.31)$$

and when the current bias exceeds the supercurrent ($i > 1$) the phase evolves as [191]:

$$\phi(\tau) = 2\arctan\left(\frac{v_{dc}}{i+1}\tan\left(\frac{v_{dc}\tau}{2}\right)\right) + \frac{\pi}{2} \quad (3.32)$$

and the voltage $v(\tau)$ is given by its derivative:

$$v(\tau) = \frac{v_{dc}}{i+1} \frac{v_{dc}}{\cos^2\left(\frac{v_{dc}\tau}{2}\right) + \left(\frac{v_{dc}}{i+1}\right)^2 \sin^2\left(\frac{v_{dc}\tau}{2}\right)} \quad (3.33)$$

The d-c voltage derives by taking the (normalized) time average of $\dot{\phi} = v$, thus given by [177]:

$$v_{dc} = \sqrt{i^2 - 1} \quad (3.34)$$

Hence at large current biases, $i \gg 1$ and the IV curve joins the ohmic branch $v_{dc} = i$ ($V_{dc} = R_n I_b$ in dimensioned units). Now, at a fixed current bias, the voltage v oscillates in time and according to 3.32 its period is:

$$T = \frac{2\pi}{v_{dc}} = \frac{2\pi}{\sqrt{i^2 - 1}} \quad (3.35)$$

Thus the voltage oscillates only at $i > 1$. Figure 3.9 shows the simulation of an IV curve, along with voltage oscillations. We can see that the mean value v_{dc} of $v(\tau)$ increases with bias current.

For $i \gg 1$, the period diminishes and the oscillations get closer to a sinusoidal shape, added to a d-c background that tends to $I_c R_n$, and thus $v_{dc} \rightarrow i$. In the mechanical analogy, it corresponds to a situation where the driving torque is so high that the pendulum turns entirely over 2π , with a negligible influence of the gravity torque. For $i \gtrsim 1$, $v(\tau)$ has many harmonics, that create a set of periodic pulses. The latter are being exploited in the rapid single flux quantum logic (RSFQ) [132]. In this situation, the pendulum is given just enough energy to make an entire revolution.

3.3.3 Model of a real Josephson junction

So far, the model describes an *ideal* Josephson junction. But due to the fluctuation-dissipation theorem [50], the resistance inevitably generates voltage and current fluctuations that must be taken into account when describing any *real* Josephson junction.

3.3.3.1 Fluctuations

In the Rayleigh-Jeans limit ($h\nu \ll k_B T$) the spectral density of the voltage fluctuations is given by the Johnson-Nyquist theorem [150]:

$$S_V(\nu) = 4k_B T R \quad (3.36)$$

Equivalently, the current fluctuations are given by:

$$S_I(\nu) = \frac{4k_B T}{R} \quad (3.37)$$

When $h\nu \sim k_B T$, i.e. at low temperature or similarly at high frequencies, the energy per mode is no longer proportional to $k_B T$, and one needs a general expression for fluctuations, given by [50]:

$$S_V(\nu) = 2h\nu R \coth\left(\frac{h\nu}{2k_B T}\right) \quad (3.38)$$

Note that in the Rayleigh-Jeans limit, equation 3.38 reduces to 3.36. In the quantum regime ($h\nu \gg k_B T$), 3.38 gives $S_V(\nu) = 2h\nu R$.

In our range of operating temperatures, we will always be in the Rayleigh-Jeans limit: as shown on table 3.4, at 50 K the cross-over from Johnson limited to quantum limited noise occurs at 1 THz, well above the maximum operating frequency of our mixer so far (of about 400 GHz).

T (K)	$k_B T$	$\nu = k_B T / h$
1	86 μeV	20 GHz
4.2	0.36 meV	87 GHz
50	4.3 meV	1 THz

Table 3.4: Correspondance between temperature, energy and frequency.

The common way to account for fluctuations is to add a stochastic current source $\delta i_n(\tau)$ ($\delta I_n(t)$ in dimensioned units), thus forming a Langevin equation such that the system writes as:

$$\begin{cases} \dot{\phi} + \sin\phi = i + \delta i_n(\tau) \\ v = \dot{\phi} \end{cases} \quad (3.39)$$

It is possible to solve it analytically, but only for the unpumped regime. Instead, numerical resolution allows to find the IV curves in all the situations that are of interest for us, i.e. with any LO and any signal. Averaging gives the d-c voltage v_{dc} , Fourier transforming gives the oscillation or

noise spectra and furthermore, this method will be proven of crucial advantage when computing the conversion efficiency of the mixer (see chapter 7).

We introduce fluctuations as an additive white and gaussian noise (AWGN). The current source is a random variable $\delta I_n(t)$, characterized by its power spectral density (PSD) given by 3.37 (a constant, i.e. a white noise). According to the Wiener-Khinchin theorem, the PSD is equal to the Fourier transform of its autocorrelation function. Hence, in the temporal domain, the latter is a Dirac function: $\langle I(t_0)I(t_0 - t) \rangle = \frac{2k_B T}{R_n} \delta(t)$. In addition, $\delta I_n(t)$ is chosen to have a temporal Gaussian probability density, and thus the autocorrelation function gives the variance of the Gaussian as:

$$\sigma_I^2 = \frac{2k_B T}{R_n \Delta t} \quad (3.40)$$

where Δt is the solving pace time (dimensioned). Once again one usually prefers to use normalized quantities, hence we introduce the normalized temperature Γ :

$$\Gamma = \frac{2e k_B T}{\hbar I_c} \quad (3.41)$$

which is actually the ratio between thermal and Josephson energy. Since $\sigma_i^2 = \sigma_I^2 / I_c^2$, the normalized variance writes itself as:

$$\sigma_i^2 = 2 \frac{\Gamma}{\delta \tau} \quad (3.42)$$

where $\delta \tau$ is the normalized pace time.

3.3.3.2 Numerical resolution

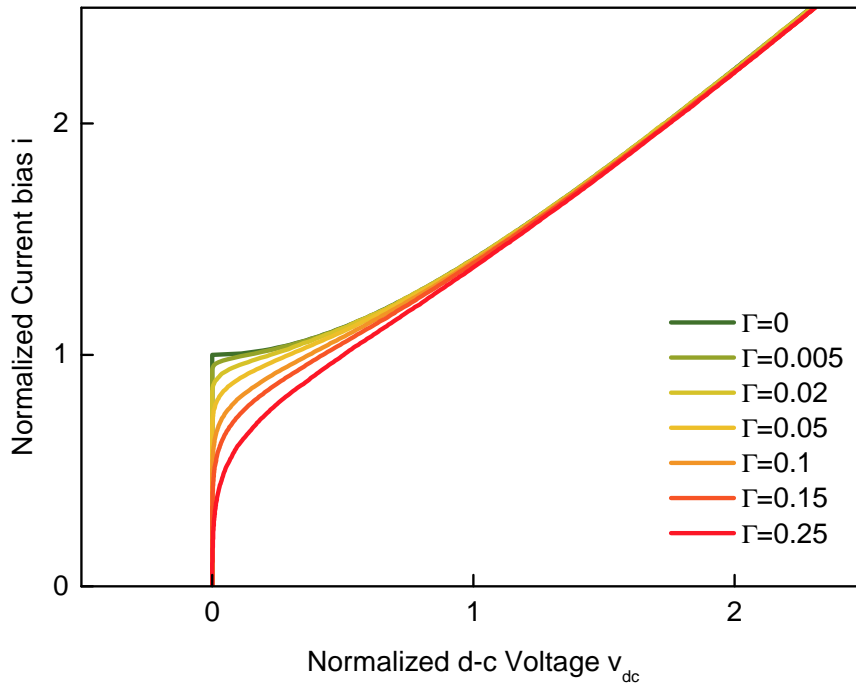


Figure 3.10: IV curves in the RSJ model (zero capacitance), in the presence of noise, for several values of normalized temperature.

In practice, the simulation of an IV curve consists in solving the system equations 3.39 by numerical integration, and we simply used Euler's method. Appendix C details the numerical computation. Figure 3.10 shows simulations of the IV curve in the presence of noise. The transition at $i = 1$ is rounded as the noise increases.

3.4 Conclusion on the electronic transport

In this chapter we have seen the nature of the Josephson effect, and we presented the two different systems in which it appears: tunnel and weak-link junctions. Our irradiated Josephson junctions belong to the second category. From the coupling between two superconducting condensates, we derived the d-c and a-c Josephson equations 3.20 and 3.21, that govern the flow of Josephson current through the junction.

We showed the experimental characterization of the Josephson effect in our junctions. In the RT curves, a plateau below the transition of the two condensates appears. It follows the RT curve of the weak-link down to T_j , at which the resistance drops to zero. T_j lowers as the irradiation dose increases. In addition, it depends on the length of the weak-link. Consequently, it does not correspond to the critical temperature of the weak-link. These dependences may be elucidated in the next chapter, when taking into account proximity effects.

The IV curves of irradiated junctions are typical of weak-links when close to T_j , with a downward curvature. As the temperature decreases, the weak-link eventually becomes superconducting and the curves take an upward curvature.

When decreasing the temperature, the critical current grows quadratically. Once again, this behavior is explained in the next chapter, when taking into account proximity effects. Also, the critical current can be modulated when an external magnetic or r-f field is applied. They are the real proof of a Josephson effect, because both d-c and a-c Josephson equations need to be valid to explain these effects. We will detail in chapter 3 the modulation of the r-f field.

Finally, we presented the RCSJ and RSJ models, equivalent circuits for weak-link Josephson junctions. They originate from the fact that one can separate the contributions of the Josephson supercurrent and the quasiparticle current, and thus express them as separate circuit branches. In our junctions, we can neglect the capacitance because we don't have a clear interface between normal and superconducting parts. In fact, we will see in chapter 3 that the RSJ model is able to fit the experimental IV curves. The noise in a real junction is accounted by an additive white Gaussian current noise source, inevitable in a circuit containing a dissipative element. It rounds up the transition at the critical current.

Chapter 4

Proximity effects in irradiated Josephson junctions

Contents

4.1 Proximity effects in metals and damaged superconductors	74
4.1.1 SNS and SS'S	74
4.1.2 Critical current	75
4.2 Theory of proximity effects	75
4.2.1 Gorkov - Nambu theory	76
4.2.2 Perturbative expansion: Eilenberger equation	78
4.2.3 Usadel equations	78
4.2.4 θ and χ parametrization	79
4.3 Adaptation for irradiated Josephson junctions	80
4.3.1 Usadel equations in irradiated $\text{YBa}_2\text{Cu}_3\text{O}_7$	80
4.3.2 Simulations results	81
4.4 Conclusion on the quasi-classical approach of proximity effects	84

In the precedent chapter, we put aside the origin of experimental behaviors observed in irradiated Josephson junctions. The present chapter will address it, explaining of the coupling mechanism between the two superconducting sides.

We have seen that the defect distribution in our irradiated $\text{YBa}_2\text{Cu}_3\text{O}_7$ junctions is about tens of nm long. Thus it rules out any Cooper pair tunneling, whose probability decreases exponentially as the barrier extends. However a Josephson effect still exists, evidenced experimentally, and therefore the coupling between the two reservoirs comes from something else.

In fact it stems from proximity effect, i.e the extension of the superconducting properties into the barrier, when it is a metal or in our case, a superconductor in its normal phase. Thus, it allows coherent states to go from one side to the other and along with it, the appearance of a Josephson oscillation.

Since the notion of proximity effect requires a fairly heavy theoretical development, we fraction the chapter as follows: we give a short answer to the coupling mechanism in section 4.1. Then in section 4.2 we give the long answer, which we adapt to our specific system in section 4.3. It allows to perform numerical simulations, and recover the experimental shape of the RT and $I_c T$ curves. In addition, simulations are helpful to adjust fabrication parameters - length of the weak-link and irradiation dose.

4.1 Proximity effects in metals and damaged superconductors

When the barrier is a metal, the junction is called SNS. When it is a damaged superconductor whose critical temperature is lowered, it is called SS'S. At a temperature where S' is normal, they behave closely.

In both cases, there exists accessible electronic states inside the barrier which enable proximity effect. More precisely, at the S-N or S-S' interface, a Cooper pair $|k \uparrow, -k \downarrow\rangle$ can transform into an electron $| -k \downarrow\rangle$ and a hole $|k \uparrow\rangle$, thus forming an *Andreev* pair. In the N or S' part, the latter progressively dephase within a characteristic length ξ_N called the *normal* coherence length. In other words, ξ_N is the characteristic length of the exponentially decreasing pair condensation amplitude $F_N(x)$. The latter represents the number of Andreev pairs at the position x (referenced to the interface).

4.1.1 SNS and SS'S

When electrons undergo many scattering events inside the barrier, their mean free path l_{tr} can get smaller than ξ_N . In other words, diffusion effects arise before dephasing to break the coherence of the Andreev pair. It is called the *dirty limit* (as opposed to the clean limit, with ballistic electron trajectories). In a metal at a temperature T , electron and hole have an energy $k_B T$ around the Fermi energy, and thus we can express the normal coherence length with a diffusion coefficient D such as:

$$\xi_N = \sqrt{\frac{\hbar D}{2\pi k_B T}} \quad (4.1)$$

The pair condensation amplitude $F_N(x)$ then writes as:

$$F_N(x) = F_N(0^-) e^{-\frac{|x|}{\xi_N}} \quad (4.2)$$

where $F_N(0^-)$ is taken at the S-N interface.

The ion damaged $\text{YBa}_2\text{Cu}_3\text{O}_7$ is a disordered system, and therefore the dirty limit is valid for this S' region. De Gennes, Guyon and Werthamer [66, 65, 194] studied the case of SNS junctions, and extended the results to SS'S junctions. In this frame they found that, when $T > T'_c$, far from the interface, ξ_N is given by:

$$\xi_N(T) = \sqrt{\frac{\hbar D}{2\pi k_B T}} \sqrt{1 + \frac{2}{\ln(T/T'_c)}} \quad (4.3)$$

The difference between SNS and SS'S is clear: with the latter, when we are at $T = 2T'_c$ we approximately double the normal coherence length that we have in the corresponding SNS system, and it grows exponentially as we get closer to T'_c . Another difference, which does not appear in these equations, is that in our SS'S system, there is no discontinuity in the pair condensation amplitude at the S-S' interfaces.

Thus, $F_{N1}(x)$ and $F_{N2}(x)$ from both sides extend into the barrier, and strongly overlap, allowing Andreev pairs to go across the barrier without being destroyed. Figure 4.1 presents schematically the situation of the pair condensation amplitude, for SNS and SS'S junctions.

This explains why we still have a Josephson coupling, even with long S' barriers. In this frame also, we can explain the origin of T'_c and T_j : T'_c is simply the critical temperature of the S' part, whereas T_j is the temperature below which thermal energy $k_B T$ is weaker than the overlap of the pair condensation amplitudes, so that thermal agitation does not destroy Andreev pairs as they go across the S' region.

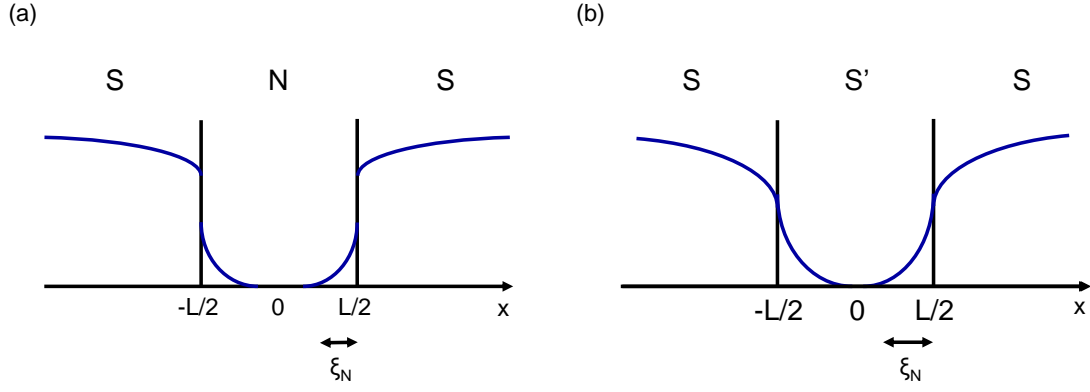


Figure 4.1: Schematic of the pair condensation amplitude in a SNS (a) and in a SS'S (b) junction. The different materials in contact at the interfaces of the SNS junction induces a discontinuity, and the amplitude decreases exponentially over a shorter length ξ_N than in the SS'S case, where there is no discontinuity.

A remark concerning the S-S' interface: as shown on the figure 2.5 of chapter 2, the T_c' of the S' region varies with position x , i.e. the S-S' interfaces of our junctions move with temperature, as mentioned in a few articles [54, 105]. Thus, the schematic vision of figure 4.1 (b) is naive, in the sense that there is no sharp transition between S and S'. Our model described below (see 4.3.1) takes this moving interface into account through a diffusion coefficient D that depends on temperature (and x). As the temperature increases, the diffusion decreases and the S' part extends.

4.1.2 Critical current

The De Gennes Werthamer theory also gives the expression of the critical current. Close to T_c , in SNS systems it is given by:

$$I_c(T) \sim e^{-L/\xi_N} \left(1 - \frac{T}{T_c}\right)^2 \quad (4.4)$$

where L is the length of the normal metal part. This quadratic dependence differs from the linear one, found in SIS junctions.

With a SS'S system, the above expression is modified as [19, 105, 36]:

$$I_c(T) = I_0 \left(1 - \frac{T}{T_j}\right)^2 \frac{L/\xi_N}{\sinh(L/\xi_N)} \quad (4.5)$$

$$I_0 = \frac{\pi \Delta_0^2}{4eR_n k_B T_c} \quad (4.6)$$

where Δ_0 is the BCS gap. In $\text{YBa}_2\text{Cu}_3\text{O}_7$ it is anisotropic, with a maximum at about 30 meV, but one can take an average value: $\Delta_0 \sim 20$ meV, which leads to $I_0 = 18.5$ mV/ R_n for $T_c = 89$ K [19]. ξ_N is given by equation 4.3.

In any case, we see that at a fixed temperature, $I_c(T) \sim (1 - T/T_j)^2$, i.e. the critical current grows quadratically as the temperature decreases. This behavior is only valid near T_j .

4.2 Theory of proximity effects

We summarize here the theory that describes the non homogeneous superconductivity. Some vocabulary first: coherent extension of the phase into the normal part is the *direct* proximity effect. Conversely, diminution of the Cooper pair density in the superconductor near the interface is the *inverse* proximity effect.

In order to study the physics of superconductivity at S-N or S-S' interfaces, one cannot use the BCS theory alone: indeed it assumes spatial invariance of the order parameter Δ . Thus, a more general theory for inhomogeneous superconductors developed by Gorkov [84, 17], and formalized by Nambu [147] is necessary.

The Gorkov equations give a general frame for inhomogeneous superconductors, but it is not possible to solve them exactly. However, the energy scale in superconducting systems is given by Δ , and for conventional superconductors $\Delta/E_F \sim 10^{-3}$. The idea of Eilenberger quasi-classical approach [72, 73] is to simplify the Gorkov equations by making a perturbative expansion with respect to Δ/E_F . For high- T_c superconductors, $\Delta/E_F \sim 10^{-2}$ to 10^{-1} and the Eilenberger equations remains valid, at least close to T_c . But then, any variation of physical quantities smaller than the superconducting coherence length ξ_0 is integrated. Therefore this approximation forbids to see any single electron interference effects such as weak localization.

In the dirty limit where $l_{tr} \ll \xi_0$, one can simplify the Eilenberger equations by averaging over all the momentum direction \mathbf{p} , so that the electronic Green functions only depend on the position \mathbf{r} . It gives the Usadel equations [188]. Strictly speaking, this approach is only valid for s-wave superconductors, where Δ is independent of the momentum direction. However we still apply this model in the case of $\text{YBa}_2\text{Cu}_3\text{O}_7$, a d-wave superconductor. Indeed, we can treat in equivalent terms an s-wave superconductor with magnetic impurities (a dirty s-wave) and a d-wave superconductor with crystalline defects [127]. The disorder in $\text{YBa}_2\text{Cu}_3\text{O}_7$ is entered *ad hoc* as a new term $\Gamma(x)$ in the Usadel equations. They can be solved numerically and enable to address fundamental and experimental quantities such as pair potential, critical current, and normal state resistance.

4.2.1 Gorkov - Nambu theory¹

The BCS theory describes the formation of pairs through the exchange of phonons [25]. It can also be expressed as an interaction between time-reversed conjugates, without specifying the nature of the coupling. This canonical transformation reveals a pairing Hamiltonian that couples quasiparticles of the normal metal. Then, the eigenstates $u(\mathbf{r})$ and $v(\mathbf{r})$ of the system are no longer the ones of the electron or the hole, but correspond to a superposition of them. They obey the Bogolubov-de Gennes equations [67]:

$$\begin{bmatrix} H_0 & \Delta \\ \Delta^* & -H_0 \end{bmatrix} \begin{bmatrix} u(\mathbf{r}) \\ v(\mathbf{r}) \end{bmatrix} = \varepsilon \begin{bmatrix} u(\mathbf{r}) \\ v(\mathbf{r}) \end{bmatrix} \quad (4.7)$$

where H_0 is the electronic Hamiltonian and Δ is the superconducting order parameter.

The Gorkov approach reformulates this matrix equation in terms of two Green functions. They allow to calculate the evolution of the electronic wave function in the normal and superconducting part, treating normal-like and superconducting-like interactions with the same formalism. More precisely it introduces the *normal* Green function $G(\mathbf{r}, \mathbf{r}', t)$ which is a propagating field such that the electronic wave function in the normal part at \mathbf{r}' and t can be calculated from the wave function at \mathbf{r} and $t = 0$. Similarly the *abnormal* Green function $F(\mathbf{r}, \mathbf{r}', t)$ enables to calculate the electronic wave function in the superconductor, and evidences the presence of Cooper pairs. $G(\mathbf{r}, \mathbf{r}', t)$ and $F(\mathbf{r}, \mathbf{r}', t)$ can be expressed as:

$$G(\mathbf{r}, \mathbf{r}', t) = \langle \{ \Psi_{\uparrow}(\mathbf{r}, t), \Psi_{\uparrow}^{\dagger}(\mathbf{r}', 0) \} \rangle \quad (4.8)$$

$$F(\mathbf{r}, \mathbf{r}', t) = \langle \{ \Psi_{\uparrow}^{\dagger}(\mathbf{r}, t), \Psi_{\downarrow}^{\dagger}(\mathbf{r}', 0) \} \rangle \quad (4.9)$$

¹in this section and up to the Usadel equations we consider $k_B = \hbar = 1$.

where $\langle \dots \rangle$ is the statistical Gibbs averaging, $\{O, O'\} = OO' + O'O$ is the anti-commutator operation, and Ψ_\uparrow and Ψ_\uparrow^\dagger the annihilation and creation operator of an electron in \mathbf{r} at t (and \uparrow or \downarrow with a spin up or down) in the Heisenberg representation. In particular:

$$F(\mathbf{r}, \mathbf{r}, 0) = \langle \{\Psi_\uparrow^\dagger(\mathbf{r}, 0), \Psi_\downarrow^\dagger(\mathbf{r}, 0)\} \rangle \quad (4.10)$$

is the pair condensation amplitude, i.e. $F^2(\mathbf{r}, \mathbf{r}, 0)$ is the Cooper pair density in \mathbf{r} . Thus, if one considers an attractive potential $V(\mathbf{r})$:

$$\Delta(\mathbf{r}) = V(\mathbf{r})F(\mathbf{r}, \mathbf{r}, 0) \quad (4.11)$$

which is a *generalized* BCS order parameter in the case of a non homogeneous system.

Now, the Green functions and the Hamiltonian can be expressed in a convenient space called the *Nambu* space. It is a 4D space $(\mathbf{r}, t, \uparrow, \dagger)$ in which one can use 2x2 matrices to group under the same formalism normal-like and superconducting-like correlations. Those matrix have the form [87, 121]:

$$\check{M}(\mathbf{r}, \mathbf{r}', t, t') = \begin{bmatrix} \langle \{\Psi_\uparrow(\mathbf{r}, t), \Psi_\uparrow^\dagger(\mathbf{r}', t')\} \rangle & \langle \{\Psi_\uparrow(\mathbf{r}, t), \Psi_\downarrow^\dagger(\mathbf{r}', t')\} \rangle \\ -\langle \{\Psi_\downarrow^\dagger(\mathbf{r}, t), \Psi_\uparrow^\dagger(\mathbf{r}', t')\} \rangle & -\langle \{\Psi_\downarrow^\dagger(\mathbf{r}, t), \Psi_\downarrow^\dagger(\mathbf{r}', t')\} \rangle \end{bmatrix} \quad (4.12)$$

The " $\check{}$ " denotes that we are in the Nambu space. The diagonal elements represent the amplitude of "normal" correlations between electrons and the off-diagonal elements represent "abnormal" correlations, which describe paired electrons. With such a formalism, the Green functions are gathered into a matrix:

$$\check{G}(\mathbf{r}, \mathbf{r}', t) = \begin{bmatrix} G(\mathbf{r}, \mathbf{r}', t) & F(\mathbf{r}, \mathbf{r}', t) \\ F^\dagger(\mathbf{r}, \mathbf{r}', t) & -G(\mathbf{r}, \mathbf{r}', t) \end{bmatrix}$$

The Gorkov equations on the Green functions are more conveniently expressed in the frequency representation. One defines the Fourier transform as:

$$\check{G}_{\omega_n}(\mathbf{r}, \mathbf{r}') = \int_0^{1/T} e^{i\omega_n \tau} \check{G}(\mathbf{r}, \mathbf{r}', \tau) d\tau \quad (4.13)$$

$$\check{G}(\mathbf{r}, \mathbf{r}', t) = T \sum_n e^{-i\omega_n t} \check{G}_{\omega_n}(\mathbf{r}, \mathbf{r}') \quad (4.14)$$

where $\omega_n = (2n + 1)\pi T$ are the Matsubara frequencies and T is the temperature. They have the unit of an energy² and can be interpreted as a base for energies at which the correlated electronic system excites. Hence one has:

$$\check{G}_{\omega_n}(\mathbf{r}, \mathbf{r}') = \begin{bmatrix} G_{\omega_n}(\mathbf{r}, \mathbf{r}') & F_{\omega_n}(\mathbf{r}, \mathbf{r}') \\ F_{\omega_n}^\dagger(\mathbf{r}, \mathbf{r}') & -G_{\omega_n}(\mathbf{r}, \mathbf{r}') \end{bmatrix} \quad (4.15)$$

Now, the general Hamiltonian can be written as:

$$\check{\mathcal{H}} = \begin{bmatrix} H_0 & i\Delta(\mathbf{r}) \\ i\Delta^*(\mathbf{r}) & -H_0 \end{bmatrix} \quad (4.16)$$

$$H_0 = \frac{1}{2m} \left(\frac{\hbar}{i} \nabla - \frac{e}{c} A(\mathbf{r}) \right)^2 - \mu + U(\mathbf{r})$$

where $U(\mathbf{r})$ accounts for a scattering potential centered in \mathbf{r} , $A(\mathbf{r})$ the vector potential of the magnetic field and μ the chemical potential (Fermi energy). Then, the Gorkov equation on the Green functions is:

$$(i\omega_n \check{\tau}_3 + \check{\mathcal{H}}) \check{G}_{\omega_n}(\mathbf{r}, \mathbf{r}') = \check{1} \delta(\mathbf{r} - \mathbf{r}') \quad (4.17)$$

²The dimensional definition of the Matsubara frequencies is $\omega_n = (2n + 1)\pi k_B T$

with

$$\check{\tau}_3 = \begin{bmatrix} 1 & 0 \\ 0 & -1 \end{bmatrix}$$

the third Pauli matrix. In other words, for any ω_n , the Green functions satisfy coupled equations:

$$\begin{bmatrix} i\omega_n + H_0 & i\Delta(\mathbf{r}) \\ i\Delta^*(\mathbf{r}) & -i\omega_n - H_0 \end{bmatrix} \begin{bmatrix} G_{\omega_n}(\mathbf{r}, \mathbf{r}') & F_{\omega_n}(\mathbf{r}, \mathbf{r}') \\ F_{\omega_n}^\dagger(\mathbf{r}, \mathbf{r}') & -G_{\omega_n}(\mathbf{r}, \mathbf{r}') \end{bmatrix} = \begin{bmatrix} \delta(\mathbf{r} - \mathbf{r}') & 0 \\ 0 & \delta(\mathbf{r} - \mathbf{r}') \end{bmatrix} \quad (4.18)$$

and we see here the reformulation of equation 4.7. In other words:

$$\begin{cases} (i\omega_n + H_0)G_{\omega_n}(\mathbf{r}, \mathbf{r}') + i\Delta(\mathbf{r})F_{\omega_n}^\dagger(\mathbf{r}, \mathbf{r}') = \delta(\mathbf{r} - \mathbf{r}') \\ i\Delta^*(\mathbf{r})G_{\omega_n}(\mathbf{r}, \mathbf{r}') + (-i\omega_n - H_0)F_{\omega_n}^\dagger(\mathbf{r}, \mathbf{r}') = 0 \end{cases} \quad (4.19)$$

4.2.2 Perturbative expansion: Eilenberger equation

The integration of the Green functions $G_{\omega_n}(\mathbf{r}, \mathbf{r}')$ and $F_{\omega_n}(\mathbf{r}, \mathbf{r}')$ over the energy in the vicinity of the Fermi energy gives respectively g_{ω_n} and f_{ω_n} . They are called *quasi classic Green functions*. The integration is not trivial, in particular one needs to write them as a function of \mathbf{p} and \mathbf{k} instead of \mathbf{r} and \mathbf{r}' . One can find in [117] a detailed calculation. Hence the matrix of the quasi classic Green functions in the Nambu formalism is:

$$\check{g}_{\omega_n}(\hat{\mathbf{p}}, \mathbf{k}) = \begin{bmatrix} g_{\omega_n} & f_{\omega_n} \\ f_{\omega_n}^\dagger & -g_{\omega_n} \end{bmatrix}$$

where $\hat{\mathbf{p}}$ is the unit vector in the direction of \mathbf{p} . \check{g}_{ω_n} satisfies the normalization condition $\check{g}_{\omega_n}^2 = \check{1}$, i.e. $g_{\omega_n}^2 + f_{\omega_n}f_{\omega_n}^\dagger = 1$. The Eilenberger equations are then given in a compact matrix form as:

$$i\mathbf{v}_F \hat{\nabla} \check{g}_{\omega_n} + \check{g}_{\omega_n} \check{H}_0 - \check{H}_0 \check{g}_{\omega_n} = \check{1} \quad (4.20)$$

where $\check{g}_{\omega_n} \check{H}_0$ is just the usual product of two matrices and where we defined:

$$\hat{\nabla} \check{g}_{\omega_n} = \begin{bmatrix} \nabla g_{\omega_n} & (\nabla - \frac{2ie}{c} \mathbf{A}) f_{\omega_n} \\ (\nabla + \frac{2ie}{c} \mathbf{A}) f_{\omega_n}^\dagger & -\nabla g_{\omega_n} \end{bmatrix}, \check{H}_0 = \begin{bmatrix} i\omega_n & i\Delta(\mathbf{r}) \\ i\Delta^*(\mathbf{r}) & -i\omega_n \end{bmatrix}$$

In other words:

$$\begin{cases} \mathbf{v}_F \nabla g_{\omega_n} - f_{\omega_n}^\dagger \Delta + f_{\omega_n} \Delta^* = 1 \\ -\mathbf{v}_F \nabla g_{\omega_n} - f_{\omega_n} \Delta^* + f_{\omega_n}^\dagger \Delta = 1 \\ \mathbf{v}_F (\nabla - \frac{2ie}{c} \mathbf{A}) f_{\omega_n} - 2\omega_n f_{\omega_n} + 2g_{\omega_n} \Delta = 0 \\ \mathbf{v}_F (\nabla + \frac{2ie}{c} \mathbf{A}) f_{\omega_n}^\dagger + 2\omega_n f_{\omega_n}^\dagger - 2g_{\omega_n} \Delta^* = 0 \end{cases}$$

4.2.3 Usadel equations

We can write the momentum dependence as a first order correction term in the Green functions³:

$$\check{g}_{\omega_n}(\hat{\mathbf{p}}, \mathbf{r}) = \check{g}_n(\mathbf{r}) + \hat{\mathbf{v}}_F \check{\mathbf{g}}_{\omega_n}(\hat{\mathbf{p}}, \mathbf{r}) \quad (4.21)$$

where " $\hat{\mathbf{p}}$ " denotes the unit vectors and $|\check{\mathbf{g}}_{\omega_n}| \ll \check{g}_n$. Hence \check{g}_n does not depend on $\hat{\mathbf{p}}$. Since $\langle \check{g}_{\omega_n} \rangle = \check{g}_n$, the normalization condition on Nambu matrices writes itself $\check{g}_n = 1$. Then the Eilenberger equation 4.20 can be written as the Usadel equation:

$$D \hat{\nabla} (\check{g}_n \hat{\nabla} \check{g}_n) + \check{g}_n \check{H}_0 - \check{H}_0 \check{g}_n = 0 \quad (4.22)$$

³We write \check{g}_n instead of $\check{g}_{\omega_n,0}$ to have lighter notations.

where $D = \frac{1}{3}v_F l_{tr}$ is the diffusion constant. In particular [117]:

$$D(\nabla - \frac{2ie}{c}\mathbf{A})[g_n(\nabla - \frac{2ie}{c}\mathbf{A})f_n - f_n\nabla g_n] - 2\omega_n f_n + 2g_n\Delta = 0 \quad (4.23)$$

In this representation, the supercurrent is given by:

$$\mathbf{j}_s = \frac{\sigma_N}{e} \pi iT \sum_{n \geq 0} [f_n^\dagger (\nabla - \frac{2ie}{c}\mathbf{A})f_n - f_n (\nabla + \frac{2ie}{c}\mathbf{A})f_n^\dagger] \quad (4.24)$$

where $\sigma_N = 2v(0)De^2$ is the normal state conductivity ($v(0)$ is the quasi-particle density at the Fermi level, in $[\text{J}^{-1}] [\text{m}^{-3}]$). The order parameter is given by the self-consistent equation [29]:

$$\Delta(\mathbf{r}) = \lambda 2\pi iT \sum_{n \geq 0} f_n(\mathbf{r}) \quad (4.25)$$

where $\lambda = v(0)|g_0|$ is the coupling constant.

4.2.4 θ and χ parametrization⁴.

We now restrict ourselves in the case of a 1D system, i.e. we consider Cooper pair and Andreev pair densities to vary only along the length x of the Josephson junction. In this case and without magnetic field, equations 4.23, 4.24 and 4.25 become:

$$\hbar D [g_n \frac{\partial^2 f_n}{\partial x^2} - f_n \frac{\partial^2 g_n}{\partial x^2}] - 2\omega_n f_n + 2g_n \Delta(x) = 0 \quad (4.26)$$

$$\omega_n = (2n+1)\pi k_B T \quad (4.27)$$

$$j_s = i\pi e v(0) D k_B T \sum_{n \geq 0} [f_n^\dagger \frac{\partial f_n}{\partial x} - f_n \frac{\partial f_n^\dagger}{\partial x}] \quad (4.28)$$

$$\Delta(x) = \lambda 2\pi k_B T \sum_{n \geq 0} f_n(x) \quad (4.29)$$

with λ the coupling constant. The current continuity equation $\nabla \cdot \mathbf{j}_s = 0$ writes itself as (considering that we can exchange sum and derivative):

$$f_n^\dagger \frac{\partial^2 f_n}{\partial x^2} - f_n \frac{\partial^2 f_n^\dagger}{\partial x^2} = 0 \quad (4.30)$$

We can see that j_s , $\Delta(x)$ and the continuity equation 4.30 only depend on f_n and its complex conjugate. It is expected since f_n is the Green function for the superconducting electrons. Recall that g_n and f_n are dimensionless quantities. Then the Usadel equation 4.26 shows two energy source terms ($-2\omega_n f_n$ and $2g_n \Delta(x)$) which drive the coupling between f_n and g_n that is to say between Cooper pairs electrons and the ones of the Andreev pairs. The coupling term $g_n \frac{\partial^2 f_n}{\partial x^2} - f_n \frac{\partial^2 g_n}{\partial x^2}$ is controlled by the diffusion constant D .

In order to handle the quasiclassical equations both analytically and numerically, two parametrization have proven very useful: the Riccati- and the θ - ϕ -parametrization [29]. In the frame of the Matsubara Green functions formalism [139] the later is frequently used, and it is the one we choose here.

f_n and g_n respect the normalization condition:

$$g_n^2 + f_n f_n^\dagger = 1 \quad (4.31)$$

⁴From now on we use the real dimensions for \hbar and k_B

which means that the total number of electrons in the system is fixed. Thus one can parametrize Usadel equations with two real functions [29], $\theta_n(x)$ and $\chi(x)$ such that, for all ω_n :

$$\begin{cases} g_n(x) = \cos(\theta_n(x)) \\ f_n(x) = \sin(\theta_n(x))e^{i\chi(x)} \end{cases} \quad (4.32)$$

If $\theta_n = 0$, then $f_n = 0$ (and $g_n = 1$) and all the electrons behave like in a normal metal. If $\theta_n = \pi/2$, then $f_n = 1$ (and $g_n = 0$) and all the electrons are paired. Thus the "pairing angle" θ_n represents the proportion between normal and superconducting electrons. χ is the superconducting phase. With those parameters, the Green functions matrix is given by:

$$\check{g}_n = \begin{bmatrix} \cos\theta_n & \sin\theta_n e^{i\chi} \\ \sin\theta_n e^{-i\chi} & -\cos\theta_n \end{bmatrix} \quad (4.33)$$

The continuity equation writes itself as:

$$\frac{\partial}{\partial x} \left[\frac{\partial \chi}{\partial x} \sin^2 \theta_n(x) \right] = 0 \quad (4.34)$$

The superconducting gap $|\Delta(x)|$ is:

$$|\Delta(x)| = \lambda 2\pi k_B T \sum_{n \geq 0} \sin(\theta_n(x)) \quad (4.35)$$

The supercurrent density is:

$$j_s = -2\pi e v(0) D k_B T \frac{\partial \chi}{\partial x} \sum_{n \geq 0} \sin^2(\theta_n(x)) \quad (4.36)$$

and the Usadel equation can be separated into its real part and its imaginary part. The real part gives:

$$\frac{\hbar D}{2} \frac{\partial^2 \theta_n}{\partial x^2} - \frac{\hbar D}{2} \left(\frac{\partial \chi}{\partial x} \right)^2 \sin\theta_n \cos\theta_n - \omega_n \sin\theta_n + |\Delta(x)| \cos\theta_n = 0 \quad (4.37)$$

and the imaginary part gives:

$$\frac{\partial^2 \chi}{\partial x^2} + 2 \frac{\partial \chi}{\partial x} \frac{\partial \theta_n}{\partial x} = 0 \quad (4.38)$$

Equation 4.37 expresses conservation of energy. The first term is the energy associated with the diffusion of the pairing angle, controlling the proportion between normal and superconducting electrons. The second is related to the pair breaking process ($\sin\theta_n \cos\theta_n$). It tells how much the local variation of the phase influences the pair breaking. The third is the energy of normal electrons and the fourth the energy of paired electrons.

4.3 Adaptation for irradiated Josephson junctions

4.3.1 Usadel equations in irradiated YBa₂Cu₃O₇

Although the Usadel equations assume a spatial invariance of the momentum direction, we can still use them once adapted to the specificity of our high- T_c irradiated Josephson junctions. It all boils down to the analogy between a s-wave superconductor with magnetic impurities and a d-wave superconductor with crystalline defects. In the former, spin-dependent impurities destroy spin coherence. In the latter, the sign of the wave vector depends upon its orientation (see figure 2.6). Consequently, a scattering center can easily induce a phase jump of one paired electron from $+k$ to $-k$ which therefore breaks the Cooper pair.

To address this analogy we place ad hoc an *extra* pair breaking term in the Usadel equations, proportional to the pair breaking rate $\Gamma(x)$. As shown in chapter 2, (equation 2.4) it is defined as:

$$\Gamma(x) = \frac{\text{dpa}(x)}{\text{dpa}_c} \Gamma_c \quad (4.39)$$

where $\text{dpa}(x)$ is the local displacement per atom, $\text{dpa}_c = 0.042$ is the critical dpa for which T_c drops to zero, and Γ_c the associated pair breaking rate (at which $T_c = 0$). We define Γ_c in [s^{-1}] such that:

$$\Gamma_c = \frac{\Delta(0)}{\hbar} \quad (4.40)$$

where $\Delta(0)$ is the superconducting gap at $T = 0$. In our case we take the mean value over the Fermi surface: $\Delta(0) = 12$ meV. The Usadel equations are then modified such as:

$$\frac{\hbar D}{2} \frac{\partial^2 \theta_n}{\partial x^2} - \left[\frac{\hbar D}{2} \left(\frac{\partial \chi}{\partial x} \right)^2 + \hbar \Gamma(x) \right] \sin \theta_n \cos \theta_n - \omega_n \sin \theta_n + |\Delta(x)| \cos \theta_n = 0 \quad (4.41)$$

and we keep equations 4.34, 4.35 and 4.36.

Let us finally underline that those equations are only valid for $I \leq I_c$. In particular, above the critical current the phase χ depends on the time, according to the a-c Josephson equation, which is not represented in the Usadel equations.

4.3.2 Simulations results

The numerical resolution of the Usadel equations is delicate and the algorithm that we used is detailed in appendix D. Figure 4.2 represents the simulated profile of the pair potential $\Delta(x)/\Delta(0)$ along the Josephson junction, at different temperatures. It is simulated at zero current bias, and with the dpa profile shown on the blue curve. Plain lines represent the pair potential in the presence of diffusion, i.e. with proximity effects while dashed lines are the same simulations without it. Thus, we clearly see the direct and the inverse proximity effect: it respectively increases the pair potential in the normal part and diminishes it in the superconducting part.

When $\Delta \leq k_B T$, thermal excitations kill the pair potential and the junction is resistive [54]. According to equations 2.7 and 2.8 of chapter 2, we compute this resistance by integrating the local resistivity over the zone in which $\Delta(x) \leq k_B T$. Thus we simulate the shape of the $R = f(T)$ curve of a $\text{YBa}_2\text{Cu}_3\text{O}_7$ Josephson junction, and extract the temperature T_j at which $R = 0 \Omega$. This happens when the overlap between the two superconducting wave functions of the reservoirs counters the effect of thermal excitations. Figure 4.3 represents in plain lines RT curves for a 40 nm long junction, at different irradiation doses. For example, at dose 4.10^{13} ions.cm $^{-2}$, we have $T_j = 51\text{K}$, as indicated by the arrow. When we compute the same curves but without proximity effect, i.e. by taking $D = 0$, we can extract T'_c , at $R = 0 \Omega$. Below T'_c , the central part itself becomes superconducting and we enter the flux-flow regime. On figure 4.3, the T'_c at the different doses are represented by triangles at $R = 0 \Omega$. For example, at dose 4.10^{13} ions.cm $^{-2}$, we find $T'_c = 43\text{K}$, as indicated by the arrow. The dashed lines are guides for the eye, and show that T'_c can also be obtained by prolonging to zero the slope of the RT curves with diffusion. The regime between T'_c and T_j is governed by the diffusion of the pair potential over a weak link. We call it the Josephson regime in which, as we shall see in 5, the transport measurements show the presence of a Josephson current.

The critical current I_c can also be computed: it is calculated at $x = 0$ with equation 4.36, when we impose a phase difference $\chi(+\infty) - \chi(-\infty) = \frac{\pi}{2}$ across the junction. In fact, the a.c. Josephson equation 3.21 gives: $I = I_c \sin[\chi(+\infty) - \chi(-\infty)]$. Circles in figure 4.3 represent the $I_c(T)$ for at different doses and plain black lines fit I_c as a function of T according to equation 4.5.

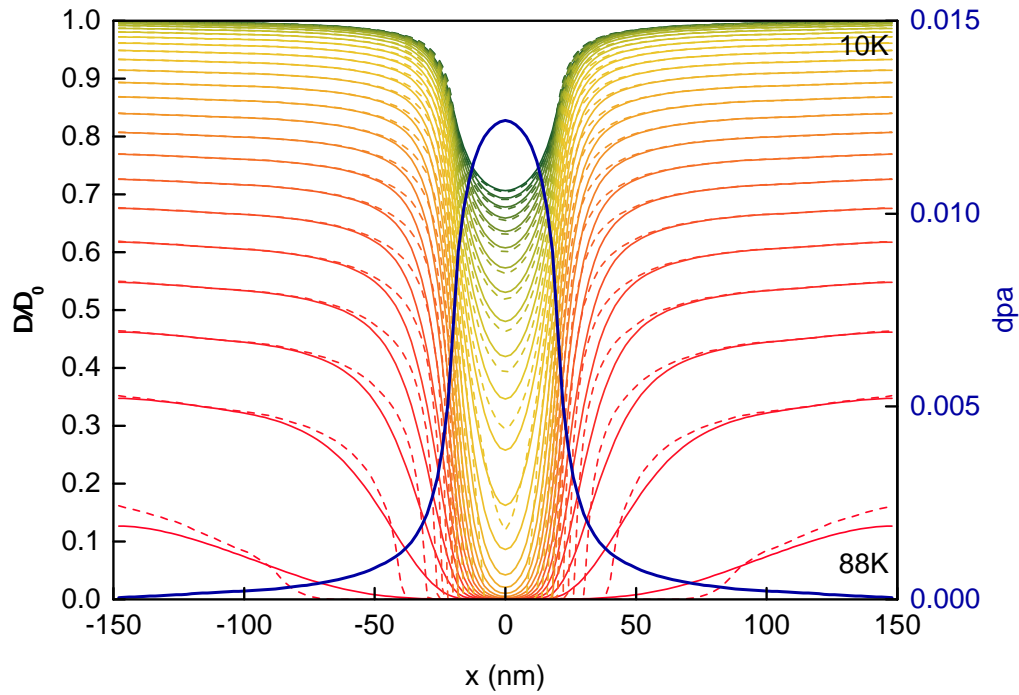


Figure 4.2: Normalized pair potential along the Josephson junction, every Kelvins from 10 to 88 K. The plain lines represent Δ/Δ_0 in the presence of proximity effects, and the dashed lines in their absence. The blue curve represents the dpa from which the pair breaking rate $\Gamma(x)$ is calculated. It is a dpa obtained for an irradiation at 110 keV, a dose of 3.10^{13} ions.cm⁻², for a 40 nm long and 70 nm thick junction.

As the length of the junction increases, the coupling between the two superconducting bulks is more difficult. Figure 4.4 represents the Josephson regime (colored areas), delimited by T'_c and T_j , as a function of the length of the slit L_s and for different doses. As the length increases, $T_j - T'_c$ diminishes, thus one should keep $L_s < 60$ nm in order to ensure $T_j - T'_c > 10$ K. Furthermore, the irradiation dose should remain between 3 and 5.10^{13} ions.cm⁻² in order to keep the operating range between 30 and 65 K.

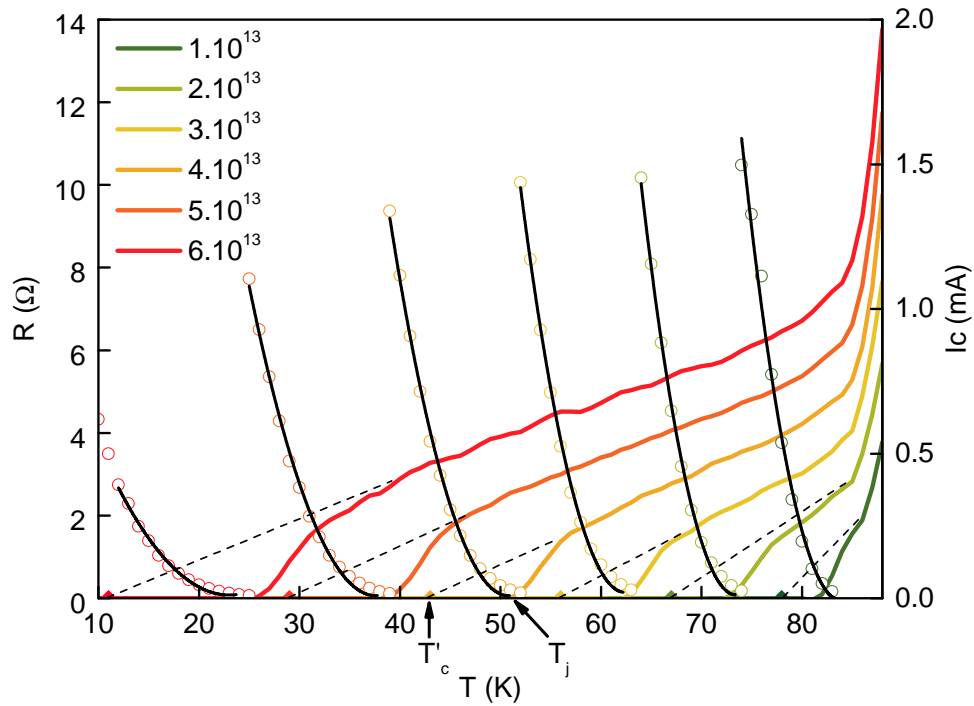


Figure 4.3: Color lines: Simulated normal resistance as a function of the temperature, for various irradiation doses. We take $\Delta < 0.1k_bT$ as the criterion for a resistive region inside the junction. Then we calculate the resistance with equations 2.7 and 2.8 of chapter 2. Circles points: critical current I_c as a function of temperature. Black lines: square fits of $I_c(T)$.

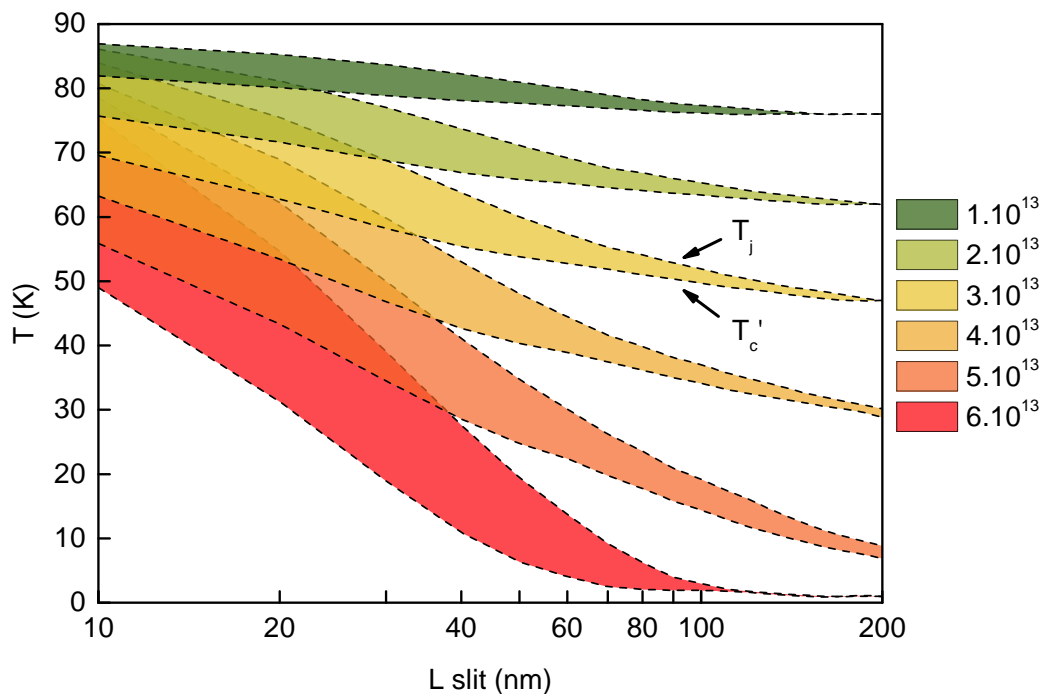


Figure 4.4: Josephson regime (colored areas) as a function of the length of the slit and for various irradiation doses. Each region spans between T'_c and T_j . The irradiation energy is 110 keV.

4.4 Conclusion on the quasi-classical approach of proximity effects

In this chapter we have seen the underlying physics of the electronic transport in irradiated Josephson junctions. Our system is well described by the SS'S model, which differs from SNS: there is a non zero attractive pair potential in the barrier, and the pair condensation amplitude is continue at the interface. In addition, the S' part extends as the temperature decreases.

The existence of coherent electronic states (Andreev pairs) in the normal part provide a very efficient coupling mechanism between the two superconducting reservoirs. It is highlighted by the expression of the normal coherence length (4.3) obtained in the dirty limit. Theoretical calculations [66, 65, 194] adapted to our junctions [105, 36] predict a quadratic dependence of the critical current as a function of the temperature (equation 4.5).

In the dirty limit and for an s-wave superconductor, theory of non equilibrium superconductivity [84, 72, 73] can be rewritten in the form of the Usadel equations (4.26). It describes the evolution of the normal and abnormal Green functions in an inhomogeneous superconductor. We modified those equations to use them in a d-wave superconductor by taking advantage of the analogy between a dirty s-wave with magnetic impurities and a d-wave with scattering centers. Thus, we added a pair-breaking term in the Usadel equation 4.41 written in the formalism of the θ - χ parametrization. This extra term is calculated from implantation simulations (see chapter 2). Then, the self-consistent equations 4.41, 4.34, 4.35 and 4.36 were solved numerically to obtain the pair potential $\Delta(x)$ along the junction (figure 4.2), the critical current (figure 4.3) and the Josephson regime (figure 4.4). The latter is the range of operating temperatures for our Josephson mixer. It spans between T'_c , below which S' becomes entirely superconducting (flux flow regime), and T_j above which thermal fluctuations kill the coupling between the superconducting wave functions of the reservoirs. Overall it seems that a comfortable Josephson regime is obtained for a slit length between 20 and 60 nm, at an irradiation dose between 3 and $5 \cdot 10^{13}$ ions.cm⁻².

There exists other techniques to write and solve the equations of inhomogeneous superconductivity. We used the decomposition over the Matsubara frequencies, but the Green functions in the Gorkov equations can also be written with the Keldysh technique [107, 29]. Also, we used the θ and χ parametrization but the Usadel equations can be expressed with the Ricatti parametrization [29, 58, 121, 87], which is known to be numerically very efficient. A further step in the study would be to compare the results obtained with the other technique.

There is a subtle effect present experimentally but absent of the above theoretical analysis. Due to the spatial distribution of defects, the critical current I_c also varies along the junction. So far we only took its value at the center, were the density of defects is the highest. However experimental data, presented in the next chapter, suggest that the normal resistance R_n depends also on the current bias. In fact, as suggested in [105], the increase of current moves the S-S' interfaces, since I_c is exceeded for more of the material. More fundamentally, the place at which the Andreev reflection occurs varies, because it depends on the energy of the charge carriers. We might account for this behavior by implementing in the model a *local* critical current (hence a local phase difference), above which the material is resistive.

Chapter 5

D-c and a-c characterization of the Josephson mixer

Contents

5.1	Experimental setups	86
5.1.1	<i>RT</i> curves: low frequency a-c setup	86
5.1.2	<i>IV</i> curves: d-c setup	86
5.2	D-c and a-c measurements	88
5.2.1	Josephson regime	88
5.2.2	Flux-flow regime	89
5.2.3	Shapiro steps	90
5.3	Comparison of the RSJ model with experimental data	95
5.3.1	Normal resistance at low current bias	95
5.3.2	Higher current biases	96
5.3.3	Fit of <i>IV</i> curves and Shapiro steps	97
5.4	Characteristics of other fabricated junctions	99
5.4.1	<i>RT</i> curves, critical currents, normal resistances	99
5.4.2	500 nm wide junctions and annealing	100
5.5	Conclusion on the d-c characterization	100

Several Josephson mixers were fabricated during this thesis. In this chapter, we present typical results obtained from d-c and low frequency a-c measurements. As we shall see, a lot of information can be extracted, which enables to foresee how the junction will respond to high frequency excitations. These results are also interesting because they validate the proximity model developed in chapter 3, as well as suggesting new ideas to understand more deeply the transport phenomenon in weak-link Josephson junctions.

After a presentation of the experimental setup in section 5.1, we expose in section 5.2 measurements performed on a device whose dimensions are routinely achieved with the fabrication process. Then we compare the RSJ model to our experimental data in section 5.3. Finally, we briefly present d-c and a-c characteristics from other devices that we fabricated, with different geometrical parameters in section 5.4.

5.1 Experimental setups

5.1.1 RT curves: low frequency a-c setup

Figure 5.1 is a sketch of the electronic setup used to measure the resistance as a function of temperature (RT curves). Inset shows a photo of a fabricated electronic chip, with six JJs embedded in their r-f structure, spiral antenna and CPW line. Their design will be explained in the next chapter, section 7.1.2. The chip is then mounted and connected through wire-bonding (four point contacts) to a sample holder as shown on the sketch. A Cernox thermometer and a heating resistance of $25\ \Omega$, also mounted on the sample holder, allow temperature regulation through a PID temperature controller (Lakeshore 340).

This setup is an a-c measurement method of RT curves, which exploits the sensitivity of lock-in amplifiers to measure voltages. Besides, such a measurement scheme is immune against any offset that a d-c voltmeter always has. It consists in biasing the JJ with a small a-c voltage (source agilent 33220A), at low frequency, typically around a few tens of Hertz. A polarization resistance $R_p = 100\ \text{k}\Omega$, whose impedance is much higher than any other in the line, ensures constant current bias. The latter is determined by the voltage V_I across a $R_I = 1\ \text{k}\Omega$ resistor, read with a lock-in amplifier (SR 7265) synchronized on the frequency excitation. An other lock-in reads the voltage V_V across the JJ and thus its resistance is simply given by $R = R_I V_V / V_I$. The current bias has to remain small compared to the critical current that we aim at measuring, about $\sim 100\ \mu\text{A}$ at the temperatures of interest.

As a safety measure against any voltage overshoot (and breakdown of JJ) when plugging and unplugging electric wires, there is always $500\ \Omega$ resistances in series on each wire connected to the junction. They are not an issue in this four points measurement because there is no potential drop in the wires where the current doesn't flow.

In addition, one can illuminate the junction with microwaves, sent from a horn antenna outside the cryostat, through a window. Section 5.3.1.1 describes how the junction's normal resistance in the superconducting state can be recovered using a strong microwave signal.

5.1.2 IV curves: d-c setup

Figure 5.2 presents the setup used to measure IV curves, and also to observe Shapiro steps. A d-c source (Yokogawa 7651) sends a constant bias, and the d-c voltage across the JJ is read using a four points measurement method by a multimeter (Keithley 2700) placed after a low noise room temperature amplifier (AD624) whose gain is set to 100.

From outside the cryostat, one can excite the JJ at high frequencies, up to 420 GHz and thus measure the d-c response under high frequency excitations. We used three different sources: a microwave signal generator (up to 30 GHz, Anritsu MG3692C), a Gunn oscillator (MMWS) for frequencies between 69 and 75 GHz, and a backward wave oscillator (BWO, brand Elmika GS-02) tunable between 109 and 188 GHz. A set of frequency doublers, triplers and quadruplers (GaAs Schottky diodes [74]) can be placed at the output of the Gunn oscillator and BWO to attain frequencies around 280 GHz and 420 GHz on each device.

For weak signals, especially at frequencies above 140 GHz where the available power is very low (tabulated less than 2 mW) it is sometimes necessary to use an optical chopper in front of the window, to modulate the amplitude of the high frequency excitation. It is synchronized to the lock-in amplifier, which measures a response that exhibits a singularity at the Shapiro step (see 5.2.2).

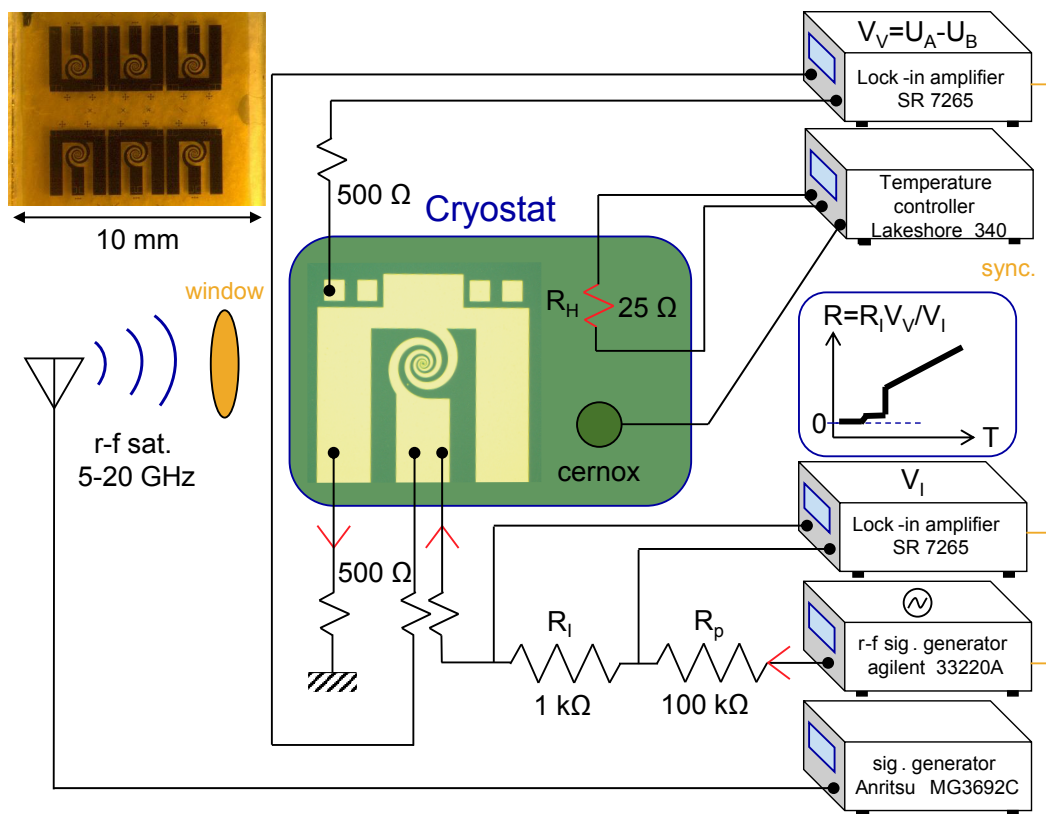


Figure 5.1: Schematic of the a-c measurement setup of the RT curves. Inset: photograph of a fabricated electronic chip, on which there are six mixers.

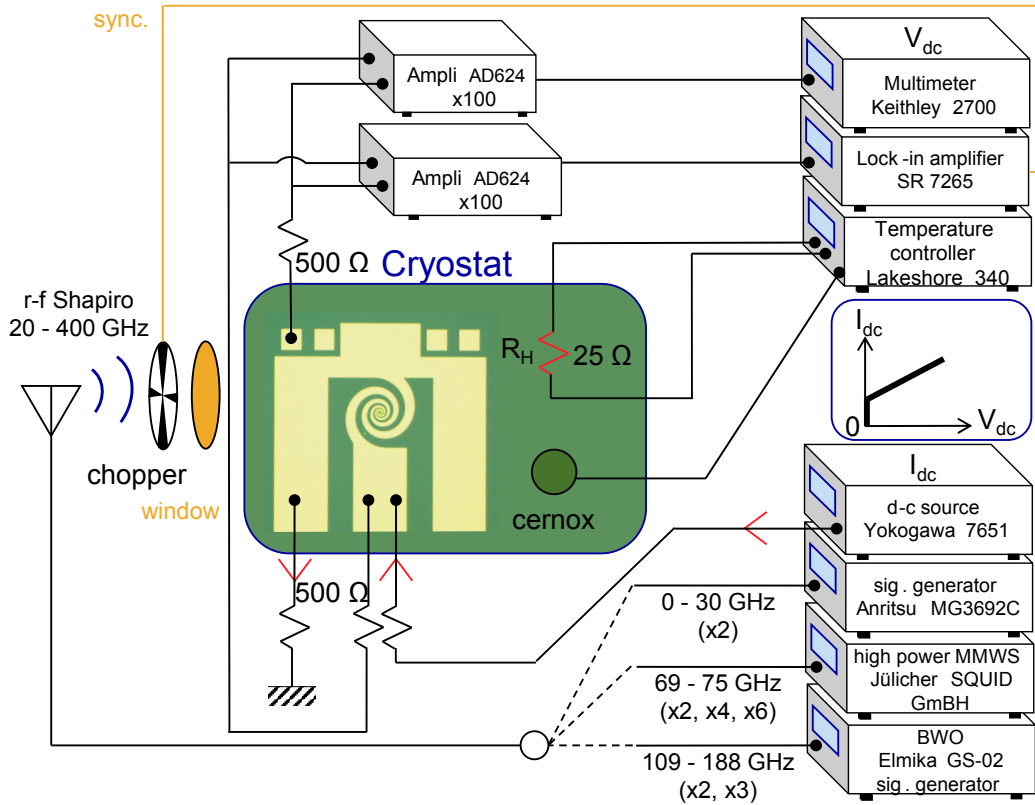


Figure 5.2: Schematic of the d-c measurement setup of the IV curves.

5.2 D-c and a-c measurements

5.2.1 Josephson regime

We measured a Josephson junction (JJ) whose geometrical characteristics are the following (see also 2.8): nominal length 20 nm, width 2 μm and thickness 70 nm. It has been irradiated at 3.10^{13} ions. cm^{-2} (second irradiation) with 110 keV oxygen ions.

The resistance of the JJ as a function of temperature (black curve on figure 5.3) is measured at very low current bias (0.3 nA) with the setup of figure 5.1. It reveals the existence of two characteristic temperatures in our device, namely T_c and T_j [135]. The highest transition at $T_c = 84$ K refers to the superconducting transition of the non-irradiated regions of sample, which corresponds to the transition temperature of the unprocessed $\text{YBa}_2\text{Cu}_3\text{O}_7$ film [33]. The second transition at the lower temperature $T_j = 66$ K corresponds to the occurrence of a clear Josephson coupling between the two electrodes, strong enough for the critical current to resist thermal fluctuations. A third characteristic temperature T'_c is also observed when the barrier itself becomes superconducting. Its existence is inherent to the irradiation fabrication technique, which lowers the T_c of the material in the region below the slit, as seen in chapter 3. To retrieve this temperature, we measured the RT curve while illuminating the junction with a sufficiently high-power r-f signal at 5 GHz (blue curve on figure 5.3 (a)) to suppress the Josephson supercurrent (see 5.3.1.1). This way, we measure the normal resistance R_n as a function of temperature (see also section 5.3.1). This curve extrapolates the linear variation of the one measured above T_j without r-f signal, and the temperature at which it reaches zero defines T'_c . The Josephson regime therefore lies between $T'_c = 45$ K and $T_j = 66$ K (figure 5.3 (b)).

Below T_j , the critical current I_c is extracted from the IV curves (figure 5.3 (b)), measured

with the setup of figure 5.2. It grows quadratically when lowering temperature (figure 5.3 (a)), as expected from Josephson coupling by proximity effect (equation 4.5). From the determination of I_c and R_n , we extract the characteristic frequency $f_c = 2eI_cR_n/h$ of the mixer. As seen in figure 5.3 (c), f_c displays a dome as a function of temperature with a maximum value f_{opt} of 85 GHz at 55 K. We will see in chapter 7 that f_c is not a cut-off frequency and Josephson mixing can be performed up to several times f_c , at the cost of a reduced conversion efficiency [136]. f_c can be seen as the frequency above which the impedance associated to the Josephson inductance $|Z_J| = L_J\omega$ becomes larger than the intrinsic shunting resistance R_n . For optimal operation, it is desirable to have f_c larger than the frequencies of the incoming local oscillator (LO) f_{LO} and signal f_s as the resulting ac current would then interact mainly with the Josephson non-linear inductive element.

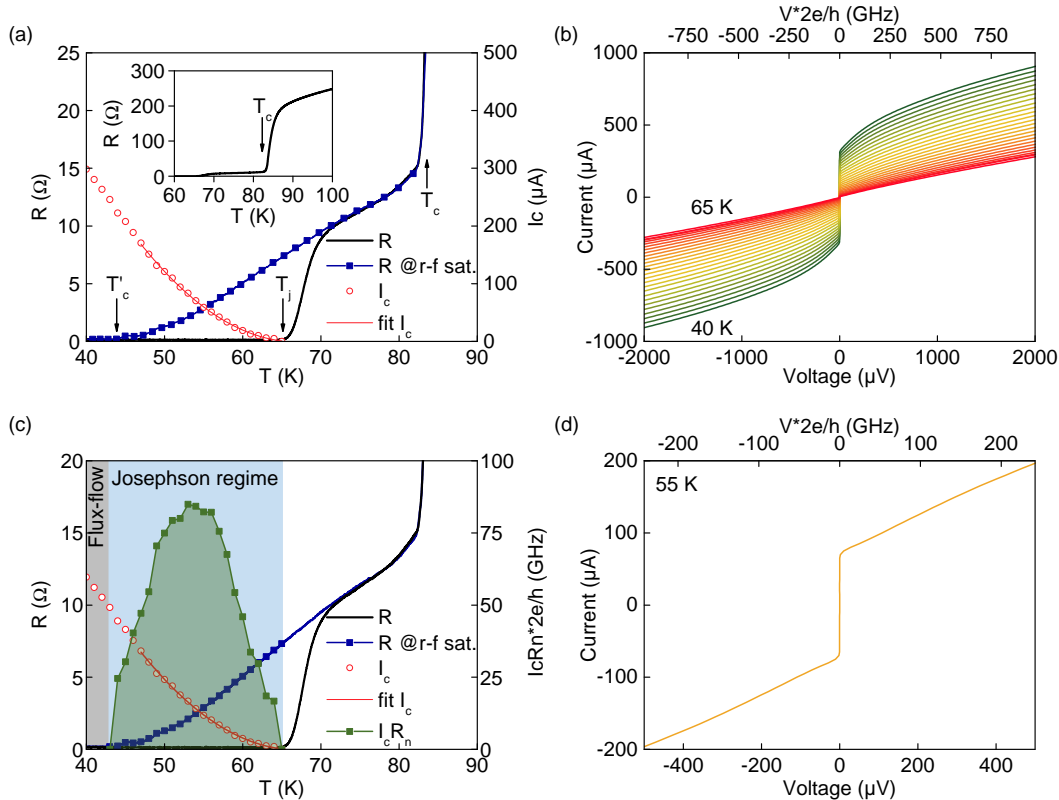


Figure 5.3: d-c and a-c characterization of the junction. (a) Resistance R and critical current I_c , as a function of temperature. The normal resistance R_n , blue curve, is obtained from the RT curve recorded when the junction is saturated with microwaves. Three temperatures T_c , T_j , and T'_c are indicated on the graph. Inset: RT curve at larger scale. (b) IV curves at each K , between 40 and 65 K. (c) $I_c R_n$ product in frequency unit superimposed to the previous curves. (d) IV curve at $T = 55$ K, i.e. in the Josephson regime.

5.2.2 Flux-flow regime

In the Josephson regime, the junction has a non-hysteretic current-voltage characteristics with an upward curvature in the dissipation branch at low voltage and no sharp feature at the gap voltage as seen on figure 5.3 (d) [33]. In the flux-flow regime, below T'_c , the barrier itself becomes superconducting, i.e. we are in the presence of a SS'S junction with S' also superconducting. The crossover between Josephson and flux-flow is not obvious on the IV curves of figure 5.3 (b). Below T'_c the pair condensation amplitude, even though not dropping to zero, diminishes in the S' ion damaged region (see figure 4.2, temperatures close to 10 K). This situation doesn't forbid *a priori* the supercurrent to oscillate (and the quasiparticles to counter oscillate) because

of the weakened interface, but the system deviates continuously from a pure Josephson oscillation, to a hybrid situation between a homogeneous superconductor and a weak-link, and a large excess current rises. A model would require to study deviations from the pure sinus in the d-c Josephson equation.

5.2.3 Shapiro steps

The discrimination between Josephson and flux flow regime is better identified on IV curves when the junction undergoes a moderately high power r-f illumination (no saturation). In a nutshell, the self-oscillation of the junction can resonate and lock to the oscillation of the external driving r-f field. It creates steps in the IV curves, first observed by Shapiro [166] and thus called Shapiro steps. In the Josephson regime, the r-f power modulates entirely the supercurrent.

More fundamentally, the presence of Shapiro steps is a clear evidence of the Josephson effect, since both Josephson equations are required to describe them.

5.2.3.1 Voltage source model

Let us describe it more formally, and to that end we need to express the r-f field as a source term, either voltage or current source. The voltage source model has the advantage of inducing equations with analytical solutions, therefore it is the one we use here to discuss Shapiro steps. The current source model has been used extensively in the RSJ model (see section 3.3.3.2 and appendix C) because it led to numerically stable equations, good for fitting simulations.

Here we consider the coherent r-f field of frequency f_{rf} as a voltage source term with the form $V_{rf}\cos(\omega_{rf}t)$ where $\omega_{rf} = 2\pi f$. The voltage developed across the junction is then given by:

$$V = V_b + V_{rf}\cos(\omega_{rf}t) \quad (5.1)$$

where the voltage bias V_b is given by the a-c Josephson equation 3.21 when there is no r-f field applied. In other words:

$$\omega_J = \frac{2e}{\hbar}V_b = \frac{2\pi}{\phi_0}V_b \quad (5.2)$$

where ω_J is the Josephson frequency, i.e. the self-oscillation (SO) frequency. Integrating the a-c Josephson equation with the total voltage V leads to:

$$\phi(t) = \omega_J t + \frac{2\pi V_{rf}}{\phi_0 \omega_{rf}} \sin(\omega_{rf}t) + \phi_c = \omega_J t + \frac{\omega_0}{\omega_{rf}} \sin(\omega_{rf}t) + \phi_c \quad (5.3)$$

where $\omega_0 = \frac{2\pi V_{rf}}{\phi_0}$ and ϕ_c is an integrating constant. Putting back $\phi(t)$ in the d-c Josephson equation 3.20:

$$I_J = I_c \left[\sin(\omega_J t + \phi_c) \cos\left(\frac{\omega_0}{\omega_{rf}} \sin(\omega_{rf}t)\right) + \sin\left(\frac{\omega_0}{\omega_{rf}} \sin(\omega_{rf}t)\right) \cos(\omega_J t + \phi_c) \right] \quad (5.4)$$

The anharmonic terms can be expanded into Fourier series:

$$\cos\left(\frac{\omega_0}{\omega_{rf}} \sin(\omega_{rf}t)\right) = J_0\left(\frac{\omega_0}{\omega_{rf}}\right) + 2 \sum_{n=1}^{\infty} J_{2n}\left(\frac{\omega_0}{\omega_{rf}}\right) \cos(2n\omega_{rf}t) \quad (5.5)$$

$$\sin\left(\frac{\omega_0}{\omega_{rf}} \sin(\omega_{rf}t)\right) = 2 \sum_{n=1}^{\infty} J_{2n-1}\left(\frac{\omega_0}{\omega_{rf}}\right) \sin((2n-1)\omega_{rf}t) \quad (5.6)$$

where J_{2n} and J_{2n-1} are the n th order Bessel functions of the first kind. Then equation 5.4 gives the expression of the Josephson supercurrent as:

$$I_J = I_c \left(J_0 \sin(\omega_J t + \phi_c) + \sum_{n=1}^{\infty} J_n\left(\frac{\omega_0}{\omega_{rf}}\right) \sin[(\omega_J + n\omega_{rf})t + \phi_c] + \sum_{n=1}^{\infty} (-1)^n J_n\left(\frac{\omega_0}{\omega_{rf}}\right) \sin[(\omega_J - n\omega_{rf})t + \phi_c] \right) \quad (5.7)$$

This expression is very interesting because it underlines a subtle physics point of the Josephson mixer. When biased, a JJ oscillates *by itself* at ω_J and due to the non linearity of the Josephson equations, this oscillation mixes with the one of the r-f field. It creates harmonics at $\omega_J \pm n\omega_{rf}$, in particular at $\omega_J - \omega_{rf}$, as expected from a square-law component (see 1.4.1.2). But in the case of heterodyne detection we intend to design, we don't use the self-oscillation (SO) as LO. In fact we just use the non linear property of the device to mix two *external* r-f fields so as to create harmonics in the same manner as shown here. For a LO at pulsation ω_{LO} and a signal at pulsation ω_{sig} we will have harmonics at $\omega_{LO} \pm n\omega_{sig}$, in particular at the IF. The main reason to use an external LO and not the SO is that the latter is per nature very broadband, due to voltage fluctuations across the junction, hence intrinsically not a good LO. However a clever engineering of the environment of the JJ might reduce its spectrum as we will see in chapter 7.

We also see that for $\omega_J = \pm n\omega_{rf}$ with n and integer, there is one term in the expression which doesn't depend on the time. Its amplitude is given by:

$$I_n = I_c J_n\left(\frac{\omega_0}{\omega_{rf}}\right) \sin\phi_c = I_c J_n\left(\frac{2\pi V_{rf}}{\phi_0 \omega_{rf}}\right) \sin\phi_c \quad (5.8)$$

This current is added or subtracted from the quasiparticle current, hence creates *Shapiro* steps at the corresponding voltage positions i.e. at $V_b = n\phi_0 f_{rf} = nh/(2e)f_{rf}$ [27]. It depends on V_{rf} i.e. on the applied r-f power.

5.2.3.2 Shapiros steps on IV curves

Figure 5.4 (a) shows IV curves of the same JJ than previously, obtained at $T = 53$ K under high frequency illumination. At 20, 70 and 140 GHz, the r-f power was chosen to reduce by about a half the initial critical current (100 μ A). For 280 and 420 GHz the lack of available power prevented us from achieving such a reduction, and the steps at those frequencies are much more tenuous to observe directly on the IV curves, as seen on the details, figures 5.4 (b) and (c) respectively.

However their presence is confirmed on the measurements (dotted lines of figure 5.4 (a)) performed with the optical chopper (spinning at a few hundred Hz) and the lock-in amplifier. The chopper enables to have the JJ illuminated periodically with r-f. Thus the d-c current across the junction varies between $I(V)$ (with r-f) and $I_0(V)$ (without), at the chopper frequency. The lock-in records a signal proportional to this variation $\Delta I = I(V) - I_0(V)$, which is similar as computing the difference between two IV curves (with and without r-f), except that it averages ΔI over many periods, hence giving much less noise. When arriving at a step, $\Delta I \rightarrow 0$ and the lock-in signal drops abruptly. We used this measurement method to ensure that the JJ was effectively seeing high-frequency illuminations, since it is far from obvious on the bare IV curves. Also, it proved to be crucial to experimentally align, and tune the signal and the LO for high frequency mixing experiments (see chapter 7).

Similar technique for low-intensity radiation has been used in Hilbert-transform spectroscopy with RSJ-like JJs [69, 118, 134]. In this frame, ΔI is the junction's response, difference between the $I(V)$ curve modified by a radiation, and the unmodified $I_0(V)$ curve. Then, one can compute a response function $H(V)$ such that:

$$H(V) = \left(\frac{8}{\pi}\right) \left(\frac{h}{2e}\right) \left[\frac{\Delta I(V) I(V) V}{I_c^2 R_n^2} \right] \quad (5.9)$$

whose inverse Hilbert transformation allows to retrieve the spectrum $S(f)$ of the incident radiation:

$$S(f) \sim \left(\frac{1}{\pi}\right) P \int_{-\infty}^{+\infty} \frac{H(f_j)}{f_j - f} df_j \quad (5.10)$$

where P is the Cauchy principal value of the integral and $f_j = 2eV_0/h$ is the frequency of Josephson oscillations.

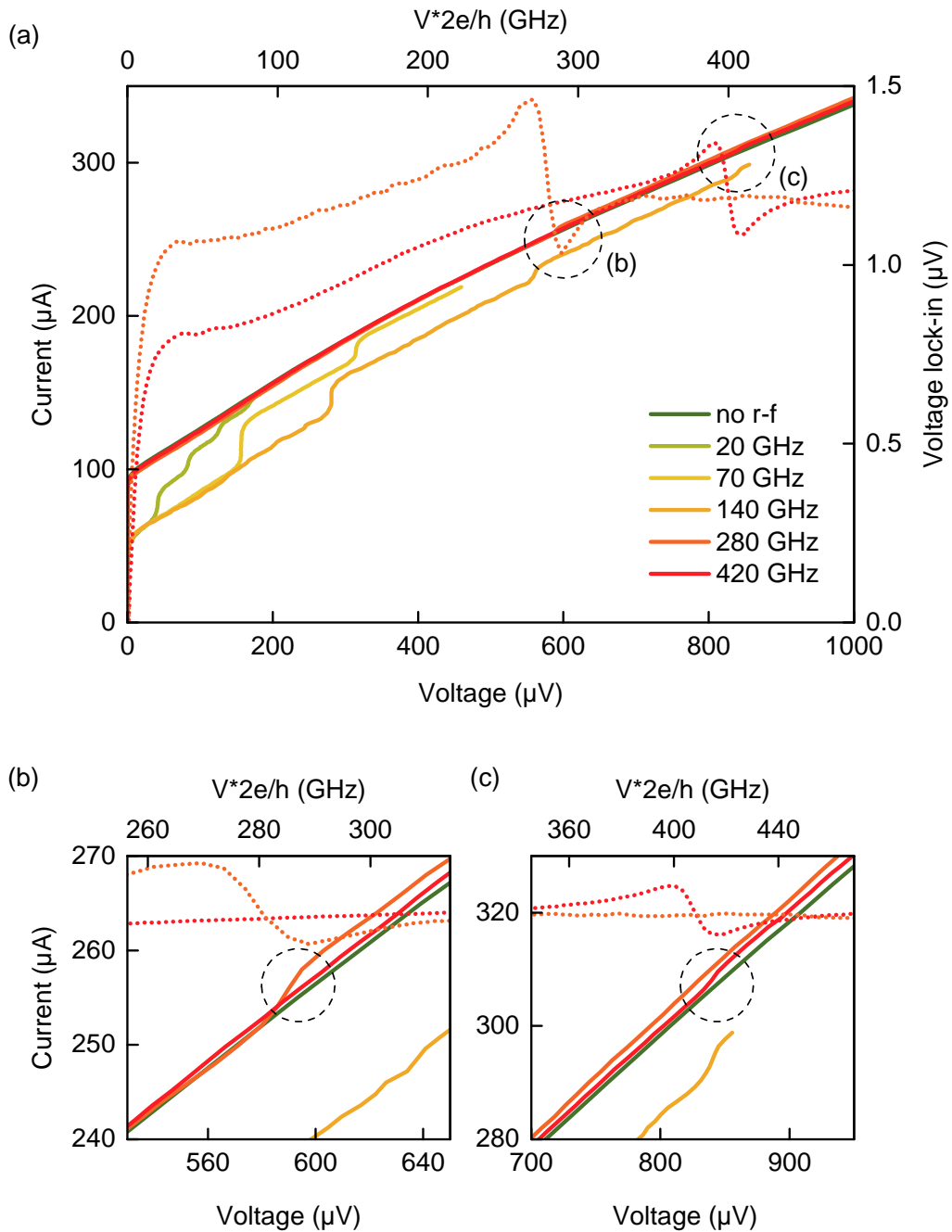


Figure 5.4: Evidence of Shapiro steps on the IV curves of the Josephson junction, at $T = 53$ K. (a), plain lines: IV curves of the Josephson junction under high frequency illumination. Shapiro steps appear at harmonics of the r-f frequency excitation. Dotted lines: lock-in response when the incoming r-f field at 280 and 420 GHz is chopped, showing important variations at the steps positions. (b) and (c), zoom on the IV curves around 280 and 420 GHz respectively.

5.2.3.3 Differential resistance

As mentioned at the beginning of section 5.2.3, r-f power modulates the height of the Shapiro steps. More specifically, in the Josephson regime, the amplitude current modulation of the n th Shapiro step as a function of the induced r-f voltage is given by expression 5.8 [136]. Figure 5.5 shows the differential resistance of the junction dV/dI as a function of bias current and power radiation (of 20 GHz) at $T = 56, 53, 42$ and 35 K (a,b,c and d) [135]. At $T = 53$ K (figure (b)) and for a power of 1 mW, we find the derivative of the IV curve presented in figure 5.4 for the Shapiro steps at 20 GHz. Also, we can follow the modulation of the 0th step on the black lines. For strong r-f power, several steps can be seen as well as their modulation with r-f power. In particular, the critical current (step at $n = 0$ in 5.2.3) can be fully suppressed by the application of the correct amount of LO power. However, below T_c' , the modulation of the critical current is no longer complete (panel (d)), indicating that the dynamics of the junction deviates from a pure Josephson one. A crossover towards a flux flow regime in which there is an excess current is then observed although the oscillations from the Josephson effect remain observable.

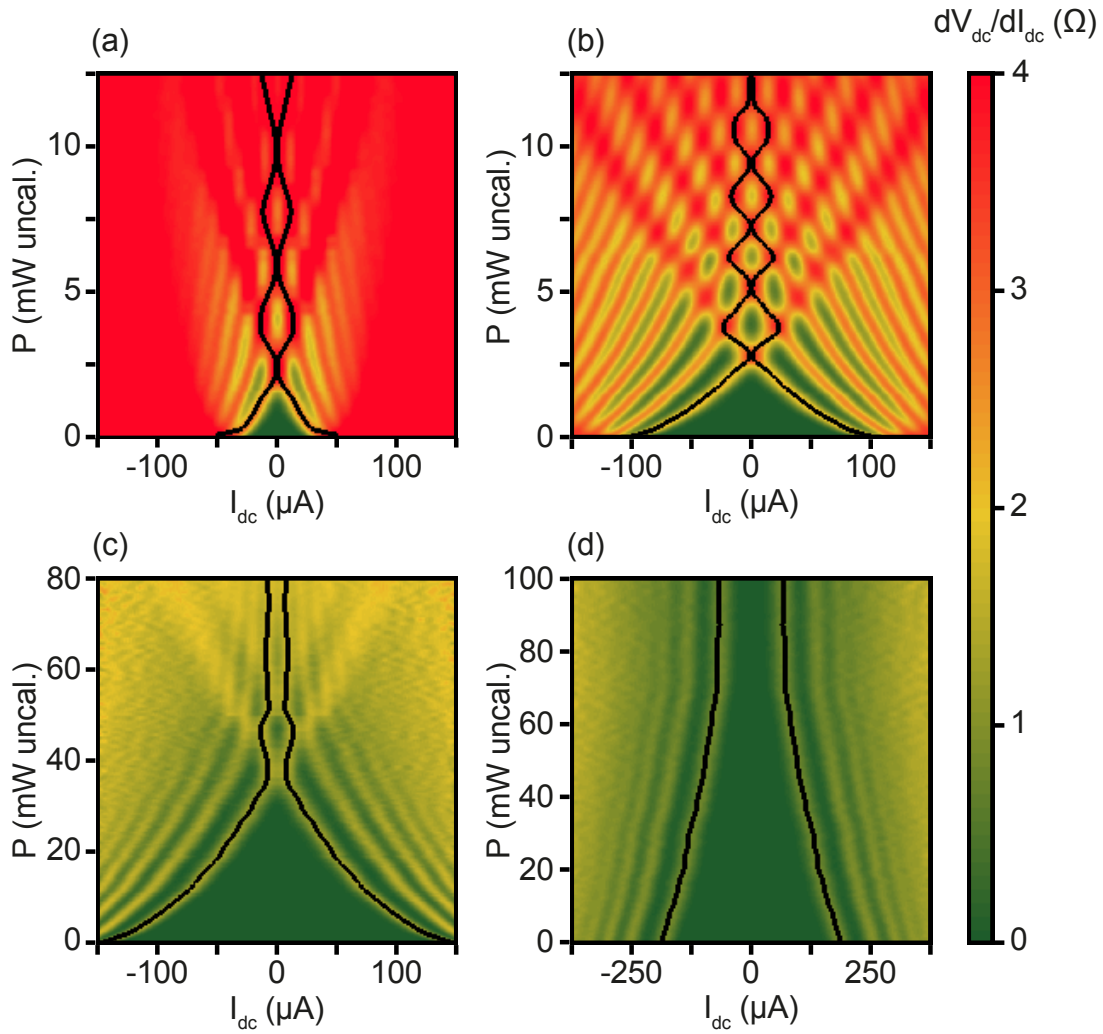


Figure 5.5: Differential resistance of junction (color scale) under a 20 GHz illumination, as a function of current bias and r-f power for different temperatures: (a) $T = 56$ K; (b) $T = 53$ K; (c) $T = 42$ K; (d) $T = 35$ K. The critical current ($n = 0$ step) as a function of r-f power is shown in full back line. Complete oscillations of the current height of the Shapiro steps can be seen only in the Josephson regime $T_c^! < T < T_j$ (panels (a)–(c)). In the flux flow regime, the critical current is never reduced to zero (panel (d)).

5.3 Comparison of the RSJ model with experimental data

From the RSJ model with fluctuations, we should be able to fit experimental IV curves in the Josephson regime. To that end, one first needs to retrieve the normal state resistance R_n . However, as already introduced at the end of chapter 3, in irradiated JJs it is expected that R_n not only depends on temperature but also on current bias I . In fact a probable distribution of the critical current along the junction causes the normal part to extend as I increases: it moves the S-S' interfaces and I_c is exceeded for more of the material. More fundamentally the increase of the current bias moves the position of the Andreev reflection because it depends on the energy of the charge carriers. Ideally, this effect should be explored in a tunneling spectroscopy experiment, where QP at known energy would probe the interface. It has been mentioned a few times in the literature, notably by Katz et al. [105] and in the PhD thesis of W. Booij [45].

Therefore, when talking about R_n in the discussion above and especially in the experimental curves of figure 5.3, we more precisely referred to the normal resistance at *low* current bias. It is actually the most pessimistic way to determine an $I_c R_n$ product since the resistance will increase with I , and perhaps explains also why, even at much higher frequencies than the characteristic frequency f_c , the mixer still operates (see chapter 7).

5.3.1 Normal resistance at low current bias

Let us here explain how we retrieve the normal resistance below T_j at low current bias. We have investigated different experimental ways, all giving consistent results.

5.3.1.1 Saturated r-f

The first one already mentioned consists in applying a strong r-f external field that saturates the Josephson oscillations. In fact, as can be seen in equation 5.7, an r-f excitation redistributes the Josephson supercurrent at frequencies $\omega_J \pm n\omega_{rf}$, with an amplitude proportional to the Bessel function J_n . Then, saturating the oscillation means that the r-f field is so strong, that I_J is being dispatched over all the frequencies, thus killing the Josephson branch.

In this context it is easier to use a fairly low frequency r-f field, since for the same power, the redistribution over a great deal of harmonics is easier, and we typically took $f_{rf} = 5$ GHz. Also, we have much more powerful sources at low frequencies. The RT curve under saturation of figure 5.3 (a) was obtained in this way.

For long-range proximity effect coupling junctions, we do not expect to have a significant excess current above T'_c . This has been confirmed experimentally close to T_j and for low current bias in [36], where Bergeal et al. showed that it is possible to obtain full modulation of the critical current under a perpendicular magnetic field. In the absence of excess current above T'_c , the r-f saturation method is very efficient and robust to obtain R_n below T_j .

5.3.1.2 Linear extrapolation of the normal state resistance

The RT curve obtained under r-f saturation is the linear extrapolation of the one measured at very low bias without r-f [105], see figure 5.3 (a). This is not surprising since we retrieve the temperature dependence of the resistance of the barrier. For a low irradiation dose (as the one used here), the latter is expected to be linear since we use an optimally doped YBa₂Cu₃O₇ sample.

5.3.1.3 Derivative of IV curves

One can also retrieve R_n from the IV curves. In fact the linear extrapolation of the derivative $dV_{dc}/dI = f(I)$ to $I = 0$ gives a resistance that matches the one of the RT curve under r-f saturation.

Figure 5.6 shows numerical derivation of IV curves presented in figure 5.3 (b). Below 46 K the extrapolation gives a negative resistance, which we interpret as the beginning of the flux flow regime, in agreement with the T_c' inferred from the saturated r-f RT curve.

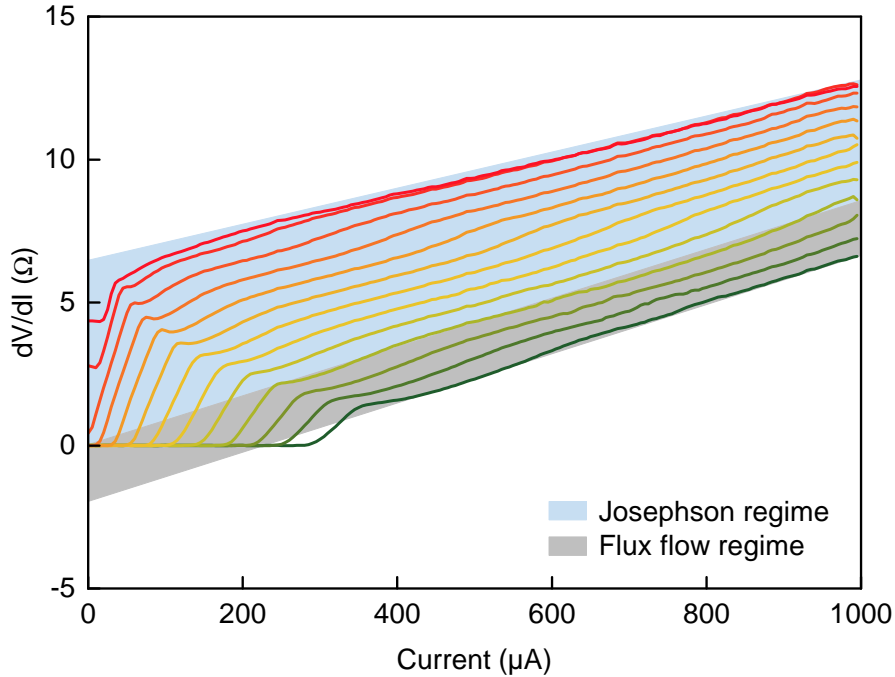


Figure 5.6: Numerical derivation of IV curves presented in 5.3 (b), dV_{dc}/dI as a function of current bias. The linear extrapolation to $I = 0$ gives the normal resistance R_n . Below 46 K it gives a negative resistance and we enter the flux flow regime.

Figure 5.7 shows the normal resistance extracted from the three different methods. As they give the same results, we are rather confident that we are able to extract correctly the normal resistance at low current bias.

5.3.2 Higher current biases

In our irradiated junctions, the normal resistance R_n of the RSJ model varies when increasing the current bias, and we can measure this dependence also with r-f saturation: instead of doing RT curves (and use the experimental setup 5.1) we simply make IV curves under saturated r-f (and use the experimental setup 5.2). One carefully needs to adjust the power so that no Shapiro step remains, indicating that the supercurrent has been redistributed homogeneously over all the frequencies. Then $R_n(I)$ is given by:

$$R_n(I) = \frac{V_{sat}}{I} \quad (5.11)$$

where V_{sat} is the d-c voltage under saturation. Figures 5.8 (a), (b) and (c) show in dashed lines the experimental IV curves thus obtained, at 53, 58, and 62 K respectively. One can see that at low current bias the curves are linear, indicating a constant R_n , but as I increases, a deviation from the linear behavior is observed, which happens at about 200 μ V. At very high biases, the curves rejoin the unsaturated IV characteristics, represented in open circles. Once again, as I increases the relative influence of Josephson branch diminishes.

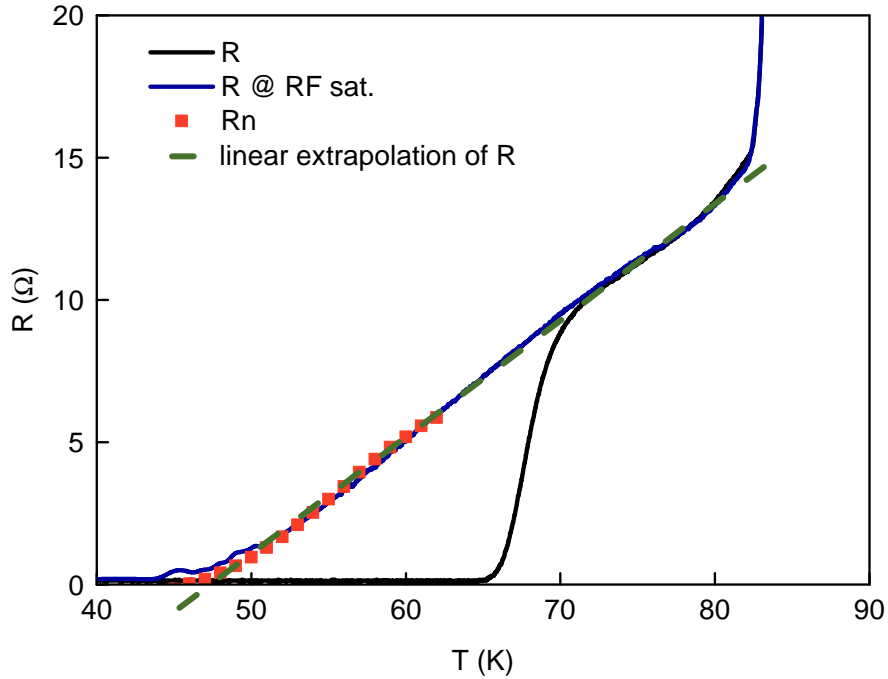


Figure 5.7: Three different methods to extract the normal state resistance R_n . Resistance measured when the junction is saturated with r-f (blue curve), linear extrapolation of the normal state resistance (dashed green line), and obtained from the derivative of IV curves (red squares).

5.3.3 Fit of IV curves and Shapiro steps

One can enter $R_n(I)$ into the RSJ model to fit the experimental datas. The LO entering as additional current source, purely coherent, the RSJ equations then write:

$$\begin{cases} V(t) = R_n(I)[I - I_c \sin\phi + \delta I_n + I_{LO} \cos(\omega_{LO} t)] \\ \frac{d\phi}{dt} = \frac{2e}{\hbar} V \end{cases} \quad (5.12)$$

The plain lines in figures 5.8 (a), (b) and (c) show simulated IV curves at 53, 58, and 62 K respectively when the r-f (LO) is absent. Furthermore, with the same parameters, one can also fit the IV curves with Shapiro steps. Figures 5.8 (d), (e) and (f) show in plain lines simulated IV curves under (unsaturated) r-f illumination at 58 K and for 20, 70 and 140 GHz respectively. The experimental data are represented in open circles. In every situation, a good agreement is found, suggesting that we accurately describe the junction with this modified RSJ model [135].

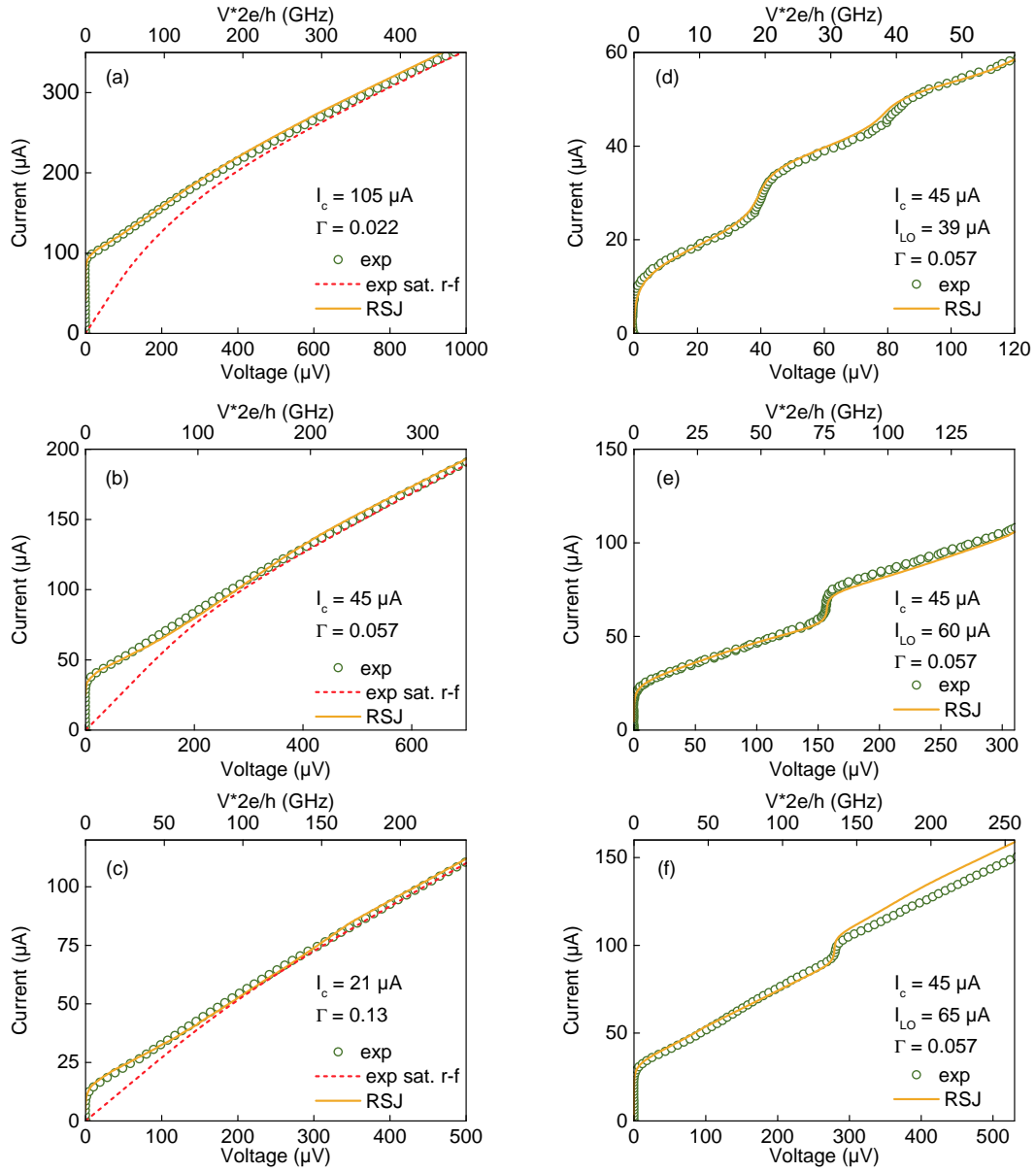


Figure 5.8: (a), (b), and (c) Current-voltage characteristics of the junction (open circles) measured at different temperatures 53 K, 58 K, and 62 K, respectively. Dashed lines correspond to the curve under strong microwave radiation and orange solid lines correspond to a fit using the RSJ model in which the non-linear resistance (i.e., dashed line) is introduced. The value of the fitting parameter I_c and the value of $\Gamma = 2ek_bT/\hbar I_c$ used in the RSJ model are indicated on the graph. (d)–(f) Current voltage characteristics of the junction (open circles) measured at $T = 58$ K under LO radiation at 20 GHz, 70 GHz, and 140 GHz. Curves are fitted using the RSJ model (equation 5.12) including the non-linear resistance. The value of the fitting parameters I_c and I_{LO} and the value of $\Gamma = 2ek_bT/\hbar I_c$ used in the RSJ model are indicated on the graph.

5.4 Characteristics of other fabricated junctions

5.4.1 RT curves, critical currents, normal resistances

We fabricated several junctions, with various widths and lengths. Similarly, we varied the dose of the second irradiation to test the reproducibility of the fabrication process. Figure 5.9 shows the RT curves, critical current and normal resistance of three junctions, taken from three different batches. The data in yellow correspond to the junction that we have studied in all the above analysis.

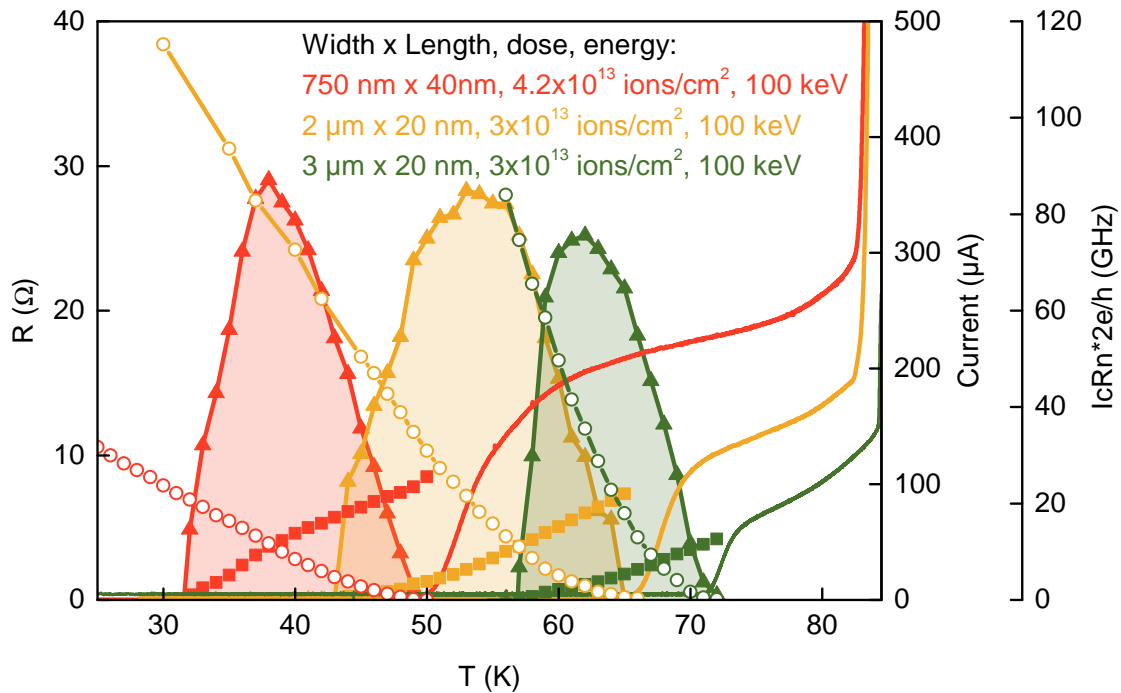


Figure 5.9: RT curves (plain lines), $I_c(T)$ (circles), $R_n(T)$ (squares) and $f_c(T)$ (triangles) for three different junctions. The normal resistance has been calculated by derivation of the IV curves.

The width of the junctions increases from left to right (750 nm - 2 μm - 3 μm), while the length decreases (40 nm - 20 nm - 20 nm). The normal resistance diminishes accordingly: the plateau of the RT curves lowers, along with $R_n(T)$, represented with square points. The latter has been calculated with derivatives of the IV curves.

The 750 nm long junction underwent a higher irradiation dose than the other two, which is in agreement with its lower T_j . However both junctions of 2 and 3 μm wide underwent the same dose (3×10^{13} ions.cm⁻²), whereas their T_j varies of about 5 K. This underlines the limits of the fabrication process: to date the dose is not perfectly similar from one irradiation to the other, especially when it is not done on the same batches.

The $I_c R_n$ products are remarkably similar for all three junctions. Thus, the geometrical parameters do not significantly improve the characteristic frequency, which remains between 80 and 90 GHz.

The model that we described in this chapter seems to also explain the behavior of the 3 μm wide junction: the critical current varies quadratically with temperature, and $R_n(T)$ is the pro-

longation of the RT curve's plateau. However, the situation in the 750 nm wide and 40 nm long junction does not appear so clearly: even if close to T_j , $I_c(T)$ is still quadratic, it seems that it gets linear very quickly. This could account for an excess of supercurrent closer to T_j than for wider junctions, and therefore the pure Josephson regime would be narrower. In addition, the normal resistance taken as derivative of the IV curves does not prolong the plateau of the RT curve. Once again this could be explained by a mixed regime between flux-flow and Josephson.

5.4.2 500 nm wide junctions and annealing

We pushed the limits of the fabrication process down to 500 nm wide junctions. Figure 5.10 (a) shows the RT curve (green line) of such a device. The second irradiation dose was 4.5×10^{13} ions.cm⁻². The T_j is surprisingly low, about 30 K, and the transition is less sharp and clean than for wider junctions: there is a first change of slope at about 50 K, and a second one at 40 K.

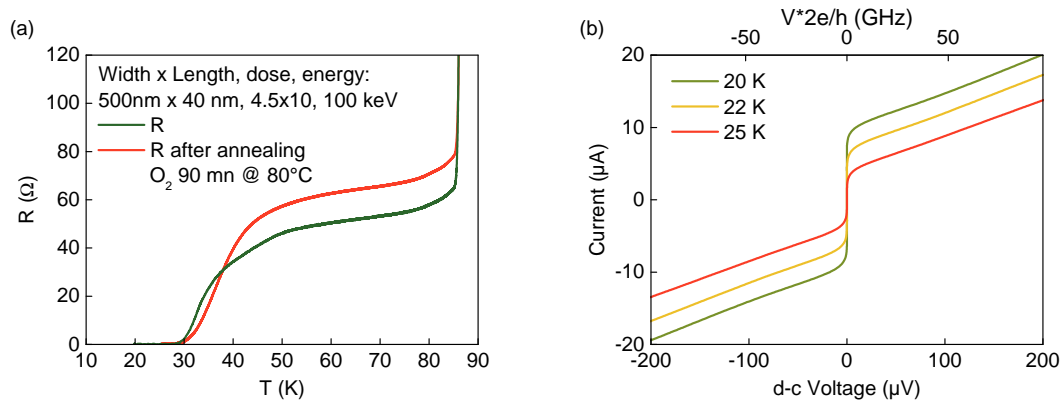


Figure 5.10: (a) RT curves before (green line) and after (red line) annealing of a 500 nm wide junctions. (b) IV curves of the junction at 20 K, 22 K and 25 K.

Nonetheless the junction's characteristics improve with oxygen annealing [171, 172], as shown by the RT curve in figure 5.10 (a), red line. The junction was placed 90 mn in an O_2 atmosphere, at 80 °C. The transition at T_j is sharper and the plateau is at higher resistance, and flatter.

Figure 5.10 (b) shows IV curves of such a junction. The transition at I_c is surprisingly round, especially for these low temperatures. Therefore it is not clear whether there is a pure Josephson effect or if there is an excess current. It should be verified with Shapiro steps, for example. Unfortunately the junctions broke after these first characterizations, and we were unable to pursue the investigation.

In any case, we expect that this 500 nm wide junction would have drifted from the behavior that we described in this chapter, as for the 750 nm wide junctions of figure 5.9. Excess current, if present, may be due to the growing importance of edge effects in the junction's transport properties: as the bridge narrows, tails in defects distributions (see figure 2.5) take more importance.

5.5 Conclusion on the d-c characterization

Let us briefly review what we have seen from the d-c and low frequency a-c measurements, and what we can infer for the high frequency mixing properties.

First, as seen in figure 5.3, the irradiated Josephson junction operates in a range of temperatures T such that $T'_c < T < T_j$. Above T_j , thermal fluctuations destroy the coupling between the two condensates, hence no supercurrent can flow across the device. Below T'_c , the S' material constituting the barrier becomes superconducting, hence the transport physics is a hybrid situation

between Josephson and flux flow. A large excess current then disables to completely modulate the Shapiro steps as a function of a r-f power drive, as shown on figure 5.5.

A corrected RSJ model, in which the normal resistance R_n varies with the current bias I accounts for the particular physics of our device. It comes from the fact that the Andreev reflection is energy dependent, hence it occurs at different positions along the junction as the bias changes. One can experimentally measure $R_n(I)$ by means of IV curves acquired under a saturating r-f excitation. The latter redistributes the supercurrent over all the frequencies, hence kills the Josephson branch. The normal resistance is then simply given by the ratio between d-c voltage and current bias. The RSJ model being modified in such manner, numerically simulated IV curves at several temperatures and r-f unsaturated excitations are in good agreement with experimental data (figure 5.8).

Above the characteristic frequency f_c , the Josephson impedance is bigger than the normal resistance R_n , hence more current flows in the latter: the non linear behavior diminishes. We therefore expect mixing performances to degrade above f_c . From the normal resistance measured at low current bias, f_c exhibits the shape of a dome as a function of temperature, figure 5.3 (c). It has an optimum of 85 GHz at 55 K. However it is a pessimistic prevision, as the normal resistance increases with the current bias. As we shall see in the following chapter, we actually managed to perform mixing operations up to several times f_c .

We improved the normal resistance R_n by diminishing the width of the junction. It is beneficial for the matching impedance issues, proper to microwave circuitry, as we are going to see in the next chapter. From 2 μm , the latest e-beam developments allow to comfortably go down to 750 nm. Hence, from a R_n of about 3 Ω at the optimum mixing points, we now can routinely obtain about 5 Ω . However the critical current diminishes accordingly, and thus it does not improve significantly the $I_c R_n$ product. Also, with narrower junctions, it is not clear whether we remain in a pure Josephson regime or not. It may be due to the effects of the irradiation, which damages the edges of the bridge. The latter being thinner, they may become important for the transport physics.

Chapter 6

Three-port model

Contents

6.1 Impedance matrix	103
6.1.1 Frequencies of interest in heterodyne detection	104
6.1.2 Definition of the mixer's impedance matrix	104
6.1.3 Terms of the impedance matrix as a function of currents and voltages	106
6.1.4 Discussion on the impedance matrix terms	107
6.2 Conversion efficiency	108
6.2.1 Definition	108
6.2.2 Mixer connected to a circuit	108
6.2.3 Conversion efficiency in terms of impedances	109
6.2.4 Numerical simulations, principle	110
6.3 Physical approach of the Josephson mixer	111
6.4 Conclusion on the three-port model	112

Heterodyne detection consists in combining an incoming (THz) *signal* radiation with a more powerful one from a (THz) *local oscillator* (LO) in the mixer. The later generates a beat-note at an *intermediate frequency* (IF), for us in the 4-8 GHz band. The LO being known, all informations on the signal (frequency and amplitude) are down-converted to the IF. This process is evaluated through the conversion efficiency η , which characterizes the performances of a detector.

In this chapter, we explain the mixing operation through a circuit model, called *three-port model*, which we will use in the next chapter to fit the mixing measurements.

The conversion efficiency directly depends on the impedance matching between the mixer and its environment. We will highlight the impedance matching terms that need to be optimized, so as to improve the detection efficiency.

After introducing the impedance matrix, we will derive the approach developed by the seminal work of Torrey and Whitmer [186] to write the coefficients of the impedance matrix in terms of currents and voltages. Then, following the pioneering work of Taur [179] we will express the conversion efficiency of a heterodyne mixer with the matrix impedance terms. This general approach will be related to the mixing with the Josephson effect by a physical explanation adapted from the work of Van Duzer [190].

6.1 Impedance matrix

We are going to use the formalism of impedance matrix of circuit theory, for which an excellent general description is given in the book of David Pozar [155]. It enables to address electronic

systems with any number of terminals, or *ports*, and hence develop equivalent circuits for any network. Electrically, the inputs and outputs of all the ports are related through the impedance and admittance matrices.

Fundamentally, one needs such an approach because the current-voltage relations at the mixer's terminals depend on the frequency, or in other words because there are several electromagnetic propagating modes, each seeing a different impedance. So far we only dealt with the normal resistance R_n , true in d-c, but we must introduce *dynamic* impedances to explain the frequency conversion.

6.1.1 Frequencies of interest in heterodyne detection

ω_s and ω_{LO} are respectively the signal and LO frequency, and $\omega_s > \omega_{LO}$. We define the IF as $\omega_{IF} = \omega_s - \omega_{LO}$. We also define the *image* frequency as $\omega_i = \omega_{LO} - \omega_{IF}$. It is the symmetric of the signal with respect to the LO frequency. The spectral band above ω_{LO} down-converted to the IF band is usually referred as the upper-side band (USB), and the one below as the lower-side band (LSB).

As we are going to show in this chapter, the Josephson mixer needs to be d-c biased to efficiently create the IF. Similarly, one can consider the LO as an r-f bias. In this frame, there are three frequencies of interest in the system driven by a LO, represented schematically in figure 6.1: signal, IF and image.

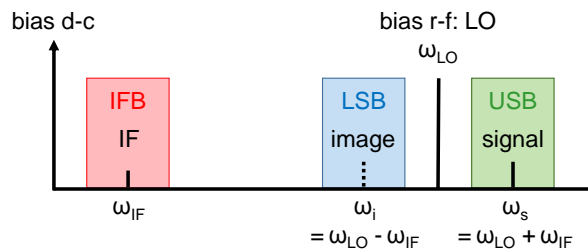


Figure 6.1: Spectral representation of the mixer operation. When biased in d-c and in r-f with a LO, it down-converts a signal at frequency ω_s to an IF at ω_{IF} . Upper-side band (USB) and lower-side band (LSB) are respectively the frequency bands above and below the LO frequency down-converted to the IF band (IFB). Their bandwidth is the same as the IFB. Then, the conversion phenomenon involves three frequencies: signal, IF, and image which is the symmetric of the signal with respect to ω_{LO} . Here we arbitrarily chose to represent the signal at the USB.

6.1.2 Definition of the mixer's impedance matrix

In the frame of the RSJ model (no capacitance), the normalized equations modeling the behavior of the Josephson junction are given by 3.30, for which there is no analytical solution. However, linearizing these equations with respect to small fluctuations and Fourier transforming them into the frequency domain, Likharev and Semenov [131] relate the Fourier transform of the voltage \tilde{v} to the one of the current \tilde{i} by:

$$\tilde{v}(\omega) = \sum_{n=-\infty}^{+\infty} z_n(\omega - n\omega_J) \tilde{i}(\omega - n\omega_J) \quad (6.1)$$

where, in the Johnson normalization $\omega_J = v_{dc}$ is the junction self-oscillation (SO), equal to the d-c voltage, and $z_n(\omega - n\omega_J)$ its normalized impedance at the frequency $\omega - n\omega_J$. When we drive the junction with a local oscillator, considered as a current source, the voltage response consists in the sum of terms $z_{n,k}(\omega - n\omega_J - k\omega_{LO}) \tilde{i}(\omega - n\omega_J - k\omega_{LO})$. Considering that the LO oscillation

is much stronger than the SO's one, we neglect all the terms for $n \neq 0$, and hence with a LO drive the response of the junction is given by:

$$\tilde{v}(\omega) = \sum_{k=-\infty}^{+\infty} z_k(\omega - k\omega_{LO})\tilde{i}(\omega - k\omega_{LO}) \quad (6.2)$$

We now illuminate the junction with a signal at frequency ω_s , such as $\omega_s > \omega_{LO}$. The mixer thus creates the IF at $\omega_{IF} = \omega_s - \omega_{LO}$ and the image at $\omega_i = \omega_{LO} - \omega_{IF}$. At those three frequencies, the voltage expressions are:

$$\begin{aligned} \tilde{v}(\omega_{LO} + \omega_{IF}) &= \sum_{k=-\infty}^{+\infty} z_k(\omega_{IF} - (k-1)\omega_{LO})\tilde{i}(\omega_{IF} - (k-1)\omega_{LO}) \\ \tilde{v}(\omega_{IF}) &= \sum_{k=-\infty}^{+\infty} z_k(\omega_{IF} - k\omega_{LO})\tilde{i}(\omega_{IF} - k\omega_{LO}) \\ \tilde{v}(\omega_{IF} - \omega_{LO}) = \tilde{v}^*(\omega_{LO} - \omega_{IF}) &= \sum_{k=-\infty}^{+\infty} z_k(\omega_{IF} - (k+1)\omega_{LO})\tilde{i}(\omega_{IF} - (k+1)\omega_{LO}) \end{aligned} \quad (6.3)$$

where we used the fact that $v \in \Re$ and a Fourier transform property to identify the image frequency. Rearranging the infinite sums we get:

$$\begin{aligned} \tilde{v}(\omega_{LO} + \omega_{IF}) &= \sum_{k=-\infty}^{+\infty} z_k^u(\omega_{IF} - k\omega_{LO})\tilde{i}(\omega_{IF} - k\omega_{LO}) \\ \tilde{v}(\omega_{IF}) &= \sum_{k=-\infty}^{+\infty} z_k^0(\omega_{IF} - k\omega_{LO})\tilde{i}(\omega_{IF} - k\omega_{LO}) \\ \tilde{v}^*(\omega_{LO} - \omega_{IF}) &= \sum_{k=-\infty}^{+\infty} z_k^l(\omega_{IF} - k\omega_{LO})\tilde{i}(\omega_{IF} - k\omega_{LO}) \end{aligned} \quad (6.4)$$

where z_k^u , z_k^0 and z_k^l are the impedances, respectively at the upper-side, IF and lower-side band. At first order, that is to say for $k = -1, 0, 1$ we have the matrix relation:

$$\begin{pmatrix} \tilde{v}(\omega_{LO} + \omega_{IF}) \\ \tilde{v}(\omega_{IF}) \\ \tilde{v}^*(\omega_{LO} - \omega_{IF}) \end{pmatrix} = \begin{bmatrix} z_{-1}^u & z_0^u & z_1^u \\ z_{-1}^0 & z_0^0 & z_1^0 \\ z_{-1}^l & z_0^l & z_1^l \end{bmatrix} \begin{pmatrix} \tilde{i}(\omega_{IF} + \omega_{LO}) \\ \tilde{i}(\omega_{IF}) \\ \tilde{i}(\omega_{IF} - \omega_{LO}) \end{pmatrix} \quad (6.5)$$

or with more classical notations:

$$\begin{pmatrix} \tilde{v}_{usb} \\ \tilde{v}_0 \\ \tilde{v}_{lsb}^* \end{pmatrix} = \begin{bmatrix} z_{uu} & z_{u0} & z_{ul} \\ z_{0u} & z_{00} & z_{0l} \\ z_{lu} & z_{l0} & z_{ll} \end{bmatrix} \begin{pmatrix} \tilde{i}_{usb} \\ \tilde{i}_0 \\ \tilde{i}_{lsb} \end{pmatrix} \quad (6.6)$$

Notice that this relation does not depend on whether the signal is at the USB and image at the LSB, or vice versa. Signal and image playing a similar role, the mixer is said to be a double side-band (DSB) receiver. In other words, both USB and LSB are down-converted to the IFB. In particular, there is twice the conversion noise than in a single-side band (SSB) receiver, where only USB or LSB is down-converted. The latter requires special schemes and filters to get rid of one of the two bands.

In a compact form, 6.6 writes as:

$$\tilde{v} = \tilde{\tilde{z}} \cdot \tilde{i} \quad (6.7)$$

\tilde{z} is the impedance matrix of the mixer, and it has the same form in dimensioned units. As in any impedance matrix, z_{ab} can be found as:

$$z_{ab} = \left. \frac{\tilde{v}_a}{\tilde{i}_b} \right|_{i_k=0 \text{ for } k \neq b} \quad (6.8)$$

which in words means that z_{ab} can be found by driving port b with the current i_b , while opening all other ports, and measuring the voltage at port a . In particular, if the off-diagonal term z_{0u} is not null, a driving current at the USB (signal in our case) generates a voltage at the IF. This is the core of the mixer principle.

The nine independent parameters of the matrix impedance fully characterize the first order mixing operations. They can be reduced to only five independent parameters when assuming that the mixer does not display any sharp resonance neither at the USB nor at the LSB, so that it does not discriminate the two bands, which are close together [186]. This assumption is valid in most practical cases, as in ours, and the symmetry between signal and image allows to write:

$$z_{ll} = z_{uu}^*, z_{0l} = z_{0u}, z_{ul} = z_{lu}^*, z_{l0} = z_{u0}^* \quad (6.9)$$

6.1.3 Terms of the impedance matrix as a function of currents and voltages

In the following discussion, when we speak of currents and voltages at a given frequency, strictly speaking it refers to the Fourier transform of the current and voltage at this frequency. But for better clarity in the notations, from now on we omit the " \sim " when the reference to a Fourier transform is obvious.

We derive expressions of the impedance matrix coefficients as a function of the d-c and LO, current and voltage. In a dual manner, Torrey [186] analyzes the mixer from the point of view of the admittance matrix. We detail in appendix F the calculations leading to the analytical expressions 6.13. The latter are almost similar to what Taur finds [179] (there is a small difference in the image conversion term and in constant coefficients, which make our analytical expressions consistent with the Van Duzer approach, see section 6.3).

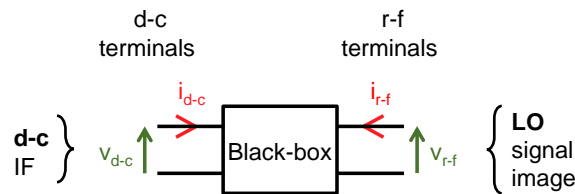


Figure 6.2: The mixer considered in circuit theory as a black-box with four ports: two for the d-c current and voltage, and two for the r-f current and voltage. As the LO is much stronger than any other power at r-f frequencies, one can consider that $i_{r-f} = i_{LO}$, and $v_{r-f} = v_{LO}$.

A mixer such as the one described above can be considered as a black-box with two kinds of terminals, as represented in figure 6.2: (i) d-c terminals, from which one sends or measures a current i_{dc} or a voltage v_{dc} , and (ii) r-f terminals from which one sends or measures a current i_{rf} or a voltage v_{rf} . Considering that the IF is much lower than the characteristic frequency, it is put at the d-c terminals. The LO is much stronger than any other r-f frequency, a good approximation is to say that $v_{rf} = v_{LO}$ and $i_{rf} = i_{LO}$. In the current source model, we shall describe the d-c voltage as depending on the d-c and LO current:

$$v_{dc} = v_{dc}(i_{dc}, i_{LO}) \quad (6.10)$$

and since we do not choose a particular time origin, $i_{LO} \in \mathbb{C}$ a priori, whereas we always have $v_{dc}, i_{dc} \in \mathfrak{R}$ since in d-c. Similarly one describes the LO voltage as:

$$v_{LO} = z_{LO}(i_{dc}, i_{LO})i_{LO} \quad (6.11)$$

where z_{LO} is the mixer impedance at ω_{LO} .

Now, the essential idea of this black-box theory is the following: small variations of signal and image currents and voltages only affect the r-f terminals; while similarly, small variations of IF current and voltage only affect the d-c terminals. It writes as:

$$\begin{aligned} di_{dc} &= \Re(i_0 e^{j\omega_{IF}t}) \\ dv_{dc} &= \Re(v_0 e^{j\omega_{IF}t}) \\ di_{LO} &= i_{usb} e^{j\omega_{IF}t} + i_{lsb} e^{-j\omega_{IF}t} \\ dv_{LO} &= v_{usb} e^{j\omega_{IF}t} + v_{lsb} e^{-j\omega_{IF}t} \end{aligned} \quad (6.12)$$

It may be interpreted as boundary conditions for the system: as $\omega_s \rightarrow \omega_{LO}$, LO variations equal the signal and image amplitudes, and similarly d-c variations equal the IF amplitude. Differentiating the complex-valued equations 6.10 and 6.11, and replacing the differentials by relations 6.12 leads to the following expressions for the voltage at the frequencies of interest (see appendix F):

$$\begin{aligned} v_{usb} &= \frac{1}{2} \frac{\partial v_{lo}}{\partial i_{dc}} i_0 + \left(\frac{v_{lo}}{i_{lo}} + \frac{\partial v_{lo}}{\partial i_{lo}} \right) i_u + \frac{\partial v_{lo}}{\partial i_{lo}} i_u^* \\ v_0 &= \frac{\partial v_{dc}}{\partial i_{dc}} i_0 + 2 \frac{\partial v_{dc}}{\partial i_{LO}} i_u + 2 \frac{\partial v_{dc}}{\partial i_{LO}} i_l^* \\ v_{lsb}^* &= \frac{1}{2} \left(\frac{\partial v_{lo}}{\partial i_{dc}} \right)^* i_0 + \left(\frac{v_{lo}}{i_{lo}} + \frac{\partial v_{lo}}{\partial i_{lo}} \right)^* i_l^* + \left(\frac{\partial v_{lo}}{\partial i_{lo}} \right)^* i_u \end{aligned} \quad (6.13)$$

so that the matrix impedance writes as:

$$\tilde{z} \equiv \begin{bmatrix} z_{uu} & z_{u0} & z_{ul} \\ z_{0u} & z_{00} & z_{0l} \\ z_{lu} & z_{l0} & z_{ll} \end{bmatrix} = \begin{bmatrix} \frac{v_{lo}}{i_{lo}} + \frac{\partial v_{lo}}{\partial i_{lo}} & \frac{1}{2} \frac{\partial v_{lo}}{\partial i_{dc}} & \frac{\partial v_{lo}}{\partial i_{lo}} \\ 2 \frac{\partial v_{dc}}{\partial i_{lo}} & \frac{\partial v_{dc}}{\partial i_{dc}} & 2 \frac{\partial v_{dc}}{\partial i_{lo}} \\ \left(\frac{\partial v_{lo}}{\partial i_{lo}} \right)^* & \frac{1}{2} \left(\frac{\partial v_{lo}}{\partial i_{dc}} \right)^* & \left(\frac{v_{lo}}{i_{lo}} + \frac{\partial v_{lo}}{\partial i_{lo}} \right)^* \end{bmatrix} \quad (6.14)$$

6.1.4 Discussion on the impedance matrix terms

In the impedances present in the matrix, note first that all of them imply either a variation of d-c or LO voltages with d-c or LO currents. The latter are triggered by the signal. In other words, the signal perturbs the LO and d-c current, which creates harmonics at the USB, LSB and IF.

- $z_{0u} = 2 \frac{\partial v_{dc}}{\partial i_{lo}}$. As already mentioned, it is the *down-conversion* impedance, from which a signal current at the USB induces a voltage at the IF. It directly depends on the variation of the d-c voltage as a function of LO current. Hence we understand why the conversion efficiency is null at the Shapiro steps: the SO being fixed by the synchronization with the LO frequency, the d-c voltage does not vary with the LO current variation. We will see in section 7.2.4 that it actually drives the whole shape of the conversion efficiency, observed experimentally on the curves 7.3. Besides, the expression does not forbid to have $z_{0u} > 1$ and hence obtain intrinsic conversion gain. Note finally that $z_{0u} \in \mathfrak{R}$ (which comes from the time origin taken such as $i_{lo} \in \mathfrak{R}$, see appendix F).

- $z_{00} = \frac{\partial v_{dc}}{\partial i_{dc}}$. It is the *d-c dynamic* impedance, or in other words the local derivative of the *IV* curve. It is junction's impedance at the IF frequency. For an optimization perspective it is the impedance at which the IF reading line should be matched, and it depends on the d-c polarization point. Note that $z_{00} \in \Re$.
- $z_{uu} = \frac{v_{lo}}{i_{lo}} + \frac{\partial v_{lo}}{\partial i_{lo}}$ is the *r-f dynamic* impedance. It is the impedance of the mixer at the signal frequency, at which the antenna should be matched. But the situation can be delicate to address since $z_{uu} \in \mathbb{C}$.
- $z_{u0} = \frac{1}{2} \frac{\partial v_{lo}}{\partial i_{dc}}$ is the *up-conversion* impedance, through which the IFB is up-converted to the USB. Not very relevant for the mixer.
- $z_{ul} = \frac{\partial v_{lo}}{\partial i_{lo}}$ is the *image conversion* impedance, through which the image (at the LSB) is converted into the signal (at the USB). Not very relevant for the mixer.

6.2 Conversion efficiency

6.2.1 Definition

In the frame of heterodyne detection, the conversion efficiency is the ratio of the output power to the available input power of the sensor:

$$\eta = \frac{P_{out}}{P_{in}^{max}} \quad (6.15)$$

The higher it is, the better is the detector. In most cases the conversion is lossy and $\eta \leq 1$, but in heterodyne mixing, it is in principle possible to exploit the pump power such that $\eta > 1$, i.e. obtain conversion gain.

6.2.2 Mixer connected to a circuit

So far we modeled the Josephson junction as an isolated mixer, but in order to compute the conversion efficiency η , we now need to connect it with the antenna and the r-f line, as described in section 7.1.3. We then define the *external* impedances matrix $\tilde{\tilde{z}}_{ext}$, such that:

$$\tilde{\tilde{z}}_{ext} = \begin{bmatrix} z_u & 0 & 0 \\ 0 & z_0 & 0 \\ 0 & 0 & z_l \end{bmatrix} \quad (6.16)$$

Here, z_u and z_l represent the impedance of the spiral antenna ($\simeq 80 \Omega$) at the USB and LSB, respectively, and taken to be identical. z_0 is the 50Ω impedance of the IF microwave readout line. Assuming that the signal V_s incoming on the antenna is from the USB, figure 6.3 represents the mixer connected to the external circuitry. Note that all internal connections are not represented: the off-diagonal terms of $\tilde{\tilde{z}}$, which enable the energy transfer between the different frequencies do not explicitly appear as impedances. But it shows that one can express the available signal power at the USB port as:

$$P_{in} = \frac{1}{2} \Re(z_u) i_{usb}^2 = \frac{1}{2} \frac{\Re(z_u)}{|z_u + z_{uu}|^2} v_s^2 \quad (6.17)$$

which is maximal when $z_u = z_{uu}^*$. Then P_{in}^{max} is given by:

$$P_{in}^{max} = \frac{1}{8} \frac{v_s^2}{\Re(z_u)} \quad (6.18)$$

At the IF port, the output available power is given by:

$$P_{out} = \frac{1}{2} \Re(z_0) i_0^2 \quad (6.19)$$

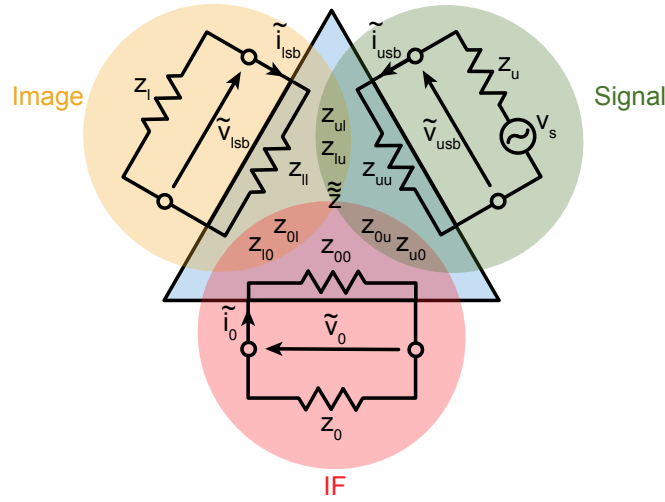


Figure 6.3: Schematic vision of the mixer (blue triangle) connected to the external circuitry, once d-c and LO biased. The signal is taken at the USB. Depending on the frequency, different load impedances are presented at the mixer terminals: z_u , z_0 and z_l respectively at the USB, IFB and LSB. The diagonal terms of the impedance matrix 6.14 can be viewed as impedances directly connected to the external ones, whereas the off-diagonal ones enable energy transfers between the three frequency bands.

Now, one needs to relate v_s and i_0 . To that end, we write the equation for the whole circuit shown in figure 6.3 as:

$$\begin{pmatrix} \tilde{v}_{usb} \\ \tilde{v}_0 \\ \tilde{v}_{lsb}^* \end{pmatrix} + \begin{bmatrix} z_u & 0 & 0 \\ 0 & z_0 & 0 \\ 0 & 0 & z_l \end{bmatrix} \begin{pmatrix} \tilde{i}_{usb} \\ \tilde{i}_0 \\ \tilde{i}_{lsb} \end{pmatrix} = \begin{pmatrix} \tilde{v}_s \\ 0 \\ 0 \end{pmatrix} \quad (6.20)$$

We therefore obtain a relation between the currents at different frequencies and the input signal:

$$\begin{pmatrix} \tilde{i}_{usb} \\ \tilde{i}_0 \\ \tilde{i}_{lsb} \end{pmatrix} = \tilde{y} \begin{pmatrix} \tilde{v}_s \\ 0 \\ 0 \end{pmatrix} \quad (6.21)$$

where $\tilde{y} = (\tilde{z} + \tilde{z}_{ext})^{-1}$ is the total admittance matrix. With coefficient notations similar to \tilde{z} we therefore get:

$$\tilde{i}_0 = y_{0u} \tilde{v}_s \quad (6.22)$$

Thus, the conversion efficiency η , defined by the ratio of the output power at the IF to the maximum input power at the signal frequency is given by [179]:

$$\eta = \frac{P_{out}}{P_{in}^{max}} = 4 \Re(z_0) \Re(z_u) |y_{0u}|^2 \quad (6.23)$$

6.2.3 Conversion efficiency in terms of impedances

In equation 6.23, η writes itself with a term of the total admittance matrix. But we can also express it with impedance matrix terms, by analytically inverting \tilde{y} (detailed in appendix G). In fact, in the

limit — well satisfied experimentally — where $|z_{ul}|$, $|z_{u0}| \ll |z_u + z_{uu}|$, and $|z_{0u}| \ll |z_0 + z_{00}|$, the conversion efficiency takes the simple form:

$$\eta = 4 \frac{\Re(z_0)}{|z_0 + z_{00}|^2} \frac{\Re(z_u)}{|z_u + z_{uu}|^2} z_{0u}^2 \quad (6.24)$$

The first two factors correspond to the matching impedance conditions at the USB and IF frequencies. The conversion is optimal when the antenna impedance z_u matches the r-f impedance of the junction z_{uu} and when the readout line impedance z_0 matches the d-c dynamic impedance of the junction z_{00} . The last factor z_{0u} represents the ability of the junction to down convert the signal at the USB to the intermediate frequency.

We can finally express η_m , the conversion efficiency when input and output impedances are matched. We will see in section 6.3 that we can find the exact same expression from a physical analysis of the Josephson mixer. When impedances are matched we have:

$$\begin{cases} z_0 = z_{00}^* \\ z_u = z_{uu}^* \end{cases} \quad (6.25)$$

equation 6.24 writes as:

$$\eta_m = \frac{1}{4} \frac{z_{0u}^2}{\Re(z_0)\Re(z_u)} \quad (6.26)$$

Now, using the expression of z_{0u} in terms of partial derivatives, found in section 6.1.3 (equation 6.14), and the fact that $\Re(z_0) = \frac{\partial v_{dc}}{\partial i_{dc}}$ (for matched impedances) we can write:

$$\eta_m = \frac{R_d}{R_s} \left(\frac{\partial i_{dc}}{\partial i_{lo}} \right)^2 \quad (6.27)$$

where $\Re(z_0) = R_d$ is the d-c dynamic impedance and $\Re(z_u) = R_s$ the signal impedance. R_d vanishing at each Shapiro step, expression 6.27 explains why the conversion efficiency drops accordingly [163].

6.2.4 Numerical simulations, principle

For a given current bias, we first need to compute the impedance matrix $\tilde{\xi}$. It is done by solving the RSJ equations in the time domain, and then by taking the Fourier transform of the total current and voltage at the frequencies of interest. Note that we take into account the non linearity of the normal resistance with current bias $R_n(I_{dc})$ along with the noise, introduced as a current source δI_n in the RSJ equations, so that the system being solved resembles equations 5.12.

More precisely, there are two ways to find $\tilde{\xi}$. Either we form the voltage to current ratios according to equation 6.8, as done by Schoelkopf [163]. Recalling the symmetric relations (equations 6.9), it is sufficient to compute the first two columns of $\tilde{\xi}$. Then one solves the system 5.12 twice (where the LO is already present), one with an extra signal at the USB (and no IF signal nor image) to compute the first column and one with an extra IF signal (and no USB signal nor image) to compute the second column. Even though this approach may be justified by the small signal hypothesis, it seems that it nonetheless infers an IF signal amplitude prior to the calculation of the conversion efficiency. Therefore, the qualitative form of η as a function of d-c current bias may be correctly found but it is not possible to compare the values of η from different signal frequencies.

The other option is to solve the RSJ equations 5.12 for the all couple of parameters ($i_{dc} \pm di_{dc}, i_{lo} \pm di_{lo}$), to take the resulting Fourier transform of voltages and currents at d-c and LO frequency, and finally to compute the impedance matrix terms according to equation 6.14. Note that no value of IF comes into play when solving the system, nor any signal amplitude. Thus

it is also numerically more stable than the first method. It requires more computation power, but nowadays computers are powerful enough, and it seems more appropriate to compare the calculated η with experimental data. Consequently we adopted this strategy.

Once \tilde{z} has been computed for any current bias, varying so as to describe an entire IV curve, one can compute the conversion efficiency η either by brute-force inversion of $\tilde{z} + \tilde{z}_{ext}$, or directly from equation 6.24. One then accesses to y_{ou} and compute η according to equation 6.23. We verified that both ways give the same results, therefore validating the simpler relation 6.24.

We employed such a method to simulate the mixer's response, and will show in the next chapter, section 7.2.4, that it fits experimental data at various operating frequencies.

6.3 Physical approach of the Josephson mixer

The description that we gave is applicable to any mixer d-c and LO biased. In the particular case of a Josephson junction, one can derive the expression of the matched conversion efficiency η_m by considering the effect of a LO and a signal on the IV curve, as treated by Van Duzer [190].

Figure 6.4 summarizes the situation. The role of the LO is double: (i) it modulates the d-c

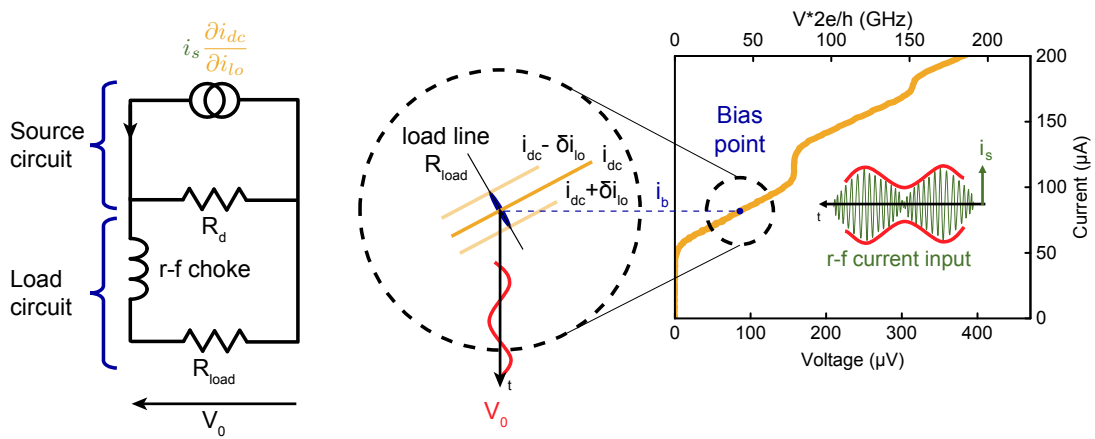


Figure 6.4: Effect of the LO on the IV curve of a Josephson junction, and equivalent circuit at the IFB.

current bias i_b at frequency ω_{LO} . Thus, at a given time t , the IV curve is actually above or below its mean d-c value, which we could see if we had a fast enough electronics. (ii) it beats with the signal, so that the r-f current sent onto the junction has a slow varying envelope, at the IF frequency, transferred to the resulting voltage.

Consequently, the equivalent IF generator is an ideal current source, whose value is the product of the signal amplitude with the d-c current variation, and it has an internal impedance R_d . The IF voltage is then given by:

$$V_0 = \frac{1}{2} R_d i_s \frac{\partial i_{dc}}{\partial i_{lo}} \quad (6.28)$$

When connected to a matched load R_{load} at the IFB, the transmitted power writes as:

$$P_0 = \frac{V_0^2}{2R_d} = \frac{1}{8} R_d i_s^2 \left(\frac{\partial i_{dc}}{\partial i_{lo}} \right)^2 \quad (6.29)$$

Thus, recalling that the input power is given by equation 6.18, the maximum conversion efficiency $\eta_m = \frac{P_0}{P_{in}^{max}}$ writes with exactly the same form than equation 6.27.

In the simplified vision where the mixer's impedance at LO frequency equals the static impedance R_n , we can give a useful order of magnitude for η_m . In fact, according to equation 5.8, the LO

modulates the critical current following a Bessel function. Then, $I_c = 0$ the first time when

$$\frac{2eV_{LO}}{\hbar\omega_{LO}} \simeq 1$$

i.e. $\Delta I_c = I_c$ for $\Delta V_{LO} = \frac{\hbar\omega_{LO}}{2e}$. It corresponds to

$$\Delta I_{LO} \simeq \frac{\Delta V_{LO}}{R_n} = \frac{\hbar\omega_{LO}}{2eR_n} = I_c \frac{f_{LO}}{f_c}$$

where $f_c = 2eI_cR_n/h$ is the characteristic frequency. Taking the ratio of ΔI_{LO} to ΔI_c , η_m therefore writes as:

$$\eta_m = \frac{R_d}{R_s} \left(\frac{f_c}{f_{LO}} \right)^2 \quad (6.30)$$

From this expression, we see that it is desirable to fabricate junctions with high f_c values, i.e., high I_cR_n products.

6.4 Conclusion on the three-port model

When the mixer is connected to the antenna on one side and to the r-f reading line on the other side, the conversion efficiency η is given in its most general form by equation 6.23. It involves a term of the total admittance matrix \tilde{y} , sum inverted of the *internal* and *external* matrices of the system, \tilde{z} and \tilde{z}_{ext} respectively. Relation 6.14 gives the coefficients in \tilde{z} , found from a black-box approach. \tilde{z}_{ext} writes itself according to equation 6.16.

Now, the analytical inversion of $\tilde{z} + \tilde{z}_{ext}$ allows to write equation 6.24, at the expense of hypothesis well verified in practice. It is a simple expression for η , function of impedances only.

When the mixer is matched at the input and output, η in turn simplifies into η_m , expression 6.27. We can find the exact same form with an other approach, based on a circuit analysis.

Finally, we can give an order of magnitude for η_m if we assume that the impedance of the mixer at the LO frequency equals the static impedance R_n , equation 6.30. Then it is directly proportional to the squared ratio of the LO frequency to the characteristic frequency. We consequently understand how the performances of the Josephson mixer degrade as the excitation frequency increases.

We used a general model for the mixer, the three-port model, to explicit the conversion efficiency η as a product of three terms (equation 6.24): two of them underline the importance of impedance matching at the input (signal) and output (IF) frequencies, and the third one characterizes the junction's intrinsic sensitivity to a signal perturbation. In addition, the three-port model is consistent with a more phenomenological approach from which derives η_m , the conversion efficiency when the external circuitry is matched (equation 6.27). It depends directly on the dynamic resistance R_d , i.e. the one of the junction at the IF, which therefore should be maximized. A rough estimation of η_m leads to equation 6.30, where the optimum conversion efficiency is expressed as the ratio of the characteristic frequency f_c to the LO frequency f_{LO} . We therefore understand why we should have f_c as high as possible.

Chapter 7

High frequency mixing properties of the Josephson mixer

Contents

7.1 Experimental setup	113
7.1.1 Test bench	113
7.1.2 Microwave design and r-f reading line	115
7.1.3 Conversion efficiency in the experimental setup	117
7.2 Heterodyne detection of high frequencies	118
7.2.1 Modulation of the intermediate frequency power	119
7.2.2 Dynamic range	120
7.2.3 Influence of the LO power	122
7.2.4 Conversion efficiency simulations	123
7.2.5 Mixing beyond 140 GHz	124
7.3 Conclusion on the high-frequency mixing measurements	124

Arriving at the core of this thesis, we present in this chapter the results of the high frequency mixing experiments that we performed on a high- T_c superconducting Josephson mixer. As a first attempt to prove the possibility to detect a broad range of frequencies, we first tested a broadband system, and we managed to detect signals from 20 to 400 GHz with the same device. The results are presented in section 7.2.1. We investigated the range over which the detector's response is linear in section 7.2.2, and the influence of LO power on the conversion efficiency in section 7.2.3. Then in section 7.2.4, we used the three-port model, exposed in the previous chapter, to simulate and fit the conversion efficiency of the detector, up to 140 GHz. It is qualitatively in agreement with what was found for low- T_c Josephson mixers by Schoelkopf and collaborators[163]. Beyond 140 GHz, the mixing operation deviates from a pure Josephson effect.

7.1 Experimental setup

7.1.1 Test bench

The experimental setup is depicted in figure 7.1. The fabricated chip usually contains six Josephson junctions (JJ), each at the center of a spiral antenna, embedded in a coplanar waveguide (CPW) transmission line. Each one is independently d-c biased with a current source (Yokogawa 7651) and a voltmeter (Keithley 2700) reads the d-c voltage through a four-point measurement method.

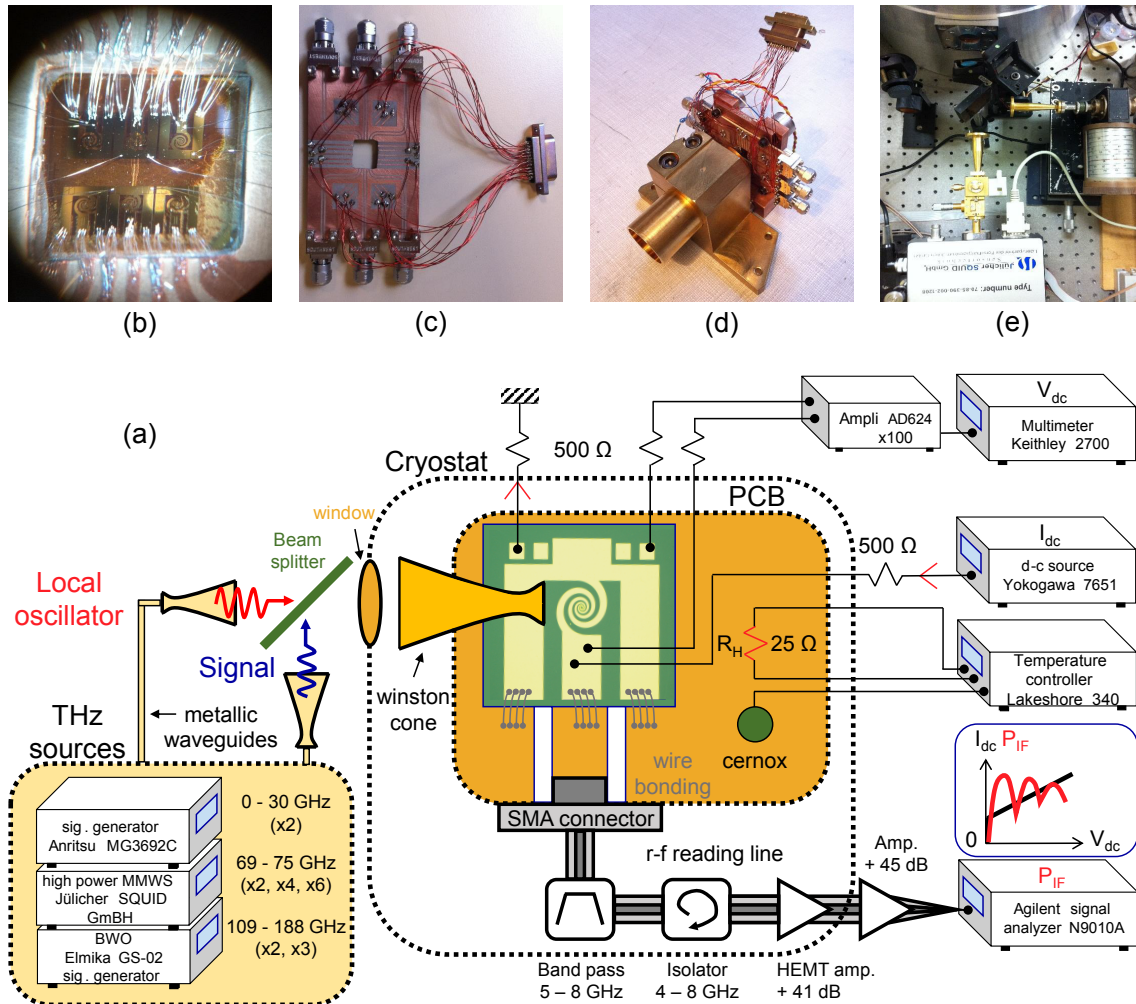


Figure 7.1: (a) Schematic of the experimental setup to test heterodyne detection of the Josephson mixer. Junction is embedded in a spiral antenna at the center of a CPW transmission line. It is d-c biased and the microwave line reads the intermediate frequency between 4 and 8 GHz. LO and the signal are sent from outside the cryostat through a window (mylar $50 \mu\text{m}$), guided through a quasi-optic setup onto the antenna. (b) Picture of the electronic chip, wire-bonded in d-c and in r-f onto the PCB. Many wires are required to connect the r-f line, in order to minimize their inductive effect. (c) Photograph of the homemade PCB. (d) Photograph of the whole cryogenic quasi-optic system: PCB and chip are glued to a copper plate and placed in front of the Winston cone. The whole mount is then placed on the 4 K stage of the cryostat, the copper plate being thermally decoupled. (e) Picture of the local oscillator and signal sources, placed in front of the cryostat window and coupled with a beam splitter.

The CPW lines and d-c polarization pads are wire-bonded (Al wires, 25 μm , photo 7.1 (b)) to a homemade printed circuit board (PCB, photo 7.1 (c)), fabricated from a high frequency laminate, designed for cryogenic use (double-sided dielectric, bought from the Rogers Corporation, type RO3010-1ED/1ED-0500, total thickness 1.20 mm, Cu thickness 35 μm , $\epsilon_r = 11.20$ [11]). The latter is then glued with a general electric varnish to a copper plate, on which the temperature regulation (heating resistance and cernox thermometer) is also fixed. Then, the mixer under study is placed at the focal point of a Winston cone (photo 7.1 (d)), facing the cryostat window (behind an infrared filter). Alternatively, one can also collimate the incoming radiations with a silicon hyper-hemispheric lens, glued on the sapphire substrate and located at the focal point of a parabolic mirror (not shown in the present sketch).

In any case (Winston cone or lens), the quasi-optical setup collects local oscillator and signal powers, combined in front of the window through a beam splitter. Mixing experiments were performed in five different frequency ranges centered on 20, 70, 140, 280, and 420 GHz. At 20 GHz, signals are provided by microwave generators (Anritsu MG3692C); whereas for higher frequencies, signals are provided either by a Gunn diodes (MMWS Jüglicher SQUID) or by a backward wave oscillator (BWO, Elmika GS-02). All can independently be coupled to a set of frequency doublers and triplers, guided through the multiplication chain by metallic waveguides and coupled to free space by horn antennae (photo 7.1 (d)).

7.1.2 Microwave design and r-f reading line

The LO and signal traveling in free space are coupled to the Josephson mixer (JM) through a spiral antenna. At the output, IF travels from the JM to the electrical spectrum analyzer (EXA, Agilent N9010A) through CPW lines first, and then dielectric waveguides, as represented in figure 7.1 (a). Here, we briefly detail each stage of this path.

7.1.2.1 Antenna

In order to have the same device working over a large range of frequencies, we used a planar spiral antenna. In fact it belongs to the so-called *frequency independent antennas*, first introduced in the 1950s by Rumsey [161], according to which when the shape of an antenna is only specified by angles, (and when the antenna itself is infinite), its performances (input impedance, radiation pattern, gain, polarization) are independent of frequency. In practice of course we don't have an infinite structure; it limits the range of frequencies in which the characteristics are flat.

More precisely, a spiral antenna is defined by three parameters [70]: an angle δ , an expansion rate a , and an initial radius k , such that one arm extends between two curves:

$$\begin{cases} \rho_1(\theta) = ke^{a\theta} \\ \rho_2(\theta) = ke^{a(\theta-\delta)} \end{cases} \quad (7.1)$$

Thus, the edges of the conductor are formed by the same curve, rotated by an angle δ . The second arm is obtained with ρ_1 and ρ_2 , rotated by an angle of π . We took $a = 0.2 \text{ rad}^{-1}$, $k = 8 \mu\text{m}$, and $\delta = \pi/2$ therefore the antenna is said to be *self-complementary* i.e. conductor and insulator have the same geometry. Some studies [128, 180] suggest that with $a = 0.5 \text{ rad}^{-1}$ and $\delta = 4/3$ the performances are the most frequency independent, but overall, they remain flat when varying those parameters [70], and furthermore it is not of crucial importance in our study.

The impedance of an planar antenna is calculated by considering a generalized version of Babinet's principle, introduced by Booker, that takes into account polarization and conducting screens [24], from which one can show that:

$$Z_a Z_c = \frac{\eta^2}{4} \quad (7.2)$$

where Z_a is the antenna's impedance, Z_c the impedance of the complementary structure, and $\eta = \sqrt{\mu_0/\epsilon}$ is the (non magnetic) medium intrinsic impedance. In our case the antenna can be considered of being at the interface between the vacuum and sapphire substrate, with a relative dielectric constant $\epsilon_r = 10$, therefore:

$$\epsilon = \epsilon_0 \epsilon_{reff} = \epsilon_0 \frac{\epsilon_r + 1}{2} \quad (7.3)$$

is a good approximation. For a self-complementary antenna, $Z_c = Z_a$, and we get:

$$Z_a = \frac{\eta_0}{2} \sqrt{\frac{2}{\epsilon_r + 1}} \simeq 80 \Omega \quad (7.4)$$

where $\eta_0 = \sqrt{\frac{\mu_0}{\epsilon_0}} \simeq 377 \Omega$ is the vacuum impedance. Z_a will play a major role when studying the conversion efficiency of the whole detector (see 6.2).

The inner ρ_{min} and outer radius ρ_{max} of the spiral define the upper and lower frequency respectively, between which performances are constant. A good rule of thumb for spirals with a small expansion rate a is to say that $\lambda = 2\pi\rho$ [199]. In our case we then chose:

$$\begin{cases} \rho_{min} = 8 \mu\text{m} \Leftrightarrow f_{max} = 6 \text{ THz} \\ \rho_{max} = 550 \mu\text{m} \Leftrightarrow f_{min} = 87 \text{ GHz} \end{cases} \quad (7.5)$$

Even though it is not perfectly designed for frequencies lower than 87 GHz, electromagnetic simulations show that its input impedance remains approximately constant at lower frequencies [199]. Nevertheless, when we will optimize the detector (see section 8.2), a detailed study of the antenna response will be carried out.

Finally let us mention that the radiated field of a spiral antenna is in principle circularly polarized between f_{min} and f_{max} , and that the radiation pattern in vacuum is a single lobe [70].

7.1.2.2 CPW lines

The antenna is embedded in a CPW transmission line, whose geometry designed in order to have a characteristic impedance of 50 Ω at 6 GHz, about the value of the IF.

Quasi-static approximation. The CPW design stems from formulas, that are true within the frame of quasi-static (QS) approximation. The latter is the limit where circuit dimensions are small compared to the relative wavelength, so that the phase delay of the propagating electromagnetic field from one point of the circuit to another is negligible. In addition, the fields in the dielectrics can be considered as transverse electromagnetic (TEM), i.e. longitudinal components are negligible. As a consequence, it is possible to define a unique potential and current at any point of the circuit, with interconnections treated as passive or active lumped elements [155].

The QS approximation is valid because the wavelength λ of the propagating field in our devices is given at first order by:

$$\lambda = \frac{c}{f\sqrt{\epsilon_{reff}}} = \frac{c}{f} \sqrt{\frac{2}{\epsilon_r + 1}} \simeq 21 \text{ mm @ 6 GHz} \equiv \text{IF} \quad (7.6)$$

which is much larger than the total dimension of the detector, of about 2x2.5 mm. At $f = 50$ GHz, equation 7.6 shows that $\lambda \simeq 2.5$ mm, therefore it is a frequency starting from which one should perform a full-wave analysis for design considerations, i.e. solve completely Maxwell's equations. It is numerically more heavy, but dedicated softwares such as HFSS or Comsol have been developed over the past twenty years, giving trustworthy results.

CPW design. Design formulas can be found in the book of Garg, Gupta et al. [80]. When using the setup where the lens is glued to the back of the sapphire substrate, we are in a situation of a CPW on top of a dielectric with a finite thickness. With PCB and Winston cone, the electronic chip is glued to a grounded copper plate and we are in the situation of a conductor-backed CPW. The QS formulas used to compute the impedance of these two different situations are reported in appendix E. For the same geometry, the backed ground plane lowers the impedance.

Having a substrate thickness $t = 500 \mu\text{m}$ (Al_2O_3 , $\epsilon_r = 10$), and an antenna whose diameter is about 1 mm, we need sufficiently large CPW transmission lines, with a characteristic impedance $Z_c = 50 \Omega$. We therefore chose to have lines with width $L_{CPW} = 500 \mu\text{m}$, separated by $S_{CPW} = 350 \mu\text{m}$ (hence $2a = 500 \mu\text{m}$ and $2b = 1200 \mu\text{m}$, in figure E.1 of appendix E). With the same parameters, in the backed ground plane situations Z_c lowers to about 33Ω , which is actually an advantage when dealing with Josephson junctions of a few Ω (see 8.2.2).

On the PCB, the conductor-backed CPW lines need to be narrow enough in order to connect each of the 6 detectors on the chip. However, the fabrication process of PCB limits the resolution down to about $150 \mu\text{m}$. Taking a dielectric constant of 10.5 [11], we chose $L_{CPW} = 800 \mu\text{m}$ and $S_{CPW} = 480 \mu\text{m}$. We verified the good transmission of the line between 4 and 8 GHz with a vector network analyzer.

Then, we wire-bond the CPW lines of the chip to those on the PCB, as shown on picture 7.1 (b). It has to be done with several wires in parallel on each line (typically 10) in order to reduce their inductive effect (about 1 nH/mm), and ensure that the majority of the r-f signal goes to the CPW line and not to d-c wires.

7.1.2.3 Dielectric microwave line

SMA connectors (Southwest microwave) placed on the PCB link the CPW to the dielectric transmission line. A cryogenic HEMT amplifier (Low Noise Factory) operating in the 4-8 GHz band amplifies the output signal at the intermediate frequency before further amplification at room temperature. An isolator and a band-pass are placed in the chain to minimize the back-action of the amplifier on the Josephson mixer. Finally, IF is read on an electrical spectrum analyzer (Agilent N9010A).

7.1.3 Conversion efficiency in the experimental setup

As defined in the previous chapter, the conversion efficiency of a sensor η is the ratio of the output power to the available input power. In the frame of heterodyne detection, its definition is then given by:

$$\eta = \frac{P_{IF}}{P_s} \quad (7.7)$$

where P_{IF} and P_s are the intermediate frequency and signal power, respectively. But it can refer to the system in full or in part. In fact P_s can be the available signal power radiated by the source, i.e. at the entrance of the quasi-optical setup, the power effectively arriving onto the antenna, or even the available power at the input of the Josephson mixer. Similarly, P_{IF} can be interpreted as the generated IF power by the junction, as the power at the entrance of the r-f reading line, or even as the power arriving at the electrical spectrum analyzer.

As a definition, we chose η as the ratio of the signal power arriving onto the antenna to the IF power coming out of the PCB. Thus, it comprises the quality of the impedance matching between the antenna and the junction, as well as between the junction and the CPW lines. It doesn't incorporate the quality of the quasi-optical setup, because we did not possess a reliable THz power-meter.

More precisely, the available power at the different stages of the system is summarized in figure 7.2. Γ are power losses, and G_{rf} is the power amplification of the r-f line. At the entrance,

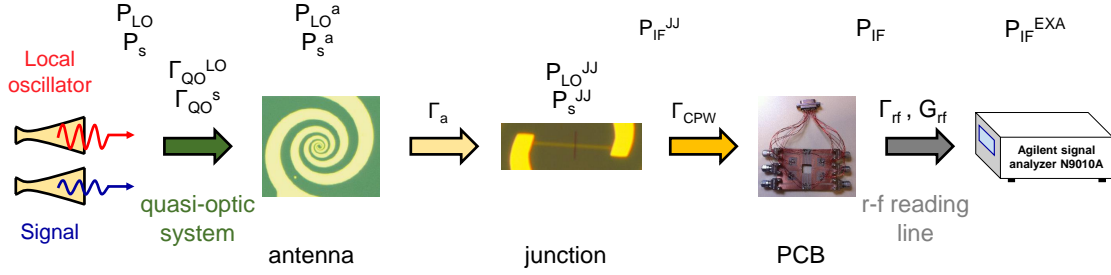


Figure 7.2: Representation of power losses (Γ_{QO}^{LO} , Γ_{QO}^S , Γ_a , Γ_{CPW} , Γ_{rf}) and gain (G_{rf}) in the heterodyne mixing setup.

the available LO and signal power are P_{LO} and P_s , respectively. They undergo power losses Γ_{QO}^{LO} and Γ_{QO}^S in the quasi-optic system. Then the impedance mismatch between the antenna and the junction induces power losses Γ_a . Following, the mixer down-converts the signal with an *intrinsic* efficiency η_{JJ} and the IF is transmitted to the r-f reading line with losses Γ_{CPW} . Finally the r-f line, with intrinsic losses Γ_{rf} and amplification G_{rf} delivers the IF power to the electrical spectrum analyzer. The power relations are summarized in table 7.1.

Quasi-optic system	Antenna	Josephson junction	r-f line	Spectrum analyzer
$\begin{cases} P_{LO}^a = P_{LO}\Gamma_{QO}^{LO} \\ P_s^a = P_s\Gamma_{QO}^S \end{cases}$	$\begin{cases} P_{LO}^{JJ} = P_{LO}^a\Gamma_a \\ P_s^{JJ} = P_s^a\Gamma_a \end{cases}$	$P_{IF}^{JJ} = \eta_{JJ}P_s^{JJ}$	$P_{IF} = \Gamma_{CPW}P_{IF}^{JJ}$	$P_{IF}^{EXA} = G_{rf}\Gamma_{rf}P_{IF}$

Table 7.1: Losses and gain in the heterodyne mixing process.

We define the conversion efficiency of the device as:

$$\eta = \frac{P_{IF}}{P_s^a} \quad (7.8)$$

Then from table 7.1:

$$\eta = \Gamma_a\Gamma_{CPW}\eta_{JJ} \quad (7.9)$$

This result shows the conversion efficiency as the product of three terms, as presented in the three-port model: one coming from impedance mismatch between the junction and the antenna at the signal frequency, another coming from impedance mismatch between the junction and the CPW line at the IF frequency, and the last one is the intrinsic conversion efficiency of the junction. The three-port model gives an analytical expression for each of these terms as a function of the system's impedances, see equation 6.24.

7.2 Heterodyne detection of high frequencies

The following measurements were performed with the junction whose d-c characteristics were presented in chapter 5. In particular, figure 5.3 showed that its characteristic frequency $f_c = 2eI_cR_n/h$ is maximal at 53 K, with $f_c^{max} = 85$ GHz.

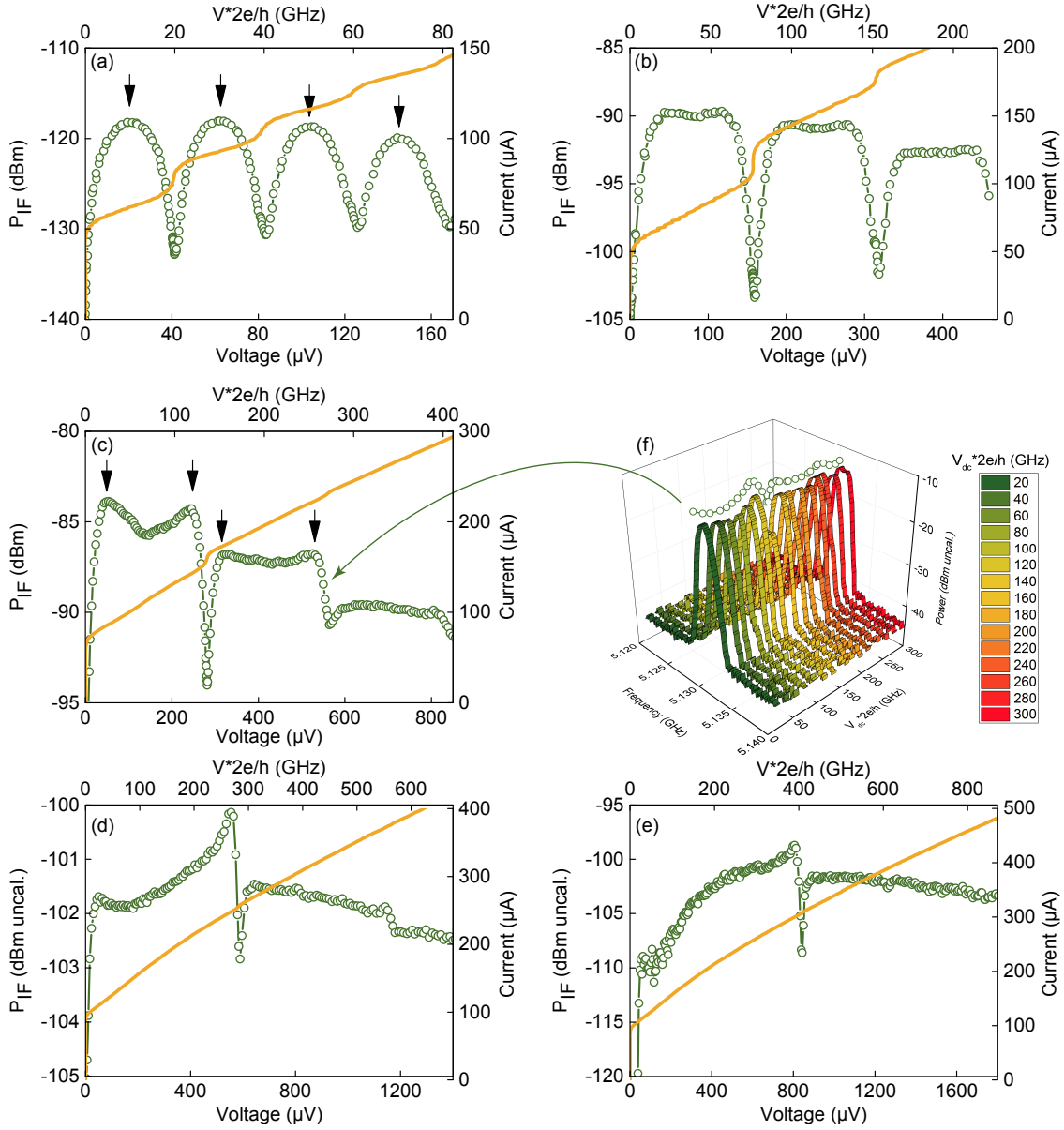


Figure 7.3: (a)–(e) Output power at the IF (left scale) and d-c current (right scale) as a function of voltage measured at $T = 53$ K for five different LO frequencies, $f_{LO} = 20$ GHz (a), $f_{LO} = 70$ GHz (b), $f_{LO} = 140$ GHz (c), $f_{LO} = 280$ GHz (d), $f_{LO} = 410$ GHz (e). The IF frequency is about 6 GHz. For the three lowest frequencies (panels (a)–(c)), the power of the signal has been set to approximately one thousandth of the LO power. For the two highest frequencies (d) and (e), the signal power is of the same order as that for the LO. (f) Recorded spectrum showing the IF peak, whose power varies with d-c voltage V_{dc} . The LO and signal excitations are set around 140 GHz, producing an IF beating at $f_{IF} = 5.13$ GHz. The power decreases at $V_{dc} \frac{2e}{h} = 140$ GHz, corresponding to the first Shapiro step on the IV curve of (c).

7.2.1 Modulation of the intermediate frequency power

The junction is illuminated via a strong LO signal at frequency f_{LO} and a much weaker test signal at frequency f_s . These conditions guarantee that the IF signal is produced by a first order mixing mechanism between signal and LO. Figure 7.3 (f) shows an example of the IF (uncalibrated) power, recorded on the electrical spectrum analyzer, as a function of d-c voltage V_{dc} . Both f_{LO} and f_s are around 140 GHz and produce an IF beating at $f_{IF} = |f_{LO} - f_s| = 5.13$ GHz. When varying

the d-c polarization, the IF power changes, and a minimum is observed at $V_{dc} \frac{2e}{h} = 140$ GHz, i.e. at the position of the first Shapiro step.

It is clearly seen on figures 7.3 (a)-(e), where the intermediate frequency power P_{IF} is represented as a function of d-c voltage V_{dc} across the junction, for different ranges of frequency. At 20, 70, and 140 GHz, the LO power has been set to approximately halve the critical current, as it corresponds to an optimal operation point for mixer's performances (see 7.2.3). P_{IF} displays strong modulations between each Shapiro step, whose period is given by the quantized voltage $\Delta V = \frac{h}{2e} f_{LO}$. Two mixing regimes can be identified. For $f_{LO} = 20$ GHz (figure 7.3 (a)), P_{IF} is maximum at voltages corresponding to the exact center between two Shapiro steps (see arrows). We will show in section 7.2.4 that such a behavior is obtained when $f_{LO} < f_c^{max}$. For $f_{LO} = 140$ GHz figure 7.3 (c)), P_{IF} has two maxima close to the Shapiro steps (see arrows), separated by a dip. It is also seen in figure 7.3 (d). This corresponds to the condition $f_{LO} > f_c^{max}$. In the intermediate situation where $f_{LO} \simeq f_c^{max}$, P_{IF} is approximately flat at the center of the steps (figure 7.3 (b)). Measurements performed at higher frequencies, $f_{LO} \simeq 280$ and 410 GHz (figure 7.3 (d) and (e)) show that the junction still works in the lower part of the THz range. However, in these cases, the power of the LO source was not sufficient to reach optimal bias conditions. Mixing at frequencies higher than 410 GHz was not investigated in this study.

7.2.2 Dynamic range

7.2.2.1 Evaluation of losses and gain in the setup

It has been very delicate to precisely evaluate all the power losses and gain of a test bench: first because measurements usually require to change the configuration of the setup, therefore the situation with and without detector is not strictly the same. Second because power-meters in the THz range are not easy to implement (and expensive).

Nonetheless, losses and gain in the r-f output line, respectively G_{rf} and Γ_{rf} can be measured with a vector network analyzer. At 6 GHz and room temperature we estimate:

$$\begin{cases} \Gamma_{rf} = -9.87 \text{ dB} \\ G_{rf} = 41 + 45 = 86 \text{ dB} \end{cases} \quad (7.10)$$

and we consider that the values are the same at cryogenic temperatures. G_{rf} is the sum (in dB) of the cryogenic amplifier (41 dB) and the room temperature amplifier (45 dB). Thus, we have access to P_{IF} (see table 7.1).

We deduce P_{LO}^{JJ} and P_s^{JJ} from the critical current diminution that they (separately) generate. Indeed, the critical current diminution from an r-f power P_{rf} has the following expression:

$$P_{rf}^{JJ} = \frac{1}{2} \Delta I_c I_c \left(\frac{\Phi_0 f_{rf}}{I_c R_n} \right)^2 R_n \quad (7.11)$$

where $\Delta I_c = I_c^{max} - I_c^{rf}$. We infer the signal power P_s^{JJ} from this equation: doing a first calibration with a strong signal that reduces I_c (without LO), we then place a known attenuator on the signal path, in the quasi-optic setup.

Also, at 53 K, we have $I_c = 90 \mu\text{A}$ and $R_n \simeq 2 \Omega$ (see figure 5.3 (a)). Then, we can estimate the LO power P_{LO}^{JJopt} that diminishes the critical current by half as:

$$\begin{cases} 0.21 \text{ nW} = -67 \text{ dBm @ 20 GHz} \\ 2.6 \text{ nW} = -56 \text{ dBm @ 70 GHz} \\ 10 \text{ nW} = -50 \text{ dBm @ 140 GHz} \\ 42 \text{ nW} = -44 \text{ dBm @ 280 GHz} \\ 94 \text{ nW} = -40 \text{ dBm @ 420 GHz} \end{cases} \quad (7.12)$$

We see here that the LO power required to halve the critical current, optimal operating point for the mixer (see 7.2.3), is strikingly low compared to the standard heterodyne technologies (see table 1.4). They need at least LO powers of two orders of magnitude higher.

Furthermore, it explains why at high frequencies (starting at 280 GHz) we don't manage to reach the optimal operating point: not only the sources deliver lower power as the frequency increases, but also the required power to have $\Delta I_c / I_c^{max} = 1/2$ increases with frequency.

Γ_a and Γ_{CPW} come from impedances mismatch. As a first estimation, with a junction of about $R_n = 2 \Omega$, an antenna at 80Ω (equation 7.4) and a CPW line of 50Ω we get:

$$\begin{cases} \Gamma_a = 10 \log \left[1 - \left(\frac{2-80}{2+80} \right)^2 \right] = -10.2 \text{ dB} \\ \Gamma_{CPW} = 10 \log \left[1 - \left(\frac{2-50}{2+50} \right)^2 \right] = -8.3 \text{ dB} \end{cases} \quad (7.13)$$

Therefore we can estimate P_s^a (see table 7.1).

7.2.2.2 Dynamic range measurements

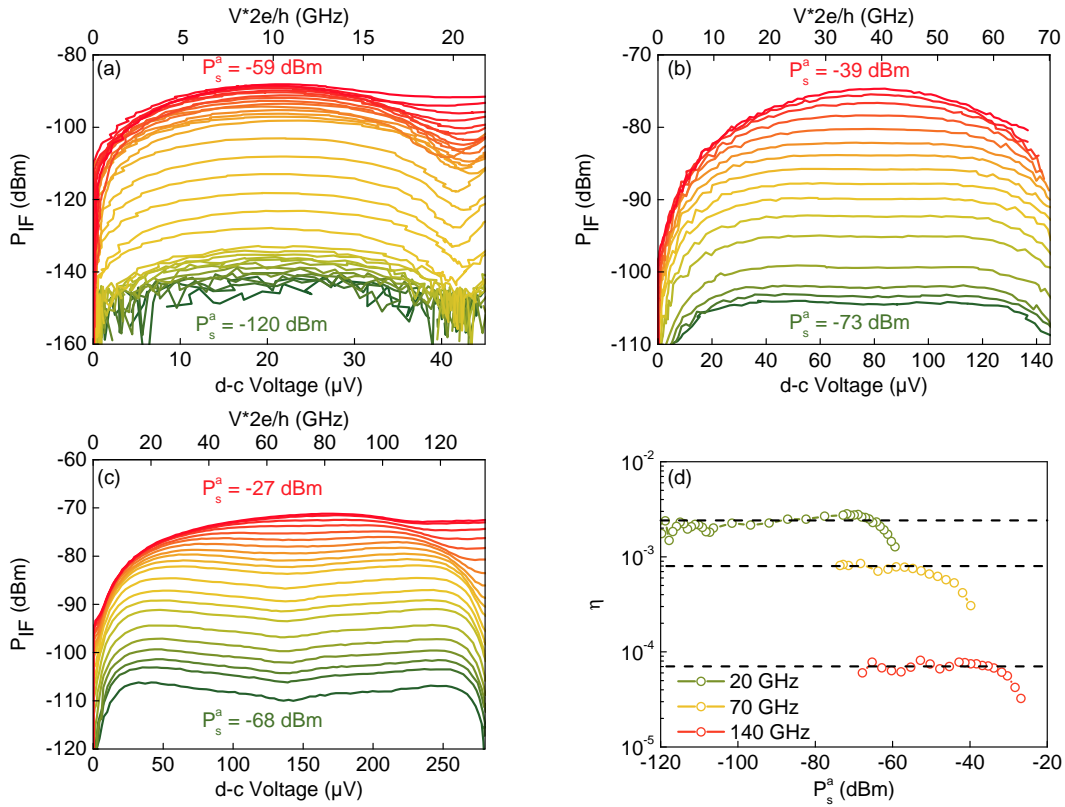


Figure 7.4: (a)-(c) Intermediate frequency power measured at $T = 53 \text{ K}$ for three different LO frequencies, $f_{LO} = 20 \text{ GHz}$ (a), $f_{LO} = 70 \text{ GHz}$ (b) and $f_{LO} = 140 \text{ GHz}$ (c). The signal power sent onto the antenna has been varied over several decades. (d) Conversion efficiency $\eta = \frac{P_{IF}}{P_s^a}$ measured at $V_{dc} * 2e/h = f_{LO}/2$, as a function of signal power. The horizontal black lines correspond to the ideal linear response of the mixer).

The output power P_{IF} at the intermediate frequency was measured as a function of the signal power for three main ranges of frequency 20, 70 and 140 GHz, as shown in figures 7.4 (a), (b) and (c) respectively. The LO power was adjusted to diminish the critical current to about a half of its nominal value. For each case, the conversion efficiency η was calculated at $V_{dc} * 2e/h = f_{LO}/2$, i.e. at the center of the first Shapiro step. η is plotted as a function of the signal power sent onto

the antenna in figure 7.4 (d). The mixer displays a linear dynamical range of constant conversion efficiency of more than 55 dB at 20 GHz and 30 dB at 140 GHz.

For strong signal power, the modulation's amplitude of the IF signal decreases and the mixer saturates. In this situation, the signal power can no longer be considered to be small compared to the LO power and second-order mixing processes take place. At 20 GHz it happens at about $P_{sat}^a = -70$ dBm, which corresponds to a signal effectively seen by the junction of about -80 dBm (equation 7.13), to be compared to the LO power, of about -67 dBm (see 7.12). At 70 GHz the saturation occurs at about $P_{sat}^a = -55$ dBm, i.e. $P_{sat}^{JJ} = -65$ dBm, and at 140 GHz $P_{sat}^a = -35$ dBm, i.e. $P_{sat}^{JJ} = -45$ dBm. Thus, as the LO frequency increases the signal power can get closer to the LO power in the linear range, probably because second-order mixing processes are more difficult to trigger as the frequency increases.

For 70 and 140 GHz the signal power does not go below -70 dBm, because the dynamics of our attenuators was at best 30 dB, hence it is in practice quite difficult to cover a dynamic range of many decades at these frequencies. In addition, at low signal powers we were limited by the noise generated by the junction and the test bench. A further study would be to harness such a problematic.

7.2.3 Influence of the LO power

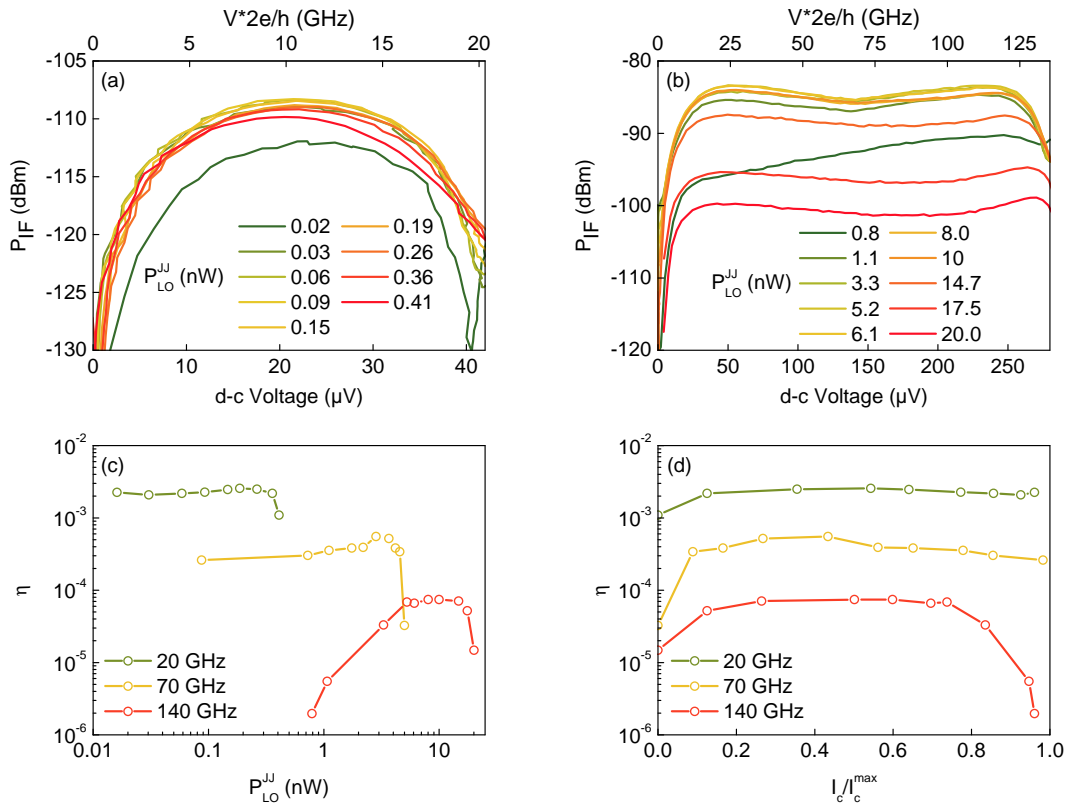


Figure 7.5: (a) and (b) Power in dBm at IF measured at $T = 53$ K for different values of the LO power received by the junction. The LO frequency is 20 GHz on panel (a) and 140 GHz on panel (b). (c) Conversion efficiency taken at $V_{dc} * 2e/h = f_{LO}/2$ as a function of LO power coupled to the junction. (d) Conversion efficiency taken at $V_{dc} * 2e/h = f_{LO}/2$ as a function of critical current reduction for the three LO frequencies.

In a practical heterodyne receiver application, the LO power necessary to optimally bias the mixer is a critical parameter and must satisfy two important requirements: (i) it has to be as low

as possible to minimize the power consumption and to be easily driven by available sources in the frequency range of interest and (ii) its variations and fluctuations must not modify significantly the performance of the mixer. For a Josephson mixer, the dependence of the conversion efficiency with the LO power is mainly determined by the characteristic frequency $f_c = 2eI_c R_n/h$. Recall that $f_c \simeq 85$ GHz at 53 K (figure 5.3). Additionally, it is generally expected that the conversion should be greatest for a LO power corresponding to a suppression by approximately 50% of the critical current [164]. However, a careful analysis of this point has never been done [135].

Figures 7.5 (a) and (b) show the behavior of the output power P_{IF} as a function of d-c voltage across the junction for different values of LO power received by the junction, for $f_{LO} = 20$ GHz and 140 GHz. The signal power is kept constant, in the linear range of response of the mixer. The conversion efficiency taken at $V_{dc} * 2e/h = f_{LO}/2$ is plotted as a function of P_{LO} (figure 7.5 (c)). For $f_{LO} < f_c$, η is constant on more than one decade and decreases at strong LO power. P_{LO} as low as 20 pW at $f_{LO} = 20$ GHz and 100 pW at $f_{LO} = 70$ are sufficient to drive optimally the mixer whereas at 140 GHz, 10 nW of power are required. It is clear that the conversion efficiency does not depend critically on the LO power as long as $f_{LO} < f_c$. Otherwise, as can be seen at 140 GHz, η is optimal for a given LO power, which corresponds approximately to a suppression by 50% of the critical current (figure 7.5 (d)).

7.2.4 Conversion efficiency simulations

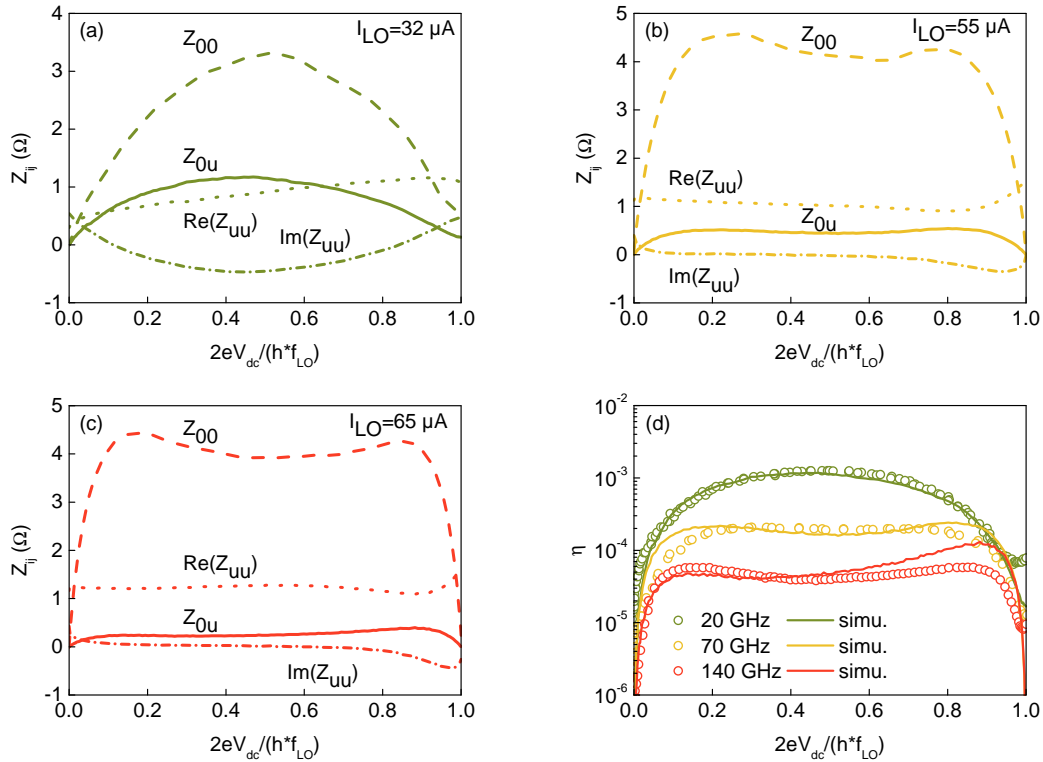


Figure 7.6: Main elements of the impedance matrix as a function of normalized voltage calculated at $T = 58$ K for $f_{LO} = 20$ GHz (panel a), $f_{LO} = 70$ GHz (panel b) and $f_{LO} = 140$ GHz (panel c). For all the curves, $I_c = 45$ μ A and $\Gamma = 0.057$. The value of I_{LO} is indicated on each panel. (d) Comparison between experimental (circles) and theoretical (full lines) conversion efficiency η calculated for the three LO frequencies.

We performed numerical simulations in order to confront the three-port model, with the con-

version efficiencies that we experimentally measured. We managed to fit the experimental data up to 140 GHz, beyond what the Josephson mixing diminishes drastically, in favor of the normal resistance mixing.

The conversion efficiency is calculated from the impedance matrix $\tilde{\tilde{Z}}$, with equation 6.23. Figures 7.6 (a)-(c) represent the important matrix elements Z_{ab} of $\tilde{\tilde{Z}}$, calculated for a LO at 20, 70 and 140 GHz respectively [135]. The d-c dynamic impedance Z_{00} and down-conversion impedance Z_{0u} reproduce the shape of the output power P_{IF} of figure 7.4. For $f_{LO} = 20$ GHz, the mixer should be d-c biased halfway between the Shapiro steps whereas for $f_{LO} = 140$ GHz, it should be biased close to the steps. The impedance Z_{0u} and therefore the ability of the junction to down-convert decreases significantly when the LO frequency is increased. Note however that it is greater than 1 at 20 GHz for an optimal bias, hence conversion gain is possible. Figure 7.6 (d) shows that the theoretical calculations of the conversion efficiency obtained from 6.24 are in good agreement with experimental data. A crossover from the first regime of mixing $f_{LO} < f_c$ to the second regime $f_{LO} > f_c$ is observed. In the latter, Z_{00} decreases in the middle of the riser and hence the best mixing moves towards its edges [163]. At $T = 58$ K, the noise parameter $\Gamma = 0.057$ is much lower than 1, which guarantees that the Josephson non-linearity is not smeared out by the noise.

The conversion efficiency takes a maximum value of 0.1% at 20 GHz and decreases to 0.01% at 140 GHz. An improvement of the mixer performances requires optimizing the three factors of expression 6.24. In particular, impedance mismatch resulting from the low values of the r-f and d-c dynamic impedances Z_{uu} and Z_{00} , compared with the impedances of the antenna and r-f line, Z_u and Z_0 respectively, leads to a significant deterioration of η . Impedance matching elements both between the antenna and junction and between the readout line and junction could be added at a cost of reduced bandwidth. It is what we intended to design in section 8.2 of the next chapter.

7.2.5 Mixing beyond 140 GHz

For $f_{LO} \gg f_c$, the signal and LO a-c current interact weakly with the inductive Josephson element. As a result, a large part of IF power is generated by mixing on the non-linear resistance. As can be seen in figures 7.3 (d) and (e), this produces a continuous background on top of which, Josephson mixing can still be distinguished.

At these high frequencies, the three-port model fails to correctly reproduce the shape of P_{IF} , even when we implement the non-linear resistance $R_n(I_b)$, determined by saturated r-f, as seen in section 5.3.2. To date, it remains unclear whether it is because of fundamental restrictions (presence of other non-linear effects) or because of numerical instability, such high frequencies being extremely heavy to compute.

7.3 Conclusion on the high-frequency mixing measurements

When d-c and r-f biased, a Josephson junction down-converts a THz signal to an intermediate frequency (IF) signal, whose power varies with bias (figures 7.3). When the local oscillator (LO) frequency f_{LO} is lower than the junction's characteristic frequency $f_c = 85$ GHz, the optimum mixing point is in the middle of the riser, at $2eV_{dc}/h = f_{LO}/2$ (figure 7.3 (a)). As f_{LO} increases, the optimum shifts towards the edges of the riser (figure 7.3 (c)). We demonstrated mixing operations up to 400 GHz.

The conversion efficiency η quantifies the sensitivity of detection. We define it as the ratio between the maximum available power arriving onto the mixer's antenna to the IF power sent into the r-f reading line. Due to impedance mismatches in our unoptimized system, we measured low values of η , about 2% at 20 GHz, and down to 0.01% at 140 GHz (figure 7.4). Nonetheless, when

the signal power is varied, we measured a linear response of the mixer over more than 55 dB at 20 GHz and 30 dB at 140 GHz.

We investigated the influence of the local oscillator power. The required LO power to operate the system is extremely low, about two order of magnitudes lower than any other existing technology. Besides, as predicted in theory, optimum mixing happens for a LO power that approximately halves the critical current. The dependence on the efficiency is not severe, especially when $f_{LO} < f_c$, and a comfortable range of LO powers can operate the mixer at optimum performances (figure 7.5).

Two important remarks are to be kept in mind: (i) as previously mentioned in this manuscript, f_c is not a cut-off frequency, i.e. the Josephson mixing still exists at higher frequencies, as proven by figures 7.3 (d) and (e), where η still drops at the Shapiro steps. (ii) When $f_{LO} \gg f_c$, high current biases necessary to drive the junction enhance the non linearity of the normal resistance R_n , which also starts to mix. It explains qualitatively the complicated η of figures 7.3 (d) and (e), where both non linearities (Josephson and R_n) seem to be at work.

We used the three-port model to simulate the conversion efficiency η . The simulations are in good agreement with experiments up to 140 GHz (figure 7.6) and it should be noted that without impedance mismatch, we expect to see conversion gain at 20 GHz.

Chapter 8

Improvements and perspectives for the Josephson mixer

Contents

8.1	An Array of Josephson junctions as a detector	127
8.2	Optimization of the design - electromagnetic simulations	128
8.2.1	Antenna	128
8.2.2	Chebyshev impedance transformers	129
8.2.3	Chebyshev filters integrated to the antenna	130
8.3	Noise measurements	132
8.3.1	Origin of noise	132
8.3.2	Measurement of noise	134
8.4	Self-pumped Josephson mixer	135
8.5	Conclusion on the improvements and perspectives	138

At this point of our discussion, we would like to propose several roads that we believe are worth investigating, in order to further assess the use of irradiated high- T_c Josephson junctions as terahertz heterodyne detectors.

Three main studies should be conducted. First, impedance matching between the detector and external impedances should be improved. To that end we propose (i) to use arrays of Josephson junctions as detectors, and (ii) from electromagnetic simulations a new design for the detector, that should boost its sensitivity in a 10 GHz window around a central frequency of 70 GHz. Second, a thorough study of the mixer's noise should be carried out, and third, the possibility of using the self-oscillation as an *internal* local oscillator should be explored.

8.1 An Array of Josephson junctions as a detector

In the irradiated junction technology, it is possible to place several junctions in series and/or in parallel, so as to increase the overall impedance of the detector thus fabricated. As long as it can be considered as a lumped element, i.e. as long as its typical dimensions are much lower than the exciting wavelength, it should be able to mix and down-convert high frequencies. The higher impedances at the USB, LSB and IFB should increase greatly the conversion efficiency. Heterodyne detecting experiments with $\text{YBa}_2\text{Cu}_3\text{O}_7$ arrays of step-edge junctions exist in the literature, that encourage to follow such a path [116].

However, synchronization is required, and the mixing mechanism will not be as simple as the one that we described all along the previous chapter, based on the two Josephson equations. We will study synchronization effects in the next chapter. Therefore, the choice of the best array (the one that will give the best conversion efficiency) will require a thorough study.

8.2 Optimization of the design - electromagnetic simulations

The junction's weak impedance at any frequency degrades the mixer's performances, because of impedance mismatch with the antenna at the signal frequency and with the r-f reading line at the intermediate frequency (equation 6.24). We can overcome this issue at the expense of a reduced bandwidth. Therefore, focusing on a high frequency band between 65 and 75 GHz and an IFB between 4 and 8 GHz, we propose a design that would match a 10Ω oscillating lumped element to the antenna and to the r-f line. It exploits Chebyshev impedance transformers, and we tested the response of the whole design with Comsol, an electromagnetic simulation program.

8.2.1 Antenna

The Chebyshev CPW filters would be connected to the junction on one side and to the antenna or transmission line on the other side. Therefore a simpler structure than the spiral seem profitable for easier implementation. However the requirement of a 10 GHz bandwidth around 70 GHz still requires the use of a broadband antenna. Thus we focused on a bow-tie - or butterfly - antenna, represented on figure 8.1 (a). It is defined by one angle only and the one can show that its quasi-static (QS) impedance is given by [55]:

$$Z_{QS}^a = \eta_0 \sqrt{\frac{2}{\epsilon_r + 1} \frac{K(\tan^2(\frac{\pi - \phi_0}{4}))}{K'(\tan^2(\frac{\pi - \phi_0}{4}))}} \quad (8.1)$$

where η_0 is the vacuum impedance, $K()$ and $K'()$ are the complete elliptic integral of first kind and its complement, respectively, and ϕ_0 is the bow-tie angle. Figure 8.1 (b) represents Z_{QS}^a as a function of ϕ_0 . We choose a self-complementary antenna, i.e. $\phi_0 = \pi/2$, therefore we have $Z_{QS}^a = 76 \Omega$. Each arm is 1.25 mm, so as to ensure a minimum frequency detection of 65 GHz.

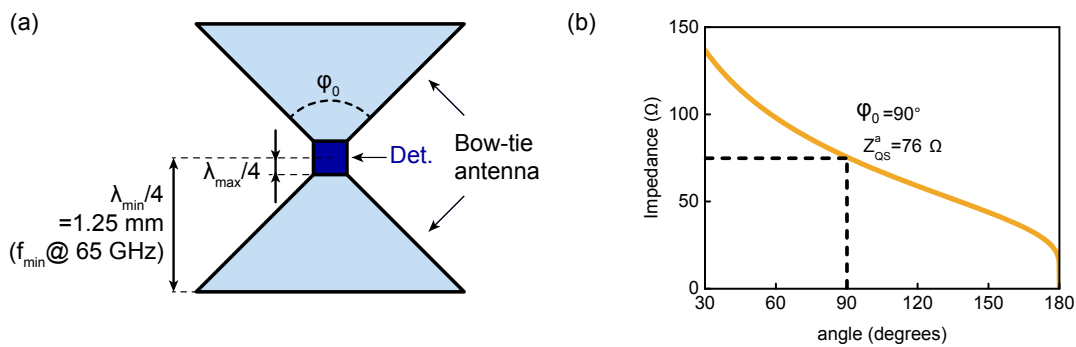


Figure 8.1: (a) Sketch of a bow-tie antenna, a detector being placed at its center. The minimum and maximum length of the arms determine the operating frequency band. (b) QS impedance of the bow-tie as a function of its angle ϕ_0 .

However at 70 GHz, QS approximation may not be completely valid (see 7.1.2.2), henceforth we simulated the antenna's response to a high-frequency excitation with Comsol, a full-wave simulation software. Figure 8.2 (a) represents the reflection coefficient s_{11} of a lumped oscillating element when varying its impedance, placed at the center of the antenna, at 70 GHz. We thus find

the bow-tie impedance at the minimum value: 68Ω at 70 GHz. It is consistent with the fact that at higher frequencies we expect lower impedances than the QS values, due to capacitive effects. Then, figure 8.1 (b) validates the broadband nature of the antenna, showing very low s_{11} when its impedance is fixed at 68Ω , in turn varying the frequency between 65 and 75 GHz.

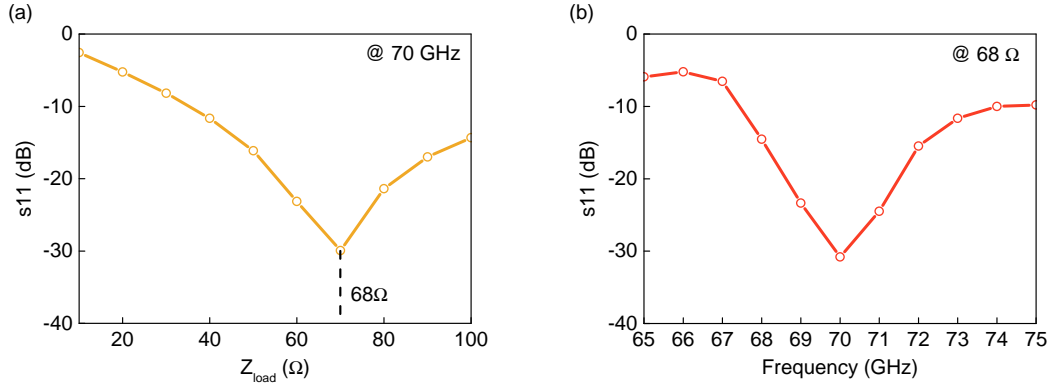


Figure 8.2: (a) reflection coefficient s_{11} of the antenna, at 70 GHz, as a function of the lumped element impedance, reaching a minimum at 68Ω . (b) s_{11} as a function of frequency when the lumped element impedance is fixed at 68Ω .

8.2.2 Chebyshev impedance transformers

A Chebyshev filter is a series of quarter wave lines, that minimize electromagnetic reflections between two unmatched impedances, in a given spectral window. In short, one can express the reflection coefficient $\Gamma(\theta)$ of a multi-section line whose sections have the length θ , as a sum of dephased terms, the latter depending on the section's impedances. In any case, $\Gamma(\lambda/4) = 0$ at the wavelength λ . Then the idea is to map $\Gamma(\theta)$ to a flat polynomial function $f(\theta)$, so that the reflection shall be small for wavelengths close to λ . Depending on f , one can favor the value (Chebyshev polynomials) or the flatness (binomial coefficients) of the reflection inside the spectral window. A detailed study can be found in David Pozar's book [155].

Choosing to have two sections in our transformers, we need to adapt 10Ω to 68Ω at the signal frequency, 70 GHz, and 10Ω to 50Ω at the IF, 6 GHz. A Chebyshev impedance transformer calculation gives the polynomial coefficients:

$$\begin{aligned} 10 - 16.2 - 42 - 68 \Omega @ 70 \text{ GHz} \\ 10 - 15.8 - 31.6 - 50 \Omega @ 6 \text{ GHz} \end{aligned} \quad (8.2)$$

If we fix the total CPW line width to $w_{CPW} = 200 \mu\text{m}$ ($2b = 200 \mu\text{m}$ in figures E.1 of appendix E), QS calculations adapted from Gupta [88] give the corresponding central line widths w of a conductor-backed coplanar waveguide:

$$\begin{aligned} \text{JJ} - w_1^{70} : 199 \mu\text{m} - w_2^{70} : 135 \mu\text{m} - \text{Antenna} \\ \text{JJ} - w_1^6 : 199 \mu\text{m} - w_2^6 : 170.2 \mu\text{m} - \text{r-f line} \end{aligned} \quad (8.3)$$

We compared and corrected these QS values to what we find in Comsol, with a 2D model of the CPW lines. The simulations give the following results:

$$\begin{aligned} \text{JJ} - w_1^{70} : 194 \mu\text{m} (22\Omega) - w_2^{70} : 128 \mu\text{m} (42\Omega) - \text{Antenna} \\ \text{JJ} - w_1^6 : 194 \mu\text{m} (21.6\Omega) - w_2^6 : 171 \mu\text{m} (31.6\Omega) - \text{r-f line} \end{aligned} \quad (8.4)$$

where we limited the maximum central line width to $194 \mu\text{m}$ to avoid any fabrication issue (the total width of the CPW line being $200 \mu\text{m}$). It nonetheless is sufficient to obtain a good impedance matching.

Then we optimized the length of these sections. The QS approximation gives:

$$\begin{aligned} \frac{\lambda}{4} &= \frac{c}{4f} \sqrt{\frac{2}{\epsilon_r + 1}} = 457 \mu\text{m} @ 70 \text{ GHz} \\ &= 5330 \mu\text{m} @ 6 \text{ GHz} \end{aligned} \quad (8.5)$$

For both frequencies, the Comsol optimization of the section's lengths gives:

$$\begin{aligned} \theta^{70} &= 270 \mu\text{m} @ 70 \text{ GHz} \\ \theta^6 &= 3100 \mu\text{m} @ 6 \text{ GHz} \end{aligned} \quad (8.6)$$

The discrepancy between QS and full-wave values is surprising, especially at 6 GHz. We chose to use the simulated values. Figures 8.3 (a) and (b) represent the s_{11} coefficients of a 10Ω oscillating lumped element, when connected to the 3D simulated Chebyshev filters. At 70 GHz (a) the end of the line is connected to a 68Ω load, and at 6 GHz (b) it is connected to a 50Ω load. The weak reflection and the bandwidth in both cases suggest a good optimization.

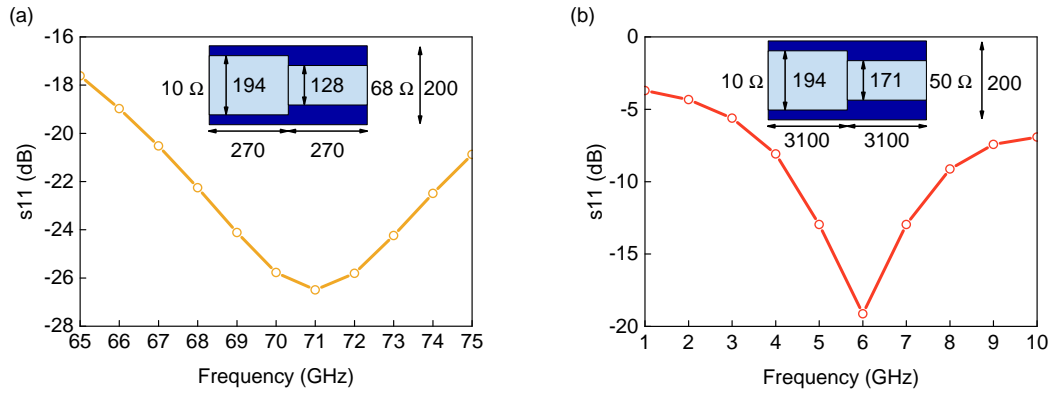


Figure 8.3: Reflection coefficients s_{11} of the 10Ω lumped element, as a function of frequency when connected to the Chebyshev filters whose characteristics are summarized on the sketches. The dimensions are in μm .

8.2.3 Chebyshev filters integrated to the antenna

Finally, we integrated the above filters to the antenna, as shown on the final design, figure 8.4 (a). The sections length of the Chebyshev impedance transformer at 70 GHz have been re-optimized with the whole structure. Besides, we only kept the first section of the Chebyshev filter at 6 GHz to avoid a too long detector (our chips are only 10 mm long) and we re-optimized its length consequently. The final parameters are:

$$\begin{aligned} \text{JJ} - \theta_1^{70} &: 268 \mu\text{m} - \theta_2^{70} : 131 \mu\text{m} - \text{Antenna} \\ \text{JJ} - w_1^{70} &: 194 \mu\text{m} - w_2^{70} : 128 \mu\text{m} - \text{Antenna} \\ \text{JJ} - \theta_1^6 &: 2400 \mu\text{m} - \text{r-f line} \\ \text{JJ} - w_1^6 &: 194 \mu\text{m} - \text{r-f line} \end{aligned} \quad (8.7)$$

Figures 8.4 (b) and (c) represent the electric field amplitude when the structure undergoes an excitation at 70 GHz (b) and 6 GHz (c), from a $10\ \Omega$ lumped element placed at the junction's position, a $50\ \Omega$ load being put at the end of the transmission line. The electric field is well localized onto the antenna at 70 GHz and onto the CPW transmission line at 6 GHz. Owing to Fermat's principle, the antenna therefore couples efficiently the received radiation to the junction, and similarly the IF power efficiently couples the r-f line.

Figures 8.5 (a) and (b) represent the s_{11} reflection coefficient of the lumped element at the junction's position, as a function of its oscillating frequency. A $50\ \Omega$ load is placed at the end of the 6 GHz Chebyshev filter. The low values around 70 GHz and 6 GHz suggest a good optimization. The design has been fabricated (see figure 8.6 and soon to be tested).

The above optimization has been done for a $10\ \Omega$ Josephson junction (at any frequency) because it is in practice very difficult to adapt lower frequencies to a $50\ \Omega$ line, and even less to a $68\ \Omega$ antenna. But the use of Josephson junction arrays could circumvent the problem. Putting an array in the optimized antenna/r-f line that we presented could lead to much higher conversion efficiencies.

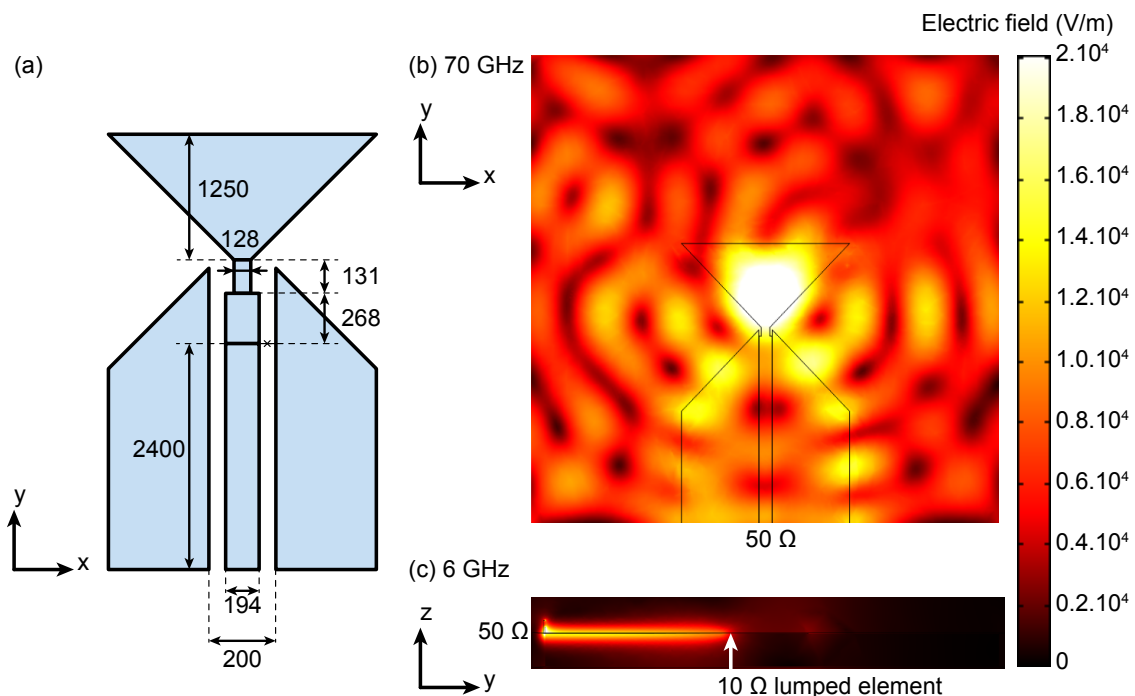


Figure 8.4: (a) Characteristic dimensions in μm of the optimized design (not to scale). (b) and (c) Electric field amplitude when the structure is excited at $1\ \text{V/m}$ by the $10\ \Omega$ lumped element at the Josephson junction's place (indicated by a cross in (a)) at 70 GHz (b) and 6 GHz (c).

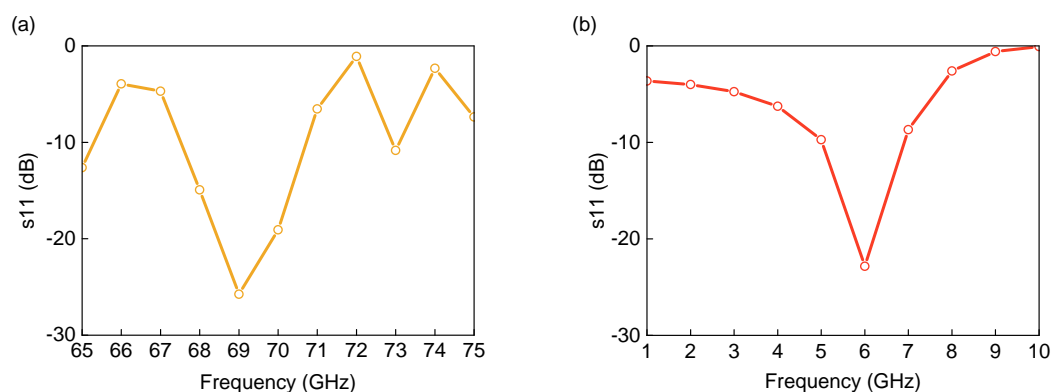


Figure 8.5: Reflection coefficients s_{11} of the $10\ \Omega$ lumped element as a function of frequency, around 70 GHz (a) and 6 GHz (b).

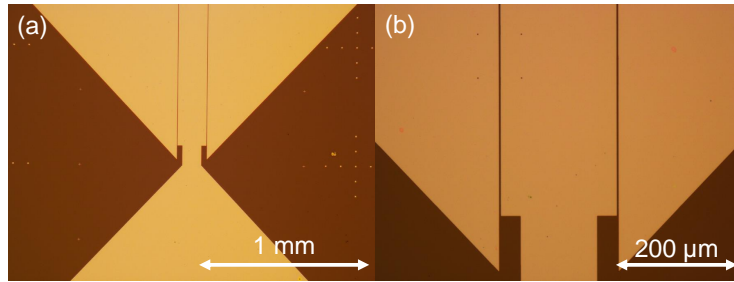


Figure 8.6: (a) Photo of the optimized design. (b), Photo, showing the detail of the Chebysev adaptation.

8.3 Noise measurements

Unavoidable will be a study of the noise in high- T_c Josephson mixers (HTS-JM), in order to evaluate their true performances. Historically, low- T_c JM are known to be noisy [164], but in our irradiated HTS-JM, possible conversion gain and fabrication of Josephson junction arrays as detectors could lead to high $I_c R_n$ products and therefore a sensitivity that could compete with other existing technologies. The mixers that we fabricated so far did not allow us to perform noise measurements under heterodyne operation, because we were penalized by severe impedance mismatch. But the two solutions that we have just seen overcome this issue. Furthermore, as we are going to explain here, the irradiated technology could lead to competitive low-noise mixers.

Recall that noise in a heterodyne detector is characterized by the noise temperature T_N . It represents the temperature of a load which placed at the input port, produces a SNR of unity at the output port (see 1.4.1.1), or equivalently exactly doubles the output noise of the device. We briefly review here what we should expect and how we could measure T_N .

8.3.1 Origin of noise

So far we took into account the noise in the RSJ and three-port model as an additive and white Gaussian noise (AWGN), introduced as a current source. But its broadening effect in the frequency domain requires a more detailed approach. Its understanding is very subtle, let us present here the ideas.

Intrinsic noise in self pumped Josephson junctions. In our range of frequency and temperature, we will always be in the Rayleigh-Jeans limit $h\nu \ll k_B T$ (see table 3.4). In addition, the $1/f$ noise contribution is negligible above ~ 10 Hz. Therefore, as already stated, the Johnson noise dominates over the shot noise. At thermodynamic equilibrium, the latter is given by the Callen-Welton fluctuation dissipation theorem, conducting to the frequency independent voltage and current spectral densities, given by equations 3.36 and 3.37 respectively.

However a d-c biased Josephson junction is not an equilibrium system, and the mixing of Johnson noise with the junction's self-oscillation (SO) does not produce a white noise. In this frame, Likharev and Semenov [131] found that the voltage fluctuations spectral density is given by:

$$S_v(\omega) = \sum_{n=-\infty}^{+\infty} |z_n(\omega - n\omega_J)|^2 S_i(\omega - n\omega_J) \quad (8.8)$$

in the unpumped regime (no LO). It derives directly from equation 6.1. In the limit where $\omega \ll \omega_J$, one can show that:

$$S_v(\omega) = r_d^2 \left[S_i(0) + \frac{1}{2i} S_i(\omega_J) \right] \quad (8.9)$$

And with Johnson noise only:

$$S_V(\omega) = 4\Gamma r_d^2 \left[1 + \frac{1}{2I^2}\right] \quad (8.10)$$

or in dimensioned units:

$$S_V(\nu) = R_d^2 \left[1 + \frac{I_c^2}{2I^2}\right] \frac{4k_B T}{R_n} \quad (8.11)$$

The intrinsic noise temperature then writes as:

$$T_N = \frac{S_V(0)}{4k_B R_d} = \frac{R_d}{R_n} \left[1 + \frac{I_c^2}{2I^2}\right] T \quad (8.12)$$

Equation 8.8 means that the noise at ω results from the down-conversion of Johnson noise coming from all the harmonics of the Josephson frequency ω_J . But numerical simulations (Taur [179], Zavaleev [203], Schoelkopf [163]) showed that the intrinsic noise was more than expected here, 10 to 20 times the physical temperature.

The true nature of this *excess* of noise was explained by Schoelkopf [163]: the Johnson noise broadens each spectral component of the Josephson oscillation, whose shape as a function of d-c bias is given in figure 3.9. Its spectrum is richer at low bias, where the oscillation has a Lorentzian shape, than at high d-c bias, where it is sinusoidal. Therefore the excess of noise is particularly important at low bias, and it degrades the performances of the Josephson mixer, when there is a local oscillator.

In this frame, Schoelkopf points out that at a fixed temperature, the mixer's performances would increase with a decreasing critical current, while holding the $I_c R_n$ product constant. But as the critical current decreases, the conversion efficiency eventually diminishes, thus an trade-off between T_N and η can be found.

In this context, our technology could provide a serious advantage, because the reduction of geometrical parameters - film's thickness, junction's width - contributes to decrease I_c while increasing R_n . Furthermore, a series array of Josephson junctions could tenfold R_n while keeping I_c low.

Noise in the presence of a local oscillator. When the junction is driven by a LO, the three-port model enables to estimate the intrinsic noise temperature. In the same way as we introduced \tilde{z} , one can define the noise correlation matrix as:

$$\tilde{S} = \begin{bmatrix} S_{uu} & S_{u0} & S_{ul} \\ S_{0u} & S_{00} & S_{0l} \\ S_{lu} & S_{l0} & S_{ll} \end{bmatrix} = \frac{\tilde{\delta V} \tilde{\delta V}^{*T}}{B} \quad (8.13)$$

where B is the frequency band over which we consider voltage fluctuations, and $\tilde{\delta V}$ is the fluctuation voltage vector. The diagonal terms are the spectral densities of the noise at the USB, IFB and LSB, whereas the off-diagonal terms represent the correlation in the noise at the three frequencies of interest [163]. The current voltage fluctuations are then given by $\tilde{\delta I} = \tilde{Y} \tilde{\delta V}$, and the mean square amplitude of the noise at the IF port is:

$$|\delta I_0|^2 = \tilde{Y}_0 \tilde{S} (\tilde{Y}_0^*)^T \quad (8.14)$$

where \tilde{Y}_0 is the row admittance vector at the IF port, $\tilde{Y}_0 = [Y_{0u} \ Y_{00} \ Y_{0l}]$. The noise temperature T_N is the temperature of a load which, placed at the USB or LSB input port induces the power $P_0 = \frac{1}{2} \Re(Z_0) |\delta I_0|^2$ at the IFB output port. Consequently, one has to divide P_0 by the conversion efficiency η to find T_N :

$$T_N = \frac{\Re(Z_0) \delta I_0^2}{k_B \eta} = \frac{\tilde{Y}_0 \tilde{S} (\tilde{Y}_0^*)^T}{4k_B \Re(Z_u) |Y_{0u}|^2} \quad (8.15)$$

Notice that it is the *total* noise temperature of the mixer, i.e. it takes into account the external impedances. It does not depend on the impedance mismatch at the IF since the latter affects both signal and noise. Equation 8.15 is consistent with 1.30, found for a perfect mixer (with no internal noise).

8.3.2 Measurement of noise

With a hot-cold measurement, one can access to T_N in the presence of a LO. It consists in measuring the variation of the detector's response, when the signal comes from a blackbody, whose temperature is varied. Its emitting power being directly proportional to $k_B T$, it gives an accurate broadband source of known power. Then, in the affine range, P_{out} is proportional to P_{in} . Figure 8.7 (a) represents the situation. Thus, T_N is determined by:

$$\begin{aligned} T_N &= \frac{T_{hot} - Y T_{cold}}{Y - 1} \\ Y &= \frac{P_{hot}}{P_{cold}} \end{aligned} \quad (8.16)$$

Notice that since the source is broadband, the signal comes from both the USB and LSB, thus T_N refers here to the double side band (DSB) noise.

In practice, one uses a thermal load at room temperature (~ 300 K) and cooled down to 77 K with liquid nitrogen. It has to be a "good" blackbody in the THz range, therefore the use of THz absorbers, such as sheets of Eccosorb (AN-72), is better. In addition these sheets can easily be filled with liquid nitrogen.

Experimentally nonetheless, a hot-cold measurement is delicate: one has to keep the same setup configuration while only varying the temperature of the load. In addition, one has to mix the blackbody signal to the local oscillator, in front of the cryostat window, as shown on figure 8.7 (b). Finally, one has to optimize the setup so that the cold load signal is not too much buried into the hot thermal environment. A setup such as the one designed in figure 8.7 (c) could be used. The apparatus consists in two separate chambers, isolated from each other by a mylar window. The load is placed in the first chamber, which can be filled with liquid nitrogen. The second chamber is in vacuum, in front of the cryostat window. Inside, a beam splitter combines the thermal signal to a local oscillator signal and sends them into the cryostat. Both chamber walls are painted with a THz absorber (Eccosorb CRS-117).

It is difficult to evaluate what noise value we should expect. For bicrystal Josephson junctions and impedance matching between the mixer and r-f line, Scherbel et al. find $\eta = -1.2$ dB (6%) and $T_N = 1003$ K at a 20 K temperature operation [162]. They had a system quite close to ours: LO frequency at 345 GHz, IF at 1.4 GHz, $I_c = 100$ -150 μ A and $R_n = 9$ -16 Ω . Therefore we could expect T_N to be between 1000 K and 2000 K at 100 GHz, 50 K, with a single junction.

In fact, calculations [203] predict that when $f > f_c$, and for matched impedances, the noise temperature is given by:

$$T_{Nmin} \simeq 10.5T \left(\frac{f}{f_c} \right)^2 \quad (8.17)$$

In our case, with $f_c = 85$ GHz, at 140 GHz and 50 K we would get $T_{Nmin} \simeq 1400$ K. When $f \simeq 0.3f_c$ the minimum value of noise would be obtained, with $T_{Nmin} \simeq 6T$. These performances should tenfold with an array of synchronized detecting junctions, or with an external shunt circuit, that we present in the next section.

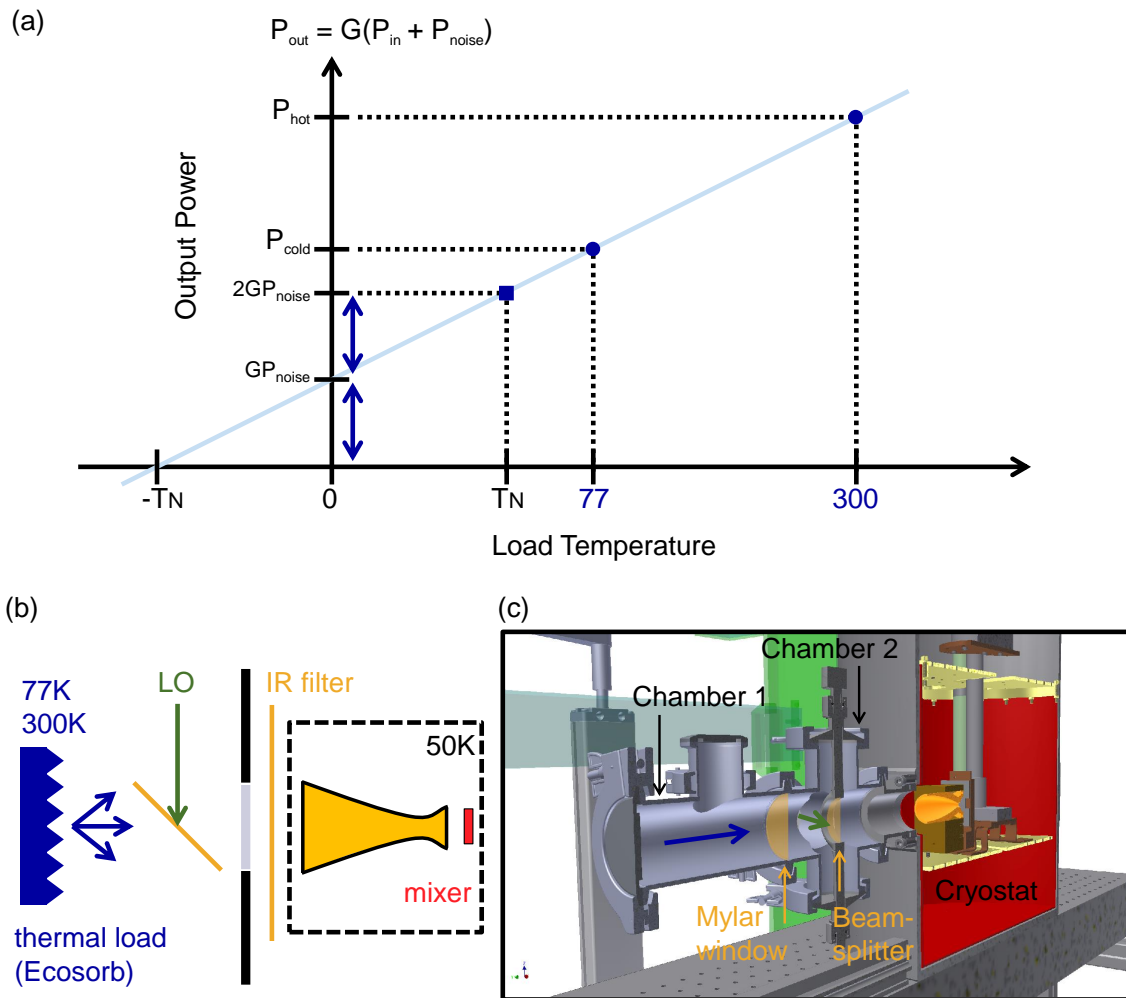


Figure 8.7: (a) Definition of the noise temperature T_N and Y factor. (b) Principle of the experiment. An thermal load radiates as a blackbody, with a power depending on its temperature. The mixing with LO enables to calibrate the detector. (c) Design of the experimental setup: two separated chambers allow to send a weak hot or cold load signal onto the mixer.

8.4 Self-pumped Josephson mixer

The idea of the self-pumped Josephson mixer was proposed by Schoelkopf in his PhD thesis [163] but was never investigated in practice. It consists in using the self-oscillation as a local oscillator instead of an external source. Theoretical calculations [68] and some experiments [112, 111] in low- T_c materials suggest that quantum noise limited performances are possible.

As seen in section 8.3.1, voltage fluctuations arising from the normal resistance convolute with all the spectral components of the Josephson oscillation, therefore producing an intrinsic broad spectrum. However, if we could make it narrower, we would greatly benefit from the use of the self-oscillation (SO) as local oscillator: we would not need an expensive external source and we could decrease the excess of noise.

The fluctuations being proportional to the square of the dynamic resistance R_d (equation 8.11) if we engineer an *external* circuit to diminish R_d , we lower the fluctuations. One can propose to externally shunt the junction by a weakly resistive and inductive (LR) loop, as represented in figure 8.8.

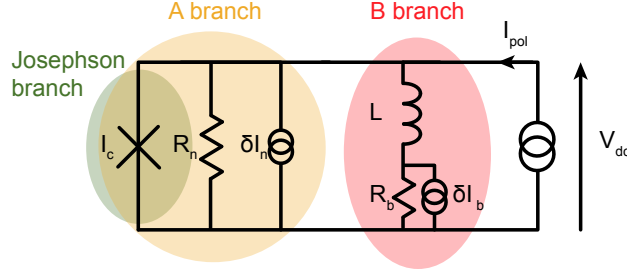


Figure 8.8: RSJ model of a Josephson junction, externally shunted by an inductive (L) and resistive R_b loop in parallel.

Fundamentally, the main problem of the Josephson mixer is that for pulsations smaller than the characteristic pulsation, $\omega < \omega_c$, the Josephson oscillation is clearly non sinusoidal, as shown on figure 3.9. There are a lot of spectral components, each adding a noise term, hence the broad self-oscillation. When $\omega > \omega_c$ the conversion efficiency diminishes, and we cannot use the SO in this range either. Then the solution consists in filtering the oscillation spectrum when at $\omega < \omega_c$, so that ideally, only a sinusoid remains. To that end we need to use a high-pass filter, to keep the high-frequency oscillations, and get rid of the noisy low frequencies, like d-c. Indeed they contribute to increase R_d , the mean voltage variation with respect to the current bias. Thus, it becomes possible to use the SO, a spectrally pure source, as LO.

Ideally we need to place a pure inductance in parallel with the RSJ model. But then it becomes impossible to d-c current bias the junction. That is why in practice we also have to put a small resistance. The smaller it is, the higher is the driving current, but the purer is the Josephson oscillation spectrum.

More precisely, the equivalent impedance Z_{eq} formed by R_n in parallel with L and R_b (figure 8.8) writes as:

$$Z_{eq} = \frac{R_n(R_b + jL\omega)}{R_n + R_b + jL\omega} \quad (8.18)$$

and then:

$$|Z_{eq}| = R_n \sqrt{\frac{R_b^2 + L^2\omega^2}{R_n^2 + L^2\omega^2}} = R_b \sqrt{\frac{1 + (\frac{\omega}{\omega_L})^2}{1 + (\frac{\omega}{\omega_n})^2}} \quad (8.19)$$

with $\omega_L = R_b/L$ and $\omega_n = R_n/L$. It is always lower than R_n , if $R_b < R_n$. Z_{eq} replaces R_d , and the linewidth of the Josephson oscillation, given by:

$$\Delta v_1 = \frac{4\pi}{\phi_0^2} k_B T \frac{R_d^2}{R_n} \quad (8.20)$$

thus decreases.

Notice that self-pumped mixer operation becomes less interesting when $\omega > \omega_c$, because then the self-oscillation is already sinusoidal, and furthermore the equivalent circuit of branch B is an open circuit.

We performed numerical simulations that clearly support the self-oscillation mixer idea: figures 8.9 (a) and (c) represent (at different current scales) the oscillation spectrum in color scale of a Josephson junction (RSJ model, 50 K), as a function of d-c current and voltage, with the external LR loop. We chose $L = 100$ pH and $R_b = 0.5 \Omega$ so that it filters frequencies lower than 0.8 GHz. The SO (brightest diagonal line), as well as its harmonics appears clearly and sharply. It mixes with the signal at 70 GHz (vertical line) and produces an intermediate frequency (counter-diagonal lines in panel (c)). This situation is clearly improved compared to the case with no external LR

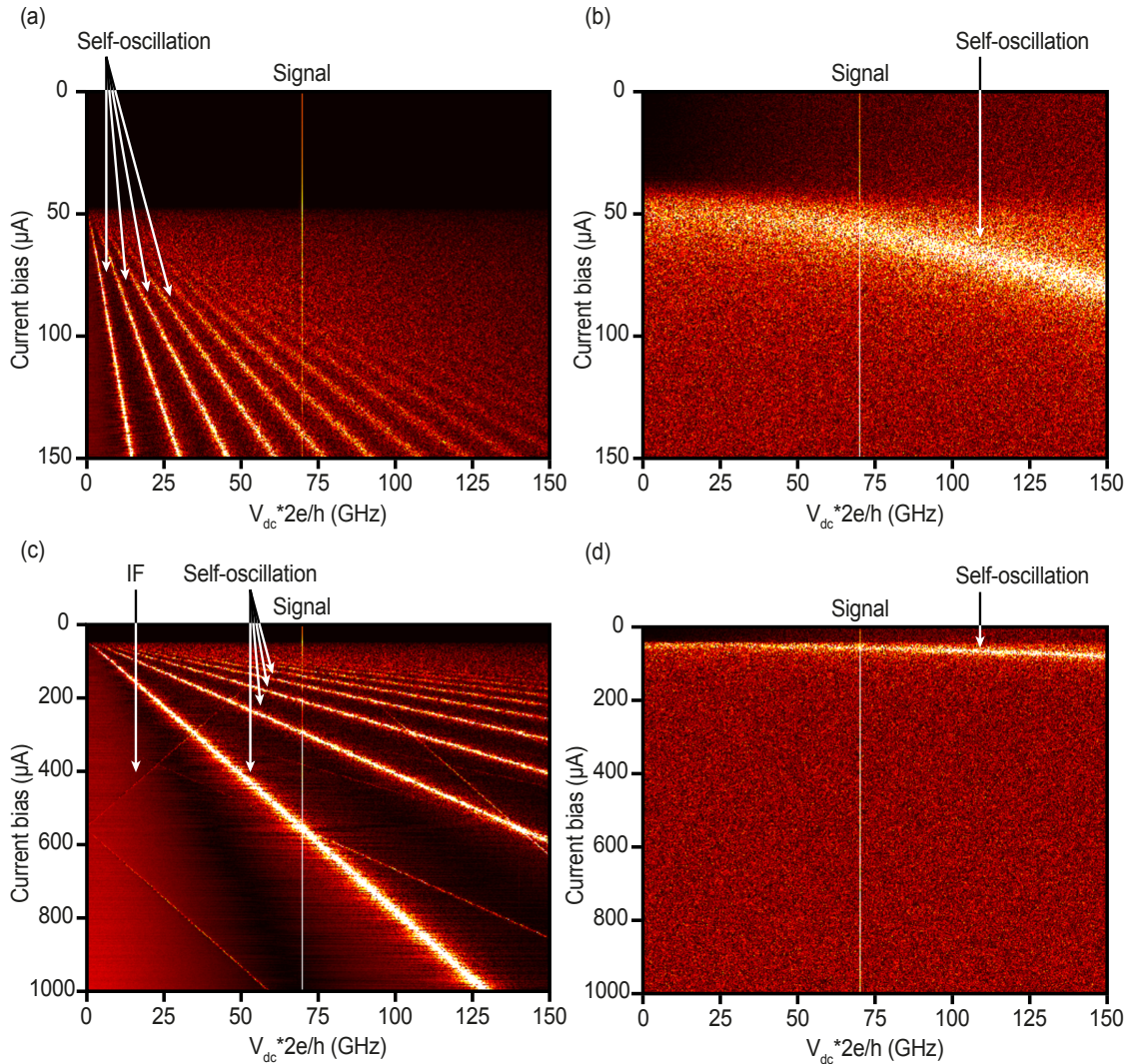


Figure 8.9: Simulated spectrum of the Josephson junction oscillation with (a,c) and without (b,d) an external LR shunting loop, as a function of the d-c current and voltage bias. The normal resistance is taken constant equal to 5Ω , and the critical current $I_c = 50 \mu\text{A}$. In the LR loop, $L = 100 \text{ pH}$ and $R_b = 0.5 \Omega$.

loop, figures 8.9 (b) and (d), where the broad intrinsic SO, diffuse yellow line, does not allow any efficient mixing with the signal.

This mode of operation of the Josephson mixer is very interesting, but as always, one cannot cheat nature, and there is a drawback: as we shunt the high-frequency components of the voltage, we therefore diminish the variation of V_{dc} with the current bias, i.e. we decrease R_d . Then it becomes more difficult to match the circuit to the r-f reading line. We might overcome this issue with, once again, a Josephson junction array.

Our fabrication technology allows to design parallel inductive and resistive loops: a superconducting line can be drawn to have a specific geometrical and kinetic inductance, while a long and wide irradiated slit in $\text{YBa}_2\text{Cu}_3\text{O}_7$ is a resistance. The ongoing work is promising, with this new design being fabricated and soon to be tested.

8.5 Conclusion on the improvements and perspectives

We suggested four roads to improve and further characterize the Josephson mixer. First, we pointed out the fact that an array of Josephson junctions could tenfold the performances of a JM. Second, we proposed a design that simultaneously matches the input and output impedances to the junction. It should be sensitive to signals between 65 and 75 GHz, and we adapted the IFB between 4 and 8 GHz (figures 8.4 and 8.5). Third, we exposed the principles and the experimental setup to address the noise properties of the mixer. The conversion efficiency η being improved, the noise temperature T_N is the second figure of merit that should be measured. Finally we suggested an operating principle, the self-pumped Josephson mixer, for which simulations reveal a promising behavior.

Chapter 9

Josephson oscillators: synchronization of Josephson junctions

Contents

9.1	Effects of junctions synchronization	140
9.1.1	Need for arrays of Josephson junctions	140
9.1.2	Rules of thumb to achieve phase-locking	142
9.1.3	Coupling mechanisms	142
9.2	Designs and circuitry for synchronization	144
9.2.1	Possible designs for junction arrays	145
9.2.2	Effect of an external feedback loop	147
9.2.3	Simulation results	150
9.3	Characterization of externally coupled Josephson junctions	152
9.3.1	Fabricated 2D array	152
9.3.2	Evidences of synchronization in the IV curves	153
9.4	Conclusion on the synchronization of Josephson junctions	155

The heterodyne detection setup that we presented in the previous chapter requires an external source as local oscillator (LO), and it constraints the receiver's integration. Furthermore in the THz range, integrated, powerful, frequency tunable and stable LO is not a straightforward technology, even if, as we have seen in the first chapter, some solutions exist already. However they still present drawbacks, like power consumption, heating, or inability to reach the lower part of the THz spectrum (below 1 THz).

It has been long known that a Josephson junction (JJ) naturally oscillates in the THz region: we see from the Josephson equations 3.20 and 3.21 that a 1 mV d-c bias creates a current oscillation at about 484 GHz, owing to the value of the ratio $2e/h$.

Finally, we saw that the required LO power to drive our Josephson mixer is extremely low, in fact much lower than any other existing technology. Therefore it is interesting to wonder whether we could engineer a local oscillator out of irradiated JJs, so as to couple it on the same chip with a Josephson mixer. In this frame, THz emission from $\text{Bi}_2\text{Sr}_2\text{CaCu}_2\text{O}_8$ mesas [151] is very inspiring for our work. There is intrinsically a vertical Josephson coupling between the CuO_2 atomic planes, and consequently a 1 μm thick $\text{Bi}_2\text{Sr}_2\text{CaCu}_2\text{O}_8$ mesa contains 652 identical intrinsic Josephson junctions [103]. Due to atomic closeness, they synchronize very easily and coherently radiate. In a sense, our goal here is to fabricate an *extrinsic* array of JJ in $\text{YBa}_2\text{Cu}_3\text{O}_7$, following the promising results of *intrinsic* arrays in $\text{Bi}_2\text{Sr}_2\text{CaCu}_2\text{O}_8$.

Beyond the practical achievement that it would constitute, it raises the prolific question of oscillators phase synchronization. We will see in section 9.1 the principles of junctions synchronization. In section 9.2 we will review the possible array designs found in the literature, fabricated and tested with low or high- T_c materials. Then, we will study and simulate a shunted two-junction cell, from which we explain synchronization physics. In this frame, we will always consider that our junctions are heavily damped, i.e. there is no capacitance (pure RSJ). Finally we will present in section 9.3 encouraging experimental results, performed on a shorted 2D array.

Phase locking between JJs has been long sought in low- T_c and more recently in high- T_c materials. A vast theoretical literature exist on the subject; among others, let us cite the most influential reviews: first and foremost the seminal work of Jain and Likharev [100], then the work of Hansen and Lindelof [91] and the more recent work of Wiesenfeld et al. [196]. Finally let us mention the work of Darula [64], reporting results with high- T_c materials.

9.1 Effects of junctions synchronization

In this section we explain why we need an array of JJs to design a local oscillator, and then converge towards the most promising coupling mechanism to synchronize our irradiated JJs.

9.1.1 Need for arrays of Josephson junctions

9.1.1.1 Linewidth of synchronized junction arrays

In the frame of the RSJ model, the linewidth of a Josephson radiation is given by [100]:

$$\Delta\omega_1 = 2\pi\Delta\nu_1 = \pi\left(\frac{2\pi}{\phi_0}\right)^2 R_d^2 S_I(0) \quad (9.1)$$

where $S_I(0)$ is the current noise spectral density at low frequency. If only fluctuations due to thermal noise are considered we get $S_I(0) = \frac{2k_B T}{\pi R_n}$ [196, 39] and then:

$$\Delta\nu_1 = \frac{4\pi}{\phi_0^2} k_B T \frac{R_d^2}{R_n} \quad (9.2)$$

With our irradiated junctions, for $R_d \simeq R_n = 2 \Omega$ and $T = 50 \text{ K}$ we get $\Delta\nu \simeq 4 \text{ GHz}$. Thus the self-oscillation of a single junction is too broad to be used as a local oscillator (as already seen in section 8.4).

However, one can show that a 1 dimensional (1D) array of N phase-locked junctions reduces the radiation linewidth as $1/N$ ([100], p 378):

$$\Delta\omega_N^{1D} = \frac{\Delta\omega}{N} \quad (9.3)$$

In fact, as pointed out by Likharev, the mutual phase-locking of N series junctions in 1D lowers the differential resistance R_d by N but at the same time increases the current spectral density $S_I(0)$ by the same factor N , canceling each other in equation 9.2 to leave only the $1/N$ term.

For 2 dimensional (2D) arrays of $N \times M$ synchronized junctions, one simply has [64]:

$$\Delta\omega_{NM}^{2D} = \frac{\Delta\omega}{NM} \quad (9.4)$$

Thus, we expect the radiation linewidth to be greatly reduced: with a 100×10 2D array of synchronized junctions, we could reach $\Delta\nu \simeq 4 \text{ MHz}$, clearly competing with existing technologies.

9.1.1.2 Power of synchronized junction arrays

The oscillation power of a Josephson junction depends of course on the load R_L of the coupling circuit (R_L can be the vacuum impedance, the power being then radiated in free space). More precisely when $V_{dc} > V_c = I_c R_n$, the power transmitted to R_L writes as:

$$P_1 = \frac{V_c^2 R_L}{2(R_n + R_L)^2} \quad (9.5)$$

a situation described in figure 9.1. When the load is matched, $R_n = R_L$ and one gets [100]:

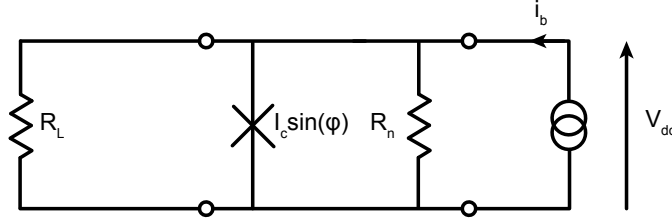


Figure 9.1: A current biased RSJ coupled to a load R_L .

$$P_1^{max} = \begin{cases} \frac{R_n I_c^2}{8} & \text{for } V_{dc} \geq V_c \\ \frac{2\sqrt{3}}{9} \sqrt{\left(\frac{I}{I_c}\right)^2 - 1} R_n I_c^2 \simeq 0.4 R_n I_c^2 & \text{for } V_{dc} < V_c \end{cases} \quad (9.6)$$

that is to say, for a junction with $R_n = 2 \Omega$ and $I_c = 100 \mu\text{A}$, we have $P_1^{max} = 2.5 \text{ nW}$ ($V_{dc} > V_c$). Consequently, a single junction is not powerful enough to operate as a LO. In addition, the generally low R_n makes impedance matching very difficult, as seen in the previous chapter.

For a 1D array of N synchronized junctions, the transmitted power to the load becomes [64]:

$$P_N^{1D} = \frac{(NV_c)^2 R_L}{2(NR + R_L)^2} \quad (9.7)$$

when $V > V_c$. Consequently, for the *unmatched* case where $NR \ll R_L$, it scales with N^2 . For the matched case where $R_L = NR_n$, the delivered power is $P_N^{1Dmax} = \frac{NR_n I_c^2}{8}$. The 1D array can achieve impedance matching to typical loads, simply by summing the normal resistances of each junctions.

For a 2D array of $N \times M$ (rows per columns) synchronized junctions, the transmitted power becomes:

$$P_{NM}^{2D} = \frac{NV_c^2 R_L}{2(NR/M + R_L)^2} \quad (9.8)$$

i.e. the available power $P_N^{2Dmax} = \frac{NMR_n I_c^2}{8}$ is proportional to the number of synchronized junctions, as in 1D, totally transmitted to the load when matching $N/M = R_L/R_n$ is achieved. Notice that the array's impedance can be tuned with the number of rows and columns.

Roughly, with our junctions we have $R_L/R_n \simeq 10$ if we want to deliver power to an r-f transmission line. Then a 2D array of 100×10 phase-locked junctions would provide $2.5 \mu\text{W}$ to the transmission line, clearly enough to overcome losses and operate the Josephson mixer.

9.1.2 Rules of thumb to achieve phase-locking

Synchronizing a large number of junctions is the crux of the matter. Before addressing the different coupling mechanisms, two rules of thumb are to be kept in mind for practical fabrication.

First, the typical size L of the array should be kept smaller than $\lambda/8$ [64, 196, 192], so that it can be considered as a lumped element. λ is the targeted radiation wavelength. When $L > \lambda/8$, the array is said to be distributed. The latter has also been shown to evidence synchronization effects, but with less agility, because of resonance phenomena. Note that λ is the effective wavelength. In our chips with sapphire substrate, for a 100 GHz emission we get:

$$L < \frac{c}{8f} \sqrt{\frac{2}{\epsilon_r + 1}} = 160 \text{ } \mu\text{m} @ 100 \text{ GHz} \quad (9.9)$$

With the irradiated technology, it still leaves some degree of freedom in the design.

Second, the spread of the junctions' characteristics disfavors phase-locking, and the spread in critical currents is the most important. Of course, depending on the array geometry, more or less dispersion can be tolerated, which is in fact one of the criteria to consider when choosing a design. For a 1D series array, the least flexible type in terms of parameters dispersion, one commonly advises that $\Delta I_c^{max}/I_c^{mean} < 7\%$ [64, 196] when it is matched to a resistive load. We are not far to achieve such requirements inside the same chip, with our fabrication technology.

Overall, it is difficult to evaluate a priori the effect of the spread in characteristics (I_c and R_n). Nonetheless, we will try to harness this question with simulations in section 9.2.3.2.

9.1.3 Coupling mechanisms

Synchronization between two oscillating systems at frequencies $\omega_1 = \dot{\phi}_1$ and $\omega_2 = \dot{\phi}_2$ does not only mean frequency-locking $\omega_1 = \omega_2$, but also $\phi_1 = \phi_2 + \Delta\psi$ where $\Delta\psi$ is constant in time. For instance, parallel junctions are doomed to be frequency-locked since they share the same bias voltage, however their emission may not be coherent because of the phase difference free evolution inside the array.

Several coupling mechanisms have been identified in theory, to achieve phase-locking. They can be divided into three main categories: external locking, short, and long range interactions [100, 91]. In any case, coupling involves a share of information of one junction's state to another. In terms of circuits, it means a feedback loop.

The external locking is simply the one that happens with an external local oscillator (LO), as seen in the previous chapter. The array being considered as lumped, every junction will synchronize with the LO field. Notice that $L < \lambda/8$ is then the criteria to respect, if one wants to design a detector with several junctions in series.

We will briefly review the basics of short range interactions, after what we will focus on long range interactions since it is the only relevant ones with irradiated Josephson junctions. In fact, with the present technology, junctions cannot be placed closer than 500 nm, thus forbidding short-range coupling mechanisms.

9.1.3.1 Short range interactions

This type of interactions implies to be able to place junctions relatively close to each other, so that each one feels its closest neighbors. More precisely, they are of three kinds: d-c or a-c order parameter interaction, and quasiparticle interaction.

d-c and a-c order parameter interaction. In the stationary (zero voltage) state, when the distance d between the junctions is lower than the superconducting coherence length ξ , the junctions tend to share the same phase. Of course, it is stronger close to T_c where ξ is long [91].

Similarly, when $d < \xi$, in the non stationary ($V_{dc} \neq 0$) state, the a-c Josephson oscillations in the two weak links tend to phase-lock, as the order parameter Δ oscillates on a characteristic length ξ .

The coherence length ξ in $\text{YBa}_2\text{Cu}_3\text{O}_7$ is known to be very short, typically 2 nm in the ab plane [113], the one that we use for fabrication. Therefore we cannot rely on these types of interactions, unless we could place the junctions closer than 1 nm to each other.

Quasiparticle interaction. It is the case where junctions are placed so close that their non-equilibrium regions overlap. The shared information is then the quasiparticle (QP) potential and charge imbalance. It appears when $d < \Lambda_{Q^*}$, where Λ_{Q^*} is the length of the QP charge imbalance. To our knowledge, the latter has never been measured in $\text{YBa}_2\text{Cu}_3\text{O}_7$. In any case, we expect it to be very short, of a few nm, and once again, the current fabrication process rules out such synchronization effect.

9.1.3.2 Long range interactions

This type of interactions involves an external circuitry. Then theoretically, junctions can be placed an arbitrary distance to one another. They are of three kinds: high-frequency coupling, i.e. via an impedance, low-frequency coupling, also called SQUID coupling, and finally coupling via a resonator. The high-frequency coupling will be the one that we intend to favor by engineering an adequate external feedback loop. In this frame, the RSJ model is of great help to analyze and simulate synchronization effects.

High-frequency coupling. Likharev and Jain [100] analyze the high-frequency coupling for two junctions and then generalize to a 1D array. Given two nearly identical junctions independently biased, in series (figure 9.2 (a)) or in parallel (9.2 (b)), they find that the range of current bias I_L over which phase-locking occurs is proportional to the loop complex admittance $Y(\omega) = (Z_e(\omega) + 2Z_i(\omega))^{-1}$. More precisely:

$$I_L = 2I_c R_n \sqrt{1 - \left(\frac{I_c}{I_b}\right)^2 \Im(Y)} \quad (9.10)$$

where $I_c = I_{c1} = I_{c2}$ is the critical current in both junctions. Notice that there cannot be any locking if the loop is purely resistive. The evidence of synchronization is thus found on the IV characteristics, where as in figure 9.2 (c), they should overlap between $\pm I_L$. When coupled by an LR loop, I_L is optimal for $\omega L = R_{n1} + R_{n2} + R_s$ [130, 91], with what we could specify the locking position.

However, these results are somewhat difficult to use in practice, given the uncertainty on the parameter spread that they allow. Let us just remember that the feedback loop should have a complex inductance, and that synchronization should be evidenced by an overlap of the IV curves.

Low-frequency coupling. It consists in synchronizing junctions with a purely inductive loop, thus forming a d-c SQUID. One can neglect the high frequency currents flowing through the loop when $\omega \gg \omega_c$, or for capacitive junctions, and then phase-locking is achieved by applying an external magnetic flux ϕ_{ext} . More precisely, flux quantization imposes:

$$2\pi n = \Delta\psi + \frac{2\pi}{\phi_0} \left(\phi_{ext} + L \frac{I_{AB} - I_{BC}}{2} \right) \quad (9.11)$$

where $\Delta\psi$ is the phase difference between the junctions, and L the loop inductance. In principle, there is no definite locking range since any external field achieve $\Delta\psi = const$. However when

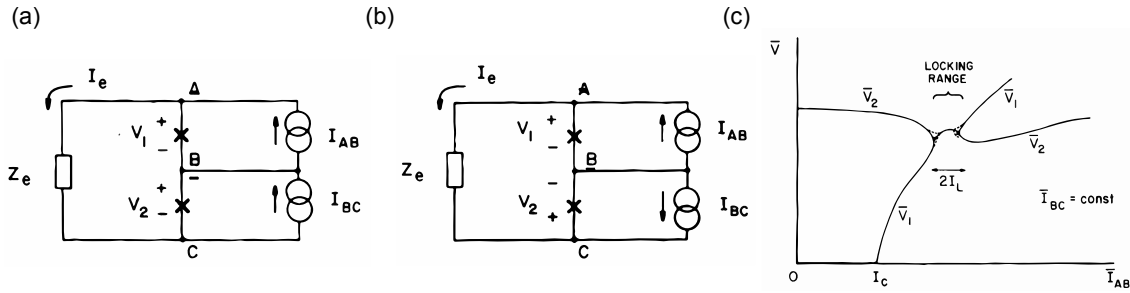


Figure 9.2: Two-junction cell, biased in series (a), and in parallel (b). (c) Evidence of synchronization on the IV curves. Adapted from [100].

$\phi_{ext} = n\phi_0$ and $I_{AB} = I_{BC}$, one gets $\Delta\psi = 0$, i.e. the junctions are in phase. Similarly, when $\phi_{ext} = (n + 1/2)\phi_0$, the junctions are in anti-phase.

This is an efficient way to couple junctions, nonetheless it requires the application of an external magnetic flux.

Coupling via a resonator. Finally, if one places the array inside a resonator, such as a resonant transmission line (figure 9.3), the junctions' oscillations may undergo a strong coupling and lock at the resonator's frequency, at the cost of a narrowed bandwidth, i.e. locking range. Considering over-damped junctions (low capacitance), the important effects of a resonant loop are: (i) reduction by Q (quality factor of the feedback) of impedance mismatch between the junctions and the microwave circuit. (ii) Linewidth reduction of the junctions' self-oscillation (similar to what we exposed in section 8.4). (iii) Parametric generation of the so-called non-Josephson oscillations [91, 174].

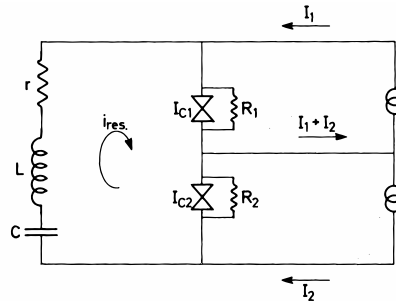


Figure 9.3: Two-junction cell coupled to a RLC resonant circuit [91].

Since we wanted to keep a broad locking range, we did not investigate this option, however it would be a solution worth to explore in the future, for a targeted narrow range of frequencies.

9.2 Designs and circuitry for synchronization

Many arrays exist in 1D and in 2D, that would favor synchronization. In general, connecting junctions in series helps impedance matching to the external load, while parallel schemes circumvent the problem of voltage (frequency) differences across the nonuniform Josephson junctions.

We will briefly review the main designs, that were proven to work with low or high- T_c materials. Then we will approach the issue of external locking with simulations. The latter are not only helpful from an experimental perspective, where actual normal resistances and critical currents

have to be thought through, but they prove also fruitful to grasp the mechanism underneath oscillators coupling. It is of crucial importance with our technology, where we cannot expect junctions to synchronize by themselves from short-range interactions.

9.2.1 Possible designs for junction arrays

Many designs for Josephson junction arrays have been proposed in the literature. The first attempts in the eighties used 1D arrays of low- T_c JJs [99], but as explained earlier, the search for high emission power and narrow linewidth, lead people to quickly adopt 2D array designs, if possible. Nonetheless, the 1D array constitutes an excellent model to understand the synchronization mechanisms, that also take place in 2D.

We focus on lumped arrays, figure 9.4 (a), and put aside quasilumped (b) or distributed arrays (c): in fact our technology favors the fabrication of closely placed JJs, and furthermore we aim at having a broadband local oscillator. Besides, we believe lumped arrays to be the most promising candidates to observe a first synchronization effect with irradiated Josephson junctions. The interested reader can refer to the work of Han and Lukens [90] or Booi and Benz [43] for experiments on distributed arrays.

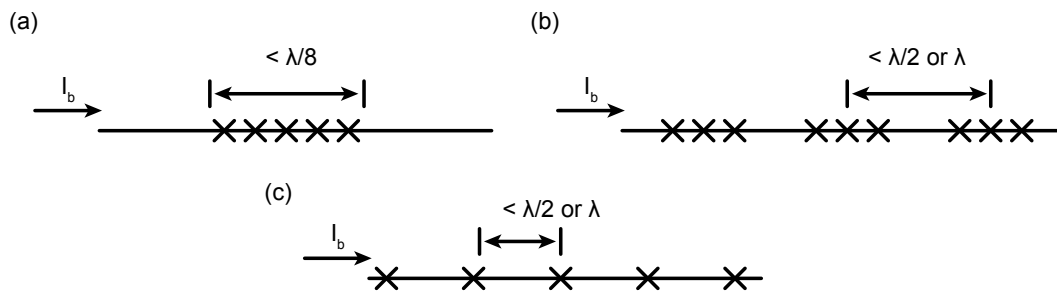


Figure 9.4: Different categories of arrays, depending on the space between the junctions. (a) Lumped, (b) quasilumped and (c) distributed arrays. λ is the radiation's effective wavelength, see equation 9.9. Adapted from [90].

9.2.1.1 1D arrays

Three types of 1D arrays have been classically studied, represented on figure 9.5: 1D series (a), 1D parallel (b) and of course d-c-parallel/a-c-series (c)-(d). In (a), one benefits from the increased impedance from the series junctions, to better match the array to the coupling circuit. In (b), one benefits from the parallel scheme to have all junctions biased with the same voltage, and hence have them oscillate with the same frequency (but not necessarily in phase). Notice however, that if N is the number of junctions put in parallel, the array requires a d-c current bias N times higher than for the dual 1D series. The current bias of the later is in principle independent on the number of junctions.

Furthermore, series geometry seems more favorable for junctions' synchronization, owing to the fact that short range interactions, like quasiparticle coupling, arise more easily. Thus, the d-c-parallel/a-c-series, first proposed by Jain et al. [99], figure 9.5 (c), benefits from the perks of the two first schemes (a) and (b) at the same time. In fact, junctions are d-c biased in parallel, so as to have the same voltage across any of them; at the same time, they are closely put on the same line, and the strong inductance of the d-c biasing wires leads to have a series array at high frequencies (a-c).

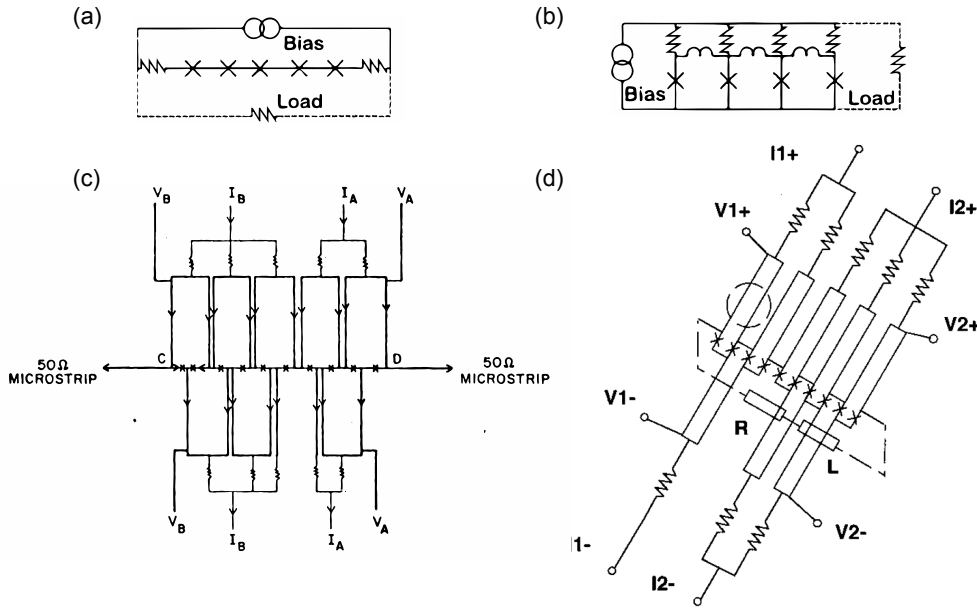


Figure 9.5: Different architectures for 1D arrays: (a) 1D series, (b) 1D parallel and (c)-(d) d-c-parallel/a-c-series array. In (d), junctions are placed in half-wavelength resonators, favoring synchronization [64, 119, 99].

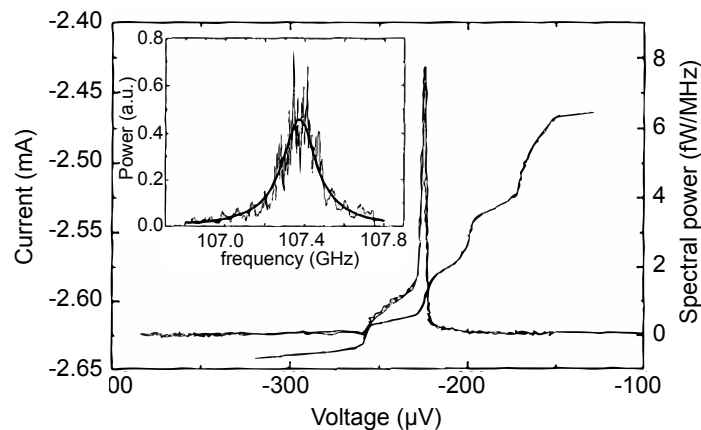


Figure 9.6: IV curve, and radiation of 1D array (10 junctions), measured with a radiometer. Inset: spectrum of the emission peak. The IV curve shows resonant steps at $\lambda/2$ and subharmonics, due to the microstrip resonators structure that helps the array's synchronization, see figure 9.5 (d). The radiation is at 110 GHz, with an integrated power of 18 pW. From [120].

Kunkel et al. [119, 120] successfully synchronized a 1D array of 10 high- T_c bicrystal $\text{YBa}_2\text{Cu}_3\text{O}_7$ JJs through the d-c-parallel/a-c-series scheme. They helped synchronization with half-wavelength resonator microstrip lines in which pairs of Josephson junctions were placed (figure 9.5 (d)). They managed to measure a radiation emission up to 110 GHz, of about 18 pW see figure 9.6, and synchronization effects were observed up to 1 THz at 45 K.

9.2.1.2 2D arrays

As seen in section 9.1.1, 2D Josephson junction arrays have many advantages compared to 1D: narrower emission linewidth, higher emitted power, and possibility to match them with a load

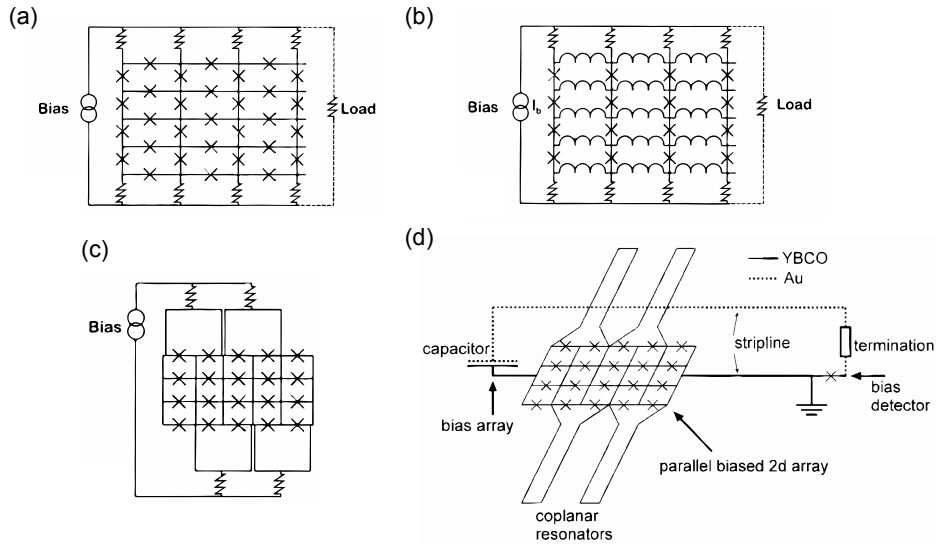


Figure 9.7: Different architectures for 2D arrays: (a) X-Y, (b) 2D shorted and (c)-(d) parallel biased. In (d), junctions are placed in resonators, favoring synchronization [64, 38].

impedance, by adjusting the number of rows and columns. Finally, the tolerable parameter spread is higher, about twice as high as in series arrays: $\Delta I_c^{max} / I_c^{mean} \simeq 0.12-0.13$ [64]. However they are more sensitive to any external magnetic field, because of their intrinsic superconducting loops.

Figure 9.7 presents the three principal designs: (a) X-Y array (b) shorted array and (c) parallel biased 2D array. The X-Y array has been mostly used in low- T_c , with reported tunable radiation frequencies between 60 to 210 GHz, with an estimated emitted power of $0.4 \mu\text{W}$ at 150 GHz for a 10×10 array [32]. When coupled to a resonator, a linewidth of 10 kHz at 100 GHz was measured [42].

Shorted 2D arrays 9.7 (b) and parallel biased arrays 9.7 (c) demonstrated promising synchronization effects when fabricated with $\text{YBa}_2\text{Cu}_3\text{O}_7$ step-edge Josephson junctions [38], but the phase-locking required either an external magnetic field (to enhance low-frequency coupling), or coplanar resonators, because the step-edge technology suffers from a poor reproducibility in the junctions characteristics. Nonetheless, Beuven et al. [38] were able to detect array's oscillation with a capacitively coupled Josephson detector (figure 9.7 (c)), where Shapiro steps observed up to 460 GHz.

Our fabrication process hopefully circumvent the parameter spread, and we will show in section 9.3 that we observed evidences of synchronization in a 10×10 shorted 2D array, with no external magnetic field applied.

9.2.2 Effect of an external feedback loop

We identified the high frequency coupling as the main (if not only) mechanism to achieve phase-locking over a wide range of frequencies with $\text{YBa}_2\text{Cu}_3\text{O}_7$ Josephson junctions. If we had a powerful emission from many synchronized junctions, as in $\text{Bi}_2\text{Sr}_2\text{CaCu}_2\text{O}_8$ mesas, we could quantify its efficiency through radiation linewidth. However in the absence of any obvious synchronization, the emitted power is extremely small and the linewidth very large, therefore such technique is not applicable.

Similarly, no heterodyne detection scheme can work with such low powers (which we actually tried, with an emitting series array placed in front of a detecting junction, and mixed with an external LO). Then at first, only traces of overlapping IV curves would be a guide towards

synchronization.

In order to understand it more precisely, we numerically studied (with Matlab) a simple system of two junctions, biased in series and shunted by a resistive and inductive (LR) loop, as shown in figure 9.8.

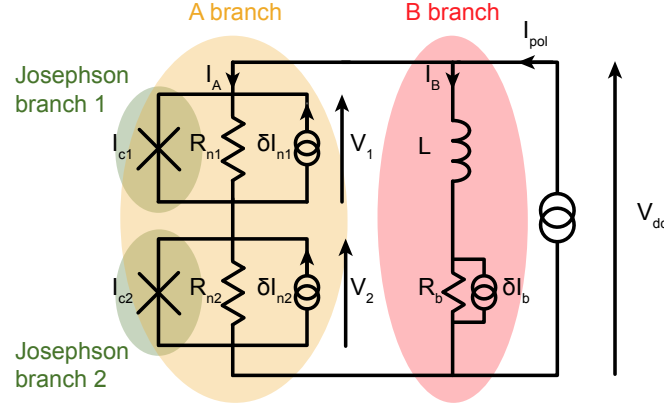


Figure 9.8: Two Josephson junctions in series (branch A), shunted by a LR circuit (branch B) that allows phase-locking.

9.2.2.1 Open-loop circuit

When there is no external shunt (i.e. when $R_b \rightarrow \infty$) the circuit equations are simply:

$$\begin{cases} I_{pol} = I_{c1} \sin \phi_1 + \frac{V_1}{R_{n1}} - \delta I_1 \\ I_{pol} = I_{c2} \sin \phi_2 + \frac{V_2}{R_{n2}} - \delta I_2 \\ \frac{d\phi_1}{dt} = \frac{2e}{\hbar} V_1 \\ \frac{d\phi_2}{dt} = \frac{2e}{\hbar} V_2 \end{cases} \quad (9.12)$$

Therefore V_1 and V_2 are two decoupled variables, and the junction's oscillations are independent. More precisely, the normalized system writes as:

$$\begin{cases} \frac{d\phi_1}{d\tau_1} + \sin \phi_1 - (i_{pol1} + \delta i_1) = 0 \\ \frac{d\phi_2}{d\tau_2} + \sin \phi_2 - (i_{pol2} + \delta i_2) = 0 \end{cases} \quad (9.13)$$

with normalization constants summarized in table 9.1. The phases ϕ_1 and ϕ_2 evolve independently.

If one considers two different JJ, with characteristics $\{I_{c1}, R_{n1}\}$ and $\{I_{c2}, R_{n2}\}$ there are two options regarding their IV curves: either $\{I_{c1} < I_{c2}, R_{n1} > R_{n2}\}$ and the IV curves don't cross, as in figure 9.9 (a), or $\{I_{c1} > I_{c2}, R_{n1} > R_{n2}\}$ and the curves cross once, as in figure 9.9 (b). Thus, there is at best only one bias point for which $V_{dc1} = V_{dc2}$ (necessary condition to have $V_1 = V_2$), therefore, in the RSJ model one cannot phase-lock series junctions without a feedback loop.

9.2.2.2 Closed-loop: LR shunt

When adding the LR shunt, the circuit equations are given by:

$$\begin{aligned} \frac{dV_1}{dt} + \left(\frac{R_{n1} + R_B}{L} + I_{c1} R_{n1} \frac{2e}{\hbar} \cos \phi_1 \right) V_1 + \frac{R_B}{L} R_{n1} (I_{c1} \sin \phi_1 - I_{pol} - \delta I_1 - \delta I_b) &= -\frac{R_{n1}}{L} V_2 \\ \frac{dV_2}{dt} + \left(\frac{R_{n2} + R_B}{L} + I_{c2} R_{n2} \frac{2e}{\hbar} \cos \phi_2 \right) V_2 - \frac{R_B}{L} R_{n2} (I_{c2} \sin \phi_2 - I_{pol} - \delta I_2 - \delta I_b) &= -\frac{R_{n2}}{L} V_1 \end{aligned} \quad (9.14)$$

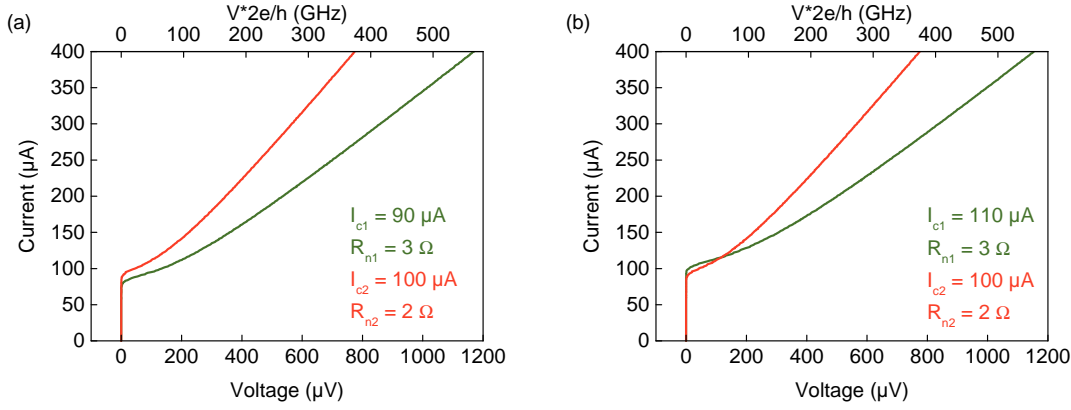


Figure 9.9: IV characteristics of series junctions without a feedback loop Depending on their I_c and R_n , the curves never cross (a) or cross only once (b).

Characterisitc pulsations	Normalized currents	Normalized times
$\omega_{ck} = \frac{2e}{\hbar} I_{ck} R_{nk} = \frac{R_{nk}}{L_{Jk}}$	$i_{polk} = \frac{I_{pol}}{I_{ck}}$	
$\omega_L = \frac{R_B}{L}$	$i_k = \frac{I_k}{I_{ck}}$	$\tau_k = \frac{2e}{\hbar} I_{ck} R_{nk} t$
$\omega_{nk} = \frac{R_{nk}}{L}$	$\delta i_k = \frac{\delta I_k}{I_{ck}}$	$= \omega_{cj} t$

Table 9.1: Normalization of the Josephson equations, $k = 1$ or 2 . $L_{Jk} = \frac{\hbar}{2eI_c}$ is the maximum value of the Josephson inductance.

One can normalize them separately with the same normalization as previously (see table 9.1):

Then the system writes as:

$$\begin{aligned}
 \frac{d^2\phi_1}{d\tau_1^2} + \left(\frac{\omega_{n1} + \omega_L}{\omega_{c1}} + \cos\phi_1 \right) \frac{d\phi_1}{d\tau_1} + \frac{\omega_L}{\omega_{c1}} (\sin\phi_1 - i_{pol1} - \delta i_1 - \delta i_b) &= -\frac{\omega_{n1}}{\omega_{c1}} \frac{d\phi_2}{d\tau_1} \\
 \frac{d^2\phi_2}{d\tau_2^2} + \left(\frac{\omega_{n2} + \omega_L}{\omega_{c2}} + \cos\phi_2 \right) \frac{d\phi_2}{d\tau_2} + \frac{\omega_L}{\omega_{c2}} (\sin\phi_2 - i_{pol2} - \delta i_2 - \delta i_b) &= -\frac{\omega_{n2}}{\omega_{c2}} \frac{d\phi_1}{d\tau_2}
 \end{aligned} \tag{9.15}$$

These are coupled second order differential equations, each describing a damped oscillator, driven by the right hand side term that indicates the influence of the second junction on the first, and vice versa. They reveal how the synchronization occurs, and for discussion's clarity, let us focus on only one equation, say the first one.

The strength of the driving term depends on the ratio $\omega_{n1}/\omega_{c1} = L_{J1}/L$. When $L_{J1} > L$, the driving force is strong because the non linear Josephson inductance is damped by the linear L . Conversely, when $\omega_{n1} < \omega_{c1}$ the importance of branch B diminishes before the one of the Josephson branch, as the frequency increases, therefore it is more difficult to drive the oscillation of the junction. Consequently, one favors the influence of one junction on the other when $\omega_{n1} > \omega_{c1}$ and $\omega_{n2} > \omega_{c2}$, i.e. $L < \min\{L_{J1}, L_{J2}\}$.

But, at the same time, the argument that we gave to explain the mechanism of the self-pumped Josephson mixer still holds: at low frequencies ($\omega < \omega_c$), the oscillation spectrum of each junction contains a lot of harmonics, therefore it is difficult to have the two of them perfectly overlap (situation of phase-locking). The high-pass filter of the LR branch diminishing the junctions' SO

linewidths, it favors their synchronization. Then, its cut-off frequency being ω_L , we see that L should not be too small, so as to ensure a good filtering. Notice that the circuit equation of the self-pumped Josephson mixer (figure 8.8) is exactly the first (or second) equation of system 9.15, without the driving term on the right-hand side.

Seeing the right-hand side terms of equations 9.15, one can interpret the overlap in the IV curves of synchronized junctions as a moving Shapiro step: the frequency of the driving oscillation on junction 1 changes according to the d-c voltage in junction 2, and vice versa.

At high-frequencies, two phenomena degrade synchronization: first, influence of branch B diminishes, as it becomes an open circuit. Second, the two Josephson oscillations, although spectrally pure, are very far from each other. In fact, the normal resistances being different, the d-c voltage difference $\Delta V_{dc} = \Delta R_n I_b$ increases with current bias.

Finally, thermal noise also disfavors synchronization, for any bias, because it independently perturbs the oscillation of each junction.

9.2.3 Simulation results

9.2.3.1 Overlapping IV curves

In practice, with $I_{c1} \simeq I_{c2} \simeq 100 \mu\text{A}$ it leads to $L_J = 3.3 \text{ pH}$, and we take $L = 20 \text{ pH}$, so as to have it not too low (and within reasonable fabrication realities). With $R_b = 0.5 \Omega$ (not too small either, to keep a reasonable d-c bias) it gives $f_L = \omega_L/2\pi = 4 \text{ GHz}$, reasonable to synchronize junctions at frequencies higher than a few GHz. Then the system 9.15 can be solved numerically, with Euler's method for example.

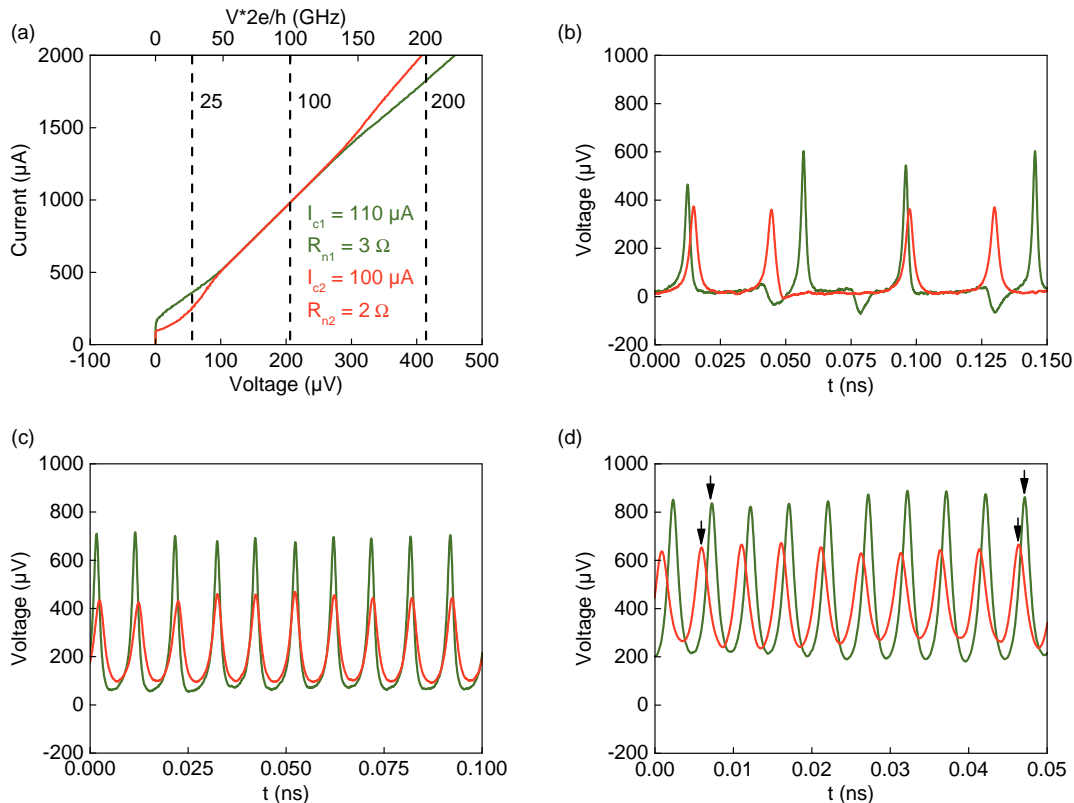


Figure 9.10: (a) Simulated IV curves of two junctions in series, shunted by the LR branch, as in figure 9.8. (b), (c) and (d) voltage as a function of time for both junctions, at 25, 100 and 200 GHz respectively. $I_{c1} = 110 \mu\text{A}$, $R_{n1} = 3 \Omega$, $I_{c2} = 100 \mu\text{A}$ and $R_{n2} = 2 \Omega$. The simulation temperature is $T = 50 \text{ K}$, $L = 20 \text{ pH}$ and $R_b = 0.5 \Omega$.

Figure 9.10 (a) shows the IV curves of two JJs in series, at 50 K, simulated with the same parameters as in figure 9.9 (b), but when the LR shunting branch is added. The situation is clearly different, with curves overlapping due to synchronization, between $V_{dc} * 2e/h = 75$ and 140 GHz. To make sure that it means phase-locking, we plotted in figures 9.10 (b), (c) and (d) a part of the temporal voltage variation at $V_{dc} * 2e/h = 25, 100$ and 200 GHz respectively. The corresponding positions are indicated by vertical dashed lines in panel (a). From dephased Lorentzian-like oscillations (a), the junctions progressively synchronize, reach phase-locked oscillations (b), and finally recover their natural behavior $V_{dc} = R_n I_{dc}$ at high biases (d), for which they are not synchronized (see arrows). Notice that the locking starts approximately at $f = (R_{n1} + R_{n2} + R_b)/(2\pi L) = 44$ GHz, as predicted by the literature [130, 91].

In figure 9.10 (a), the junction 1 seems to transit into the resistive state at a higher value than $I_{c1} = 110 \mu\text{A}$, what we defined for its critical current. It is due to the fact that when the first junction transit (JJ 2, in red), the bias current is redistributed between the two branches A and B, since branch A becomes resistive. Thus, one has to reach a bias current more important than $I_b = I_{c1}$ to have the part that actually goes into branch A exceed I_{c1} . When the second junction transits, a change of slope can be observed in the IV curve of the other one, because once again the current is brutally redistributed between the two branches at this point.

9.2.3.2 Parameter spread

We investigated in simulations the spread in parameters that we can afford, while still have phase-locking. To that end we fixed the critical current and normal resistance of one junction, at $I_{c2} = 100 \mu\text{A}$ and $R_{n2} = 2 \Omega$. Then, we varied the parameters of the second junction: $I_{c1} \in \{80, 120\} \mu\text{A}$, and $R_{n1} \in \{1, 3\} \Omega$. This gave us a set of IV curves such as the one in figure 9.10 (a), from which we determined the locking range as the situation where the difference between the d-c voltages of the two JJs is lower than 1 GHz in frequency units. It is four times lower than the oscillation's linewidth of a single junction (4 GHz at 50 K, for $R_n = 2 \Omega$, see equation 9.2) so it seems a sufficient criteria.

Figure 9.11 represents the span over which the two JJs are locked in color scale, when I_{c1} and R_{n1} vary, at 100 K. We limited the maximum frequency to $V_{dc} * 2e/h = 400$ GHz, i.e. it shows how well the junctions are synchronized up to this value.

When $I_{c1} = I_{c2}$ and $R_{n1} = R_{n2}$ the junctions are perfectly synchronized. When the parameters are not equal, the span follows the first diagonal, suggesting that the junctions are easier locked when the inequalities $I_{c1} < I_{c2}$ and $R_{n1} < R_{n2}$ are similarly ordered. In other words, as previously explained, it means that the uncoupled IV curves of the two junctions would cross each other (see figure 9.9). The locking tendency is therefore understandable, insofar as the natural junctions' oscillations have to be already close to each other.

When modifying geometrical parameters of our junctions, at first order it does not increase the $I_c R_n$ product. In other words, if make a longer barrier and a thinner junction, we increase its R_n but we decrease its I_c accordingly. Therefore in general, for two junctions, if $I_{c1} < I_{c2}$, we will likely have $R_{n1} > R_{n2}$. On figure 9.11 it corresponds to the other diagonal, on which the parameter spread is more restrictive.

Nonetheless, with these simulations we find back two commonly stated rules of thumb for synchronization: (i) the spread in the critical currents is more damaging than the one in the normal resistances, and (ii) the acceptable difference between critical currents is about $\pm 7\%$. In fact the map clearly shows that a difference of more than $\pm 15\%$ is tolerable on R_n , whereas only $\Delta I_c^{max}/I_c^{mean} < 7\%$ is acceptable. This gives us the reproducibility performances that we need to achieve phase-locking.

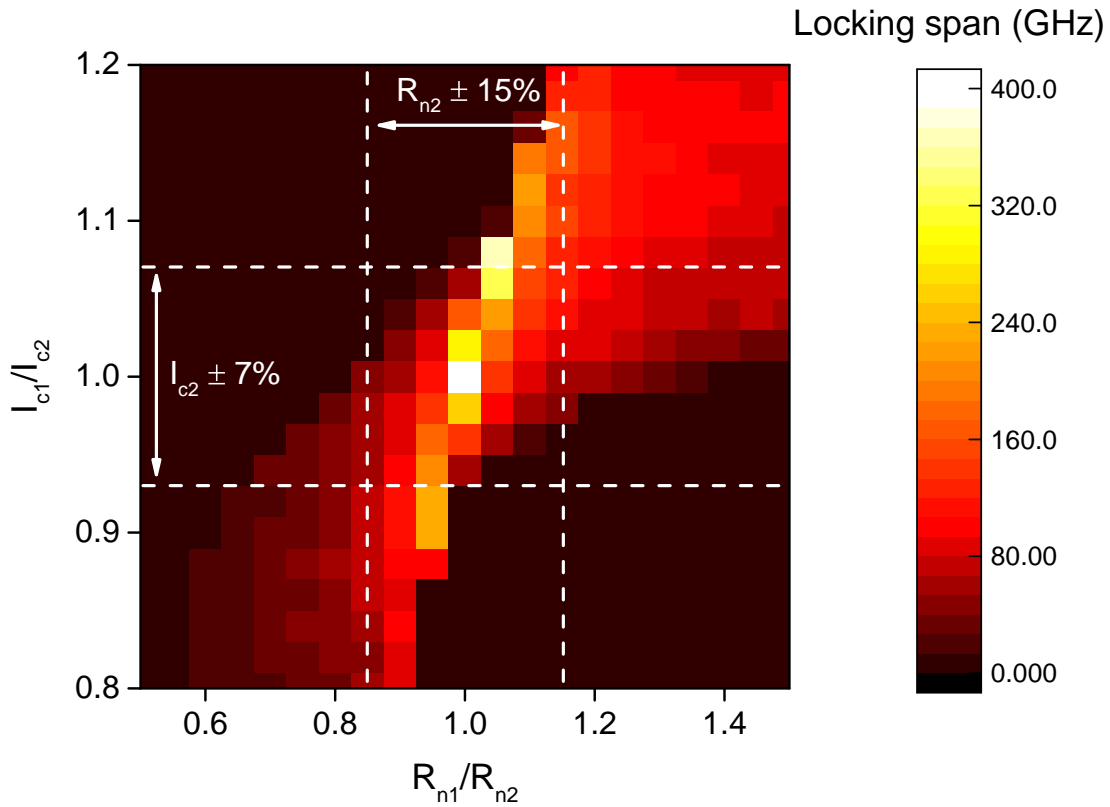


Figure 9.11: Locking span at 50 K, in color scale, when I_{c1} and R_{n1} vary. The parameters of the second junction are fixed: $I_{c2} = 100 \mu\text{A}$ and $R_{n2} = 2 \Omega$. The LR shunt branch is the same as in figure 9.10, i.e. $L = 20 \text{ pH}$ and $R_b = 0.5 \Omega$.

9.3 Characterization of externally coupled Josephson junctions

We fabricated several devices in order to test the idea of external locking, many of which are still under study. Even though the junctions could be placed in theory at an arbitrary distance, in practice one has to ensure that they are close, because any superconducting line of length l , width w and thickness t has an inductance L , sum of the geometric and kinetic terms, given by:

$$L = 0.2\mu_0 l \left(\frac{1}{2} + \ln\left(\frac{2l}{w+t}\right) \right) + \mu_0 \lambda(0)^2 \frac{l}{(1 - (T/T_c)^2)wt} \quad (9.16)$$

where $\lambda(0)$ is the London penetration depth, that we can take at 135 nm for our $\text{YBa}_2\text{Cu}_3\text{O}_7$ films [199]. For example, at 50 K, $T_c = 89 \text{ K}$ and a film thickness $t = 70 \text{ nm}$, a $1 \times 1 \mu\text{m}^2$ superconducting line has an inductance $L = 0.8 \text{ pH}$. It increases with the length of the line, for a fixed width. Thus, one has to avoid inductive effects between the junctions by placing them as close as possible. Nowadays, we can have them separated by $1 \mu\text{m}$, but a further optimization of the process (e-beam dose) could lower down the distance to a few hundreds of nm.

9.3.1 Fabricated 2D array

We end this chapter by presenting the latest measurement results, that were performed on a 10×10 shorted 2D array, in which we believe that we observe evidences of synchronization. Figure 9.12 is a photograph of the fabricated device. It is in fact a grid, that can be biased top to bottom. The

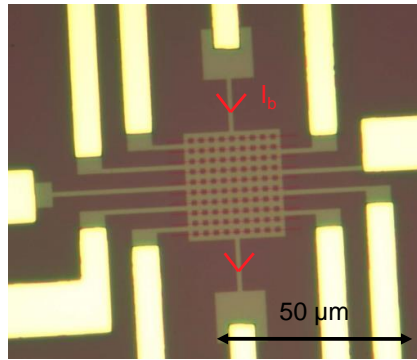


Figure 9.12: Photograph of the 10x10 2D shorted array.

grid rows and columns are all 1 μm wide superconducting lines. There is an electrode at the end of each line, so that voltages can be simultaneously measured across all of them. The junctions are at the intersecting position between the grid (light green) and the slits in the PMMA resist, horizontal brown lines, slightly visible.

The equivalent circuit is given in figure 9.13. As a first approach, we neglect the line inductances in the array, validated by the above discussion. The 2D array is a good method to overcome any parameter spread. In fact, each line acts as a single junction whose I_c and R_n depend on the ones of the junctions it harvests. More precisely the critical current of one line is simply the sum of the junctions', and its R_n is the inverse of the inverted normal resistances' sum. It is another reason why may be the most efficient way to fabricate a local oscillator.

Even though we did not explicitly fabricated an external LR shunt (what should be investigated in any further study), a coupling between the lines hopefully happens thanks to all the SQUID loops in the grid. In other words, a junction from one line can couple with one from another line through LR shunting loops, in which L is a Josephson inductance.

9.3.2 Evidences of synchronization in the IV curves

Figures 9.14 (a), (b), (c) and (d) show the IV curves of several lines, taken at 31 K, 33 K, 39 K and 41 K respectively. We emphasized synchronization effects by light blue shades. At 31 K and 33 K, line 6 (L6) clearly shows a perturbed behavior at low biases (see insets), with an obvious locking on L1 at 33 K, between 5 and 10 GHz. At these temperatures, notice also that the IV curves of L1 and L2 on one hand, and L9 and L10 on the other hand tend to join but do not overlap.

Then, at 39 K and 41 K, two different groups of IV curves overlap: one formed by L1, L2, L4 and L5, and another by L9 and L10. From the insets, we see that the IV curve of L1 (in dark green) clearly joins the ones of L2-5. Thus, the lines tend to lock with their neighbors, but as the distance increases, unified locking is lost, and they synchronize in different groups. Once again, a feedback loop between L1 and L10 could overcome this issue.

At high biases, the curves progressively drift from each other, and we lose synchronization in the same manner as in the simulation of figure 9.10. Thus, we estimate that a synchronization arise inside these two different groups, between 70 and 170 GHz at 39 K, and 60 and 110 GHz at 41 K. Therefore an optimal temperature may be found.

We did not show the IV curves of the other lines, because no synchronization effect was obvious. In addition, even if L6 interacts with L1 at 33 K, it did not obviously locked with the first group (L1-5) at higher temperatures.

In conclusion, we showed that synchronization effects arise in the array, evidenced by overlapping IV curves. At 39 K and 41 K, two different groups of lines tend to lock. This phenomenon could be greatly improved, and a unified phase-locking could be achieved in the whole 2D array

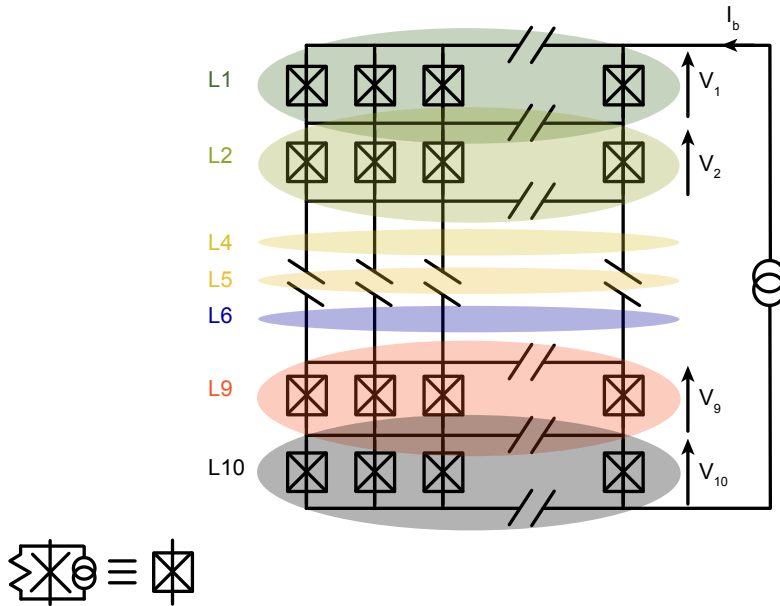


Figure 9.13: Circuit of the 10×10 2D array. When current biased top to bottom, the voltages across each line can be read independently.

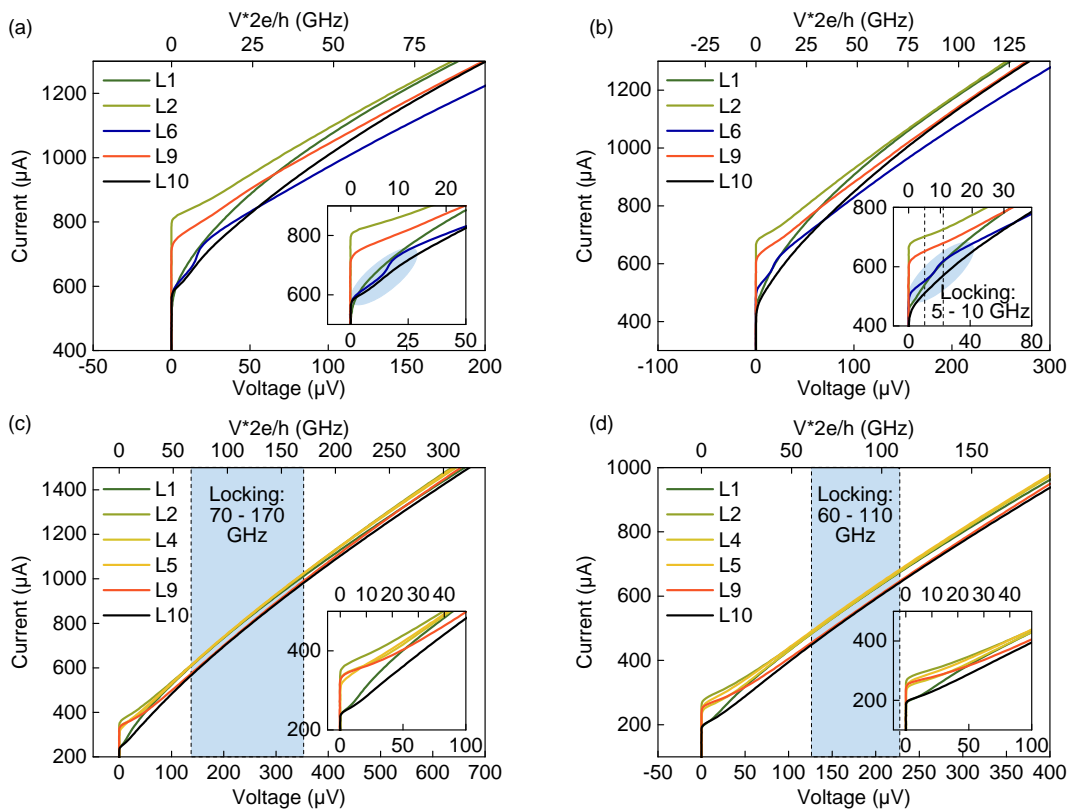


Figure 9.14: IV curves of several lines in the 10×10 2D array, at 31 K (a), 33 K (b), 39 K (c) and 41 K (d). The locking phenomena are emphasized with the light blue shades. At 31 K and 33 K, L6 tends to phase lock with the previous lines, and at 39 K and 41 K, phase-locking happens in two separate groups of lines.

with external LR shunts between lines. Another option would be to apply an external magnetic

field, in the perpendicular direction to the array plane [60], and to confront its response to simulations [63].

9.4 Conclusion on the synchronization of Josephson junctions

When synchronized, radiation characteristics of a Josephson junction array are greatly increased compared to a single junction. It improves both the linewidth, made thinner, and the emitted power, made higher. In this frame, 2D arrays give the best theoretical performances, at the expense of a more complicated design than 1D arrays.

We reviewed the different coupling mechanisms existing, and identified the long range interactions as the only efficient way to couple high- T_c Josephson junctions. In the diverse zoology of possible arrays, we identified the shorted 2D array as a promising scheme to detect a first synchronization effect with $\text{YBa}_2\text{Cu}_3\text{O}_7$ irradiated Josephson junctions. Furthermore, its rather simple structure makes it understandable, possible to simulate, and a good candidate for additional schemes such as external feedback loops.

In order to understand more deeply the physics of the high-frequency coupling, we studied the effect of an inductive and resistive feedback loop on two junctions placed in series. The parallel inductance value has to be carefully engineered, so as to enhance the feedback. We thus found reasonable parameters for our junction's characteristics, and showed that synchronization is in principle possible at 50 K. The effect of parameter spread was also investigated in simulations, comforting ourselves in the possibility to achieve a good synchronization with our technology.

Finally, we presented the first results that we obtained on a 10x10 shorted 2D array, for which evidences of synchronization are observable. With the agility of our fabrication process, further improvements will undoubtedly come up, and what we showed here paves the way to an integrated local oscillator for Josephson mixers.

Conclusion

Driven by a transverse approach, we proposed in this thesis to address terahertz detection with a high- T_c Josephson mixer, which performances were evaluated. We also harnessed the idea of creating a local oscillator with high- T_c Josephson junctions. Overall, the originality of this study stems from the unique process that has been developed to fabricate $\text{YBa}_2\text{Cu}_3\text{O}_7$ Josephson junctions, and from the multiple physics required to understand such devices. It led to the results presented in this manuscript.

Having reviewed the existing terahertz detectors and sources, we showed that our technology could be competitive in the sense that high- T_c Josephson mixers work at fairly high temperatures, and necessitate extremely low local oscillator powers. Of course, their sensitivity does not compete with low- T_c SIS mixers, but they may find a place in prolonged space observation missions, or in affordable short range communications systems. In any case, they will require further improvements and characterization.

We successfully applied a modified version of the proximity effect theory, originally developed for low- T_c materials, to describe the complex physics of Josephson junctions, fabricated by ion irradiation. Allied with data obtained from implantation simulations, we were able to quantitatively explain their behavior with temperature. From an experimental point of view, it set the range of parameters, energy and dose, that should be used during ion irradiation. The fabrication process and the implantation simulations also showed the limits of our technology in terms of resolution. Overall, it seems that working with 750 nm wide and 40 nm long junctions is the limit beyond which reproducibility is poor. This leads to $I_c R_n$ products of about 0.2 mV.

The d-c transport measurements showed that the Josephson junction respects the resistively shunted junction (RSJ) model, in a range of temperature of about 40 K to 60 K, where the transport is mainly determined by Josephson effect. Inside, the characteristic frequency displays a maximum of about 85 GHz around 50K. Below, there is a continuous transition to the flux-flow regime and the Josephson oscillations progressively disappear. Taking into account the peculiar physics of our junction, in which the normal part extends with the current bias, we successfully fitted current-voltage characteristics and Shapiro steps with a modified RSJ model.

We explained the mixing operation with the three-port model, from which we identified the conversion efficiency as the product of three terms: two depending on the impedance mismatches and the third one characterizing the intrinsic down-conversion ability. With a microwave setup, we proved the heterodyne detection of signals up to 400 GHz, and performed an extensive study of the Josephson mixer's performances. We measured its dynamic range, of more than 55 dB at 20 GHz and 30 dB at 140 GHz. We showed that it needs between 0.1 nW to 10 nW of local oscillator power, which is two orders of magnitude lower than classical cryogenic heterodyne detectors, SIS or HEB. The optimum power diminishes by half the critical current, but the mixer's performances do not severely depend on it. Finally, we evaluated its conversion efficiency: about 2% at 20 GHz and down to 0.01% at 140 GHz. These low values sprang from the fact that we were penalized by poor impedance matching, at the input and output of the mixer. We were able to fit the shape of the conversion efficiency with the three-port model at different frequencies, from 20 to 140 GHz.

It displayed a transition at the characteristic frequency, below which the optimum mixing point is in the middle of the risers, and above which it shifts towards the edges of the Shapiro steps.

Finally, we paved the way towards the use of irradiated Josephson junctions as coherent terahertz emitters. We identified the long range interactions as the only efficient mechanism to trigger synchronization in high- T_c Josephson junctions. We explained in detail the physics of an external feedback loop, and showed its effect in simulated systems. It allowed us to set experimental parameters for the design of Josephson junction arrays. Finally we saw a first evidence of synchronization in a 10×10 shorted 2D array.

What remains to be done ? We proposed several roads that we believe are worth further investigation. Many of them were supported by promising simulations, the approach which, all along the course of this thesis, bolstered our understanding of physical systems, and helped to set boundaries for experimental parameters. First, the flexibility of our fabrication technology is a unique tool to achieve coherent emission with synchronized junctions. Then, for an applicative perspective, one will have to accurately evaluate the noise temperature of the device. Josephson mixers have been known to be noisy, but Josephson junction arrays as detectors could circumvent the issue. The low conversion efficiencies thwarted us from correctly performing a noise measurement, but we proposed a design whose impedances are better matched to the junction's, and hope that it will be used in a hot/cold measurement scheme. Finally, we proposed the idea according to which the junction's self-oscillation would be used as a local oscillator, when filtered by an external inductive branch.

Appendix A

Fluctuations of a thermal and coherent radiation on a direct detector

A.1 Absorbed power

Any detector can undergo to two limit cases of radiation: coherent and thermal (completely incoherent), on which depend the minimum fluctuations, hence the noise stemming from the measurement process. The situation is particularly complex in a heterodyne detector, because the fluctuations come from two sources: a (fairly) coherent LO and an incoherent signal.

In any case, one can show that the mean incident power on a receiver can be written as:

$$\langle P_{inc} \rangle = \sum_m^M \int_{\nu_0}^{\nu_0 + \Delta\nu} h\nu \langle n_m(\nu) \rangle d\nu \quad (\text{A.1})$$

where we assume that it responds only to radiations whose frequencies lie between ν_0 and $\nu_0 + \Delta\nu$ and where $\langle n_m(\nu) \rangle$ is the mean number of photons in the spatial mode m . M is the maximum number of spatial modes that the receiver can accept, which depends on its geometry (see cite). Often in THz detecting systems, $M > 1$ but it is not high enough to approximate the sum by an integral. The discrimination between the two limit cases, thermal or coherent, enters in the shape of distribution function $\langle n_m(\nu) \rangle$. If $\eta_m(\nu)$ is the absorption efficiency of the receiver for a photon in the mode m , the mean absorption power is given by:

$$\langle P_{abs} \rangle = \sum_m^M \int_{\nu_0}^{\nu_0 + \Delta\nu} \eta_m(\nu) h\nu \langle n_m(\nu) \rangle d\nu \quad (\text{A.2})$$

Thermal radiation. For a thermal radiation, $\langle n_m(\nu) \rangle$ is given by the Planck function, which we consider identical for all spatial modes:

$$\langle n_m(\nu) \rangle = \frac{1}{e^{\frac{h\nu}{k_B T}} - 1} = f_p(\nu) \quad (\text{A.3})$$

In the "band-limited" assumption we consider that the passband is narrow enough so that ν and f_p can be considered constant over the range of integration, and that all the modes are equally well matched: $\eta_m(\nu) = \eta_m$. Then the absorbed power writes itself as:

$$\langle P_{abs} \rangle = h\nu_0 f_p \Delta\nu \sum_m^M \eta_m \quad (\text{A.4})$$

In the Rayleigh-Jeans limit, $k_B T \gg h\nu$, therefore $e^{\frac{h\nu}{k_B T}} - 1 \simeq \frac{h\nu}{k_B T}$ and if we assume that all the M modes are perfectly matched to the sensor ($\eta_m = 1$) we get:

$$\langle P_{inc} \rangle = \langle P_{abs} \rangle = k_B T \Delta\nu M \quad (\text{A.5})$$

Note that this expression is also true in the case of an arbitrarily large-band sensor, since we can make the same simplification under the integral of expression A.2.

Coherent radiation. For a coherent radiation, the probability of measuring n photons in an arbitrary time interval is given by the Poisson statistics:

$$p(n) = \frac{[\langle n \rangle (t)]^n}{n!} e^{-\langle n \rangle (t)} \quad (\text{A.6})$$

where $\langle n \rangle (t) \sim \sin^2(\omega_0 t)$. Hence, considering that all the modes are equally well matched:

$$\langle P_{abs} \rangle = \langle P_{inc} \rangle \sum_m^M \eta_m = h\nu_0 \Delta\nu \langle n \rangle \sum_m^M \eta_m \quad (\text{A.7})$$

which, for a monomode coherent radiation ($m = 1$) gives:

$$\langle P_{abs} \rangle = \eta \langle P_{inc} \rangle = \eta h\nu_0 \Delta\nu \langle n \rangle \quad (\text{A.8})$$

A.2 Fluctuations

Under the band-limited assumption, one can show that the fluctuations of the absorbed power, for any radiation can be written as:

$$\langle (\Delta P_{abs})^2 \rangle = (h\nu_0 \Delta\nu)^2 \langle [\Delta n_m(\nu_0)]^2 \rangle > \sum_m^M \eta_m \quad (\text{A.9})$$

In the special case of only one spatial mode:

$$\langle (\Delta P_{abs})^2 \rangle = (h\nu_0 \Delta\nu)^2 \langle \Delta n(\nu_0) \rangle^2 \eta \quad (\text{A.10})$$

which gives in general the best case prediction experimentally. Let us compute the power spectral density $S_p(\nu)$ defined as:

$$S_p(\nu) \equiv \frac{\sqrt{\langle (\Delta P_{abs})^2 \rangle}}{\Delta\nu} \quad (\text{A.11})$$

in the two limit cases, thermal and coherent.

Thermal radiation. In a thermal radiation the fluctuations $\langle \Delta n(\nu) \rangle^2$ are given by:

$$\langle \Delta n(\nu) \rangle^2 = f_p(f_p + 1) \quad (\text{A.12})$$

Therefore

$$\langle (\Delta P_{abs})^2 \rangle = (h\nu_0 \Delta\nu)^2 f_p(f_p + 1) \sum_m^M \eta_m \quad (\text{A.13})$$

There are two important situations: first the low frequency limit, i.e. the Rayleigh-Jeans limit $k_B T \gg h\nu$. In this situation $\langle \Delta n(\nu) \rangle^2 \simeq (k_B T / h\nu)^2$ and:

$$\langle (\Delta P_{abs})^2 \rangle = (k_B T \Delta\nu)^2 \sum_m^M \eta_m \quad (\text{A.14})$$

The power spectral density $S_p(\nu)$ is then given by the famous Johnson-Nyquist theorem:

$$S_p(\nu) = k_B T \sqrt{\sum_m^M \eta_m} \quad (\text{A.15})$$

Second, in the high frequency limit, i.e. $k_B T \ll h\nu$, we have $f_p \ll 1$ hence $f_p(f_p + 1) \simeq f_p$ and considering that (in the band-limited assumption) $\langle P_{inc} \rangle = h\nu_0 f_p \Delta\nu$ (equation A.1) we get:

$$S_p(\nu) = \sqrt{\frac{h\nu_0 \langle P_{inc} \rangle \sum_m^M \eta_m}{\Delta\nu}} \quad (\text{A.16})$$

which is the expression of the photon shot noise. In general we are more familiar to its expression in terms of the current spectral density fluctuations that the radiation measurement induces on a square-law detector. In these devices, an absorbed photon generates charge carriers, hence a photocurrent given by:

$$I = \frac{eg}{h\nu_0} P_{inc} \quad (\text{A.17})$$

where g is the photoconductive gain. A square-law detector can only measure $\langle I \rangle^2$:

$$\langle I \rangle^2 = 2 \left(\frac{eg}{h\nu_0} \right)^2 \langle P_{inc} \rangle^2 \quad (\text{A.18})$$

Thus the current spectral density fluctuations (for a perfectly matched monomode incoming radiation) are given by:

$$S_I(\nu) = 2 \left(\frac{eg}{h\nu_0} \right)^2 S_p(\nu)^2 \Delta\nu = 2egI_{dc} \quad (\text{A.19})$$

where $I_{dc} = \langle P_{inc} \rangle = \frac{\sqrt{\langle I \rangle^2}}{\sqrt{2}}$ is the d-c. current. As we can see, although similar to the current fluctuations in electronic devices, the photon shot noise is *not* due to current fluctuations, but arise from the measurement process of a coherent radiation.

Coherent radiation. Given the Poisson statistics of coherent radiations (equation A.6), the variance is equal to the mean:

$$\langle n \rangle = \langle (\Delta n)^2 \rangle \quad (\text{A.20})$$

Therefore, for a monomode coherent radiation we get from equation A.8:

$$\langle P_{abs} \rangle = \eta h\nu_0 \Delta\nu \langle (\Delta n)^2 \rangle \quad (\text{A.21})$$

and replacing in equation A.10:

$$S_p(\nu) = \sqrt{\frac{\eta h\nu_0 \langle P_{inc} \rangle}{\Delta\nu}} \quad (\text{A.22})$$

A.3 Number of collected modes

It is in general difficult to calculate and measure the number of modes M collected by a detector. However a simple estimation can be done, using the Antenna theorem. For a beam with a solid angle Ω_B shined onto a detector having a field of view Ω_{FOV} we estimate:

$$M = \frac{\Omega_{FOV}}{\Omega_B} \quad (\text{A.23})$$

Now, the antenna theorem states that:

$$\Omega_B \geq \frac{\lambda^2}{A} \quad (\text{A.24})$$

where A is the area of the collecting antenna. The equality is reached for a diffraction limited situation. Hence a good estimation is:

$$M = \frac{\Omega_{FOV} A}{\lambda^2} \quad (\text{A.25})$$

The number of modes traveling into WR-N metallic waveguides can be exactly computed. In fact in this standard, the ratio between the width and the height of the rectangular waveguide is $W/h = 2$, and the N gives the width in 1/100 th of inches. Then, the cut-off low frequency is given by:

$$v_{cLow} = \frac{c}{2W} \quad (\text{A.26})$$

so for example, a WR5 has a cut-off low frequency at 118 GHz. More generally, the cut-off frequency for any TEM_n mode is given by:

$$v_c^{m,n} = c \sqrt{\left(\frac{m}{2W}\right)^2 + \left(\frac{n}{2h}\right)^2} \quad (\text{A.27})$$

Hence, given a traveling frequency v_0 into the waveguide, one can count the number of different combinations of m and n such that $v_c^{m,n} < v_0$, which gives the number of modes M .

In both cases (free space or waveguide) a good approximation is given by:

$$M = \left[\frac{v_0}{v_R} \right]^2 + 1 \quad (\text{A.28})$$

where v_0 is the traveling frequency, $[\]$ is the rounding down integer function, and v_R is a fitting frequency parameter. Usually v_R is somewhat greater than v_{cLow} . For example for a WR10 waveguide, $v_{cLow} = 59$ GHz and $v_R = 85$ GHz. For a golay cell whose area is 6 mm and whose focal length is 50 mm, the number of modes given by equation A.25 is:

$$M = 2\pi \left[1 - \cos\left(\frac{6}{50}\right) \right] \pi (6 \cdot 10^{-3})^2 \left(\frac{400 \cdot 10^9}{3 \cdot 10^8} \right) \simeq 9 \quad (\text{A.29})$$

And the formula A.28 gives also $M = 9$ with $v_R = 125$ GHz.

A.4 NEP in direct detection

Coherent radiation. For a single mode coherent radiation, one can form the SNR before detection from equations A.8 and A.21:

$$SNR_{BD} = \sqrt{\frac{\eta P_{inc}}{h\nu\Delta\nu}} \quad (\text{A.30})$$

Hence the NEP_{BD} is given by:

$$NEP_{BD} = \frac{h\nu}{\eta} \Delta\nu \quad (\text{A.31})$$

which again, states the quantum limit of the measurement. Equations 1.6 and 1.8 give the NEP_{AD} and NEP'_{AD} :

$$NEP_{AD} = \frac{h\nu}{\eta} \sqrt{2\Delta\nu\Delta f} \quad (\text{A.32})$$

$$NEP'_{AD} = \frac{h\nu}{\eta} \sqrt{2\Delta\nu} \quad (\text{A.33})$$

Thermal signal. Equations A.4 and A.13 yield to the SNR before detection:

$$SNR_{BD} = \frac{\sqrt{\sum_m^M \eta_m f_p}}{\sqrt{f_p(f_p + 1)}} = e^{-\frac{h\nu_0}{k_B T}} \sqrt{\sum_m^M \eta_m} \quad (\text{A.34})$$

the quantum limit of the NEP appears more clearly if we use $\langle P_{inc} \rangle = Mh\nu_0\Delta\nu f_p$ (from equation A.4). Then:

$$SNR_{BD} = \sqrt{\frac{\sum_m^M \eta_m \langle P_{inc} \rangle}{\langle P_{inc} \rangle + Mh\nu\Delta\nu}} \quad (\text{A.35})$$

and therefore we find the NEP_{BD} :

$$NEP_{BD} = \frac{Mh\nu_0\Delta\nu}{\sum_m^M \eta_m - 1} \quad (\text{A.36})$$

Equations 1.6 and 1.8 allow to compute the NEP_{AD} and NEP'_{AD} :

$$NEP_{AD} = \frac{Mh\nu_0}{\sum_m^M \eta_m - 1} \sqrt{2\Delta\nu\Delta f} \quad (\text{A.37})$$

$$NEP'_{AD} = \frac{Mh\nu_0}{\sum_m^M \eta_m - 1} \sqrt{2\Delta\nu} \quad (\text{A.38})$$

In the Rayleigh-Jeans limit, $k_B T \gg h\nu_0$ and with equation A.5, $\langle P_{inc} \rangle = k_B T \Delta\nu M$ therefore:

$$NE\Delta T = \frac{NEP_{AD}}{k_B \Delta\nu M} \quad (\text{A.39})$$

Appendix B

Fabrication details of $\text{YBa}_2\text{Cu}_3\text{O}_7$ irradiated Josephson junctions

The samples contain a 70 nm $\text{YBa}_2\text{Cu}_3\text{O}_7$ film (CeO_2 buffered), 9x9 mm, single sided, E-Type. On $\text{YBa}_2\text{Cu}_3\text{O}_7$ is grown in situ 250 nm of a gold layer. The substrate is Al_2O_3 , on r-cut, 10x10x0.5 mm thick, one side polished. The company gives a typical critical temperature of about 85 K and a critical current density of about $3 \text{ MA}\cdot\text{cm}^{-2}$.

B.1 Step 1: structuring the gold layer

The MAN-2405 deposition is done the following way:

- Clean the sample: 5 min in acetone with ultrasounds, followed by 5 min in isopropanol (IPA) with ultrasounds.
- Dehydrate the sample: 1 min on a heating plate at 90°C . All along the process, one should avoid to heat the sample beyond 100°C , otherwise one might deplete the oxygens.
- Spin coat an adhesion promoter, the bis(trimethylsilyl)amine (HMDS) at 6000/4000/30, which means at an acceleration of 600 rpm, a speed of 4000 rpm and for 30 s.
- Wait for a few seconds and spin coat the MAN-2405 at 3000/3000/30. This gives a 500-550 nm thickness (measured with a profilometer and in agreement with the spin coating specifications of the resist [10]).
- Bake 3 min at 90°C .

It is photosensitive, hence one has to manipulate it in a UV free environment until its chemical development. Depending on the size of the areas to scan, one uses two different sets of parameters for the first e-beam:

- Layer 0, for big areas (greater than a few tenth of μm^2). Dose: $190\text{-}200 \mu\text{C}\cdot\text{cm}^{-2}$, step: $0.1 \mu\text{m}$ and current: 6.4 nA. The higher the current, the shorter the exposure. The writing field is $100 \mu\text{m}^2$ (magnification 600 X).
- Layer 1, for smaller areas (a few μm^2). Dose: $170 \mu\text{C}\cdot\text{cm}^{-2}$, step: $0.02 \mu\text{m}$ and a current: 0.4 nA. The writing field is $100 \mu\text{m}^2$ (magnification 600 X).

This parameters were optimized for a SEM FEG-SEM, Magellan FEI. One should better separate the total exposing field and have one per device, so as to ensure the smallest alignment shift.

Indeed there is always a global shift between the different writing fields when the beam scans the whole sample surface. Moreover, the layer 1 harvests the realignment marks for the next e-beam exposures, so they must be perfectly aligned with respect to each device.

The MAN-2405 is a negative photo and electro resist, hence the zones exposed to the electron beam remain after the chemical development. The developing procedure removes the unexposed resist:

- Develop 30 s in a solution of AZ 726 MIF developer. The best way is for the sample to rise an eight in the solution.
- Wash 20 s in distilled water.
- Repeat three times the first two steps, then change the distilled water.
- Repeat one more time the first two steps.
- Develop 15 s in the AZ 726 MIF developer.
- wash 15 s in distilled water.
- repeat one time the last two steps.

Thus, the total developing time is 150 s, and the switch between water and developer ensures a smooth process. Also, that way one can optically control the operation during the development. Figure 2.8 (b) represents the sample at this stage.

The Ar etching is done in a Plassys MEB 550S (at Paris 7 clean room). In order to ensure an homogeneous etching, one should place the sample at the center of the sample holder, tilt the it by 10° with respect to the Ar beam, and rotate it at 10°s^{-1} . The etching time depends on the thickness of the gold layer: it can be controlled with a secondary ion monitor system (SIMS) but without it, a good rule of thumb indicates that 20 nm of Au is etched per minute, so for 250 nm the process lasts 750 s.

After cleaning 15 to 20 min in acetone with ultrasounds, then 10 min in isopropanol with ultrasounds, the sample is a $\text{YBa}_2\text{Cu}_3\text{O}_7$ layer on top of which the gold layer is patterned. Figure 2.8 (d) represents a spiral antenna embedded in a microwave transmission line at the end of such a step, for which a photograph is at figure 2.9 (c).

B.2 Step 2: patterning the $\text{YBa}_2\text{Cu}_3\text{O}_7$ layer

The second deposition of the resist is similar to the first one. A fine realignment on each design has to be done. We expose only $100\ \mu\text{m}^2$, hence no write field alignment is needed. The fine structures of each design are then bound to fit inside $100\ \mu\text{m}^2$ but it always has been large enough. We also pattern protections between islands of gold for the 4 point measurement of the d-c current and voltage. The e-beam parameters are the following:

- Layer 2, for the protections. Dose: $190\text{-}200\ \mu\text{C}\cdot\text{cm}^{-2}$, step: $0.1\ \mu\text{m}$ and current: 6.4 nA. The writing field is $100\ \mu\text{m}^2$ (magnification 600 X).
- Layer 3, for the fine realignments. The alignment procedure uses 4 markers for each design, patterned in the gold layer during the first e-beam. Dose: $160\ \mu\text{C}\cdot\text{cm}^{-2}$, step: $0.02\ \mu\text{m}$ and current: 13 pA. The writing field is $100\ \mu\text{m}^2$ (magnification 600 X), no write field alignment is needed since we only expose $100\ \mu\text{m}^2$.

Then the sample undergoes the first ion implantation. It is done at the INESS Laboratory in Strasbourg. We prepare them in a clean room environment where they are carbon taped at the center of a 2 inches silicon wafer or metallic plate. The carbon tape ensures a good charge evacuation, but one might improve the process by clamping the samples.

The implantation parameters are: O^+ ions sent at 70 keV, with a dose of 2.10^{15} ions.cm⁻². Also one should ensure that the current flowing through a 3 inches wafer does not exceed 20 μ A to avoid any heating effect. Hence the current should not exceed 0.44μ A.cm⁻². Given such a dose and current, the typical ion irradiation time is 10-15 minutes.

B.3 Step 3: creating the weak-link.

After the first implantation one needs to clean the sample prior to the third e-beam lithography. Very often, the irradiated MAN-2405 is quite difficult to remove. Thus one has to:

- put the sample 30 min in acetone with ultrasounds, followed by 30 min in isopropanol with ultrasounds.
- Finish with a short reactive ion etching with oxygen ions (50 mTorr, 100 sccm O₂, 60 W). The O₂ plasma should not exceed 3 minutes, which is enough to remove the remains of the resist (optically controlled).

The last e-beam lithography is done at the LPN laboratory (in Marcoussis), with a vistec ebpg 5000+. It generates a 100 keV beam, has a writing speed of 50 MHz and an ultimate resolution of 10 nm. One needs such high performances to open the 40 nm narrow slits in the 500 – 550 nm thick PMMA. The PMMA is a positive electro sensitive resist, hence the exposed part come off during the chemical development.

Before the e-beam, one has to prepare the sample:

- Spin coat the PMMA (type "A7", 50 g.L⁻¹) at 4000/4000/30.
- Bake 3 minutes at 100°C.
- Optionally, deposit a thin aluminum layer (20-30 nm) to ensure a good charge evacuation during the e-beam.

We then expose the PMMA to the electron beam with the following parameters:

- Layer 4 for the thin slits. Dose of 2500μ C.cm⁻², step: 2.5 nm and current: 1 nA. The writing field is 100μ m².
- Layer 5 to remove the PMMA on the d-c pads. Dose of 1100μ C.cm⁻², step: 20 nm and current: 100 nA. The writing field is 100μ m².

Then, one removes the aluminum metalization in a NaOH solution (5-10 g.L⁻¹) and develop the PMMA 45 s in a diluted solution of MIBK/IPA (proportions 1/3). The figures B.1 represent the different fabrication steps of a 10×10 2D array of Josephson junctions. The picture B.1 (a) is captured after the IBE, the picture B.1 (b) is taken at the end of the second e-beam lithography and the picture B.1 (c) at the end of the third one. On the later we distinguish the result of the e-beam in the PMMA: thin horizontal brown lines inside the 10×10 square matrix. The figure 2.10 (b) represents the central part of an antenna, on which we also distinguish a slit in the PMMA.

For the oxygen annealing, one should avoid to heat too much the samples to prevent the oxygen depletion. Hence we chose the following parameters: annealing for 3 hours at 110°C in a saturated oxygen atmosphere. The O₂ flow is controlled by a bubbler at the exit of the oven (approximately one bubble per second).

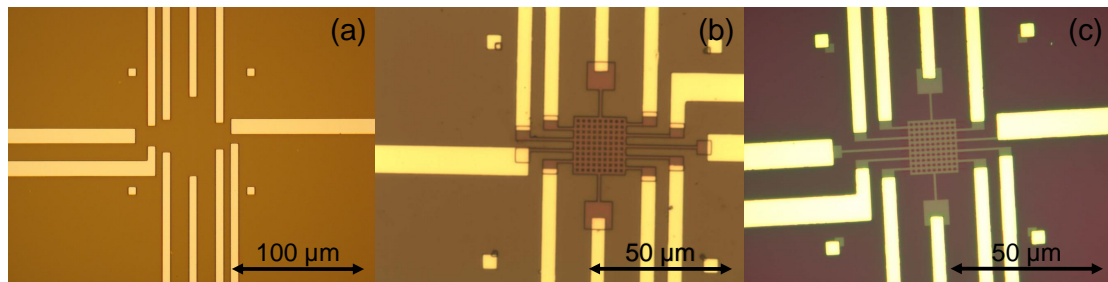


Figure B.1: (a) Optical photo of *d-c* Au contacts on $\text{YBa}_2\text{Cu}_3\text{O}_7$, after the IBE. (b) Optical photo of the same contacts connected to a design of a 10×10 2D array, after the second *e*-beam lithography. (c) Optical photo of the same design after the third *e*-beam lithography. The slits (brown thin lines inside the square matrix) appear on the PMMA.

Appendix C

Numerical resolution of the RSJ equations

In practice, the simulation of an IV curve consists in solving the system equations 3.39 by numerical integration, and we simply used the Euler method. A LO enters in the model as additional current source, purely coherent. Hence the system to be numerically solved (with a homemade C program running with Matlab) is:

$$\begin{cases} v[n+1] = R_n(i_b)(i_b - \sin\phi[n] + \delta i_n + i_{LO}\cos(\kappa_{LO}\tau[n])) \\ \phi[n+1] = \phi[n] + v[n+1]\delta\tau \end{cases} \quad (\text{C.1})$$

where the bracket notation means discrete time steps, of pace $\delta\tau$. i_b is the (static) current bias and κ_{LO} is the LO normalized frequency. For each current bias, a voltage vector is thus found iteratively, for each step $\tau = 0 : d\tau : \tau_{max}$, starting with a random initial phase and $v[0] = 0$. The initial conditions in the RCSJ model are more subtle, since one needs to enter the history of the system. Thus one takes $v[0] = v_{dc}^{[i-1]}$, for an increasing current and $v[0] = v_{dc}^{[i+1]}$ for a decreasing one. In any case, the noise δi_n is a random variable changed at every step, whose variance is given by 3.42.

The system is numerically heavy to solve: first because one needs a sufficiently small $\delta\tau$ to account for the rapid variation of the voltage oscillations, especially at low bias where there are short pulses, and at the same time one needs at sufficiently high τ_{max} in order to have enough oscillations to average. With the LO, $\delta\tau$ must be much smaller than $1/\kappa_{LO}$, and τ_{max} should be sufficiently high to average enough IF oscillations. We typically have vectors of 200000 points, and $\delta\tau \sim 0.01$. Second because the presence of the (actually pseudo random) noise also requires to average the calculation of each v_{dc} over several iterations of the same IV curve (especially for mixing simulations). Typically, 10 averages give smooth enough curves (500 are required for the mixing simulations).

Appendix D

Numerical resolution of the Usadel equations

D.1 Equations to solve

In the θ - χ parametrization, the self-consistent Usadel equations to be solved are the three following expressions, for any integer n :

$$\frac{\hbar D}{2} \frac{\partial^2 \theta_n}{\partial x^2} - \left[\frac{\hbar D}{2} \left(\frac{\partial \chi}{\partial x} \right)^2 + \hbar \Gamma(x) \right] \sin \theta_n \cos \theta_n - \omega_n \sin \theta_n + 2\Delta(x) \cos \theta_n = 0 \quad (\text{D.1})$$

$$\frac{\partial}{\partial x} \left[\frac{\partial \chi}{\partial x} \sin^2 \theta_n(x) \right] = 0 \quad (\text{D.2})$$

$$|\Delta(x)| = \lambda 2\pi k_B T \sum_{n \geq 0} \sin(\theta_n(x)) \quad (\text{D.3})$$

$\omega_n = (2n + 1)\pi k_B T$ are the Matsubara frequencies. The second one is the continuity equation and the third one is the expression of the superconducting gap $|\Delta(x)|$. $\Gamma(x)$ is the displacement per atom, given by the implantation simulations. It acts as a pair-breaking term.

After resolution, the supercurrent density will be given by:

$$j_s = -2\pi e v(0) D k_B T \frac{\partial \chi}{\partial x} \sum_{n \geq 0} \sin^2(\theta_n(x)) \quad (\text{D.4})$$

D.2 Boundary conditions

The Usadel equations describe the evolution of the Green functions for the normal electrons and the paired electrons. In order to solve [D.1](#) we need to add boundary conditions, through which we will specify the nature of the S-N interface (located at $x = 0$). In the case of a transparent interface, the boundary conditions are given by:

$$\sigma_S \left(\frac{\partial \theta_n}{\partial x} \right)_{x=0^-} = \sigma_N \left(\frac{\partial \theta_n}{\partial x} \right)_{x=0^+} \quad (\text{D.5})$$

$$\sin(\theta_n(x = 0^-)) = \sin(\theta_n(x = 0^+)) \quad (\text{D.6})$$

where σ_N and σ_S are the electrical conductivity in the normal and in the superconducting part respectively. Equation [D.5](#) represents the momentum conservation during the Andreev reflection and equation [D.6](#) indicates the continuity of the Green functions amplitudes at the interface (transparency). Far from the interface, for a BCS superconductor, one has:

$$\tan \theta_n = \frac{\Delta}{\omega_n} \quad (\text{D.7})$$

D.3 Algorithm

The numerical resolution of the system consists in finding θ_n and χ . It is delicate since equation D.1 is strongly non linear. We intend to solve an equation of the form $\forall x, f(\theta_n(x)) = 0$ for a given Matsubara frequency ω_n . To do so we use a relaxation method. It consists in starting with a first estimation of $\theta_n(x)$ and then correct this approximation with a $\delta\theta_n(x)$ term that is found by saying that $f(\theta_n(x) + \delta\theta_n(x)) = 0$. Then one iterates the process with a new value $\theta_n(x)' = \theta_n(x) + \delta\theta_n(x)$ until a stopping condition is reached (such as $\delta\theta_n < \varepsilon$, where ε is a small numerical constant). We linearize $f(\theta_n(x) + \delta\theta_n(x))$ such that:

$$f(\theta_n(x_i) + \delta\theta_n(x_i)) = f_i(\theta_n(x_i)) + g_i(\delta\theta_n(x_{i+1}), \delta\theta_n(x_i), \delta\theta_n(x_{i-1})) = 0 \quad (\text{D.8})$$

where x_i is a discrete position along the x axis, so we can form the matrix relation with all the x_i :

$$\begin{bmatrix} f_1(\theta_n(x_1)) \\ \dots \\ f_M(\theta_n(x_M)) \end{bmatrix}_{(M,1)} + \begin{bmatrix} \frac{\partial g_i}{\partial \delta\theta_n(x_i)} \end{bmatrix}_{(M,M)} \begin{bmatrix} \delta\theta_n(x_1) \\ \dots \\ \delta\theta_n(x_M) \end{bmatrix}_{(M,1)} = 0 \quad (\text{D.9})$$

Notice that $\begin{bmatrix} \frac{\partial g_i}{\partial \delta\theta_n(x_i)} \end{bmatrix}_{(M,M)}$ is trigonal. More precisely, the numerical algorithm is the following:

1. fix a Matsubara frequency n (starts a $n = 1$).
2. estimate $\theta_n([x]_{1\dots M})$, $\Delta([x]_{1\dots M})$ and $\frac{d\chi}{dx}([x]_{1\dots M})$ (initial conditions: a constant, given by the boundary condition D.7, a constant equal to $\Delta(0)$ and a *tanh* function for $\chi([x]_{1\dots M})$, such that $\chi(x_{max}) - \chi(x_{min})$ has a fixed value).
3. compute the spectral current $Q_n = \frac{d\chi}{dx} \sin^2 \theta_n$.
4. inverse $\begin{bmatrix} \frac{\partial g_i}{\partial \delta\theta_n(x_i)} \end{bmatrix}_{(M,M)}$ (with the *LU* decomposition algorithm).
5. calculate

$$[\delta\theta_n[x]]_{(M,1)} = - \begin{bmatrix} \frac{\partial g_i}{\partial \delta\theta_n[x_i]} \end{bmatrix}_{(M,M)}^{-1} [f(\theta_n[x])]_{(M,1)}$$
6. assign the new value $\theta_n' = \theta_n + \delta\theta_n$ to θ_n and reiterate steps 2 to 4 until $|\theta_n' - \theta_n| < \varepsilon$.
7. proceed steps 2 to 6 for every Matsubara frequencies (up to the one where $\omega_{n_{max}} > \omega_D$, the Debye frequency. We take $n_{max} = 25$).
8. compute the new gap $\Delta(x)$ with equation D.3.
9. compute the new phase derivative $\frac{d\chi}{dx} = \frac{Q_n}{\sin^2 \theta_n}$.
10. compute the new spectral current.
11. reiterate steps 2 to 10 until the gap value has stabilized.

Appendix E

Quasi-static impedance of a CPW line

Depending on the experimental setup that we used, there are two situations of interest for the CPW lines represented in figure E.1: a coplanar waveguide (CPW) on top of a dielectric with a finite thickness h (a), and a conductor-backed CPW (b). In the quasi-static approximation, one can compute the line characteristic impedance in a close form, for each case. We consider the thickness of the conductors forming the lines infinitely small (compared to the effective wavelength), which is valid in our case ($t_{Au} = 250$ nm). The following formulas are taken from [88].

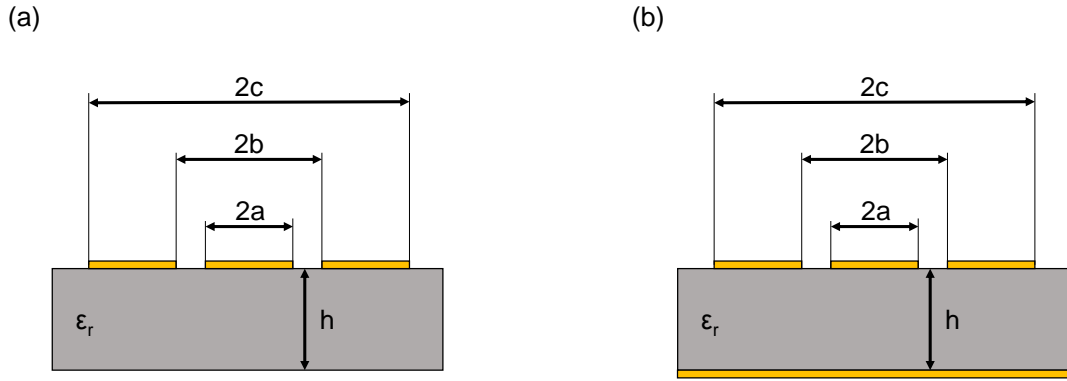


Figure E.1: (a) coplanar waveguide and (b) conductor-backed coplanar waveguide.

One defines:

$$k_1 = \frac{a}{b} \quad (\text{E.1})$$

$$k_2 = \frac{\sinh(\frac{\pi a}{2h})}{\sinh(\frac{\pi b}{2h})} \quad (\text{E.2})$$

$$k_3 = \frac{a}{b} \sqrt{\frac{1 - b^2/c^2}{1 - a^2/c^2}} \quad (\text{E.3})$$

$$k_4 = \frac{\sinh(\frac{\pi a}{2h})}{\sinh(\frac{\pi b}{2h})} \sqrt{\frac{1 - \sinh^2(\frac{\pi b}{2h})/\sinh^2(\frac{\pi c}{2h})}{1 - \sinh^2(\frac{\pi a}{2h})/\sinh^2(\frac{\pi c}{2h})}} \quad (\text{E.4})$$

In addition one defines $K()$ and $K'()$ as the complete elliptic integral of the first kind and its complement, respectively. They are related to each other by:

$$K'(k) = K(\sqrt{1 - k^2}) \quad (\text{E.5})$$

Then in situation E.1 (a), the effective relative dielectric constant ϵ_{reff}^a is given by:

$$\epsilon_{reff}^a = 1 + \frac{\epsilon_r - 1}{2} \frac{K(k_4)}{K'(k_4)} \frac{K'(k_3)}{K(k_3)} \quad (\text{E.6})$$

and the QS impedance Z_{QS}^a is given by:

$$Z_{QS}^a = \frac{30\pi}{\sqrt{\epsilon_{reff}}} \frac{K'(k_3)}{K(k_3)} \quad (\text{E.7})$$

In situation E.1 (b) one needs to define additionally:

$$k_5 = \frac{\tanh(\frac{\pi a}{2h})}{\tanh(\frac{\pi b}{2h})} \quad (\text{E.8})$$

then, the effective relative dielectric constant ϵ_{reff}^b is given by:

$$\epsilon_{reff}^b = 1 + (\epsilon_r - 1) \frac{K(k_5)/K'(k_5)}{K(k_1)/K'(k_1) + K(k_5)/K'(k_5)} \quad (\text{E.9})$$

and the characteristic impedance writes as:

$$Z_{QS}^b = \frac{60\pi}{\sqrt{\epsilon_{reff}}} \frac{1}{K(k_1)/K'(k_1) + K(k_5)/K'(k_5)} \quad (\text{E.10})$$

Appendix F

Expression of the matrix impedance terms

In the frame of the black-box theory, a mixer can be considered as having two sets of ports: two d-c ports and two r-f ports, see figure 6.2. At the d-c ports, one sends or measure a d-c current i_{dc} and voltage v_{dc} . At the r-f ports, one sends or measure an r-f current i_{rf} and voltage v_{rf} . Since the local oscillator (LO) is much stronger than any other r-f signals in the circuit, it is fair to assume that $i_{rf} = i_{lo}$ and $v_{rf} = v_{lo}$. Now, considering a d-c and r-f current bias, the d-c voltage writes as:

$$v_{dc} = v_{dc}(i_{dc}, i_{lo}) \quad (\text{F.1})$$

Since we do not (for now) chose any time origin, $i_{lo} \in \mathbb{C}$, but we always have $v_{dc}, i_{dc} \in \mathfrak{R}$ since in d-c. Thus, $v_{dc} : \mathfrak{R} \times \mathbb{C} \rightarrow \mathfrak{R}$.

Similarly, the LO voltage writes as:

$$v_{lo} = z_{lo}(i_{dc}, i_{lo})i_{lo} \quad (\text{F.2})$$

where z_{lo} is the mixer impedance at the LO frequency, and for the same reasons than previously, $v_{lo} : \mathfrak{R} \times \mathbb{C} \rightarrow \mathbb{C}$.

The black-box theory (in fact boundary conditions) leads to write the d-c and r-f differentials as:

$$\begin{aligned} di_{dc} &= \Re(i_0 e^{j\omega_{IF}t}) \\ dv_{dc} &= \Re(v_0 e^{j\omega_{IF}t}) \\ di_{lo} &= i_u e^{j\omega_{IF}t} + i_l e^{-j\omega_{IF}t} \\ dv_{lo} &= v_u e^{j\omega_{IF}t} + v_l e^{-j\omega_{IF}t} \end{aligned} \quad (\text{F.3})$$

where $\{i_0, v_0, i_u, v_u, i_l, v_l\} \in \mathbb{C}$ a priori.

Now the idea is to differentiate the complex-valued functions F.1 and F.2, and then replace the differential elements by the ones in F.3.

F.1 Complex differentiation

Let us define f as a complex-valued function:

$$\begin{aligned} f &: \mathbb{C} \rightarrow \mathbb{C} \\ z &\mapsto f(z) \end{aligned}$$

We define the complex differentials as :

$$\begin{cases} \frac{\partial f}{\partial z}(z_0) = \frac{1}{2} \left(\frac{\partial f}{\partial x}(z_0) - j \frac{\partial f}{\partial y}(z_0) \right) \\ \frac{\partial f}{\partial z^*}(z_0) = \frac{1}{2} \left(\frac{\partial f}{\partial x}(z_0) + j \frac{\partial f}{\partial y}(z_0) \right) \end{cases}$$

Then, one can write (with the correct the continuity and derivability hypothesis):

$$df(z_0) = \frac{\partial f}{\partial z}(z_0)dz + \frac{\partial f}{\partial z^*}(z_0)dz^*$$

Applied to v_{dc} it gives:

$$dv_{dc} = \frac{\partial v_{dc}}{\partial i_{dc}} di_{dc} + \frac{\partial v_{dc}}{\partial i_{lo}} di_{lo} + \frac{\partial v_{dc}}{\partial i_{lo}^*} di_{lo}^*$$

Now we choose a time origin such that $i_{lo} \in \Re$. Then one gets:

$$dv_{dc} = \frac{\partial v_{dc}}{\partial i_{dc}} di_{dc} + \frac{\partial v_{dc}}{\partial i_{lo}} (di_{lo} + di_{lo}^*) \quad (\text{F.4})$$

The differentiation of v_{lo} gives:

$$dv_{lo} = z_{lo} di_{lo} + i_{lo} \left(\frac{\partial z_{lo}}{\partial i_{dc}} di_{dc} + \frac{\partial z_{lo}}{\partial i_{lo}} di_{lo} + \frac{\partial z_{lo}}{\partial i_{lo}^*} di_{lo}^* \right)$$

Since $z_{lo}(i_{dc}, i_{lo}) = \frac{v_{lo}}{i_{lo}}$ and $i_{lo} \in \Re$ we get:

$$\begin{aligned} dv_{lo} &= \frac{v_{lo}}{i_{lo}} di_{lo} + \frac{\partial v_{lo}}{\partial i_{dc}} di_{dc} + \frac{\partial v_{lo}}{\partial i_{lo}} (di_{lo} + di_{lo}^*) \\ dv_{lo} &= \frac{\partial v_{lo}}{\partial i_{dc}} di_{dc} + \left(\frac{v_{lo}}{i_{lo}} + \frac{\partial v_{lo}}{\partial i_{lo}} \right) di_{lo} + \frac{\partial v_{lo}}{\partial i_{lo}} di_{lo}^* \end{aligned} \quad (\text{F.5})$$

F.2 Replacement of the differential terms

Let us now replace the differential terms from F.3 in F.4 and F.5. For dv_{dc} it gives in F.4:

$$\Re(v_0 e^{j\omega_0 t}) = \frac{\partial v_{dc}}{\partial i_{dc}} \Re(i_0 e^{j\omega_0 t}) + \frac{\partial v_{dc}}{\partial i_{lo}} 2\Re(di_{lo})$$

$$\Re(v_0 e^{j\omega_0 t}) = \frac{\partial v_{dc}}{\partial i_{dc}} \Re(i_0 e^{j\omega_0 t}) + \frac{\partial v_{dc}}{\partial i_{lo}} 2[\Re(i_u e^{j\omega_0 t}) + \Re(i_l e^{-j\omega_0 t})]$$

Since $\Re(z_1 z_2) = \Re(z_1^* z_2^*)$ we get:

$$\Re(v_0 e^{j\omega_0 t}) = \frac{\partial v_{dc}}{\partial i_{dc}} \Re(i_0 e^{j\omega_0 t}) + 2 \frac{\partial v_{dc}}{\partial i_{lo}} \Re(i_u e^{j\omega_0 t}) + 2 \frac{\partial v_{dc}}{\partial i_{lo}} \Re(i_l^* e^{j\omega_0 t}) \quad (\text{F.6})$$

Since $\Re(z_1 z_2) = \Re(z_1) \Im(z_2) - \Im(z_1) \Re(z_2)$, on the left-hand side, the expression $\Re(v_0 e^{j\omega_0 t})$ writes as $\Re(v_0) \cos(\omega_0 t) - \Im(v_0) \sin(\omega_0 t)$, and similarly for the right-hand side elements. Then, for any t , the equation has the form:

$$\begin{bmatrix} \Re(v_0) & \Im(v_0) \end{bmatrix} \begin{bmatrix} \cos(\omega_0 t) \\ \sin(\omega_0 t) \end{bmatrix} = \begin{bmatrix} \Re(rhs) & \Im(rhs) \end{bmatrix} \begin{bmatrix} \cos(\omega_0 t) \\ \sin(\omega_0 t) \end{bmatrix} \quad (\text{F.7})$$

where rhs is the right-hand side of equation F.6. We thus conclude that $v_0 = rhs$, that is to say:

$$v_0 = \frac{\partial v_{dc}}{\partial i_{dc}} i_0 + 2 \frac{\partial v_{dc}}{\partial i_{lo}} i_u + 2 \frac{\partial v_{dc}}{\partial i_{lo}} i_l^* \quad (\text{F.8})$$

Replacing the differentials F.3 in the expression of dv_{LO} (equation F.5) gives:

$$v_u e^{j\omega_0 t} + v_l e^{-j\omega_0 t} = \frac{\partial v_{lo}}{\partial i_{dc}} \Re(i_0 e^{j\omega_0 t}) + \left(\frac{v_{lo}}{i_{lo}} + \frac{\partial v_{lo}}{\partial i_{lo}} \right) (i_u e^{j\omega_0 t} + i_l e^{-j\omega_0 t}) + \frac{\partial v_{lo}}{\partial i_{lo}} (i_u^* e^{-j\omega_0 t} + i_l^* e^{j\omega_0 t})$$

For which the equality between the real and the imaginary part of the left and right-hand side (form as in F.7) gives:

$$\begin{aligned} v_u + v_l &= \frac{\partial v_{lo}}{\partial i_{dc}} \Re(i_0) + \left(\frac{v_{lo}}{i_{lo}} + \frac{\partial v_{lo}}{\partial i_{lo}} \right) (i_u + i_l) + \frac{\partial v_{lo}}{\partial i_{lo}} (i_u^* + i_l^*) \\ v_u - v_l &= \frac{\partial v_{lo}}{\partial i_{dc}} \Im(i_0) + \left(\frac{v_{lo}}{i_{lo}} + \frac{\partial v_{lo}}{\partial i_{lo}} \right) (i_u - i_l) + \frac{\partial v_{lo}}{\partial i_{lo}} (-i_u^* + i_l^*) \end{aligned}$$

If we now make the assumption that $i_0 \in \Re$, by making the sum and the conjugated difference of the two equation, one gets:

$$\begin{aligned} v_u &= \frac{1}{2} \frac{\partial v_{lo}}{\partial i_{dc}} i_0 + \left(\frac{v_{lo}}{i_{lo}} + \frac{\partial v_{lo}}{\partial i_{lo}} \right) i_u + \frac{\partial v_{lo}}{\partial i_{lo}} i_u^* \\ v_l^* &= \frac{1}{2} \left(\frac{\partial v_{lo}}{\partial i_{dc}} \right)^* i_0 + \left(\frac{v_{lo}}{i_{lo}} + \frac{\partial v_{lo}}{\partial i_{lo}} \right)^* i_l^* + \left(\frac{\partial v_{lo}}{\partial i_{lo}} \right)^* i_u \end{aligned} \quad (\text{F.9})$$

Thus, we can conclude on the expression of the impedance matrix \tilde{z} :

$$\begin{bmatrix} z_{uu} & z_{u0} & z_{ul} \\ z_{0u} & z_{00} & z_{0l} \\ z_{lu} & z_{l0} & z_{ll} \end{bmatrix} = \begin{bmatrix} \frac{v_{lo}}{i_{lo}} + \frac{\partial v_{lo}}{\partial i_{lo}} & \frac{1}{2} \frac{\partial v_{lo}}{\partial i_{dc}} & \frac{\partial v_{lo}}{\partial i_{lo}} \\ 2 \frac{\partial v_{dc}}{\partial i_{lo}} & \frac{\partial v_{dc}}{\partial i_{dc}} & 2 \frac{\partial v_{dc}}{\partial i_{lo}} \\ \left(\frac{\partial v_{lo}}{\partial i_{lo}} \right)^* & \frac{1}{2} \left(\frac{\partial v_{lo}}{\partial i_{dc}} \right)^* & \left(\frac{v_{lo}}{i_{lo}} + \frac{\partial v_{lo}}{\partial i_{lo}} \right)^* \end{bmatrix} \quad (\text{F.10})$$

Appendix G

Expression of conversion efficiency with impedances

The impedance matrix is defined by:

$$\tilde{z} = \begin{bmatrix} z_{uu} & z_{u0} & z_{ul} \\ z_{0u} & z_{00} & z_{0l} \\ z_{lu} & z_{l0} & z_{ll} \end{bmatrix}$$

and the external impedance matrix by:

$$\tilde{z}_{ext} = \begin{bmatrix} z_u & 0 & 0 \\ 0 & z_0 & 0 \\ 0 & 0 & z_l \end{bmatrix}$$

from which we define the total admittance matrix as:

$$\tilde{y} = (\tilde{z} + \tilde{z}_{ext})^{-1} = \begin{bmatrix} y_{uu} & y_{u0} & y_{ul} \\ y_{0u} & y_{00} & y_{0l} \\ y_{lu} & y_{l0} & y_{ll} \end{bmatrix}$$

with the latter, the conversion efficiency η writes as (see section 6.2):

$$\eta = 4\Re(z_0)\Re(z_u)|y_{0u}|^2 \quad (\text{G.1})$$

Let us express it with the impedance matrix terms. The brute-force inversion of \tilde{y} yields to:

$$y_{0u} = \frac{-z_{0u}(z_l + z_{ll}) + z_{0l}z_{lu}}{(z_0 + z_{00})[(z_u + z_{uu})(z_l + z_{ll}) - z_{ul}z_{lu}] - z_{0l}z_{l0}(z_u + z_{uu}) - z_{0u}z_{u0}(z_l + z_{ll}) + z_{0l}z_{lu}z_{u0} + z_{0u}z_{l0}z_{ul}} \quad (\text{G.2})$$

The equivalence between signal and image leads to infer:

$$z_{ll} = z_{uu}^*, z_{0l} = z_{0u}, z_{ul} = z_{lu}^*, z_{l0} = z_{u0}^* \quad (\text{G.3})$$

In addition, we consider that $z_u = z_l^*$, and that we can choose a time origin such that $z_{0u} \in \Re$ [179]. Finally, by definition, $z_{00} \in \Re$. Then equation G.2 simplifies in:

$$y_{0u} = \frac{-z_{0u}(z_u^* + z_{uu}^*) + z_{0u}z_{ul}^*}{(z_0 + z_{00})[|z_u + z_{uu}|^2 - |z_{ul}|^2] + 2z_{0u}(\Re(z_{ul}^*z_{u0}) - i\Im[z_{u0}^*(z_u + z_{uu})])}$$

Let us now compute $y_{0u}y_{0u}^*$:

$$y_{0u}y_{0u}^* = \frac{z_{0u}^2[|z_u + z_{uu}|^2 + |z_{ul}|^2 - 2\Re(z_{ul}(z_u + z_{uu}^*))]}{(z_0 + z_{00})^2[(|z_u + z_{uu}|^2 - |z_{ul}|^2) + 2z_{0u}\Re(z_{ul}^*z_{u0})]^2 + 4|z_{0u}|^2\Im(z_{u0}^*(z_u + z_{uu}))^2} \quad (\text{G.4})$$

which is difficult to interpret as it is. However, we can add the following hypothesis:

$$|z_{ul}|, |z_{u0}| \ll |z_u + z_{uu}|, \text{ and } |z_{0u}| \ll |z_0 + z_{00}| \quad (\text{G.5})$$

It is valid since in general, the external impedances $|z_u|$ and $|z_0|$ are much higher than any term in the impedance matrix of the mixer. Thus, the relation G.4 simplifies in:

$$y_{0u}y_{0u}^* = \frac{z_{0u}^2}{|z_0 + z_{00}|^2 |z_u + z_{uu}|^2} \quad (\text{G.6})$$

Consequently, the conversion efficiency η writes itself as:

$$\eta = 4z_{0u}^2 \frac{\Re(z_0)}{|z_0 + z_{00}|^2} \frac{\Re(z_u)}{|z_u + z_{uu}|^2} \quad (\text{G.7})$$

Bibliography

- [1] The 10 frequency bands of the alma antennas. <http://www.almaobservatory.org/en/about-alma/how-does-alma-work/technology/front-end>. Accessed: 2015-03-03.
- [2] Bolometers. <http://www.infraredlaboratories.com/Bolometers.html>. Accessed: 2015-11-03.
- [3] Cisco global mobile data traffic forecast update, 2014–2019. http://www.cisco.com/c/en/us/solutions/collateral/service-provider/visual-networking-index-vni/white_paper_c11-520862.html. Accessed: 2015-03-03.
- [4] Definition of technology readiness levels. http://esto.nasa.gov/files/trl_definitions.pdf. Accessed: 2015-03-03.
- [5] European frequency allocation chart. <http://www.erodocdb.dk/Docs/doc98/official/pdf/ercrep025.pdf>. Accessed: 2015-03-03.
- [6] The heterodyne instrument for the far-infrared. <https://herschel.jpl.nasa.gov/hifiInstrument.shtml>. Accessed: 2015-03-03.
- [7] High-resolution transmission molecular absorption database. <http://www.cfa.harvard.edu/hitran/>. Accessed: 2015-03-03.
- [8] The international technology roadmap for semiconductors. <http://www.itrs.net/>. Accessed: 2015-03-03.
- [9] International technology roadmap for semiconductors explores next 15 years of chip technology. http://www.semiconductors.org/news/2014/04/01/press_releases_2013/international_technology_roadmap_for_semiconductors_explores_next_15_years_of_chip_technology/. Accessed: 2015-03-03.
- [10] Man-2405 resist. http://www.microchem.com/PDFs_MRT/ma-N%202400%20overview.pdf. Accessed: 2015-02-04.
- [11] Rogers corporation laminates. <http://www.rogerscorp.com/documents/722/acs/R03000-Laminate-Data-Sheet-R03003-R03006-R03010-R03035.pdf>. Accessed: 2015-15-04.
- [12] Teraview spectrometer. <http://www.teraview.com/products/TeraPulse%204000/index.html>. Accessed: 2015-16-03.
- [13] Thz components and systems. <http://www.mtinstruments.com/>. Accessed: 2015-11-03.

- [14] U.S. frequency allocation chart. <http://www.ntia.doc.gov/page/2011/united-states-frequency-allocation-chart>. Accessed: 2015-03-03.
- [15] AA Abrikosov. Influence of the gap anisotropy on superconducting properties. Physica C: Superconductivity, 214(1):107–110, 1993.
- [16] AA Abrikosov and LP Gor’Kov. On the problem of the knight shift in superconductors. Soviet Physics JETP, 12(2), 1961.
- [17] Alekseĭ Abrikosov. Methods of quantum field theory in statistical physics.
- [18] Vinay Ambegaokar and Alexis Baratoff. Tunneling between superconductors. Phys. Rev. Letters, 10, 1963.
- [19] L Antognazza, BH Moeckly, TH Geballe, and K Char. Properties of high- T_c Josephson junctions with $y \approx 0.7$ and $a \approx 0.3$ $bcu_2O_{7-\delta}$ barrier layers. Physical Review B, 52(6):4559, 1995.
- [20] S Ariyoshi, C Otani, A Dobroiu, H Sato, K Kawase, HM Shimizu, T Taino, and H Matsuo. Terahertz imaging with a direct detector based on superconducting tunnel junctions. Applied physics letters, 88(20):203503, 2006.
- [21] Seiichiro Ariyoshi, Tohru Taino, Adrian Dobroiu, Hiromi Sato, Hiroshi Matsuo, and Chiko Otani. Terahertz detector based on a superconducting tunnel junction coupled to a thin superconductor film. Applied Physics Letters, 95(19):193504, 2009.
- [22] Philip C Ashworth, Emma Pickwell-MacPherson, Elena Provenzano, Sarah E Pinder, Anand D Purushotham, Michael Pepper, Vincent P Wallace, et al. Terahertz pulsed spectroscopy of freshly excised human breast cancer. Optics express, 17(15):12444–12454, 2009.
- [23] DD Bai, J Du, T Zhang, and YS He. A compact high temperature superconducting bandpass filter for integration with a Josephson mixer. Journal of Applied Physics, 114(13):133906, 2013.
- [24] Constantine A Balanis. Antenna theory: analysis and design. John Wiley & Sons, 2012.
- [25] John Bardeen, Leon N Cooper, and J Robert Schrieffer. Theory of superconductivity. Physical Review, 108(5):1175, 1957.
- [26] U Barkow, D Menzel, and SS Tinchev. Creating homogeneous depth profiles in YBaCuO films by ion beam implantation for uniform suppression of T_c . Physica C: Superconductivity, 370(4):246–252, 2002.
- [27] Antonio Barone and Gianfranco Paterno. Physics and applications of the Josephson effect, volume 1. Wiley New York, 1982.
- [28] J Baselmans, SJC Yates, R Barends, YJY Lankwarden, JR Gao, H Hoevers, and TM Klapwijk. Noise and sensitivity of aluminum kinetic inductance detectors for sub-mm astronomy. Journal of Low Temperature Physics, 151(1-2):524–529, 2008.
- [29] Wolfgang Belzig, Frank K Wilhelm, Christoph Bruder, Gerd Schön, and Andrei D Zaikin. Quasiclassical Green’s function approach to mesoscopic superconductivity. Superlattices and microstructures, 25(5):1251–1288, 1999.

- [30] TM Benseman, KE Gray, AE Koshelev, W-K Kwok, U Welp, H Minami, K Kadowaki, and T Yamamoto. Powerful terahertz emission from δ mesa arrays. Applied physics letters, 103(2):022602, 2013.
- [31] TM Benseman, AE Koshelev, KE Gray, W-K Kwok, U Welp, K Kadowaki, M Tachiki, and T Yamamoto. Tunable terahertz emission from δ mesa devices. Physical Review B, 84(6):064523, 2011.
- [32] SP Benz and CJ Burroughs. Coherent emission from two-dimensional josephson junction arrays. Applied physics letters, 58(19):2162–2164, 1991.
- [33] N Bergeal, X Grison, J Lesueur, G Faini, M Aprili, and JP Contour. High-quality planar high- T_c josephson junctions. Applied Physics Letters, 87(10):102502–102502, 2005.
- [34] N Bergeal, J Lesueur, M Aprili, G Faini, JP Contour, and B Leridon. Pairing fluctuations in the pseudogap state of copper-oxide superconductors probed by the josephson effect. Nature Physics, 4(8):608–611, 2008.
- [35] N Bergeal, J Lesueur, G Faini, M Aprili, and JP Contour. High T_c superconducting quantum interference devices made by ion irradiation. Applied physics letters, 89(11):112515–112515, 2006.
- [36] N Bergeal, J Lesueur, M Sirena, G Faini, M Aprili, JP Contour, and B Leridon. Using ion irradiation to make high- T_c josephson junctions. Journal of Applied Physics, 102(8):083903, 2007.
- [37] Nicolas Bergeal. Effet Josephson pour l'étude des supraconducteurs à haute température critique. PhD thesis, Université Pierre et Marie Curie-Paris VI, 2005.
- [38] S Beuven, O Harnack, and M Darula. Shorted two-dimensional high- T_c josephson arrays for oscillator applications. Applied superconductivity, 6(10):675–680, 1999.
- [39] Baokang Bi, Siyuan Han, and James E Lukens. Radiation linewidth of phase-locked distributed array in the submillimeter wave range. Applied physics letters, 62(22):2745–2747, 1993.
- [40] M Bode, M Grove, M Siegel, and AI Braginski. Superconductor–normal–superconductor step-edge junctions with Au barriers. Journal of applied physics, 80(11):6378–6384, 1996.
- [41] Niels Bohr. The penetration of atomic particles through matter, volume 18. I kommission hos E. Munksgaard, 1948.
- [42] PAA Booi and Samuel P Benz. Emission linewidth measurements of two-dimensional array josephson oscillators. Applied physics letters, 64(16):2163–2165, 1994.
- [43] PAA Booi and Samuel P Benz. High power generation with distributed josephson-junction arrays. Applied physics letters, 68(26):3799–3801, 1996.
- [44] WE Booiij, AJ Pauza, EJ Tarte, DF Moore, and MG Blamire. Proximity coupling in high- T_c josephson junctions produced by focused electron beam irradiation. Physical Review B, 55(21):14600, 1997.
- [45] Wilfred Edwin Booiij. Josephson Junctions and Devices Fabricated by Focused Electron Beam Irradiation. PhD thesis, University of Cambridge, 1997.

- [46] ER Brown. Fundamentals of terrestrial millimeter-wave and thz remote sensing. International journal of high speed electronics and systems, 13(04):995–1097, 2003.
- [47] MA Brun, F Formanek, A Yasuda, M Sekine, N Ando, and Y Eishii. Terahertz imaging applied to cancer diagnosis. Physics in Medicine and Biology, 55(16):4615, 2010.
- [48] LO Bubulac and WE Tennant. Role of hg in junction formation in ion-implanted hgccte. Applied physics letters, 51(5):355–357, 1987.
- [49] LO Bubulac, WE Tennant, DS Lo, DD Edwall, JC Robinson, JS Chen, and G Bostrup. Ion implanted junction formation in hg1- xcdxte. Journal of Vacuum Science & Technology A, 5(5):3166–3170, 1987.
- [50] Herbert B Callen and Theodore A Welton. Irreversibility and generalized noise. Physical Review, 83(1):34, 1951.
- [51] Federico Capasso, Carlo Sirtori, Jerome Faist, Deborah L Sivco, Sung-Nee G Chu, and Alfred Y Cho. Observation of an electronic bound state above a potential well. 1992.
- [52] Jian Chen, Yunqing Chen, Hongwei Zhao, Glenn J Bastiaans, and X-C Zhang. Absorption coefficients of selected explosives and related compounds in the range of 0.1-2.8 thz. Optics Express, 15(19):12060–12067, 2007.
- [53] GJ Clark, FK LeGoues, AD Marwick, RB Laibowitz, and R Koch. Ion beam amorphization of yba2cu3ox. Applied physics letters, 51(18):1462–1464, 1987.
- [54] John Clarke, SM Freake, ML Rappaport, and TL Thorp. A new experimental technique for determining the bcs interaction parameter in normal metals. Solid State Communications, 11(5):689–693, 1972.
- [55] Richard C Compton, Ross C McPhedran, Zorana Popovic, Gabriel M Rebeiz, Peter Tong, and David B Rutledge. Bow-tie antennas on a dielectric half-space: theory and experiment. Antennas and Propagation, IEEE Transactions on, 35(6):622–631, 1987.
- [56] Thomas W Crowe. Gaas schottky barrier mixer diodes for the frequency range 1–10 thz. International Journal of Infrared and Millimeter Waves, 10(7):765–777, 1989.
- [57] AM Cucolo, R Di Leo, A Nigro, P Romano, F Bobba, E Bacca, and P Prieto. Quasiparticle tunneling properties of planar yba2cu3o7-d/prba2cu3o7-d/hoba2cu3o7-d heterostructures. Physical review letters, 76(11):1920, 1996.
- [58] JC Cuevas, J Hammer, J Kopu, JK Viljas, and M Eschrig. Proximity effect and multiple andreev reflections in diffusive superconductor–normal-metal–superconductor junctions. Physical Review B, 73(18):184505, 2006.
- [59] S Cybart, P Yen, E Cho, J Huh, V Glyantsev, C Yung, Brian Moeckly, J Beeman, and R Dynes. Comparison of y-ba-cu-o films irradiated with helium and neon ions for the fabrication of josephson devices. 2014.
- [60] Shane A Cybart, Steven M Anton, Stephen M Wu, John Clarke, and Robert C Dynes. Very large scale integration of nanopatterned yba2cu3o7- δ josephson junctions in a two-dimensional array. Nano letters, 9(10):3581–3585, 2009.

- [61] Shane A Cybart, Ke Chen, and RC Dynes. Planar $\text{YBa}_2\text{Cu}_3\text{O}_{7-\delta}$ ion damage Josephson junctions and arrays. Applied Superconductivity, IEEE Transactions on, 15(2):241–244, 2005.
- [62] Shane A Cybart, EY Cho, TJ Wong, Björn H Wehlin, Meng K Ma, Chuong Huynh, and RC Dynes. Nano Josephson superconducting tunnel junctions in $\text{YBa}_2\text{Cu}_3\text{O}_{7-\delta}$ directly patterned with a focused helium ion beam. Nature nanotechnology, 2015.
- [63] TN Dalichaouch, SA Cybart, and RC Dynes. The effects of mutual inductances in two-dimensional arrays of Josephson junctions. Superconductor Science and Technology, 27(6):065006, 2014.
- [64] M Darula, T Doderer, and S Beuven. Millimetre and sub-mm wavelength radiation sources based on discrete Josephson junction arrays. Superconductor Science and Technology, 12(1):R1, 1999.
- [65] PG De Gennes. Boundary effects in superconductors. Reviews of Modern Physics, 36(1):225, 1964.
- [66] PG De Gennes and E Guyon. Superconductivity in “normal” metals. Physics Letters, 3(4):168–169, 1963.
- [67] Pierre-Gilles De Gennes and Philip A Pincus. Superconductivity of metals and alloys, volume 86. WA Benjamin New York, 1966.
- [68] IA Devyatov, LS Kuzmin, KK Likharev, VV Migulin, and AB Zorin. Quantum-statistical theory of microwave detection using superconducting tunnel junctions. Journal of applied physics, 60(5):1808–1828, 1986.
- [69] Yu Ya Divin, H Schulz, U Poppe, N Klein, K Urban, and VV Pavlovskii. Millimeter-wave Hilbert-transform spectroscopy with high- T_c Josephson junctions. Applied physics letters, 68(11):1561–1563, 1996.
- [70] J Dyson. The equiangular spiral antenna. Antennas and Propagation, IRE Transactions on, 7(2):181–187, 1959.
- [71] B Egner, J Geerk, HC Li, G Linker, O Meyer, and B Strehlau. The influence of irradiation-induced defects on the superconductivity of $\text{YBa}_2\text{Cu}_3\text{O}_7$. Japanese Journal of Applied Physics, 26(S3-3):2141, 1987.
- [72] Gert Eilenberger. General approximation method for the free energy functional of superconducting alloys. Zeitschrift für Physik, 190(2):142–160, 1966.
- [73] Gert Eilenberger. Transformation of Gorkov’s equation for type II superconductors into transport-like equations. Zeitschrift für Physik, 214(2):195–213, 1968.
- [74] H Eisele. State of the art and future of electronic sources at terahertz frequencies. Electronics Letters, 46(26):8–11, 2010.
- [75] Jerome Faist, Federico Capasso, Deborah L Sivco, Carlo Sirtori, Albert L Hutchinson, and Alfred Y Cho. Quantum cascade laser. Science, 264(5158):553–556, 1994.
- [76] John Federici and Lothar Moeller. Review of terahertz and subterahertz wireless communications. Journal of Applied Physics, 107(11):111101, 2010.

- [77] Bradley Ferguson and Xi-Cheng Zhang. Materials for terahertz science and technology. Nature materials, 1(1):26–33, 2002.
- [78] RP Feynman, RB Leighton, and M Sands. The schrödinger equation in a classical context: A seminar on superconductivity, volume iii of the feynman lectures on physics, 1965.
- [79] Yoshito Fukumoto, Rikuo Ogawa, and Yoshio Kawate. Millimeter-wave detection by ybaco step-edge microbridge josephson junction. Journal of applied physics, 74(5):3567–3571, 1993.
- [80] Ramesh Garg, Inder Bahl, and Maurizio Bozzi. Microstrip lines and slotlines. Artech house, 2013.
- [81] Andrew J Gatesman, Andriy Danylov, Thomas M Goyette, Jason C Dickinson, Robert H Giles, William Goodhue, Jerry Waldman, William E Nixon, and Weber Hoen. Terahertz behavior of optical components and common materials. In Defense and Security Symposium, pages 62120E–62120E. International Society for Optics and Photonics, 2006.
- [82] Maryvonne Gerin, M De Luca, John Black, JR Goicoechea, E Herbst, DA Neufeld, Edith Falgarone, B Godard, JC Pearson, DC Lis, et al. Interstellar oh+, h₂o+ and h₃o+ along the sight-line to g10. 6–0.4. Astronomy & Astrophysics, 518:L110, 2010.
- [83] Paul F Goldsmith, Institute of Electrical, Electronics Engineers, Microwave Theory, and Techniques Society. Quasioptical systems: Gaussian beam quasioptical propagation and applications. IEEE press New York, 1998.
- [84] Lev Petrovich Gorkov. Microscopic derivation of the ginzburg-landau equations in the theory of superconductivity. Sov. Phys. JETP, 9(6):1364–1367, 1959.
- [85] EN Grossman, CR Dietlein, J Chisum, A Luukanen, JE Bjarnasson, and ER Brown. Spectral decomposition of ultra-wide-band terahertz imagery. In Defense and Security Symposium, pages 654807–654807. International Society for Optics and Photonics, 2007.
- [86] Erich Grossman, Aaron J Miller, and Arttu Luukanen. Terahertz imaging and security applications. Bulletin of the American Physical Society, 90(91):100, 2005.
- [87] Sophie Gueron. Quasiparticles in a diffusive conductor: Interaction and pairing. PhD thesis, Université Pierre et Marie Curie-Paris VI, 1997.
- [88] Raju P Gupta and Michèle Gupta. Order-disorder-driven change in hole concentration and superconductivity in yba₂cu₃o_{6.5}. Physical Review B, 44(6):2739, 1991.
- [89] M Gurvitch, MA Washington, and HA Huggins. High quality refractory josephson tunnel junctions utilizing thin aluminum layers. Applied Physics Letters, 42(5):472–474, 1983.
- [90] Siyuan Han, Baokang Bi, Wenxing Zhang, and JE Lukens. Demonstration of josephson effect submillimeter wave sources with increased power. Applied physics letters, 64(11):1424–1426, 1994.
- [91] J Bindslev Hansen and PE Lindelof. Static and dynamic interactions between josephson junctions. Reviews of modern physics, 56(3):431, 1984.
- [92] Hans Hilgenkamp and Jochen Mannhart. Grain boundaries in high-t_c superconductors. Reviews of Modern Physics, 74(2):485, 2002.

- [93] Akihiko Hirata, Hiroyuki Takahashi, Ryoichi Yamaguchi, Toshihiko Kosugi, Koichi Murata, Tadao Nagatsuma, Naoya Kukutsu, and Yuichi Kado. Transmission characteristics of 120-ghz-band wireless link using radio-on-fiber technologies. Journal of Lightwave Technology, 26(15):2338–2344, 2008.
- [94] Akihiko Hirata, Ryoichi Yamaguchi, Toshihiko Kosugi, Hiroyuki Takahashi, Koichi Murata, Tadao Nagatsuma, Naoya Kukutsu, Yuichi Kado, Naohiko Iai, Satoshi Okabe, et al. 10-gbit/s wireless link using inp hemt mmics for generating 120-ghz-band millimeter-wave signal. Microwave Theory and Techniques, IEEE Transactions on, 57(5):1102–1109, 2009.
- [95] Warren A Holmes, James J Bock, Brendan P Crill, Timothy C Koch, William C Jones, Andrew E Lange, and Christopher G Paine. Initial test results on bolometers for the planck high frequency instrument. Applied optics, 47(32):5996–6008, 2008.
- [96] Hiromichi Hoshina, Yoshiaki Sasaki, Aya Hayashi, Chiko Otani, and Kodo Kawase. Noninvasive mail inspection system with terahertz radiation. Applied spectroscopy, 63(1):81–86, 2009.
- [97] Simon Hurand. Contrôle de la supraconductivité à l’interface d’oxydes LaAlO3/SrTiO3 par effet de champ électrique. PhD thesis, Université Pierre et Marie Curie-Paris VI, 2015.
- [98] KD Irwin. An application of electrothermal feedback for high resolution cryogenic particle detection. Applied Physics Letters, 66(15):1998–2000, 1995.
- [99] AK Jain, P Mankiewich, and JE Lukens. Observation of phase coherence among multiple josephson oscillators. Applied Physics Letters, 36(9):774–776, 1980.
- [100] Alope Kumar Jain, KK Likharev, JE Lukens, and JE Sauvageau. Mutual phase-locking in josephson junction arrays. Physics Reports, 109(6):309–426, 1984.
- [101] Brian David Josephson. Possible new effects in superconductive tunnelling. Physics letters, 1(7):251–253, 1962.
- [102] F Kahlmann, A Engelhardt, J Schubert, W Zander, Ch Buchal, and J Hollkott. Superconductor–normal–superconductor josephson junctions fabricated by oxygen implantation into $\text{YBa}_2\text{Cu}_3\text{O}_{7-\delta}$. Applied physics letters, 73(16):2354–2356, 1998.
- [103] Takanari Kashiwagi, Manabu Tsujimoto, Takashi Yamamoto, Hidetoshi Minami, Kazuhiro Yamaki, Kaveh Delfanazari, Kota Deguchi, Naoki Orita, Takashi Koike, Ryo Nakayama, et al. High temperature superconductor terahertz emitters: fundamental physics and its applications. Japanese Journal of Applied Physics, 51(1R):010113, 2012.
- [104] AS Katz, AG Sun, SI Woods, and RC Dynes. Planar thin film $\text{YBa}_2\text{Cu}_3\text{O}_{7-\delta}$ josephson junctions via nanolithography and ion damage. Applied physics letters, 72(16):2032–2034, 1998.
- [105] AS Katz, SI Woods, and RC Dynes. Transport properties of high- T_c planar josephson junctions fabricated by nanolithography and ion implantation. Journal of Applied Physics, 87(6):2978–2983, 2000.
- [106] Kodo Kawase, Yuichi Ogawa, Yuuki Watanabe, and Hiroyuki Inoue. Non-destructive terahertz imaging of illicit drugs using spectral fingerprints. Optics express, 11(20):2549–2554, 2003.

- [107] LV Keldysh. Diagram technique for nonequilibrium processes. Sov. Phys. JETP, 20(4):1018–1026, 1965.
- [108] DH Kim, CW Lee, TW Lee, HG Hwang, GY Sung, CH Choi, and TS Hahn. Effect of columnar defects in $\text{YBa}_2\text{Cu}_3\text{O}_{7-x}$ ramp-edge josephson junctions. Applied Physics Letters, 77(20):3239–3241, 2000.
- [109] Marquis A Kirk. Irradiation defect structures in $\text{YBa}_2\text{Cu}_3\text{O}_{7-x}$ and their correlation with superconducting properties. In MRS Proceedings, volume 209, page 743. Cambridge Univ Press, 1990.
- [110] Thomas Kleine-Ostmann and Tadao Nagatsuma. A review on terahertz communications research. Journal of Infrared, Millimeter, and Terahertz Waves, 32(2):143–171, 2011.
- [111] Roger H Koch, Dale J Van Harlingen, and John Clarke. Measurements of quantum noise in resistively shunted josephson junctions. Physical Review B, 26(1):74, 1982.
- [112] Roger H Koch, DJ Van Harlingen, and John Clarke. Quantum-noise theory for the resistively shunted josephson junction. Physical Review Letters, 45(26):2132, 1980.
- [113] D Koelle, R Kleiner, F Ludwig, E Dantsker, and John Clarke. High-transition-temperature superconducting quantum interference devices. Reviews of Modern Physics, 71(3):631, 1999.
- [114] Rüdiger Köhler, Alessandro Tredicucci, Fabio Beltram, Harvey E Beere, Edmund H Linfield, A Giles Davies, David A Ritchie, Rita C Iotti, and Fausto Rossi. Terahertz semiconductor-heterostructure laser. Nature, 417(6885):156–159, 2002.
- [115] Christopher T Konek, Brian P Mason, Joseph P Hooper, Chad A Stoltz, and John Wilkinson. Terahertz absorption spectra of 1, 3, 5, 7-tetranitro-1, 3, 5, 7-tetrazocane (hmx) polymorphs. Chemical Physics Letters, 489(1):48–53, 2010.
- [116] J Konopka, I Wolff, S Beuven, and M Siegel. Mixing and detection in YBaCuO step-edge josephson junction arrays up to 670 ghz. Applied Superconductivity, IEEE Transactions on, 5(2):2443–2446, 1995.
- [117] Nikolai B. Kopnin. Theory of Nonequilibrium superconductivity. Oxford University Press, 2001.
- [118] EL Kosarev, A Ya Shul'man, MA Tarasov, and T Lindstroem. Deconvolution problems and superresolution in hilbert-transform spectroscopy based on ac josephson effect. Computer Physics Communications, 151(2):171–186, 2003.
- [119] G Kunkel and Ronald H Ono. Mutual phase-locking of ten $\text{YBa}_2\text{Cu}_3\text{O}_7$ step-edge josephson junctions up to 45 k. Applied physics letters, 69(13):1960–1962, 1996.
- [120] Gerhard Kunkel, Gerd Hechtfisher, Michael Frommberger, Klaus Veit, Reinhold Kleiner, P Müller, Werner Prusseit, Helmut Kinder, Lars Ferchland, Gabriel Daalmans, et al. Millimeter-wave radiation in high- T_c josephson junctions. IEEE transactions on applied superconductivity, 7(2):3339–3342, 1997.
- [121] Hélène Le Sueur. Cryogenic AFM-STM for mesoscopic physics. PhD thesis, Université Pierre et Marie Curie-Paris VI, 2007.

- [122] Alan WM Lee, Benjamin S Williams, Sushil Kumar, Qing Hu, and John L Reno. Real-time imaging using a 4.3-thz quantum cascade laser and a 320/spl times/240 microbolometer focal-plane array. Photonics Technology Letters, IEEE, 18(13):1415–1417, 2006.
- [123] Soon-Gul Lee, Yunseok Hwang, Jin-Tae Kim, and Gun Yong Sung. Effects of d-wave symmetry in high t_c step-edge josephson junctions. Physica C: Superconductivity, 341:1473–1474, 2000.
- [124] Yun-Shik Lee. Principles of Terahertz Science and Technology: Proceedings of the International Conference, Held in Mainz, Germany, June 5-9, 1979, volume 170. Springer Science & Business Media, 2009.
- [125] A Legris, F Rullier-Albenque, E Radeva, and P Lejay. Effects of electron irradiation on $\text{YBa}_2\text{Cu}_3\text{O}_{7-\delta}$ superconductor. Journal de physique I, 3(7):1605–1615, 1993.
- [126] J Lesueur, L Dumoulin, S Quillet, and J Radcliffe. Ion-beam induced metal insulator transition in YBCO films. Journal of alloys and compounds, 195:527–530, 1993.
- [127] J Lesueur, P Nedellec, H Bernas, JP Burger, and L Dumoulin. Depairing-like variation of t_c in $\text{YBa}_2\text{Cu}_3\text{O}_{7-\delta}$. Physica C: Superconductivity, 167(1):1–5, 1990.
- [128] M-Y Li, K Tilley, J McCleary, and K Chang. Broadband coplanar waveguide-coplanar strip-fed spiral antenna. Electronics Letters, 31(1):4–5, 1995.
- [129] Konstantin Konstantinovic Likharev and Konstantin Konstantinovich Likharev. Dynamics of Josephson junctions and circuits. Gordon and Breach Science Publ., 1991.
- [130] KK Likharev. Superconducting weak links. Reviews of Modern Physics, 51(1):101, 1979.
- [131] KK Likharev and VK Semenov. Fluctuation spectrum in superconducting point junctions. ZhETF Pisma Redaktsiiu, 15:625, 1972.
- [132] Konstantin K Likharev and Vasilii K Semenov. Rsfq logic/memory family: a new josephson-junction technology for sub-terahertz-clock-frequency digital systems. Applied Superconductivity, IEEE Transactions on, 1(1):3–28, 1991.
- [133] Jens Lindhard, Morten Scharff, and Hans E Schioett. Range concepts and heavy ion ranges (notes on atomic collisions, ii). Kgl. Danske Videnskab. Selskab. Mat. Fys. Medd., 33(14), 1963.
- [134] M Lyatti, Y Divin, U Poppe, and K Urban. Liquid identification by hilbert spectroscopy. Superconductor Science and Technology, 22(11):114005, 2009.
- [135] M Malnou, C Feuillet-Palma, C Ulysse, G Faini, P Febvre, M Sirena, L Olanier, J Lesueur, and N Bergeal. High- t_c superconducting josephson mixers for terahertz heterodyne detection. Journal of Applied Physics, 116(7):074505, 2014.
- [136] M Malnou, A Luo, T Wolf, Y Wang, C Feuillet-Palma, C Ulysse, G Faini, P Febvre, M Sirena, J Lesueur, et al. Toward terahertz heterodyne detection with superconducting josephson junctions. Applied Physics Letters, 101(23):233505, 2012.
- [137] CM Mann. Towards terahertz communications systems. In Terahertz sources and systems, pages 261–267. Springer, 2001.

- [138] Steven M Marazita, William L Bishop, Jeffrey L Hesler, Kai Hui, Willie E Bowen, and Thomas W Crowe. Integrated gaas schottky mixers by spin-on-dielectric wafer bonding. Electron Devices, IEEE Transactions on, 47(6):1152–1157, 2000.
- [139] Takeo Matsubara. A new approach to quantum-statistical mechanics. Progress of theoretical physics, 14(4):351–378, 1955.
- [140] Hiroshi Matsuo. Future prospects of superconducting direct detectors in terahertz frequency range. Nuclear Instruments and Methods in Physics Research Section A: Accelerators, Spectrometers, Detectors and Associated Equipment, 559(2):748–750, 2006.
- [141] DE McCumber. Effect of ac impedance on dc voltage-current characteristics of superconductor weak-link junctions. Journal of Applied Physics, 39(7):3113–3118, 1968.
- [142] EE Mitchell and CP Foley. Ybco step-edge junctions with high icrn. Superconductor Science and Technology, 23(6):065007, 2010.
- [143] EE Mitchell and CP Foley. Ybco step-edge junctions: influence of morphology on junction transport. Applied Superconductivity, IEEE Transactions on, 21(3):371–374, 2011.
- [144] EE Mitchell, JC Macfarlane, and CP Foley. Transport properties of variable-angle $yba_2cu_3o_{7-\delta}$ step-edge junctions in the a–b plane. Superconductor Science and Technology, 24(5):055004, 2011.
- [145] Naoto Nagai, Ryoichi Kumazawa, and Ryoichi Fukasawa. Direct evidence of intermolecular vibrations by thz spectroscopy. Chemical physics letters, 413(4):495–500, 2005.
- [146] Tadao Nagatsuma, Hiroshi Ito, and Tadao Ishibashi. High-power rf photodiodes and their applications. Laser & Photonics Reviews, 3(1-2):123–137, 2009.
- [147] Yoichiro Nambu. Quasi-particles and gauge invariance in the theory of superconductivity. Physical Review, 117(3):648, 1960.
- [148] DA Neufeld, JR Goicoechea, P Sonnentrucker, John H Black, J Pearson, S Yu, TG Phillips, DC Lis, M De Luca, E Herbst, et al. Herschel/hifi observations of interstellar oh+ and h2o+ towards w49n: a probe of diffuse clouds with a small molecular fraction. Astronomy & Astrophysics, 521:L10, 2010.
- [149] T Noguchi, A Ueda, H Iwashita, S Takano, Y Sekimoto, M Ishiguro, T Ishibashi, H Ito, and T Nagatsuma. Millimeter wave generation using a uni-traveling-carrier photodiode. In Proc. 12th Int. Symp. Space Terahertz Technology, volume 2001, pages 73–80, 2001.
- [150] Harry Nyquist. Thermal agitation of electric charge in conductors. Physical review, 32(1):110–113, 1928.
- [151] L Ozyuzer, AE Koshelev, C Kurter, N Gopalsami, Q Li, M Tachiki, K Kadowaki, T Yamamoto, H Minami, H Yamaguchi, et al. Emission of coherent thz radiation from superconductors. Science, 318(5854):1291–1293, 2007.
- [152] AJ Pauza, WE Booij, K Herrmann, DF Moore, MG Blamire, DA Rudman, and LR Vale. Electron-beam damaged high-temperature superconductor josephson junctions. Journal of applied physics, 82(11):5612–5632, 1997.

- [153] Nianhua Peng, Dae Joon Kang, Chris Jeynes, Roger P Webb, David F Moore, Mark G Blamire, and Ivan R Chakarov. High quality $yBa_2Cu_3O_{7-\delta}$ Josephson junctions and junction arrays fabricated by masked proton beam irradiation damage. Applied Superconductivity, IEEE Transactions on, 13(2):889–892, 2003.
- [154] U Poppe, YY Divin, MI Faley, JS Wu, CL Jia, P Shadrin, and K Urban. Properties of $yBa_2Cu_3O_{7-\delta}$ thin films deposited on substrates and bicrystals with vicinal offcut and realization of high i_c junctions. Applied Superconductivity, IEEE Transactions on, 11(1):3768–3771, 2001.
- [155] David M Pozar. Microwave Engineering. 4th. Wiley, 2011.
- [156] Albert Redo-Sanchez, Norman Laman, Brian Schulkin, and Thomas Tongue. Review of terahertz technology readiness assessment and applications. Journal of Infrared, Millimeter, and Terahertz Waves, 34(9):500–518, 2013.
- [157] MO Reese, DF Santavicca, DE Prober, AB True, and CA Schmittenmaer. Niobium direct detectors for fast and sensitive terahertz spectroscopy. Review of Scientific Instruments, 78(8):086111–086111, 2007.
- [158] CD Reintsema, RH Ono, G Barnes, L Borchardt, TE Harvey, G Kunkel, DA Rudman, LR Vale, N Missert, and PA Rosenthal. The critical current and normal resistance of high- t /sub c /step-edge junctions. Applied Superconductivity, IEEE Transactions on, 5(2):3405–3409, 1995.
- [159] CC Rousseau, WK Chu, and D Powers. Calculations of stopping cross sections for 0.8- to 2.0-MeV alpha particles. Physical Review A, 4(3):1066, 1971.
- [160] M-O Ruault, H Bernas, J Lesueur, L Dumoulin, M Nicolas, J-P Burger, M Gasgnier, H Noel, P Gougeon, M Potel, et al. Irradiation-induced orthorhombic-to-tetragonal phase transition in $RbBa_2Cu_3O_{7-x}$ ($x = 0, 0.1, 0.2$). EPL (Europhysics Letters), 7(5):435, 1988.
- [161] V Rumsey. Frequency independent antennas. In 1958 IRE International Convention Record, volume 5, pages 114–118. IEEE, 1957.
- [162] Jens Scherbel, Marian Darula, Oliver Harnack, and Michael Siegel. Noise properties of HTS Josephson mixers at 345 GHz and operating temperatures at 20 K. Applied Superconductivity, IEEE Transactions on, 12(2):1828–1831, 2002.
- [163] Robert J Schoelkopf. Studies of noise in Josephson-effect mixers and their potential for submillimeter heterodyne detection. PhD thesis, 1995.
- [164] Robert J Schoelkopf, Jonas Zmuidzinas, Thomas G Phillips, Henry G LeDuc, and Jeffrey A Stern. Measurements of noise in Josephson-effect mixers. Microwave Theory and Techniques, IEEE Transactions on, 43(4):977–983, 1995.
- [165] S Sekimoto, C Watanabe, H Minami, T Yamamoto, T Kashiwagi, Richard A Klemm, and K Kadowaki. Continuous 30 μ W terahertz source by a high- T_c superconductor mesa structure. Applied Physics Letters, 103(18):182601, 2013.
- [166] Sidney Shapiro. Josephson currents in superconducting tunneling: The effect of microwaves and other observations. Phys. Rev. Letters, 11, 1963.

- [167] Yao-Chun Shen and Philip F Taday. Development and application of terahertz pulsed imaging for nondestructive inspection of pharmaceutical tablet. Selected Topics in Quantum Electronics, IEEE Journal of, 14(2):407–415, 2008.
- [168] VV Shirotov and Yu Ya Divin. Frequency-selective josephson detector: Power dynamic range at subterahertz frequencies. Technical physics letters, 30(6):522–524, 2004.
- [169] Peter H Siegel et al. Terahertz technology. IEEE Transactions on microwave theory and techniques, 50(3):910–928, 2002.
- [170] M Sirena, N Bergeal, J Lesueur, G Faini, R Bernard, J Briatico, DG Crete, and JP Contour. Study and optimization of ion-irradiated high tc josephson junctions by monte carlo simulations. Journal of applied physics, 101(12):123925, 2007.
- [171] M Sirena, S Matzen, N Bergeal, J Lesueur, G Faini, R Bernard, J Briatico, and DG Crete. Improving ion irradiated high t c josephson junctions by annealing: The role of vacancy-interstitial annihilation. Applied Physics Letters, 91(14):142506–142506, 2007.
- [172] M Sirena, S Matzen, N Bergeal, J Lesueur, G Faini, R Bernard, J Briatico, and DG Cr  t  . Annealing of ion irradiated high t c josephson junctions studied by numerical simulations. Journal of Applied Physics, 105(2):023910–023910, 2009.
- [173] F Sizov and A Rogalski. Thz detectors. Progress in Quantum Electronics, 34(5):278–347, 2010.
- [174] Fengbin Song, Franz M  ller, Thomas Scheller, Alexei Semenov, Ming He, Lan Fang, Heinz-Wilhelm H  bers, and Alexander M Klushin. Compact tunable sub-terahertz oscillators based on josephson junctions. Applied Physics Letters, 98(14):142506, 2011.
- [175] Ho-Jin Song and Tadao Nagatsuma. Present and future of terahertz communications. Terahertz Science and Technology, IEEE Transactions on, 1(1):256–263, 2011.
- [176] Benjamin St Peter, Sigfrid Yngvesson, Paul Siqueira, Patrick Kelly, Ashraf Khan, Stephen Glick, and Andrew Karellas. Development and testing of a single frequency terahertz imaging system for breast cancer detection. Biomedical and Health Informatics, IEEE Journal of, 17(4):785–797, 2013.
- [177] WC Stewart. Current-voltage characteristics of josephson junctions. Applied Physics Letters, 12(8):277–280, 1968.
- [178] MD Strikovski, F Kahlmann, J Schubert, W Zander, V Glyantsev, G Ockenfuss, and CL Jia. Fabrication of yba2cu3ox thin-film flux transformers using a novel microshadow mask technique for insitu patterning. Applied physics letters, 66(25):3521–3523, 1995.
- [179] Yuan Taur. Josephson-junction mixer analysis using frequency-conversion and noise-correlation matrices. Electron Devices, IEEE Transactions on, 27(10):1921–1928, 1980.
- [180] Jesper Thaysen, Kaj B Jakobsen, and J  rgen Appel-Hansen. A logarithmic spiral antenna for 0.4 to 3.8 ghz. Applied Microwave and Wireless, 13(2):32–45, 2001.
- [181] SS Tinchev. Investigation of rf squids made from epitaxial ybco films. Superconductor Science and Technology, 3(10):500, 1990.
- [182] SS Tinchev. Properties of ybco weak links prepared by local oxygen-ion induced modification. Physica C: Superconductivity, 256(1):191–198, 1996.

- [183] Sergey K Tolpygo, J-Y Lin, Michael Gurvitch, SY Hou, and Julia M Phillips. Effect of oxygen defects on transport properties and T_c of $YBa_2Cu_3O_{6+x}$: Displacement energy for plane and chain oxygen and implications for irradiation-induced resistivity and T_c suppression. Physical Review B, 53(18):12462, 1996.
- [184] Sergey K Tolpygo, J-Y Lin, Michael Gurvitch, SY Hou, and Julia M Phillips. Universal T_c suppression by in-plane defects in high-temperature superconductors: Implications for pairing symmetry. Physical Review B, 53(18):12454, 1996.
- [185] Masayoshi Tonouchi. Cutting-edge terahertz technology. Nature photonics, 1(2):97–105, 2007.
- [186] Henry C Torrey and Charles A Whitmer. Crystal rectifiers. 1948.
- [187] J Trastoy, M Malnou, C Ulysse, R Bernard, N Bergeal, G Faini, J Lesueur, J Briatico, and Javier E Villegas. Freezing and thawing of artificial ice by thermal switching of geometric frustration in magnetic flux lattices. Nature nanotechnology, 9(9):710–715, 2014.
- [188] Klaus D Usadel. Generalized diffusion equation for superconducting alloys. Physical Review Letters, 25(8):507, 1970.
- [189] JM Valles Jr, AE White, KT Short, RC Dynes, JP Garno, AFJ Levi, M Anzlowar, and K Baldwin. Ion-beam-induced metal-insulator transition in $YBa_2Cu_3O_{7-\delta}$: A mobility edge. Physical Review B, 39(16):11599, 1989.
- [190] Theodore Van Duzer and Charles William Turner. Principles of superconductive devices and circuits. 1981.
- [191] AN Vystavkin, VN Gubankov, LS Kuzmin, KK Likharev, VV Migulin, and VK Semenov. Scs junctions as nonlinear elements of microwave receiving devices. Revue de Physique Appliquée, 9(1):79–109, 1974.
- [192] K Wan, AK Jain, LA Fetter, W Zhang, S Han, and JE Lukens. Development of a rapidly tunable microwave source. Superconductor Science and Technology, 4(11):647, 1991.
- [193] Kanglin Wang and Daniel M Mittleman. Metal wires for terahertz wave guiding. Nature, 432(7015):376–379, 2004.
- [194] NR Werthamer. Theory of the superconducting transition temperature and energy gap function of superposed metal films. Physical Review, 132(6):2440, 1963.
- [195] Alice E White, KT Short, RC Dynes, AFJ Levi, M Anzlowar, KW Baldwin, PA Polakos, TA Fulton, and LN Dunkleberger. Controllable reduction of critical currents in $YBa_2Cu_3O_{7-\delta}$ films. Applied physics letters, 53(11):1010–1012, 1988.
- [196] K Wiesenfeld, Samuel P Benz, and PAA Booï. Phase-locked oscillator optimization for arrays of josephson junctions. Journal of applied physics, 76(6):3835–3846, 1994.
- [197] Benjamin S Williams. Terahertz quantum-cascade lasers. Nature photonics, 1(9):517–525, 2007.
- [198] WD Wilson, LG Haggmark, and JP Biersack. Calculations of nuclear stopping, ranges, and straggling in the low-energy region. Physical Review B, 15(5):2458, 1977.
- [199] Thomas Wolf. High temperature superconductor Josephson nano-junctions as terahertz detection devices. Theses, Université Pierre et Marie Curie - Paris VI, December 2010.

-
- [200] Ruth M Woodward, Bryan E Cole, Vincent P Wallace, Richard J Pye, Donald D Arnone, Edmund H Linfield, and Michael Pepper. Terahertz pulse imaging in reflection geometry of human skin cancer and skin tissue. Physics in medicine and biology, 47(21):3853, 2002.
- [201] GC Xiong, HC Li, G Linker, and O Meyer. Transport properties, phase transition, and recovery near 200 k of proton-irradiated y ba 2 cu 3 o 7 thin films. Physical Review B, 38(1):240, 1988.
- [202] SJC Yates, JJA Baselmans, A Endo, RMJ Janssen, L Ferrari, P Diener, and AM Baryshev. Photon noise limited radiation detection with lens-antenna coupled microwave kinetic inductance detectors. Applied Physics Letters, 99(7):073505, 2011.
- [203] V Zavaleev and KK Likharev. Performance limits of the josephson junction microwave receivers. Magnetics, IEEE Transactions on, 17(1):830–833, 1981.
- [204] James F Ziegler, Jochen P Biersack, and Matthias D Ziegler. SRIM, the stopping and range of ions in matter. Lulu. com, 2008.
- [205] Jonas Zmuidzinas and Paul L Richards. Superconducting detectors and mixers for millimeter and submillimeter astrophysics. Proceedings of the IEEE, 92(10):1597–1616, 2004.

